

Numerical Simulations of Blazar Jets and their Non-thermal Radiation

Dissertation
der Fakultät für Physik
der
Ludwig-Maximilians-Universität München

angefertigt von
Petar Mimica
aus Mimice

München, den September 22, 2004

1. Gutachter: Prof. Dr. Gerhard Börner
2. Gutachter: Prof. Dr. Harald Lesch

Tag der mündlichen Prüfung: 22. November 2004

Teče i teče, teče jedan slap;
Što u njem znači moja mala kap?

Gle, jedna duga u vodi se stvara,
I sja i dršće u hiljadu šara.

Taj san u slapu da bi mogo sjati,
I moja kaplja pomaže ga tkati.

“Slap” - Dobriša Cesarić

Contents

Abstract	7
1 Introduction	11
1.1 Active galactic nuclei	11
1.2 Observations of AGNs	13
1.2.1 AGN morphology	14
1.2.2 AGN classification	15
1.2.3 Parsec scale jets	18
1.3 BL Lac objects	18
1.3.1 Blazar spectra	20
1.3.2 Variability	22
1.3.3 Blazar X-ray light curves	23
1.4 Theoretical models	25
1.4.1 Apparent superluminal motion	25
1.4.2 AGN unification	26
1.4.3 Internal shock model	27
1.5 Existing numerical methods used to produce synthetic light curves	29
1.6 Motivation	33
2 Non-thermal radiation	35
2.1 Synchrotron radiation	35
2.1.1 Radiation emitted by a single charged particle	35
2.1.2 Radiation emitted by a distribution of particles	41
2.1.3 Radiation from a power law distribution of particles	45
2.2 Inverse-Compton scattering	46
2.2.1 Scattering of the monochromatic radiation	46
2.2.2 Scattering of radiation whose intensity per unit fre- quency is a power law	52
3 Non-thermal particles	57
3.1 Acceleration of particles at the shock fronts	57
3.1.1 Non-relativistic shocks	57
3.1.2 Relativistic shocks	59
3.2 Evolution of non-thermal particles	62
3.2.1 Kinetic equation	62

4	Numerical method	67
4.1	Numerical RHD	67
4.1.1	Applicability of the ideal RHD approximation	67
4.1.2	Equations of ideal RHD	68
4.1.3	RHD numerical scheme	69
4.2	Treatment of the non-thermal particles	71
4.2.1	Spatial transport: non-thermal particles as tracers	71
4.2.2	The kinetic equation solver	71
4.2.3	The treatment of the source term	73
4.3	Non-thermal radiation	76
4.3.1	Treatment of the synchrotron radiation	76
4.3.2	Light curve computation	78
4.4	Method validation	81
4.4.1	Tests of the kinetic-equation solver	81
4.4.2	Test of the synchrotron radiation code	86
5	Simulations of blazar flares	91
5.1	Introduction to blazar simulations	91
5.1.1	The physical model	91
5.1.2	Numerical details of the simulations	92
5.2	Two dimensional simulations	95
5.2.1	Hydrodynamic evolution	95
5.2.2	S0 light curve	98
5.2.3	Influence of the density	100
5.2.4	Influence of the pressure	101
5.3	One dimensional simulations	102
5.3.1	Spacetime analysis of the light curve	103
5.3.2	Light curves of one-dimensional models	105
5.3.3	Spacetime evolution of the emissivity	111
5.3.4	Spectral evolution	111
5.4	Analytic flare model	116
5.4.1	Application to models G0E, G1E and G2E	127
5.5	Comparison with observations of blazar flares	130
5.6	Simulations of multiple collisions	132
5.6.1	A model of an inhomogeneous blazar jet	132
6	Summary and conclusions	137
6.1	Summary of the results	137
6.2	Next steps	138
A	The fitting algorithm	141
	List of tables	145
	List of figures	145
	Bibliography	148

Abstract

In the past years relativistic (magneto)hydrodynamic simulations have been used extensively to study the time-dependent hydrodynamic properties of extra galactic jets. While these simulations have been very successful in studying the formation, collimation, propagation and termination of relativistic jets, the models used to compute synthetic images from the hydrodynamic properties were relatively simple (but see, e.g., Jones et al. (1999) for an example of a more sophisticated model). On the other hand, there exist several theoretical models which assume a very simple hydrodynamic evolution, but treat the non-thermal particles and their emitted radiation with great detail.

It was the aim of this work to include a detailed treatment of the non-thermal particles and their synchrotron radiation in high-resolution shock-capturing relativistic hydrodynamic (RHD) simulations. To achieve this goal we have developed a transport scheme for the non-thermal particles by treating them as “tracer” fluids in the RHD equations. Their temporal evolution is calculated using an analytic kinetic equation solver, and their synchrotron radiation is computed in a time-dependent manner taking into account the relevant relativistic effects, (e.g., light travel times to the observer). The energy density of a dynamically negligible magnetic field is assumed to be a fraction of the energy density of the thermal fluid. Two models have been developed for the parameterization of the acceleration of non-thermal particles at relativistic shocks: A type-E model where only the strength of the shock influences the number of accelerated particles and a type-N model where the shock strength only influences their energy distribution.

We have demonstrated that our numerical method is able to capture the essentials of the temporal and spatial evolution of the non-thermal particles and the observed synchrotron radiation with a reasonable accuracy when applied to subparsec scale relativistic jets.

Understanding the physical processes connected to the observed X-ray blazar light curves has been the main object of research with our new numerical tool. For the first time, the hydrodynamic evolution and the synchrotron radiation of a blazar jet was simulated consistently. We have simulated collisions of density inhomogeneities (shells) within a blazar jet. The results have shown that the efficiency of the observed synchrotron radiation varies with the relative velocities of the shells as well as with the amount of initially available mass. The surrounding medium plays an important role, because it heats up the shells prior to the collision, a fact which is neglected

in simpler models.

Assuming that the observed radiation results from the interaction of shells within a blazar jet, we have developed an analytic model which enables the determination of the unobservable parameters of the jets (i.e., length and velocity of the shells) from the light curve. The parameters predicted by the model have been compared to results of our simulations and we find that the agreement is surprisingly good, given the simplicity of the model.

In addition, several long-term simulations of collisions of many shells have shown that a model of an intermittently working central engine seems to produce light curves more similar the observed ones than a model in which the central engine ejects a continuous outflow.

Astronomy treated its students kindly, providing many tasks that were true, solid science and even might lead to an important result. The universe was still so poorly known that surprises lurked everywhere, especially when one had a new instrument with greater seeing power, or the ability to peer into the fresh region of the spectrum. The newer 'scopes were mostly distant hardware operated by a corps of technicians. Astronomers themselves ruled these by long distance, asking for spots in the night sky to be scrutinized, all over a Net connection. Nobody squinted through eyepieces anymore.

from "Eater" - Gregory Benford

Chapter 1

Introduction

In this chapter the observations of relativistic jets and the theoretical models constructed to explain them are discussed.

1.1 Active galactic nuclei

In the early 1960s the source 3C273 was observed by Marteen Schmidt. It was not resolved at optical wavelengths and had a stellar-like appearance. 3C273 and other objects of its class were named *quasars* (from Quasi-Stellar Objects or QSOs). At that time 3C273 was peculiar due to the fact that it emitted 100 times more light than a typical galaxy.

The big leap forward came with the advances in astrophysical observations, especially with the introduction of the *aperture synthesis* (for which Martin Ryle got the Nobel prize in physics in 1974). This technique combines several radio-telescopes into one big “virtual” telescope which has a baseline equivalent to the largest distance between any pair of telescopes which are being combined. When telescopes located all around the Earth are combined we talk of *Very Long Baseline Interferometry* (VLBI). It was VLBI that enabled us to observe quasars at a resolution of the order of several tenths of an arcsecond. This type of observations revealed that the radio emission of quasars is often dominated by structures which look like *jets*, connecting the central compact region of a quasar with external structures, which are sometimes located at very large distances (of the order of a megaparsec¹) from the quasar.

Today we know that quasars are a sub-class of the type of objects known as *active galactic nuclei* (AGN). AGNs are characterized by the presence of the central compact region (with a size of the order of a parsec) emitting enormous quantities of energy with a luminosity which, in many cases, exceeds the luminosity of a typical galaxy by a factor of 10^4 .

The first hint that ejection of matter plays an important role in AGNs came, in retrospect, from the discovery of the jet (described at the time as a “curious straight ray connected to the nucleus of M87”) on photographs of the galaxy M87 taken with Lick Observatory’s 0.9-m Crossley reflector in 1918 (Curtis 1918). Fig. 1.1 shows the Hubble Space Telescope (HST)

¹A *parsec* (pc) is the distance traveled by the light in 3.26 years, $1 \text{ pc} = 3.085678 \times 10^{18} \text{ cm}$.

image of the M87 galaxy. The bright spot towards the lower left corner is the AGN. The jet in this image can be identified with the outflow of matter from the AGN (in section 1.2.1 we will give a quantitative definition of a jet).



Figure 1.1: HST image of the M87 galaxy and its jet. The bright spot towards the lower left corners the AGN from which matter is being ejected in the form of a jet. (Credits for the image: John Biretta).

One of the first evidences for highly collimated astrophysical jets goes back to the early radio observations of twin lobes in extended radio galaxies (e.g., Cygnus A (Jennison & Das Gupta 1953); see Fig. 1.2). Many of these radio sources have been identified to be extra-galactic objects, i.e., their distance from Earth is much larger than the typical dimension of our Galaxy (≈ 30 kpc). Soon it became clear that both jets and lobes had linear dimensions up to megaparsecs and that they emit a large amount of non-thermal radiation (up to 10^{47} erg s^{-1}) in the radio band. The measurements of the optical polarization of the jet of M87 (Baade 1956) proved the assumption that the non-thermal *synchrotron radiation*² was due to emission of relativistic electrons. Attempts to explain observed jet features with the ejection of relativistic balls of plasma from the central object failed, because to support such a model the energies involved had to be huge and

²As we shall see in section 2.1, the synchrotron radiation is produced by very fast moving electrons which gyrate in a magnetic field. Due to the radiation they slow down so that their energy loss rate dE/dt is proportional to E^2 , where E is the total energy of the gyrating electron. This determines a typical time scale, the *synchrotron cooling time* (see section 3.2.1), after which there are no electrons above some energy E .

because the synchrotron cooling time of the emitting electrons is too short (i.e. $< 10^6$ years), requiring an electron re-acceleration mechanism.

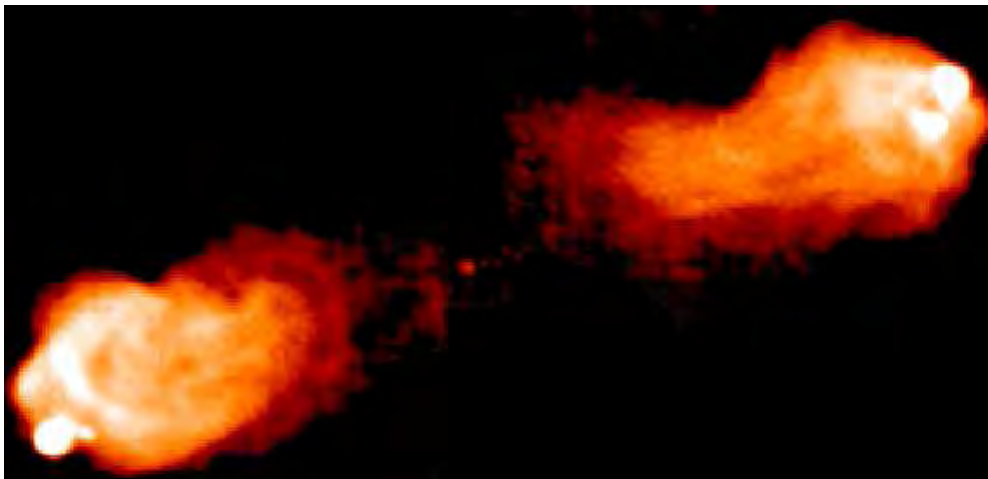


Figure 1.2: A radio map (at a wavelength of 22cm) of the powerful radio galaxy Cygnus A, produced from observations at the Very Large Array (VLA) by John Conway and Philip Blanco in March 1994. The image shows Cygnus A's double radio lobes, spanning over 500,000 light years, which are fed by jets of energetic particles beamed from the compact radio core between them.

In an attempt to explain the nature of the M87 jet, and of jets in general, Shklovskii (1963) first proposed a number of ideas which are still essential for the theoretical modeling of extra-galactic jets today: the notion that the plasma is accreted onto the AGN, heated and then ejected along a preferred axis into the intergalactic medium. In 1974 another important suggestion concerning the way in which energy is transported along the jet was made: energy is transported in the form of beams where most of the accreting plasma's internal energy is transformed into kinetic energy (Blandford & Ressler 1974), which is then converted back into thermal energy (and eventually radiated) due to the interaction of the beam with the surrounding medium (e.g., lobes in Fig. 1.2). As the angular resolution of the radio observations increased, it was discovered that the jets reach all the way from the radio-lobes to the core of the AGN. The astonishing fact is that the jets remain collimated from the sub-parsec out to the megaparsec scale (Bridle et al. 1980; Linfield & Perley 1984)!

1.2 Observations of AGNs

In order to understand the nature of AGNs, it is necessary to describe their main morphological features. Section 1.2.1 contains a description of main parts of an AGN, and its main characteristics. The classification, a prerequisite for the general understanding of AGNs is given in section 1.2.2. Finally, section 1.2.3 focuses on properties of the parsec-scale jets which are the object of our research.

1.2.1 AGN morphology

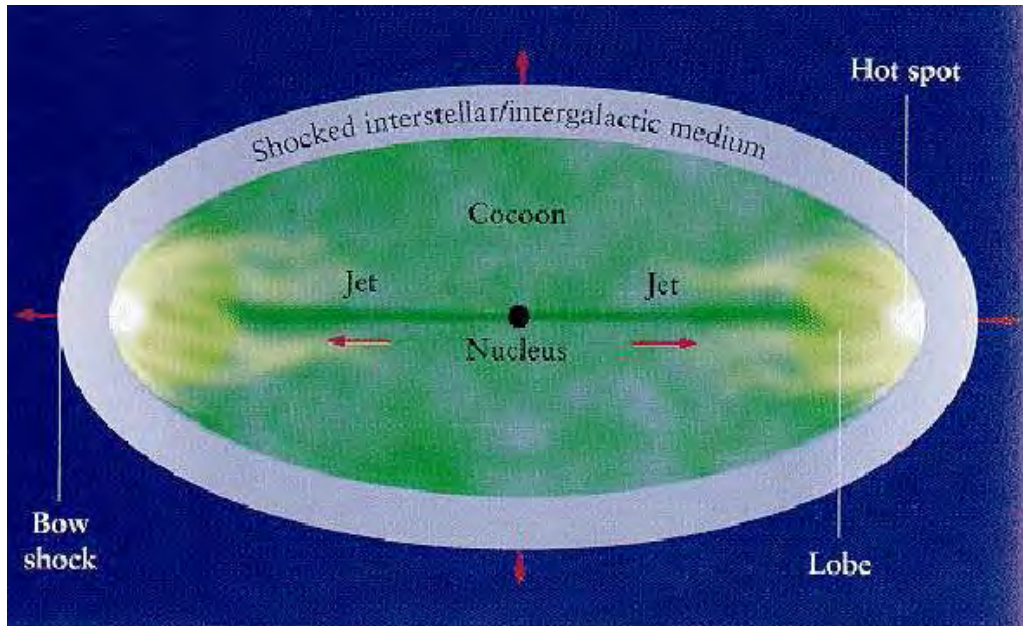


Figure 1.3: A scheme of the structure of a typical AGN: A well collimated jet expands into the intergalactic and interstellar medium of a galaxy buried in the nucleus of the AGN. As the jets expand they form a cavity or cocoon which is made of gas from the jet as it is recycled back towards the nucleus or core of the source. The termination of the jet occurs in a structure called lobe. The brightest region in the lobes is called hot spot. It is a product of the collision of the jet with the interstellar or intergalactic medium. The expansion of the cocoon into the interstellar or intergalactic medium produces a bow shock. (The diagram was taken from Begelman & Rees (1996)).

The most important morphological structures of AGNs are (Fig. 1.3):

- **Core** (nucleus) is usually a stationary radio feature associated with the source of power in the nucleus of the radio galaxy. It is characterized by a *flat* spectrum (see footnote in the next section) and is usually so small that only VLBI observations can resolve it (see bottom left panel of Fig. 1.4).
- **Cocoon** is the cavity made out of jet material which, after being shocked at the terminal shock of the jet, returns towards the core.
- **Jets** are linear features linking the core to the lobe(s). According to Bridle (1984), in order to properly speak about a jet, a radio jet has to fulfill the following criteria:
 1. its length has to be at least four times larger than its width,
 2. it should be separable at high resolution from other structures either by brightness contrast or spatially,
 3. it should be aligned with the compact radio core where closest to it.

Jets may be visible on one (*one-sided*) or both sides (*two-sided*) of the core and can look smooth or knotty (usually at higher resolution, see Fig. 1.4) in radio maps.

- **Components** are features in the radio map where the brightness peaks (with respect to the background radio emission) with sufficient statistical significance. They usually change their angular distance (relative to the core) when observed at different epochs and are, thus, associated with the moving regions in temporal series of observations.
- **Lobes** are extended regions of diffuse radio emission. They are assumed to consist of plasma transported by the jets from the core of the galaxy to large distances. In Fig. 1.4 they are seen as the plume-like structures in the images taken by the Very Large Array (VLA) at 90 and 20 cm.
- **Hotspots** are bright regions at the outer edges of the lobes, which are interpreted as the working surface where the jet hits the ambient medium, creating shocks. Therefore, that is the place where most of the kinetic energy of the jet is converted into the internal energy of the relativistic particles which then radiate (giving hotspots their name).

Very little is known about the central nucleus of radio sources because of the limited resolution of present observations, i.e., structures smaller than 0.1 parsec (pc) are not resolved. However, at intermediate (0.1 – 100 pc) scales jets emit synchrotron and, in some cases, also inverse Compton radiation (see chapter 2). Up to now they have been observed with VLBI or the *Very Large Baseline Array* (VLBA)³. At these scales jets are collimated, relativistic and variable, sometimes with an intra-day variability of the radio emission. If this variability is intrinsic to the source of emission, it constraints the size of the source to less than a light day⁴.

At kiloparsec (1 kpc - 1 Mpc) scales jet morphologies can be influenced by the interaction with the surrounding medium. Evidence for relativistic velocities of kpc-scale jets have been found in radio (Bridle et al. 1994) and X-rays (Sambruna et al. 2002) observations.

1.2.2 AGN classification

AGNs have been observed in a wide variety of forms. Several classification schemes which will be described here. Large scale radio sources were divided into two groups: *extended, steep spectrum*⁵ objects with a roughly collinear double lobe structure extending out to either side of the host galaxy, and *compact, flat spectrum* sources where no or very little extended structure is observed. However, as the imaging techniques advanced with the advent of more sensitive and higher resolution interferometers, it became clear that

³The Very Long Baseline Array is a set of ten radio antennas spread across the United States.

⁴If the typical variability time scale of a source is ΔT , then its maximum size must be smaller than the distance light can travel in that time, $c\Delta T$

⁵If the flux density S is a power law in frequency ν with index α , i.e., $S = S_0\nu^{-\alpha}$, then flat spectra are defined through $\alpha \leq 0.5$, while steep spectra have $\alpha > 0.5$ (Zensus 1997)

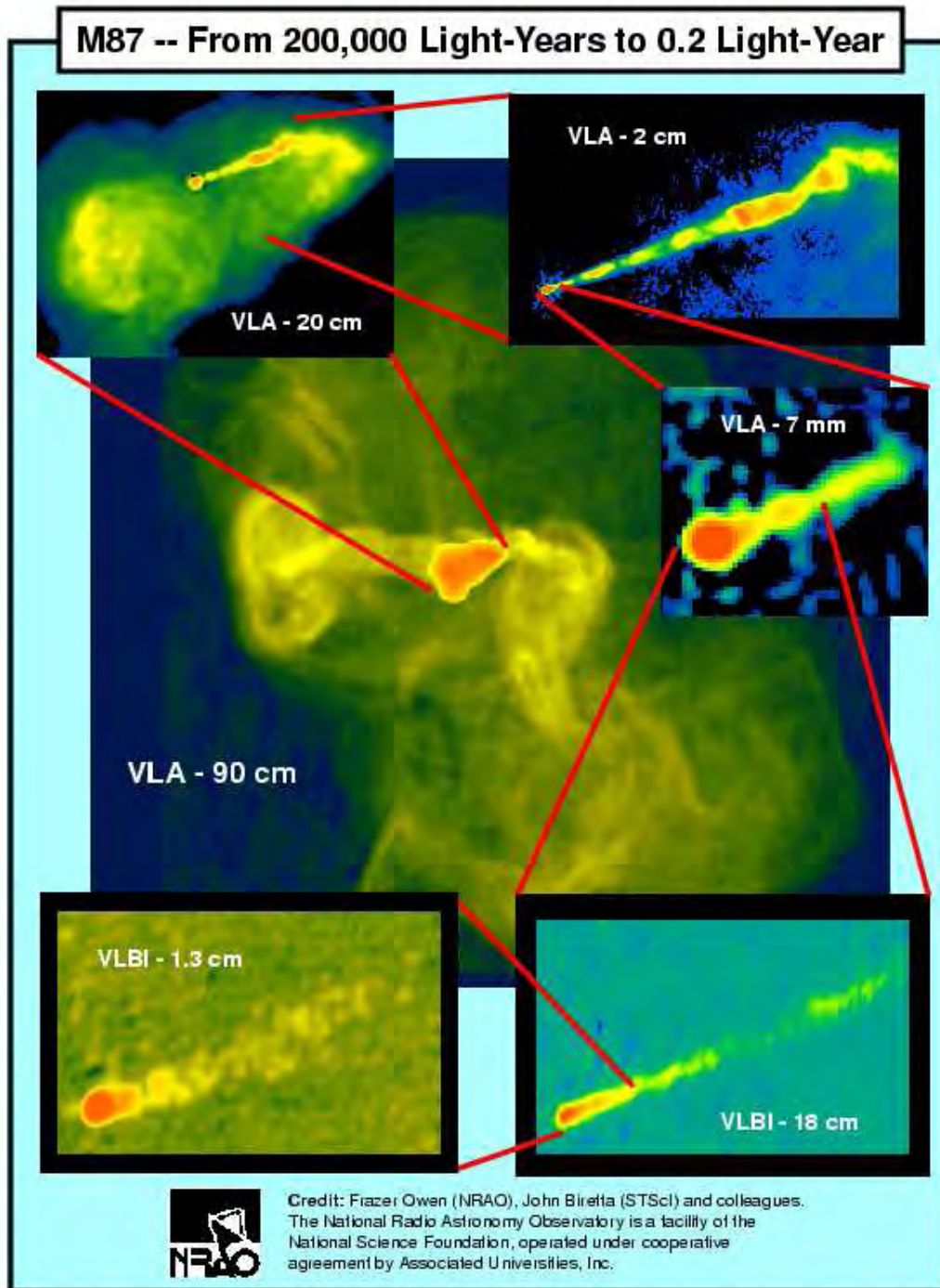


Figure 1.4: Montage of different images of the radio galaxy M87. The central panel clearly displays the huge outer lobes, while the next inset shows the inner plume-like lobes. Zooming further in we can see that the jet is knotty, with components appearing and disappearing over time. This figure illustrates the need for many observations at many different spatial scales in order to fully resolve radio galaxies.

many of the compact, flat spectrum sources contain a certain amount of steep spectrum emission (Muxlow & Garrington 1991). Thus the division has been changed to *core-dominated* and *lobe-dominated* sources.

Core dominated objects⁶ are characterized by a very luminous core which tends to dominate the overall source flux density. A very large number of these sources have been mapped using VLBI, at its highest angular resolution (Pearson & Readhead 1988). Many core dominated sources exhibit some form of activity indicating relativistic motion in their core regions, like, e.g., *apparent superluminal motion* (see section 1.4.1) or variability time-scales which are of the order of the light crossing time of the size of the variable structures.

Lobe dominated AGNs can be divided into three distinct types of AGNs: radio Seyfert galaxies⁷, lobe-dominated radio-galaxies and lobe-dominated radio-loud quasars.

A large number of Seyfert galaxies show S-shaped radio structure which suggests jet disruption at kiloparsec scales (Wilson 1983) and they are often less powerful than elliptical radio galaxies. The usual explanation is that this is due to the lower power output of the central engine and the difficulties encountered by the plasma jets when propagating through the dense rotating interstellar medium found in discs of spirals. The typical luminosity of the radio structures is in the range $P_{1\text{GHz}} = 10^{21} - 10^{25} \text{ W Hz}^{-1}$. If present, the jet structure is usually two sided.

The lobe-dominated radio galaxies have an interesting property. Their structure seems to undergo an abrupt transition around $P_{178\text{MHz}} = 5 \times 10^{25} \text{ W Hz}^{-1}$ (Fanaroff & Riley 1974). Thereby, the sources below this critical luminosity are called the FR I objects, while those above it became known as FR II objects.

The FR I sources display smooth continuous two-sided jets running into large-scale lobe structures (plumes). The lobes are *edge-darkened*, meaning that the ratio of the separation of the peak emission of the radio lobe to the total size of the source falls significantly below unity. The steepest lobe spectra are located in the plumes, implying that there resides the most radiatively-aged⁸ material (Muxlow & Garrington 1991).

FR II objects have *edge-brightened* (peak brightness separation to total size of the source ratio close to unity) large-scale structures, with bright outer hotspots. The steepest radio spectra are found in the innermost parts of the lobes. FR II jets (when detected) differ from those found in FR I objects. They are usually one-sided with a jet/counter-jet intensity ratio $> 4 : 1$ (Bridle & Perley 1984). The situation is complicated by the fact that these jets are in general not smooth but dominated by bright knots with the ratio of knot to jet luminosity being > 4 .

⁶For an object to be core-dominated, its core has to be unresolved by VLA, i.e. it has to be smaller than $20(D_{\text{A}}H_0/c)(h/0.75)^{-1}$ kpc, where $H_0 = 100h \text{ km s}^{-1} \text{ Mpc}^{-1}$ is the Hubble constant, h being its scale factor and D_{A} is the angular diameter distance (the distance from the observer at which two objects on the sky with angular separation θ have mutual distance θD_{A}).

⁷Seyfert galaxies are spiral galaxies named named after Carl K. Seyfert who in 1943, described them as their central regions having peculiar spectra with notable emission lines. Today we know that they have an AGN in their center.

⁸Due to the synchrotron cooling the power law index of the electron distribution (and therefore also the power law index of the emitted radiation) increases, i.e., the spectrum steepens (see section 3.2.1)

1.2.3 Parsec scale jets

In the previous two sections we have discussed the properties of AGNs and their jets on kpc and Mpc scales. In this section we focus on the inner regions of the jets, i.e., on parsec and sub-parsec scales. VLBI observations of the nuclei of radio-loud active galaxies reveal the following important facts (Pearson 1996): (1) well-collimated parsec-scale jets are seen, indicating that the central energy source is confined to a small region and that jets are formed on a scale of a few pc or even less; (2) superluminal expansion (see section 1.4.1) occurs frequently, indicating relativistic outward motion; and (3) jets are usually one-sided or at least highly asymmetric, consistent with relativistic beaming of the emitted radiation.

The most detailed information about the conditions within parsec-scale jets is obtained from the observations of the brightest well-known sources such as 3C345 (Zensus et al. 1995), 3C273 (Davis et al. 1991) and 0836+710 (Hummel et al. 1992). These observations show a stationary, flat-spectrum core and, connected to it, a steeper-spectrum, one-sided jet. Brightness peaks (“components”) in the jet show outward motion with apparent superluminal speeds ($v_{\text{app}}/c \approx 2 - 10$).

The source 3C345 (Fig. 1.5) is the one of the best-studied parsec-scale jets (Zensus et al. 1995) and its components follow curved rather than “ballistic” (radial outflow from the nucleus) trajectories. Also, different components follow different trajectories, although they converge to the ridge-line of the jet at larger distances from the core. It has been estimated (Zensus et al. 1995) that the Lorentz factor of 3C345 jet is $\Gamma = 12$ (assuming a Hubble constant $H_0 = 100 \text{ km s}^{-1} \text{ Mpc}^{-1}$).

The detailed monitoring of the radio spectra and the polarization of the moving components gives additional clues about the physical conditions within the emission regions: the emission generally rises rapidly at high frequencies as the component emerges from the optically-thick core and then decays more slowly while propagating to lower frequencies.

1.3 BL Lac objects

BL Lac objects or blazars have been named after the first such object was discovered, the “variable star” BL Lacertae (Hoffmeister 1929) which was subsequently identified with the unusual radio source VRO 42.22.01 (Schmitt 1968). Soon afterwards, rapid variations in the radio flux of VRO 42.22.01 were detected (Biraud & Veron 1968).

Subsequent optical, infrared and radio observations suggested that objects similar to BL Lac comprise a class of quasi-stellar objects (QSOs) with some combination of the following characteristics (Strittmatter et al. 1972; Stein et al. 1976): (a) absence of emission lines in the core source; (b) rapid variability at radio, infrared and visual wavelengths; (c) nonthermal continuum with most of the luminosity radiated at infrared wavelengths; and (d) strong and rapidly varying polarization.

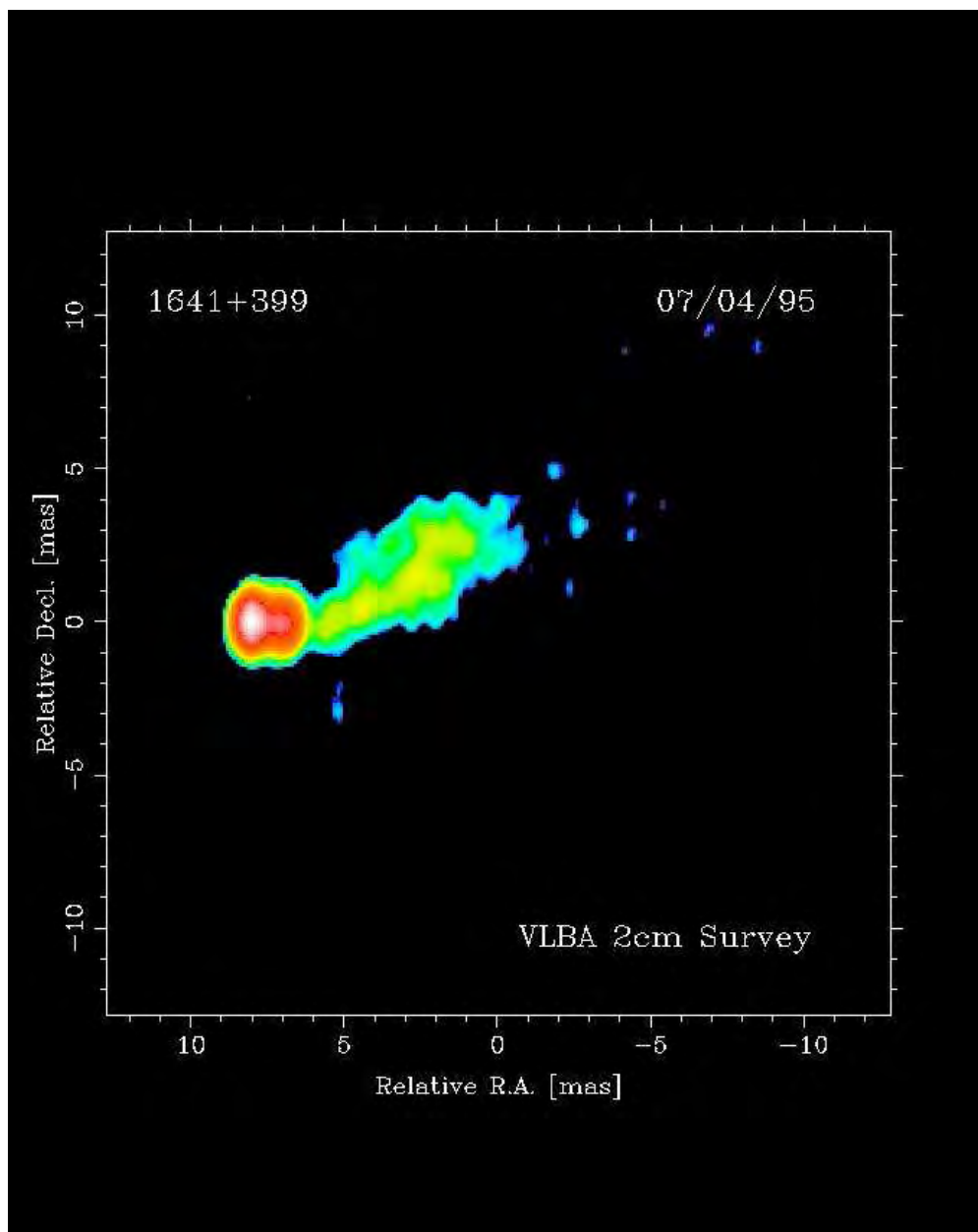


Figure 1.5: Color-coded contours of the VLBA 2 cm radio image of the source 3C345. The unresolved core is seen as the red spot and the parsec-scale jet to the right of it. The scale of the image is such that 1 milliarcsecond corresponds to ≈ 4.5 pc.

More recently, multi-wavelength studies have provided the first global support for the idea of bulk relativistic motion in blazars (Ulrich et al. 1997): The observed radio emission was sufficiently luminous and rapidly variable that, assuming it was due to synchrotron radiation, high X-ray fluxes would be expected from Compton up-scattering of the synchrotron photons unless the radio emission was relativistically beamed (Hoyle et al. 1966). As will be discussed in section 1.4.2, the deduced bulk relativistic motion in blazars nicely coincides with the inferred bulk relativistic motion

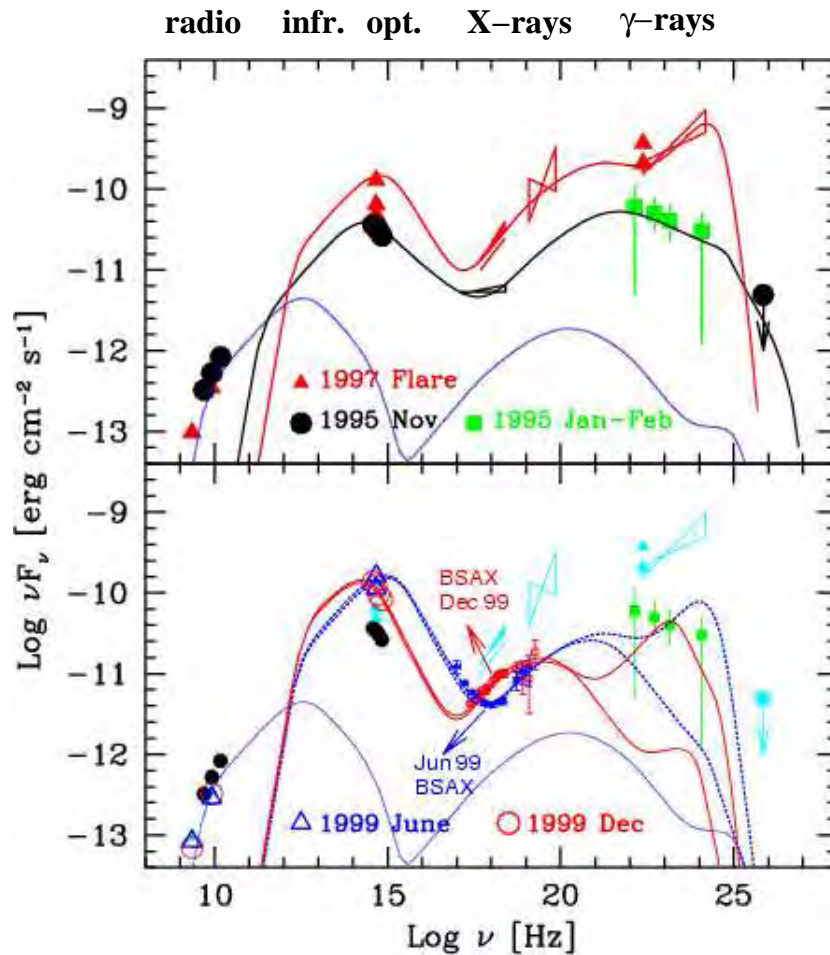


Figure 1.6: Four simultaneous spectral energy distributions (SEDs) of BL Lac together with the best fit models (lines) of Ravasio et al. (2002). In the top panel we see the data from 1995 and 1997. In the bottom panel the data from June and December of 1999 are plotted.

in parsec scale jets (see section 1.2.3).

In short, the observations of blazars all agree on the fact that they are highly variable, have non-thermal continuum spectra without any lines, they are polarized and seem to indicate the presence of a highly relativistic jet moving almost directly towards the observer.

1.3.1 Blazar spectra

Due to temporal variations in the spectral flux (see next section), the shape of the radio spectrum at any time is difficult to determine. For example, the recent *BeppoSAX* observations of BL Lac (Ravasio et al. 2002) show that the shape of the spectrum in the radio band changes rapidly on the time-scales of months (see Fig. 1.6), i.e., between the November 1995 and 1997 (upper panel) and June 1999 and December 1999 (lower panel) observations.

Despite the high variability of blazars, it is possible to construct the so-

called *logarithmically average*⁹ spectra, according to which (Fig. 1.7) blazars can be classified in two classes (Padovani & Giommi 1995; Fossati et al. 1998),

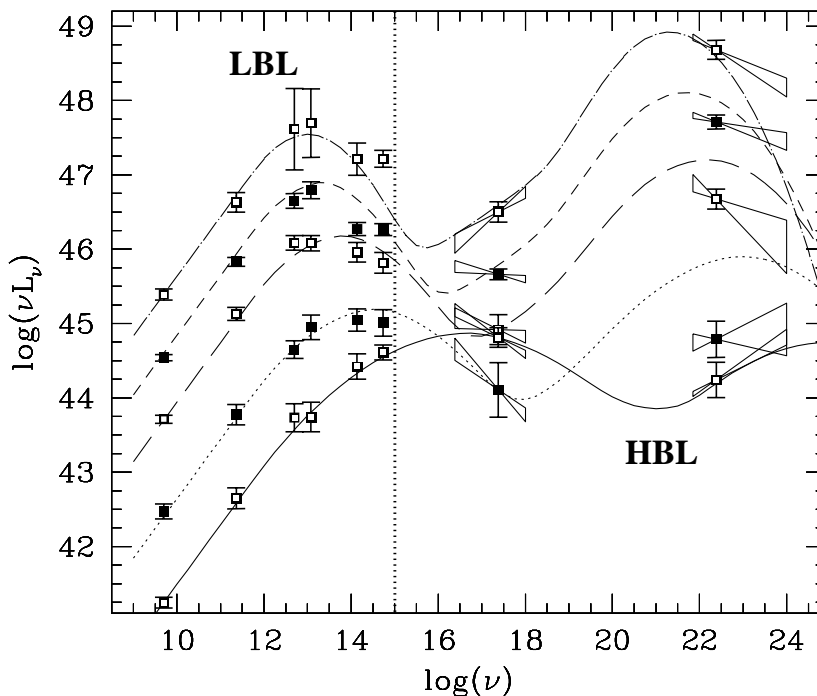


Figure 1.7: Averaged spectral energy distributions (SEDs) of the 126 blazars analyzed by Fossati et al. (1998) binned according to the radio luminosity and irrespective of the original classification. The curves are one-parameter analytic approximations to the averaged SEDs. The frequency range extends from the radio to γ -rays. The dotted vertical line denotes the line separating SEDs of LBL from SEDs of HBL blazars (see text).

- **LBL** blazars: the first (synchrotron) spectral peak is located in the infrared ($\nu_{\text{syn}} \lesssim 10^{14}$ Hz, where ν_{syn} is the synchrotron peak frequency) band and the spectral index α_{rx} from 5 GHz to 1keV (Padovani & Giommi 1995) satisfies $\alpha_{\text{rx}} \gtrsim 0.75$, and
- **HBL** blazars: the synchrotron peak is located in X-rays ($\nu_{\text{syn}} \gtrsim 10^{16}$ Hz) and $\alpha_{\text{rx}} \lesssim 0.75$,

The characteristic shape of the blazar average spectrum is the double-peaked curve. The first peak (at low frequencies) is the synchrotron peak, produced by ultra-relativistic electrons which gyrate in the magnetic field (see section 2.1). The second peak (at high frequencies) is the inverse-Compton peak, produced by the up-scattering of the synchrotron photons on the ultra-relativistic electrons (see section 2.2).

⁹Due to the variability over several orders of magnitude the logarithm of the flux is averaged rather than the flux itself.

Fossati et al. (1998) find that:

1. The frequency of the synchrotron peak is *anti-correlated* with the source luminosity, i.e., larger blazar luminosity corresponds to the lower frequency of the synchrotron peak.
2. The frequencies of the synchrotron and inverse-Compton peak are correlated, i.e., their ratio is a constant.
3. The γ -ray flux dominance is correlated with the source luminosity, i.e., sources with larger luminosity show a more prominent high energy peak.

In this PhD thesis we consider only the subclass of HBL blazars whose main emission falls in the X-ray band and is synchrotron in nature. Although the method has been developed to treat the inverse Compton radiation too, due to the lack of time, the study of LBL blazars has been postponed to the future work.

1.3.2 Variability

There are several clues pointing towards a relativistic nature of blazars. On the one hand, blazars exhibit the most rapid and the largest amplitude variations of all AGN (Stein et al. 1976). The combination of extreme variability and relatively weak spectral features suggests that the continuum is emitted by a relativistic jet close to the line of sight and hence that the observed radiation is strongly amplified by relativistic beaming (Blandford & Ressler 1974). On the other hand many blazars exhibit large-amplitude extremely fast X-ray variations (Feigelson et al. 1986) that would violate limits on $\Delta L/\Delta t$ criterion¹⁰ for Eddington-limited accretion (Fabian 1979).

Recent observations of blazars have shed some light on the understanding of the continuum emission (Ulrich et al. 1997):

1. In the part of the spectrum below the synchrotron peak frequency the variability amplitudes are generally smaller than for frequencies above the synchrotron peak frequencies. Moreover, for frequencies above the synchrotron peak frequency spectra harden with increasing frequency.
2. The high energy component (near the second peak) of the spectrum also seems to vary more frequently and to harden with increasing frequency above its peak frequency.
3. Finite time lags between optical and X-ray light curves have been measured in flares of two HBL, PKS 2155-304 (Makino et al. 1996, redshift $z=0.116$), and Mrk 421 (Brinkmann et al. 2003; Takahashi et al. 1996, $z=0.03$). In the case of PKS 2155-304 the soft radiation (photon energies $\lesssim 1$ keV) lags the hard radiation (photon energies $\gtrsim 2$ keV) by

¹⁰ ΔL is the typical source size, Δt is the typical variability time scale. Fabian (1979) introduced the a limit on the luminosity of an outburst arising from the opacity of the matter responsible for the emission. Assuming that luminosity is produced by a conversion of mass M with an efficiency $\eta = (L\Delta t)/(Mc^2)$, the maximum permitted luminosity is $\log \Delta L = 41.3 + \ln(\eta/0.1) + \log \Delta t$.

3 – 4 ks, while in the case of Mrk 421 time lags of both soft and hard radiation have been detected from several flares. However, Edelson et al. (2001) place an upper limit on any time lag of PKS 2155-304 to $\tau < |3|$ hours, and interpret the previous claims as artifacts caused by the periodic interruptions of observations of the low-Earth orbits of satellites every 1.6 hours.

It seems that the study of the variability properties (light curves in particular) can yield more constraints on the actual physical properties in blazar jets than the study of the average spectral properties alone.

1.3.3 Blazar X-ray light curves

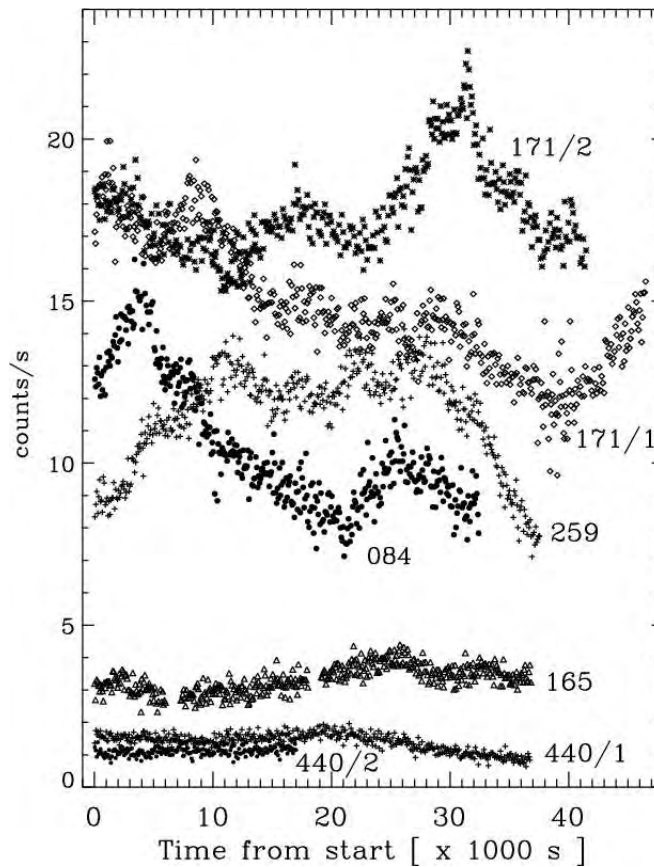


Figure 1.8: Background subtracted, 2.4-10 keV light curves of Mrk 421 (Brinkmann et al. 2003). The curves are labeled by the orbit of the observation.

Figure 1.8 shows the observation of the blazar Mrk 421 with the *XMM-Newton* X-ray satellite (Brinkmann et al. 2003). The light curves shown are in units of number of photons (photon counts) per second. Each light curve is about 40 ks (about half a day) long. The labels denote different orbits of *XMM-Newton* satellite. One sees immediately that the source is highly

variable both within a single observation as well as between the different observations (each orbit of *XMM-Newton* takes about two days).

Mrk421 is probably the best-studied blazar, along with the source PKS 2155-304. The X-ray light show variability from as short as 100 seconds in some observations to the long-term variability as seen in Fig. 1.8. The intra-day variability of PKS 2155-304 has been found to be in form of quasi-periodic oscillations (Wagner & Witzel 1995), which are well resolved, and occur at constant amplitudes for 5 to 8 oscillatory cycles.

The temporal analysis of blazar light curves faces the problem that the time series involve gaps due to the periodic eclipsing of the source by the Earth. Thus, one of the tools used to study the characteristics of the light curves with gaps in observations is the structure function, which avoids problems caused by the traditional Fourier analysis (Simonetti et al. 1985). If we assume that we have a discretely sampled time series $F(i)$, $i = 1, \dots, N$ with the sampling interval Δt , then the first order structure function is defined as

$$SF(j) = \sum_i [F(i) - F(i+j)]^2, \quad (1.1)$$

where the sum only extends over those pairs where both $F(i) \neq 0$ and $F(i+j) \neq 0$. As we can see from (1.1), the structure function is simply the mean square deviation of the points separated by the time lag $j\Delta t$.

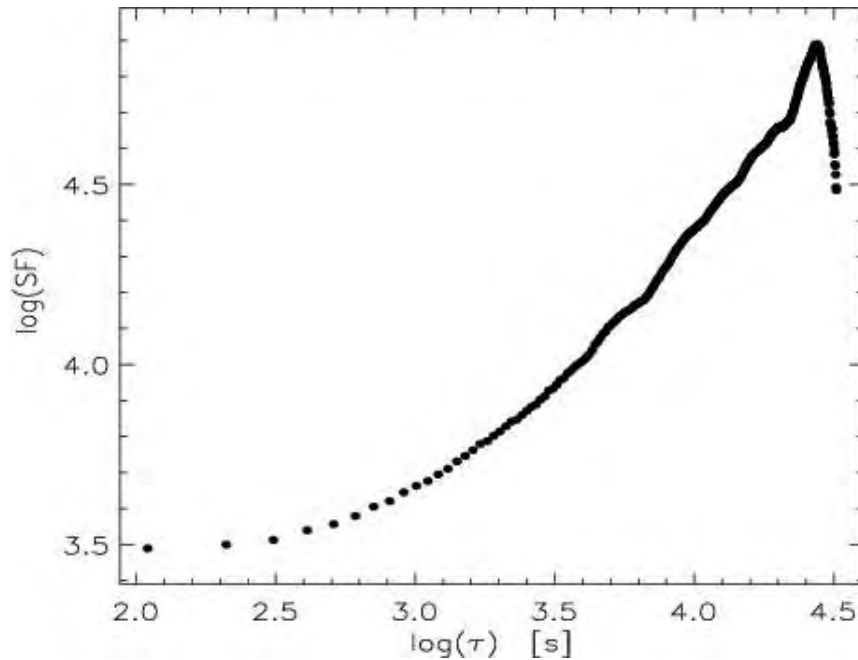


Figure 1.9: Structure function of Mrk 421 (Brinkmann et al. 2001). The characteristic power-law structure can be seen.

Figure 1.9 shows an archetypical structure function of Mrk 421 (Brinkmann et al. 2001). Structure functions display usually a power law rise at shorter time scales and then (if the observations last long enough) flatten after some characteristic *break time*. As we will see in section 1.5, the break time may

be related to the physical processes within a blazar jet which give rise to the rapid variability in the light curve.

1.4 Theoretical models

1.4.1 Apparent superluminal motion

The apparent superluminal motion might occur as a result of relativistic motion of the radiating jet component directed at an angle θ to the observer's line of sight with speed $v = \beta c$ (Cawthorne 1991).

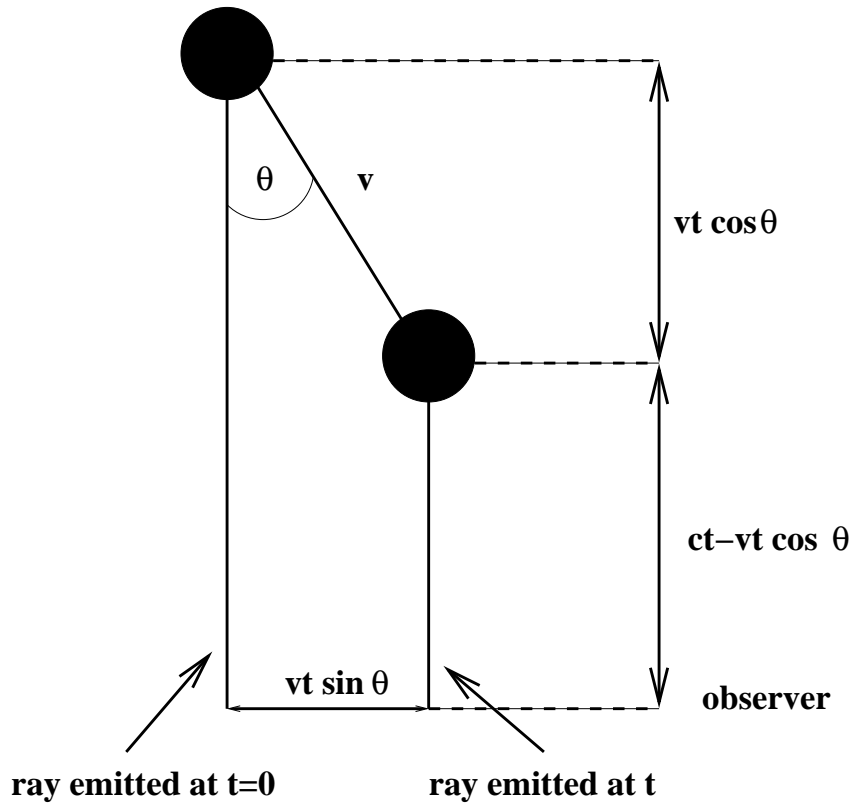


Figure 1.10: Schematic description of the superluminal motion: the source (black circle) moves with velocity $v = \beta c$ towards the observer so that its velocity makes an angle θ with the observer's line of sight. The source emits two signals, at $t = 0$ and at t . The observer sees the travel time of the source compressed to $t(1 - v/c \cos \theta)$ and deduces an apparent velocity $c\beta \sin \theta / (1 - \beta \cos \theta)$.

Figure 1.10 illustrates the idea: the source (black circle) moves with velocity $v = \beta c$ towards the observer so that its velocity makes an angle θ with the observer's line of sight. The apparent velocity measured by the observer is given by the formula

$$v_{\text{app}} = \frac{\beta c \sin \theta}{1 - \beta \cos \theta}, \quad (1.2)$$

which can exceed c for small enough θ and β close to 1. Thus we see that the apparent superluminal motion is the consequence of the relativistic motion of the emitting component towards the observer.

1.4.2 AGN unification

Active galactic nuclei are classified according to their orientation with respect to the observer (Urry & Padovani 1995). Light from the centers of many AGN is obscured by optically thin circumnuclear matter. In radio-loud AGN, bipolar jets emanating from the nucleus emit radio through γ -ray radiation that is relativistically beamed along the jet axis.

The prevailing (but not necessarily correct) picture of the physical structure of AGN (Holt et al. 1992) is the following:

- At the center there is a supermassive black hole whose gravitational potential energy is the ultimate source of the AGN luminosity. Matter is pulled towards the black hole center and loses its angular momentum through viscous or turbulent processes in an accretion disk which glows at ultraviolet or perhaps soft X-ray wavelengths.
- Strong optical and ultraviolet emission lines are produced in clouds of gas moving rapidly in the potential of the black hole, the so-called “broad line clouds” (dark blobs on Fig. 1.11). The optical and ultraviolet radiation is obscured along some lines of sight by a torus or warped disk of gas and dust well outside the accretion disk and the broad line region.
- Beyond the torus, slower moving clouds of gas produce emission lines with narrower widths (light blobs on Fig. 1.11 which form the so-called narrow line region).
- Outflows of energetic particles occur along the poles of the disk or torus, escaping and forming collimated radio-emitting jets (Fig. 1.11 shows twin jets emanating from the central engine).

The central regions of many AGN appear to contain obscuring material, probably in the form of dust, that prevents infrared through ultraviolet light from penetrating some lines of sight (Rowan-Robinson 1977). This dust may be distributed in a torus (Pier & Krolik 1992) or in a warped disk. In any case, it causes AGN to look markedly different from different observing angles.

Another source of anisotropy is the relativistic beaming: when an emitting plasma has a bulk relativistic motion relative to a fixed observer, its emission is beamed in the forward direction (in the fixed frame), a direct consequence of the transformation of angles in special relativity. An observer located near or in the path of such plasma sees much more intense emission than if the same plasma were at rest. The scales for variability are also shorter, causing the emission region to appear to move superluminally (see section 1.4.1).

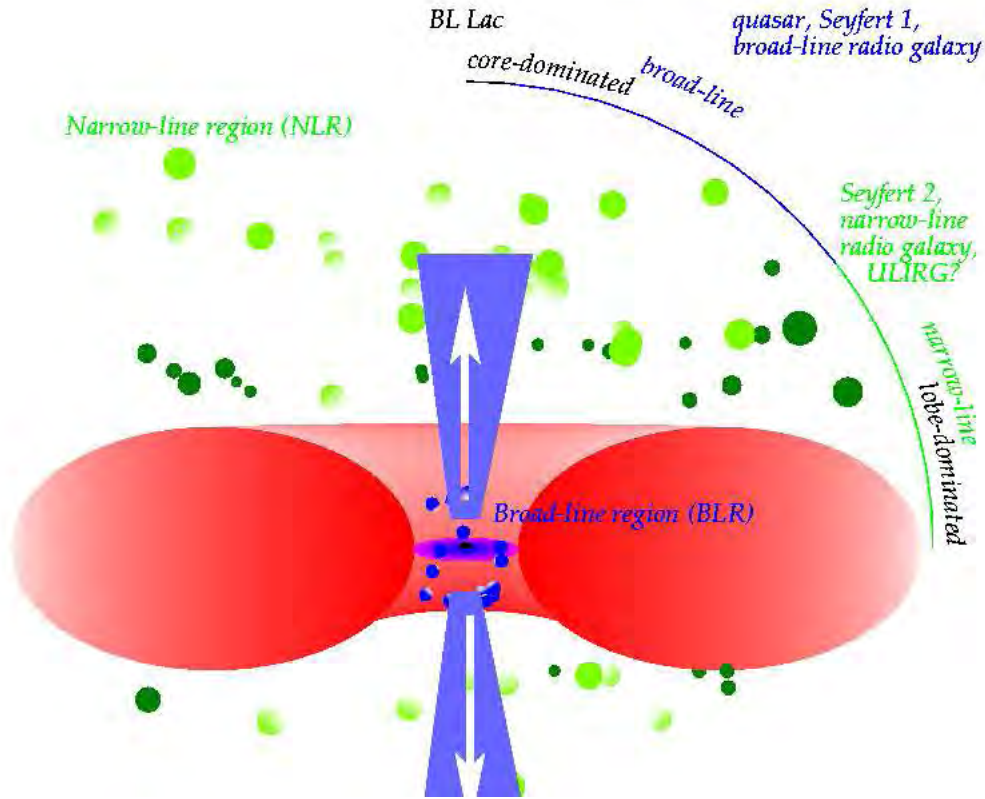


Figure 1.11: Schematic description of the AGN model used in the unification scenario (credits: Chris Simpson, source: <http://www.naoj.org/staff/chris/research/>). The appearance of the AGN depends strongly on the observation angle. See text for details.

1.4.3 Internal shock model

According to our current understanding, in a blazar we are seeing a jet pointing directly towards us. In order to explain the observed variability of the emission, especially the high-energy X-ray and γ -ray emission, several models address the physical process of non-thermal emission which takes place in these objects. Here we discuss the internal-shock or shock-in-jet model which has become the standard paradigm in the field. This model was first used to explain the variability of early gamma ray bursts light curves (Rees & Meszaros 1994; Kobayashi et al. 1997), and later applied to blazars (Bicknell & Wagner 2002; Mimica et al. 2004; Spada et al. 2001; Tanihata et al. 2003).

The basic assumption is that the central engine ejects plasma with variable velocity (Lorentz factor) along a preferred direction (a channel or a jet). Due to the velocity differences, faster shells catch up with the slower ones producing internal shocks. In these shocks a fraction of the kinetic energy of the shells which is dissipated into thermal energy is used to accelerate non-thermal particles which emit non-thermal synchrotron radiation. We can idealize this by considering two shells being ejected with a Lorentz factor of the order γ , the second (back) shell being faster than the first

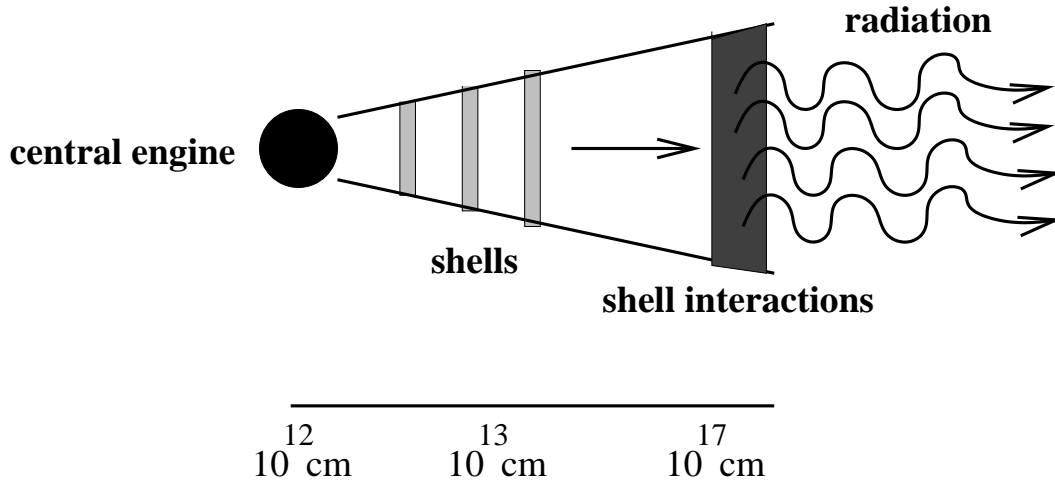


Figure 1.12: The internal shock scenario: the central engine ejects fluid (shells) with variable velocity, so that faster shells catch up with the slower shells producing internal shocks in the jet.

(front) one. If L is the initial separation of the shells, they will catch up at a radius $R \simeq \gamma^2 L$ (Kobayashi et al. 1997). At that point two shocks appear, a *reverse shock* (RS) moving into the faster shell and a *forward shock* moving into the slower shell (Fig. 1.13).

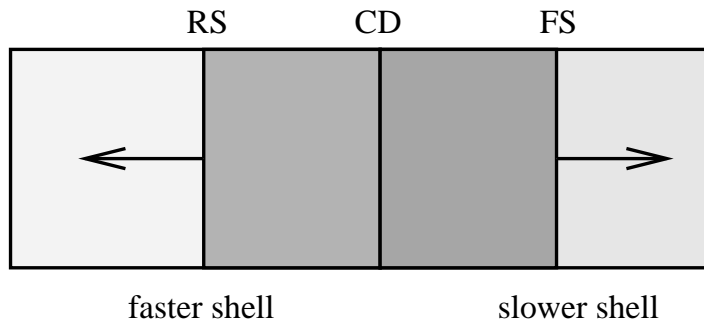


Figure 1.13: The simplified interaction of two shells in the rest frame of the contact discontinuity (CD): the CD forms at the interface of the two shells. The forward (FS) and reverse (RS) shocks propagate into the slower and the faster shell, respectively. At these shocks the kinetic energy is dissipated into thermal energy the non-thermal particles are accelerated at the shock fronts.

As the shocks propagate through the shells the accelerated nonthermal particles radiate, and a fixed observer sees a flare whose duration can be estimated to l_r/c (Kobayashi et al. 1997), where l_r is the width of the faster shell. Therefore, the model relates the physical properties of the jet fluid (i.e. the shell size) to a robust observable (the duration of the flare). The generic shape of the flare computed by Kobayashi et al. (1997) is shown in the Fig. 1.14.

The rapid variability of blazars as well as the multitude of peaks in their light curves is attributed in the internal-shock model to the interaction of many shells which eventually collide yielding individual flares within the

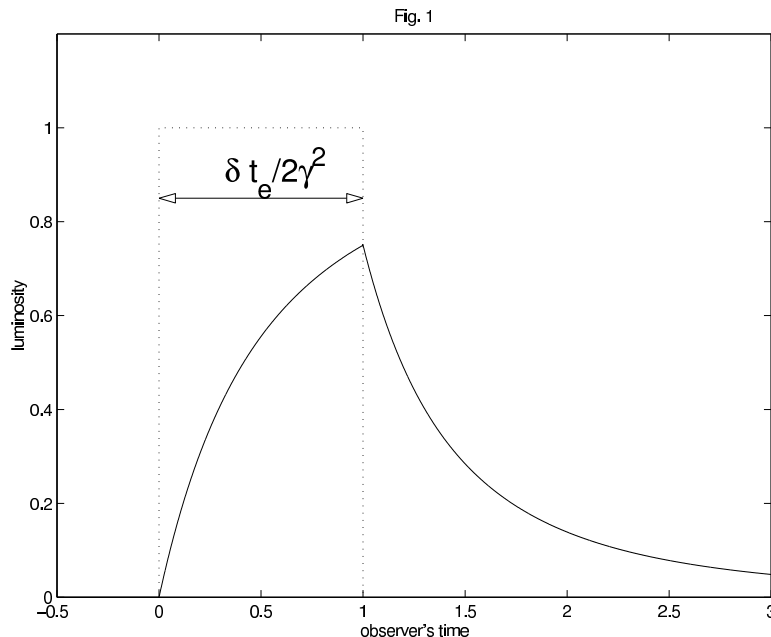


Figure 1.14: The generic shape of the flare resulting from the collision of two shells in the jet (Kobayashi et al. 1997). δt_e is the duration of the flare in the jet rest frame and γ is the bulk Lorentz factor of the jet.

global light curve.

1.5 Existing numerical methods used to produce synthetic light curves

In this section we review some of the numerical methods which use the internal shock scenario to reproduce the rapid variability found in light curves of blazars.

The basic building block of a blazar light curve is a single flare, i.e. it is necessary to compute the non-thermal radiation produced by a single shock or a shocked region.

A possible approach to the problem is the so-called one-zone homogeneous model. This is the procedure followed by Chiaberge and Ghisellini (1999) who assume that the emission is produced by a distribution of relativistic electrons injected in a region of typical dimension R embedded in a tangled magnetic field B , at a rate $Q(\gamma)[\text{cm}^{-3} \text{s}^{-1}]$ (γ is the Lorentz factor). Electrons lose energy by emitting synchrotron and synchrotron self-Compton (SSC) radiation; they can also escape from the emitting region on a time scale t_{esc} independent of energy. The evolution of the electrons is followed by solving the kinetic equation (3.18) with an additional term $-n(\gamma, t)/t_{\text{esc}}$ on the right-hand side, where $n(\gamma, t)$ is the number density of non-thermal electrons at a time t in the Lorentz-factor interval $[\gamma, \gamma + d\gamma]$. The method used to solve this equation is that of Chang and Cooper (1970).

It takes into account the light travel time to the observer. The observer sees “slices” and, although each slice is homogeneous, the fact that slices from different times in the source rest frame are observed at the same time in observer the frame enables the modeling of an inhomogeneous emitting region.

The code was applied to the source Mrk 421 and its May 1994 flare. The following parameters were deduced: the radius of the emitting region was $R = 1.5 \times 10^{16}$ cm and the magnetic field $B = 0.13$ G.

A more sophisticated approach is due to Moderski et al. (2003). Their code *BLAZAR* calculates spectra and light curves of blazars during outbursts. The basic model is that the non-thermal flares in blazars are produced in thin shells propagating down a conical jet with relativistic velocities. Such shells are representing layers of shocked plasma enclosed between the forward and reverse shocks in the internal shock scenario. The code includes synchrotron and inverse-Compton radiation. The non-thermal electron evolution is treated numerically by solving the electron-kinetic equation (3.18) in the thin shell approximation (Moderski et al. 2003). Figure 1.15 illustrates the radiation-integration method.

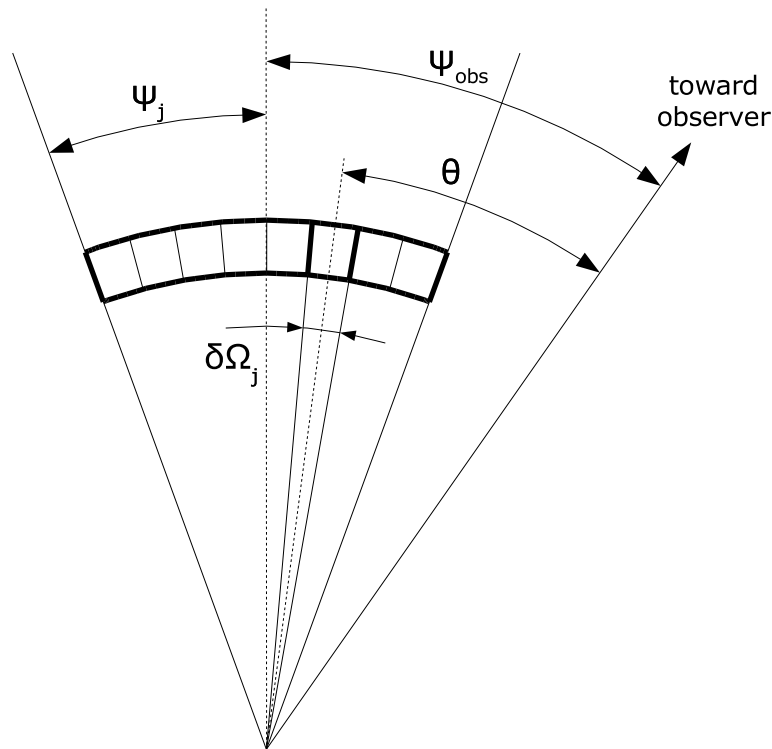


Figure 1.15: A schematic picture illustrating the Moderski et al. (2003) light curve integration procedure. A thin shell of electrons enclosed within the half-opening angle of the jet, Ψ_j is divided into cells of thickness $\delta\Omega_j$, containing δN_γ electrons. The observer is located at the angle Ψ_{obs} from the jet axis. Integration is performed by summation over θ for each shell. The total light curve results from the summation of the contributions of all the radiative shells included in the simulation.

The code was applied to the February 1996 flare of the blazar 3C 279

($z = 0.538$), and show that the synchrotron radiation component is strongly diluted. This effect is often ignored in one-zone/homogeneous models and can lead to very large errors in the model parameters (Moderski et al. 2003). The code *BLAZAR* uses a method which can tackle inhomogeneous radiating components approximately.

A step forward in the computation of synthetic light curves consists in including a hierarchy of internal shocks moving in a relativistic wind. In the hierarchical shock scenario the entire jet emission is simulated by adding pulses (flares) radiated in the mentioned set of internal shocks.

Spada et al. (2001) assume that the jet (which can also be a wind) is discretized as a sequence of $N = t_w/t_v$ shells, where t_w is the duration time of the wind ejection from the central source and $t_v \ll t_w$ is the average interval between consecutive ejections. Each shell is characterized by a mass M_j , a Lorentz factor Γ_j and an ejection time t_j : at $t = t_j$ the j th shell is at a distance $R_j = R_0$, where $R_0 = 10^{14}$ cm is the dimension of the central source. The initial shell width is equal to R_0 .

The wind dynamics is followed by computing when each pair of shells collide. In case that the shell $j - 1$ is faster than the shell j ($\beta(j - 1) > \beta(j)$) two consecutive shells will collide. Assuming that the adiabatic expansion velocity of the shells is $\beta_e(j)$, the collision time is (Spada et al. 2001)

$$t_{j,j-1} = \frac{R(j) - R(j - 1) - 0.5[\Delta(j) + \Delta(j - 1)]}{\beta(j - 1) - \beta(j) + 0.5[\beta_e(j) - \beta_e(j - 1)]}, \quad (1.3)$$

where $R(j)$ and $\Delta(j)$ are the radii and widths of the shells at a given time, respectively. The simulation starts from the initial configuration $t = 0$, and then proceeds until the next collision time $t_1 = \delta t_1 = \min(t_{j,j-1})$. After the two shells have interacted, new sets of values for $\beta(j)$, $R(j)$ and $\Delta(j)$ are recomputed. These new variables are used as the new initial values for calculating the next collision.

The two shell interaction is computed following the procedure of Kobayashi et al. (1997). The comoving magnetic field energy density is assumed to be a fraction of the fluid internal energy density. The energy spectrum of non-thermal electrons injected at shocks is assumed to form a power-law distribution. However, the particles are assumed to have the same energy distribution throughout the whole emitting region between the forward and reverse shocks. This does not allow for the study of time-scales shorter than the light-crossing time of a single shell. The radiation processes considered include synchrotron and inverse-Compton processes. The radiation from each collision is transformed into the observer frame taking into account light travel time delays. The Lorentz factors of the ejected shells are randomly taken from the interval $[10, 25]$. Figure 1.16 shows the distribution of the radiative efficiency within a jet which seems to be concentrated on the scales between $10^{16} - 10^{18}$ cm. Applying the model to several flares of the source 3C 279, it was found out that the bulk Lorentz factor at a parsec scale should be $\Gamma \approx 15$.

The model used by Tanihata et al. (2003) is essentially the same as that of Spada et al. (2001), but the Lorentz factor distribution of the shells is assumed to follow a Gaussian probability distribution with an average

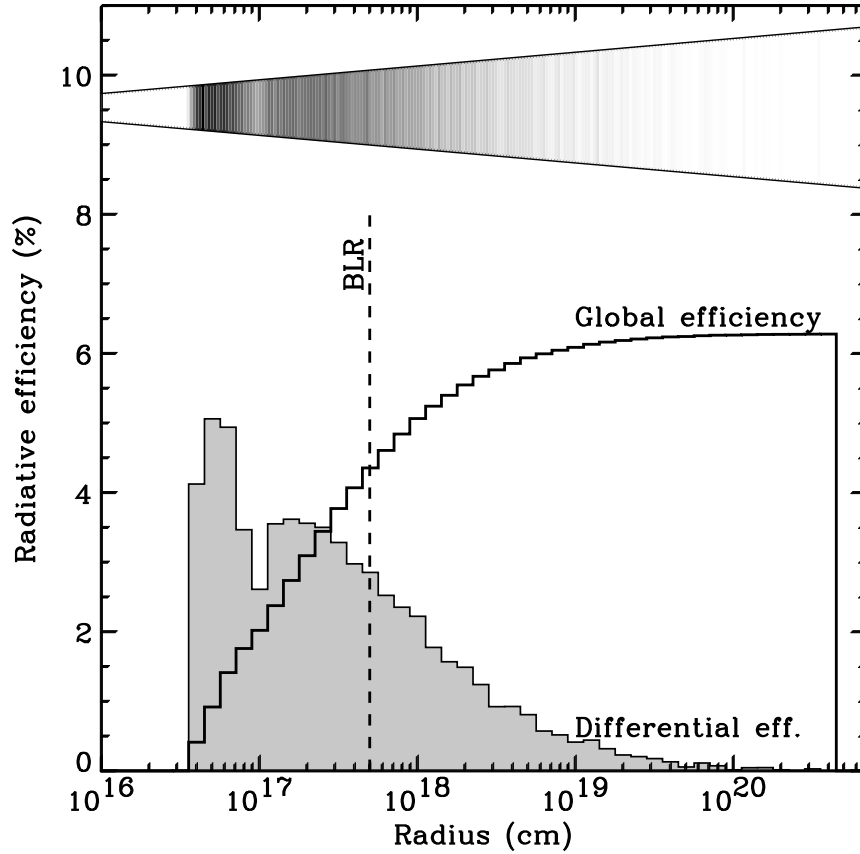


Figure 1.16: The radiative efficiency versus the collision radius (Spada et al. 2001). The full line corresponds to the global efficiency, i.e. the fraction of the total kinetic energy of the wind radiated on scales smaller than a given light-radius; the shaded histogram shows the differential efficiency multiplied by 10. The cone-like insert in the upper part of the figure shows a grey-scale representation of the differential efficiency of the jet (darker means higher efficiency).

value Γ_{avg} and a scatter σ'_{Γ} . The initial separation of the colliding shells is D_0 . As can be seen in Fig. 1.17, the change of σ'_{Γ} affects the position of the break in the structure function, i.e. the smaller the average relative velocity of colliding shells, the higher the separation time at which the break is observed.

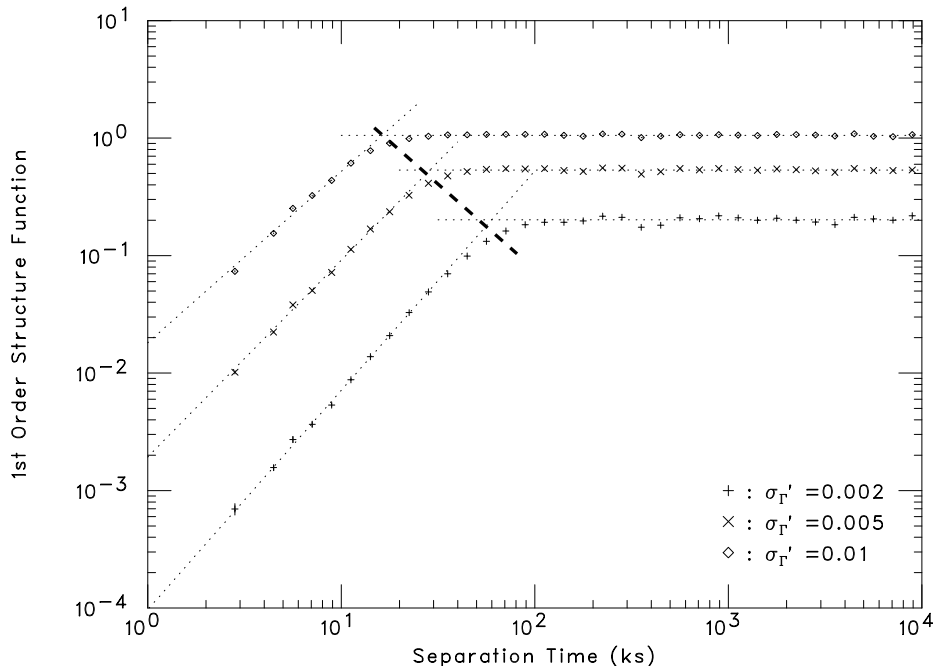


Figure 1.17: Structure function calculated from the simulated light curves (Tanihata et al. 2003) for the cases $\sigma'_\Gamma = 0.002$, 0.005 and 0.01 , where σ'_Γ is the standard deviation of the Gaussian probability distribution used to generate random Lorentz factors of the shells. Γ_{avg} is fixed to 10 and D_0 is fixed to 3×10^{13} cm. The dashed line shows how the location of the break moves to shorter separation times as σ'_Γ increases.

1.6 Motivation

Blazars are among the most intriguing astrophysical objects in the Universe because, even after more than three decades of observations, we know very little about the physics underlying their phenomenology and their actual origin. Their non-thermal, radio-to-gamma-ray emission displays, in the high-energy part of the spectra, light curves showing variable episodes of higher power.

In the last years relativistic (magneto)hydrodynamic codes have reached a high level of sophistication, enabling three-dimensional relativistic jet simulations to be performed with realistic physical parameters. However, these codes are not able to provide the values of observable quantities, namely, the intensity of the radiation emitted by the fluid and its spectrum.

Therefore, it is a natural step forward to include non-thermal radiation processes in such codes, the transport of non-thermal electrons, their radiative losses, the synchrotron radiation and the inverse-Compton scattering. The advantage of this approach is that the model is intrinsically multi-zone, inhomogeneous and internal shocks appear naturally as a consequence of an inhomogeneous fluid ejection. Far from being completed, the work done during this PhD thesis shows some new insights into the blazar physics.

Chapter 2

Non-thermal radiation

According to our current understanding, the observed radiation from relativistic jets and, more specifically, from blazars is produced by means of two main radiation mechanisms: synchrotron radiation and inverse-Compton scattering. In this chapter we summarize the basic theoretical concepts necessary to understand these two processes. Some of the derived expressions will be later used in our numerical algorithm.

2.1 Synchrotron radiation

2.1.1 Radiation emitted by a single charged particle

2.1.1.1 MOTION OF A CHARGED PARTICLE IN A MAGNETIC FIELD

We consider a particle of mass m and charge $-q < 0$ moving in a constant homogeneous magnetic field \mathbf{B} . Next we define a Cartesian coordinate system $(\hat{\mathbf{x}}, \hat{\mathbf{y}}, \hat{\mathbf{z}})$ such that $\mathbf{B} = B\hat{\mathbf{x}}$. Let the initial position of the particle be $\mathbf{r}(0)$ and its initial velocity $\mathbf{v}(0)$. The particle will move due to the Lorentz force acting onto it according to the equation

$$m \frac{d}{dt}(\gamma \mathbf{v}(t)) = -\frac{q}{c}(\mathbf{v}(t) \times \mathbf{B}), \quad (2.1)$$

where $\gamma \equiv (1 - v^2/c^2)^{-1/2}$ is the Lorentz factor. From the equation of motion (2.1) the trajectory of the particle will be

$$\mathbf{r}(t) = \mathbf{r}(0) + \frac{1}{\omega_B} \begin{pmatrix} \omega_B v_x(0)t \\ v_z(0) + v_z(0) \cos(\omega_B t) + v_y(0) \sin(\omega_B t) \\ -v_y(0) + v_z(0) \sin(\omega_B t) - v_y(0) \cos(\omega_B t) \end{pmatrix}, \quad (2.2)$$

where

$$\omega_B \equiv \frac{qB}{\gamma mc} \quad (2.3)$$

is the relativistic gyro-frequency.

We now chose the initial velocity such that $v_x(0) \equiv v_{\parallel} = v \cos(\alpha)$, $v_y(0) = 0$ and $v_z(0) \equiv v_{\perp} = v \sin(\alpha)$, where α is the angle between the velocity

vector and the magnetic field (*pitch angle*). Furthermore, we choose the initial position to be $\mathbf{r}(0) \equiv (0, -v_z(0)/\omega_B, 0)$ so that the equations for the trajectory and velocity become, using (2.2),

$$\mathbf{r}(t) = \begin{pmatrix} v_{\parallel} t \\ v_{\perp} \cos(\omega_B t)/\omega_B \\ v_{\perp} \sin(\omega_B t)/\omega_B \end{pmatrix}; \quad \mathbf{v}(t) = \begin{pmatrix} v_{\parallel} \\ -v_{\perp} \sin(\omega_B t) \\ v_{\perp} \cos(\omega_B t) \end{pmatrix}. \quad (2.4)$$

Obviously, the trajectory is a helix whose projection onto the $y-z$ plane is a circle with radius

$$a \equiv \frac{v_{\perp}}{\omega_B} = \frac{\beta \gamma m c^2 \sin(\alpha)}{qB}, \quad (2.5)$$

where $\boldsymbol{\beta} \equiv \mathbf{v}/c$.

2.1.1.2 ELECTRIC FIELD

The electric field which (seen by an observer located at \mathbf{x}) produced by a charged particle is given by the equation (Jackson 1962)

$$\mathbf{E}(\mathbf{x}, t) = \frac{q}{Rc^2 \left(1 - \mathbf{n} \frac{\mathbf{v}}{c}\right)^3} \mathbf{n} \times \left[\left(\mathbf{n} - \frac{\mathbf{v}}{c}\right) \times \dot{\mathbf{v}} \right], \quad (2.6)$$

where \mathbf{R} is the vector from the observer to the particle and $\mathbf{n} \equiv \mathbf{R}/R$ (where R is the magnitude of vector \mathbf{R}) is the unit vector pointing from the observer towards the particle. The velocity and the acceleration $\dot{\mathbf{v}}$ have to be evaluated at a retarded time. The derivative of the velocity is taken with respect to the retarded time

$$t_{\text{ret}} = t - R(t_{\text{ret}})/c. \quad (2.7)$$

We now assume that the particle is located at a large distance from the observer, i.e. x is much larger than the radius a (see equation (2.5)). Then we replace \mathbf{R} by \mathbf{x} except when computing derivatives. The relation (2.7) reads in this case

$$t \approx t_{\text{ret}} + \frac{1}{c} |x - \mathbf{n} \mathbf{r}(t_{\text{ret}})| \quad (2.8)$$

and the electric field (2.6) can be written, using (2.8), as

$$\mathbf{E}(\mathbf{x}, t) = \frac{q}{c^2 x (1 - \mathbf{n} \boldsymbol{\beta})^3} \mathbf{n} \times [(\mathbf{n} - \boldsymbol{\beta}) \times \dot{\mathbf{v}}]. \quad (2.9)$$

To compute the spectral decomposition of the electric field we consider only frequencies which are much larger than the relativistic gyro-frequency ω_B . Then the spectrum of the electric field is computed according to the equation (Rybicki & Lightman 1979)

$$\bar{\mathbf{E}}(\omega, T) = \frac{1}{2\pi\sqrt{T}} \int_{-T/2}^{T/2} dt \mathbf{E}(\mathbf{x}, t) e^{i\omega t}, \quad (2.10)$$

where $T \equiv 2\pi/\omega_B$ is the period over which we average the radiation. Since the motion of the particle is periodic with period T , we can change the integration variable in (2.10) from t to t_{ret} and integrate over a full orbit by parts to obtain, after inserting (2.9),

$$\mathbf{E}(\omega, \omega_B) = \frac{i\omega q}{2\pi c x \sqrt{2\pi/\omega_B}} \int_{\text{orbit}} dt [\mathbf{n} \times (\mathbf{n} \times \boldsymbol{\beta})] e^{i\omega(t - \mathbf{n}\mathbf{r}(t)/c)}, \quad (2.11)$$

where we drop the subscript *ret*.

2.1.1.3 RADIATION FLUX

The flux of observed radiation is

$$\mathbf{F}(\omega, T) = 2\pi c \mathbf{n} |\mathbf{E}(\omega, T)|^2, \quad (2.12)$$

which becomes, after substituting (2.11),

$$\mathbf{F}(\omega, \omega_B) = \mathbf{n} \frac{\omega_B q^2 \omega^2}{4\pi^2 c x^2} \left| \int_{\text{orbit}} dt [\mathbf{n} \times (\mathbf{n} \times \boldsymbol{\beta})] e^{i\omega(t - \mathbf{n}\mathbf{r}(t)/c)} \right|^2. \quad (2.13)$$

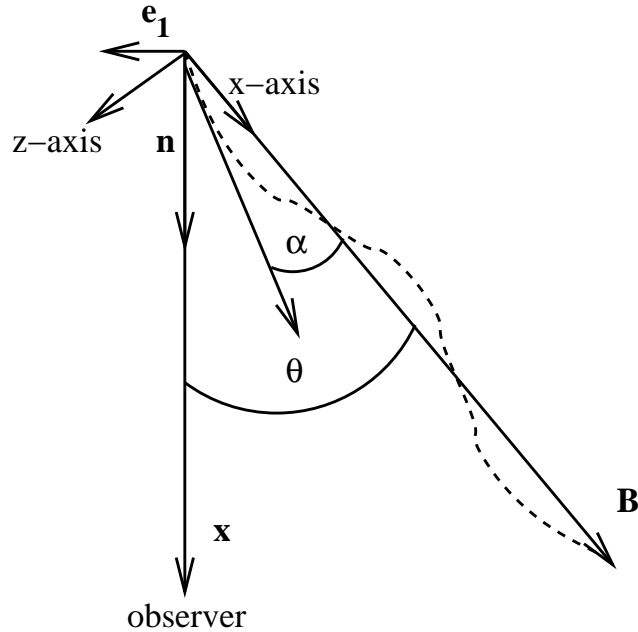


Figure 2.1: An illustration of the particle trajectory (dashed line) and various angles that appear in the calculation: θ is the angle between the direction of the magnetic field and the direction to the observer, and α is the particle pitch angle.

The unit vector \mathbf{n} can be written as a function of the angle θ between the direction to the observer and the x -axis (see Fig. 2.1)

$$\mathbf{n} = \begin{pmatrix} \mu \\ 0 \\ \sqrt{1 - \mu^2} \end{pmatrix}, \quad (2.14)$$

where $\mu \equiv \cos(\theta)$. We also introduce the unit vector

$$\mathbf{e}_1 \equiv \begin{pmatrix} -\sqrt{1-\mu^2} \\ 0 \\ \mu \end{pmatrix}. \quad (2.15)$$

\mathbf{e}_1 is anti-parallel to the projection of magnetic field on the observer's sky. We also define another unit vector perpendicular to \mathbf{n} and \mathbf{e}_1

$$\mathbf{e}_2 \equiv \begin{pmatrix} 0 \\ 1 \\ 0 \end{pmatrix}. \quad (2.16)$$

The triad $\{\mathbf{n}, \mathbf{e}_1, \mathbf{e}_2\}$ forms an orthonormal basis in which we can write

$$\mathbf{n} \times (\mathbf{n} \times \boldsymbol{\beta}) = \beta_{\perp} \sin(\omega_B t) \mathbf{e}_2 - \left[\sqrt{1-\mu^2} \beta_{\parallel} - \mu \beta_{\perp} \cos(\omega_B t) \right] \mathbf{e}_1, \quad (2.17)$$

where $\beta_{\parallel} \equiv \mathbf{v}_{\parallel}/c$ and $\beta_{\perp} \equiv \mathbf{v}_{\perp}/c$. Also, we can easily see that

$$\frac{\mathbf{nr}(t)}{c} = \mu \beta_{\parallel} t + \sqrt{1-\mu^2} \beta_{\perp} \frac{\sin(\omega_B t)}{\omega_B} \quad (2.18)$$

The flux (2.13) can be split into components whose electric field is parallel and perpendicular to the direction of the magnetic field projection on the plane of the sky

$$\mathbf{F}_1(\omega, \omega_B) = \mathbf{n} \frac{\omega_B q^2 \omega^2}{4\pi^2 c x^2} \left| \int_{-\pi/\omega_B}^{\pi/\omega_B} dt \left(\sqrt{1-\mu^2} \beta_{\parallel} - \mu \beta_{\perp} \cos(\omega_B t) \right) e^{i\omega\tau} \right|^2, \quad (2.19)$$

$$\mathbf{F}_2(\omega, \omega_B) = \mathbf{n} \frac{\omega_B q^2 \omega^2}{4\pi^2 c x^2} \left| \int_{-\pi/\omega_B}^{\pi/\omega_B} dt \beta_{\perp} \sin(\omega_B t) e^{i\omega\tau} \right|^2, \quad (2.20)$$

where

$$\tau(t) \equiv t - \frac{\mathbf{nr}(t)}{c} = t - \mu \beta_{\parallel} t - \sqrt{1-\mu^2} \beta_{\perp} \frac{\sin(\omega_B t)}{\omega_B}. \quad (2.21)$$

2.1.1.4 HIGH FREQUENCY LIMIT FOR THE RELATIVISTIC PARTICLES

We limit our considerations to high frequencies only, i.e. $\omega \gg \omega_B$. Furthermore, we assume that the particles are relativistic, i.e. $\gamma \gg 1$. In that case the approximate expression for β is

$$\beta \approx 1 - \frac{1}{2\gamma^2}. \quad (2.22)$$

In order for the integrals in (2.19) and (2.20) to be non-vanishing, the exponential factor has to vary slowly with t , i.e. the derivative

$$\frac{d\tau}{dt} = 1 - \mu \beta_{\parallel} - \sqrt{1-\mu^2} \beta_{\perp} \cos(\omega_B t) \quad (2.23)$$

has to be small. Introducing the angle $\psi \equiv \theta - \alpha$ we can write

$$\mu\beta_{\parallel} + \sqrt{1 - \mu^2}\beta_{\perp} = \beta(\cos(\theta)\cos(\alpha) + \sin(\theta)\sin(\alpha)) = \beta\cos(\psi).$$

For the derivative (2.23) to be small both t and ψ have to be close to zero ($\beta \approx 1$ due to assumption that the particles are relativistic).

From the condition that $t \approx 0$ (2.21) becomes

$$\tau \approx t - \left(\mu\beta_{\parallel} + \sqrt{1 - \mu^2}\beta_{\perp}\right)t - \sqrt{1 - \mu^2}\beta_{\perp}\frac{\omega_{\text{B}}^2 t^3}{6} \quad (2.24)$$

From the condition $\psi \approx 0$ we have $\sqrt{1 - \mu^2} = \sin(\theta) \approx \sin(\alpha)$ so that (2.24) becomes, after substituting (2.22) and expanding $\cos(\psi)$ to the leading order,

$$\tau \approx \frac{1}{2\gamma^2} \left[(1 + \gamma^2\psi^2)t + \frac{\gamma^2 \sin^2 \alpha \omega_{\text{B}}^2 t^3}{3} \right]. \quad (2.25)$$

Using the fact that

$$\sqrt{1 - \mu^2}\beta_{\parallel} - \mu\beta_{\perp} = \beta\sin(\psi) \approx \beta\psi,$$

the fluxes (2.19) and (2.20) become, with the aid of (2.25),

$$\mathbf{F}_{\parallel}(\omega, \omega_{\text{B}}) = \mathbf{n} \frac{\omega^2 q^2 \beta^2 \psi^2 (1 + \psi^2 \gamma^2)}{4\pi^2 \omega_{\text{B}} c x^2 \gamma^2 \sin^2(\alpha)} \left| \int_{-\pi/\omega_{\text{B}}}^{\pi/\omega_{\text{B}}} dy \cos \left[\frac{3}{2} \xi \left(y + \frac{y^3}{3} \right) \right] \right|^2, \quad (2.26)$$

$$\mathbf{F}_{\perp}(\omega, \omega_{\text{B}}) = \mathbf{n} \frac{\omega^2 q^2 \beta^2 (1 + \psi^2 \gamma^2)^2}{4\pi^2 \omega_{\text{B}} c x^2 \gamma^4 \sin^2(\alpha)} \left| \int_{-\pi/\omega_{\text{B}}}^{\pi/\omega_{\text{B}}} dy y \sin \left[\frac{3}{2} \xi \left(y + \frac{y^3}{3} \right) \right] \right|^2, \quad (2.27)$$

where

$$y \equiv \frac{\omega_{\text{B}} \gamma \sin(\alpha)}{\sqrt{1 + \psi^2 \gamma^2}} t, \quad (2.28)$$

$$\xi \equiv \frac{\omega (1 + \psi^2 \gamma^2)^{3/2}}{3\omega_{\text{B}} \gamma^3 \sin(\alpha)}. \quad (2.29)$$

It is possible to extend the limits of the integrals in (2.26) and (2.27) to $-\infty$ and ∞ because the main contribution comes from very small t . Then the fluxes become

$$\mathbf{F}_1(\omega, \omega_{\text{B}}) = \mathbf{n} \frac{\omega^2 q^2 \beta^2 \psi^2}{3\pi^2 \omega_{\text{B}} c x^2 \gamma^2 \sin^2(\alpha)} (1 + \psi^2 \gamma^2) K_{1/3}^2(\xi), \quad (2.30)$$

$$\mathbf{F}_2(\omega, \omega_{\text{B}}) = \mathbf{n} \frac{\omega^2 q^2 \beta^2}{3\pi^2 \omega_{\text{B}} c x^2 \gamma^4 \sin^2(\alpha)} (1 + \psi^2 \gamma^2)^2 K_{2/3}^2(\xi), \quad (2.31)$$

where $K_\nu(z)$ is the modified Bessel function. We define the characteristic frequency of the synchrotron emission

$$\omega_C \equiv \frac{3}{2}\gamma^3\omega_B \sin(\alpha) \quad (2.32)$$

and the dimensionless frequency

$$X \equiv \frac{\omega}{\omega_C}. \quad (2.33)$$

The total emitted power is computed from the relation

$$\frac{dP}{d\omega} = \frac{1}{2\pi} \int d\Omega \mathbf{nF}(\omega, \omega_B)x^2, \quad (2.34)$$

where the integral is over solid angle. Since $\alpha \approx \theta$ in this approximation, we can write

$$\int d\Omega = 2\pi \int_0^\pi d\theta \sin(\theta) \approx 2\pi \sin(\alpha) \int_0^\pi d\theta \approx 2\pi \sin(\alpha) \int_{-\infty}^\infty d\psi$$

where the last step can be made due to the fact that the range of *theta* in which a significant amount of radiation is emitted is narrow and centered on α , and then, substituting (2.32) and (2.33) into (2.30) and (2.31) and then integrating (2.34) we get

$$\frac{dP_1}{d\omega} = \frac{\sqrt{3}q^2\omega_B\beta^2 \sin(\alpha)}{4\pi c} \gamma [F(X) - G(X)], \quad (2.35)$$

$$\frac{dP_2}{d\omega} = \frac{\sqrt{3}q^2\omega_B\beta^2 \sin(\alpha)}{4\pi c} \gamma [F(X) + G(X)], \quad (2.36)$$

where

$$F(X) \equiv X \int_X^\infty dy K_{5/3}(y) \quad (2.37)$$

and

$$G(X) \equiv X K_{2/3}(X). \quad (2.38)$$

Therefore, the total (unpolarized) power emitted at frequency ω is, adding (2.35) and (2.36),

$$\frac{dP}{d\omega} = \frac{\sqrt{3}q^2\omega_B\beta^2 \sin(\alpha)}{2\pi c} \gamma F(X). \quad (2.39)$$

Equation (2.39) can be rewritten in terms of the magnetic field strength only, using definitions (2.3) and (2.32),

$$\frac{dP}{d\omega} = \frac{\sqrt{3}q^3 B \sin(\alpha) \beta^2}{2\pi mc^2} F\left(\frac{2mc}{3q\gamma^2 B \sin(\alpha)}\omega\right). \quad (2.40)$$

It should be pointed out again that the above relations are only for frequencies $\omega \gg \omega_B$. Numerically, one gets from (2.3)

$$\omega_B \approx 1.76 \times 10^4 \left(\frac{100}{\gamma} \right) \left(\frac{q}{e} \right) \left(\frac{B}{0.1\text{G}} \right) \text{Hz}, \quad (2.41)$$

where e is the absolute value of the electron charge, $e = 4.803 \times 10^{-10} \text{ cm}^{3/2} \text{ g}^{1/2} \text{ s}^{-1}$ in CGS units. On the other hand, the critical frequency (2.32) is

$$\omega_C \approx 2.64 \times 10^{10} \left(\frac{\gamma}{100} \right)^2 \left(\frac{q}{e} \right) \left(\frac{B \sin(\alpha)}{0.1\text{G}} \right) \text{Hz}. \quad (2.42)$$

We can see that for a sufficiently large γ *and* angle α the spectrum in the vicinity of ω_C is very well approximated by (2.39), since in that case $\omega_C \gg \omega_B$. This is important since the function $F(X)$ has a maximum around $X = 0.29$ (Fig. 2.2), so that most of the contribution to the radiation comes from the frequencies which are close to ω_C , i.e. the condition $\omega \gg \omega_B$ is satisfied.

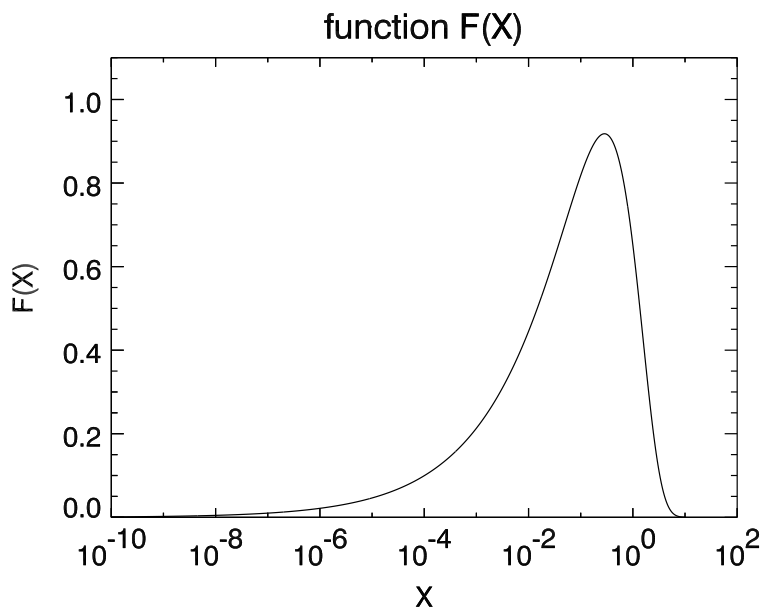


Figure 2.2: Plot of function $F(X) = X \int_X^\infty dy K_{5/3}(y)$.

2.1.2 Radiation emitted by a distribution of particles

2.1.2.1 SYNCHROTRON EMISSIVITY

We consider a distribution of particles which is homogeneous in space. We also assume that the particles have an isotropic velocity distribution, i.e. their distribution depends solely on the Lorentz factor. In the rest of this chapter $n(\gamma)$ will denote the differential number density of particles with Lorentz factors in the range $[\gamma, \gamma + d\gamma]$.

To compute the radiation from a distribution of particles, it is useful to note that most of the radiation from a single particle is emitted into a narrow cone with opening angle $2/\gamma^2$ around direction α . Therefore we approximate the power emitted by a single particle as

$$\left(\frac{dP}{d\omega d\Omega}\right)_1 = \frac{1}{2\pi} \left(\frac{dP}{d\omega}\right)_1 \delta(\cos(\alpha) - \cos(\theta)), \quad (2.43)$$

where $d\Omega = d\phi d\theta \sin(\theta)$ is the solid angle element in the direction (θ, ϕ) and $(dP/d\omega)_1$ is the single particle synchrotron power (2.40).

Although we have an isotropic particle distribution, we formally write it as

$$n(\gamma) = 2\pi \int_0^\pi d\alpha \sin(\alpha) n(\gamma, \alpha), \quad (2.44)$$

where $n(\gamma, \alpha) \equiv n(\gamma)/4\pi$.

The power emitted per unit frequency, and unit solid angle and volume is

$$\frac{dP}{d\omega d\Omega dV} = 2\pi \int_0^\pi d\alpha \sin(\alpha) \int_1^\infty d\gamma \left(\frac{dP}{d\omega d\Omega}\right)_1 n(\gamma, \alpha), \quad (2.45)$$

which becomes, after substituting (2.43) and (2.44) into (2.45),

$$\frac{dP}{d\omega d\Omega dV} = \int_1^\infty d\gamma n(\gamma, \alpha) \left(\frac{dP}{d\omega}\right)_1 \Big|_{\alpha=\theta} = \frac{1}{4\pi} \int_1^\infty d\gamma n(\gamma) \left(\frac{dP}{d\omega}\right)_1. \quad (2.46)$$

Now it is useful to switch from the power (2.46) to the emissivity $j_{\text{syn}}(\nu)$, which is defined as the energy emitted per unit volume and frequency into direction θ . This is given by (2.46) changing from the angular frequency ω to the linear frequency $\nu \equiv \omega/2\pi$, i.e.

$$j_{\text{syn}}(\nu) = \frac{\sqrt{3}q^3 B \sin(\theta)}{4\pi mc^2} \int_1^\infty d\gamma n(\gamma) F\left(\frac{\nu}{\nu_0 \gamma^2}\right), \quad (2.47)$$

where β (2.40) is set to be equal to 1 since we are dealing with ultra-relativistic particles, and the characteristic linear frequency ν_0 (independent of γ) is defined as

$$\nu_0 \equiv \frac{3qB \sin(\theta)}{4\pi mc}. \quad (2.48)$$

2.1.2.2 SYNCHROTRON SELF-ABSORPTION

The synchrotron radiation emitted by a distribution of particles can also be absorbed by the same population of particles (self-absorption) and further re-emitted. In order to account for this process, we introduce the Einstein coefficients:

- $A_{21}(\gamma, \nu, \mathbf{n})d\nu d\Omega$ is the rate at which a particle with Lorentz factor γ emits a photon with frequency in frequency range $[\nu, \nu + d\nu]$ into the solid angle $d\Omega$ in the direction \mathbf{n} ,
- $B_{12}\left(\gamma - \frac{h\nu}{mc^2}, \nu, \mathbf{n}\right) I(\nu, \mathbf{n})d\nu d\Omega$ is the rate at which a particle with Lorentz factor $\gamma - \frac{h\nu}{mc^2}$ absorbs a photon in the frequency range $[\nu, \nu + d\nu]$ coming from a direction \mathbf{n} , where $I(\nu, \mathbf{n})$ is the intensity distribution of the incoming radiation and h the Planck constant,
- $B_{21}(\gamma, \nu, \mathbf{n})I(\nu, \mathbf{n})d\nu dd\Omega$ is the rate at which a particle with Lorentz factor γ emits a photon in the direction \mathbf{n} if stimulated by radiation with frequency in the range $[\nu, \nu + d\nu]$.

The coefficients have the following properties (Rybicki & Lightman 1979),

$$\frac{A_{21}(\gamma, \nu, \mathbf{n})}{B_{21}(\gamma, \nu, \mathbf{n})} = \frac{2h\nu^3}{c^2}, \quad (2.49)$$

$$\frac{B_{12}\left(\gamma - \frac{h\nu}{mc^2}, \nu, \mathbf{n}\right)}{B_{21}(\gamma, \nu, \mathbf{n})} = \frac{\gamma^2}{\left(\gamma - \frac{h\nu}{mc^2}\right)^2}. \quad (2.50)$$

The energy emitted per unit of time from the unit volume into the solid angle around \mathbf{n} in the frequency range $[\nu, \nu + d\nu]$ is, according to the definition of $A_{21}(\gamma, \nu, \mathbf{n})$,

$$\frac{dE}{dt dV d\nu d\Omega} = h\nu \int_1^\infty d\gamma A_{21}(\gamma, \nu, \mathbf{n})n(\gamma), \quad (2.51)$$

where $n(\gamma)$ is the differential number density of particles, as in the previous section. On the other hand, from the definition of the emissivity we have

$$\frac{dE}{dt dV d\nu d\Omega} = j(\nu, \mathbf{n}), \quad (2.52)$$

where $j(\nu, \mathbf{n})$ is the emissivity of a distribution of particles which radiate into the direction \mathbf{n} at frequency ν . Comparing (2.51) and (2.52) we get the relation

$$j(\nu, \mathbf{n}) = h\nu \int_1^\infty d\gamma n(\gamma)A_{21}(\gamma, \nu, \mathbf{n}). \quad (2.53)$$

On the other hand, the radiation energy absorbed at frequency ν per unit frequency, solid angle and unit time while passing through a unit area

is (taking into account the stimulated emission at the same frequency ν)

$$\frac{dI(\nu, \mathbf{n})}{dt dA d\nu d\Omega ds} = \int_1^\infty d\gamma \left[n \left(\gamma - \frac{h\nu}{mc^2} \right) B_{12} \left(\gamma - \frac{h\nu}{mc^2}, \nu, \mathbf{n} \right) - n(\gamma) B_{21}(\gamma, \nu, \mathbf{n}) \right] I(\nu, \mathbf{n}) h\nu, \quad (2.54)$$

where $dI(\nu, \mathbf{n})$ is the radiation intensity absorbed while traveling a distance ds passing through a cylinder of cross section of area dA . We now define the absorption coefficient $\alpha(\nu, \mathbf{n})$ to satisfy the equation

$$\frac{dI(\nu, \mathbf{n})}{dt dA d\nu d\Omega ds} = \alpha(\nu, \mathbf{n}) I(\nu, \mathbf{n}). \quad (2.55)$$

Equating (2.54) and (2.55) we get

$$\alpha(\nu, \mathbf{n}) = h\nu \int_1^\infty d\gamma \left[n \left(\gamma - \frac{h\nu}{mc^2} \right) B_{12} \left(\gamma - \frac{h\nu}{mc^2}, \nu, \mathbf{n} \right) - n(\gamma) B_{21}(\gamma, \nu, \mathbf{n}) \right]. \quad (2.56)$$

Equation (2.56) simplifies if we use the properties (2.49) and (2.50), in which case we get

$$\alpha(\nu, \mathbf{n}) = \frac{c^2}{2\nu^2} \int_1^\infty d\gamma \gamma^2 A_{21}(\gamma, \nu, \mathbf{n}) \left[\frac{n(\gamma - h\nu/mc^2)}{(\gamma - h\nu/mc^2)^2} - \frac{n(\gamma)}{\gamma^2} \right]. \quad (2.57)$$

We can further simplify the expression for the absorption coefficient by noting that for ultra-relativistic particles the condition $h\nu \ll \gamma mc^2$ is fulfilled (i.e. $\nu \ll 1.24 \times 10^{20} \gamma$ Hz). In that case we can write

$$\left[\frac{n(\gamma - h\nu/mc^2)}{(\gamma - h\nu/mc^2)^2} - \frac{n(\gamma)}{\gamma^2} \right] \approx -\frac{h\nu}{mc^2} \frac{d}{d\gamma} \left(\frac{n(\gamma)}{\gamma^2} \right).$$

Substituting into (2.57) one gets

$$\alpha(\nu, \mathbf{n}) = \frac{h}{2m\nu} \int_1^\infty d\gamma \gamma^2 A_{21}(\gamma, \nu, \mathbf{n}) \left[-\frac{d}{d\gamma} \left(\frac{n(\gamma)}{\gamma^2} \right) \right]. \quad (2.58)$$

We specify our further calculation to the case of synchrotron radiation. Comparing (2.47) and (2.53) we get

$$A_{21}(\gamma, \nu, \mathbf{n}) = \frac{\sqrt{3}q^3 B \sin(\theta)}{4\pi mc^2 h\nu} F \left(\frac{\nu}{\nu_0 \gamma^2} \right). \quad (2.59)$$

From (2.58) and (2.59) we obtain the expression for the synchrotron self-absorption,

$$\alpha_{\text{syn}}(\nu) = \frac{\sqrt{3}q^3 B \sin(\theta)}{8\pi m^2 c^2} \nu^{-2} \int_1^\infty d\gamma \gamma^2 \left[-\frac{d}{d\gamma} \left(\frac{n(\gamma)}{\gamma^2} \right) \right] F \left(\frac{\nu}{\nu_0 \gamma^2} \right). \quad (2.60)$$

2.1.3 Radiation from a power law distribution of particles

We now specify our discussion to the case of a power law distribution of particles

$$n(\gamma) = n(\gamma_{\min}) \left(\frac{\gamma}{\gamma_{\min}} \right)^{-p} S(\gamma; \gamma_{\min}, \gamma_{\max}) \quad (2.61)$$

where γ_{\min} and γ_{\max} are the limiting Lorentz factor values of the power law distribution, p is the power law index, and the interval function S is defined as

$$S(x; a, b) = \begin{cases} 1 & \text{if } a \leq x \leq b \\ 0 & \text{otherwise} \end{cases}. \quad (2.62)$$

Inserting (2.61) into (2.47) and (2.60) one finds

$$j_{\text{syn}}(\nu) = \frac{\sqrt{3}q^3 B \sin(\theta)}{4\pi mc^2} n(\gamma_{\min}) \gamma_{\min}^p \int_{\gamma_{\min}}^{\gamma_{\max}} d\gamma \gamma^{-p} F\left(\frac{\nu}{\nu_0 \gamma^2}\right), \quad (2.63)$$

$$\alpha_{\text{syn}}(\nu) = \frac{\sqrt{3}q^3 B \sin(\theta)}{8\pi m^2 c^2} n(\gamma_{\min}) \gamma_{\min}^p \frac{p+2}{\nu^2} \int_{\gamma_{\min}}^{\gamma_{\max}} d\gamma \gamma^{-(p+1)} F\left(\frac{\nu}{\nu_0 \gamma^2}\right). \quad (2.64)$$

We define $\eta \equiv \gamma_{\max}/\gamma_{\min}$ and substitute $\gamma \equiv \Gamma \gamma_{\min}$ so that we get from (2.63) and (2.64)

$$j_{\text{syn}}(\nu) = \frac{\sqrt{3}q^3 B \sin(\theta)}{4\pi mc^2} n(\gamma_{\min}) \gamma_{\min} H\left(\frac{\nu}{\nu_0 \gamma_{\min}^2}, p, \eta\right), \quad (2.65)$$

$$\alpha_{\text{syn}}(\nu) = \frac{\sqrt{3}q^3 B \sin(\theta)}{8\pi m^2 c^2} n(\gamma_{\min}) \frac{p+2}{\nu^2} H\left(\frac{\nu}{\nu_0 \gamma_{\min}^2}, p+1, \eta\right), \quad (2.66)$$

where the function H is defined as

$$H(x, p, \eta) = \int_1^{\eta} d\Gamma \Gamma^{-p} F\left(\frac{x}{\Gamma^2}\right) = \int_1^{\eta} d\Gamma \Gamma^{-(p+2)} x \int_{x/\Gamma^2}^{\infty} dy K_{5/3}(y). \quad (2.67)$$

The function H can be evaluated numerically and tabulated (it turns out that H is a well behaved function), which is of importance for massive numerical computation. On the other hand, one may gain some insight in the nature of the integral in H by making the substitution

$$\xi \equiv \frac{x}{\Gamma^2}$$

which, when inserted into (2.67) gives

$$H(x, p, \eta) = \frac{1}{2} x^{(1-p)/2} \int_{x/\eta^2}^x d\xi \xi^{(p-3)/2} F(\xi). \quad (2.68)$$

Inserting (2.68) into (2.65) we get

$$j_{\text{syn}}(\nu) = \frac{\sqrt{3}q^3 B \sin(\theta)}{8\pi mc^2} n(\gamma_{\text{min}}) \gamma_{\text{min}}^p \left(\frac{\nu}{\nu_0}\right)^{(1-p)/2} H_1(\nu/\nu_0 \gamma_{\text{min}}^2, p, \eta), \quad (2.69)$$

where H_1 is simply the integral in (2.68),

$$H_1(x, p, \eta) = \int_{x/\eta^2}^x d\xi \xi^{(p-3)/2} F(\xi). \quad (2.70)$$

From the properties of the function $F(\xi)$ (Fig. 2.2) we see that the integral (2.70) changes very slowly with ξ provided that $\xi \geq 10$ and $\xi/\eta^2 < 10^{-4}$, which is easily achieved for η of at least a few hundred and $\nu > 10\nu_0\gamma_{\text{min}}^2$. The integral is almost constant and the synchrotron emissivity (2.69) becomes a power law with the spectral index $(1-p)/2$.

2.2 Inverse-Compton scattering

In this section a model for inverse-Compton scattering is developed in order to apply it to scattering of a power law radiation spectrum on a power law electron population described by a single or several piecewise power law distributions.

2.2.1 Scattering of the monochromatic radiation

In this subsection we consider the scattering of monochromatic radiation off mono-energetic electrons, and then off a population of electrons whose energy distribution is a power law.

The radiation field is assumed to be isotropic and monochromatic in the laboratory frame (the inertial frame in which the electron is moving),

$$I(\nu, \mathbf{n}) = I(\nu_0)\delta(\nu - \nu_0), \quad (2.71)$$

where $\delta(x)$ is the Dirac delta function and $I(\nu, \mathbf{n})$ is the radiation intensity, i.e. the energy per frequency interval of the radiation emitted in direction \mathbf{n} per unit solid angle centered around \mathbf{n} per unit surface per unit of time. We also consider electrons moving with velocity $v \equiv \beta c = c\sqrt{1 - \gamma^{-2}}$, where γ is the electron Lorentz factor. The coordinate system is a spherical coordinate system chosen such that the angle θ is zero in the direction of the electron motion. We also use the notation $\mu \equiv \cos(\theta)$ and mark the direction of motion of the electron in the lab frame with $\mu_0 \equiv \cos(\theta_0) = 1$. The number density of electrons is $n(\gamma)$ in the laboratory frame.

In the rest frame of the electron the radiation field is anisotropic (Rybicki & Lightman 1979),

$$I'(\nu', \mu'_0) = \left(\frac{\nu'}{\nu}\right)^3 I(\nu), \quad (2.72)$$

where the frequencies ν and ν' are related through the Doppler effect (Rybicki & Lightman 1979)

$$\nu = \nu' \gamma (1 + \beta \mu'_0) \quad (2.73)$$

μ'_0 being the direction of the incoming radiation in the electron rest frame. We note that for different directions the radiation has a different frequency. Inserting (2.71) and (2.73) into (2.72) we get

$$I'(\nu', \mu'_0) = \frac{I(\nu_0)}{\gamma^3 (1 + \beta \mu'_0)^3} \delta[\nu' \gamma (1 + \beta \mu'_0) - \nu_0]. \quad (2.74)$$

The scattering of the photons off the electron is assumed to be elastic in the electron rest frame. The differential cross section in the Thomson regime can be derived from Rybicki & Lightman (1979)

$$\frac{d\sigma'}{d\Omega'_0 d\Omega'_1 d\nu'_0 d\nu'_1} = \frac{3\sigma_T}{32\pi^2} (1 + \mu_1'^2) \delta(\nu'_1 - \nu'), \quad (2.75)$$

where Ω'_0 and Ω'_1 are the solid angles of the incoming and scattered photons respectively, μ'_0 and μ'_1 the corresponding $\cos(\theta'_0)$ and $\cos(\theta'_1)$, and ν'_0 and ν'_1 the frequencies of the incoming and scattered photons, respectively. σ_T is the Thompson cross section. The emissivity of the scattered radiation can be computed in the electron rest frame,

$$j'(\nu'_1, \mu'_1) = n'(\gamma) \int d\Omega'_0 \int d\nu' \int d\phi'_1 \frac{d\sigma'}{d\Omega'_0 d\Omega'_1 d\nu' d\nu'_1}, \quad (2.76)$$

where ϕ'_0 and ϕ'_1 are the azimuthal angles of the scattered radiation. Inserting (2.75) into (2.76) and integrating over both azimuthal angles ϕ'_0 and ϕ'_1 one obtains the equation

$$j(\nu'_1, \mu'_1) = \frac{3I(\nu_0)\sigma_T n(\gamma)}{8\gamma^3} \int_{-1}^1 d\mu'_0 \times \\ (1 + \mu_1'^2) \delta\left(\mu'_0 - \frac{\nu_0 - \gamma\nu'_1}{\gamma\beta\nu'_1}\right) (\gamma\beta\nu'_1)^{-1} (1 + \beta\mu'_0)^{-3}. \quad (2.77)$$

After integration and transformation into the laboratory frame using the equations

$$j(\nu_1, \mu_1) = \left(\frac{\nu_1}{\nu'_1}\right)^2 j'(\nu'_1, \mu'_1), \quad (2.78)$$

$$\nu'_1 = \gamma\nu_1(1 - \beta\mu_1), \quad (2.79)$$

$$\mu'_1 = \frac{\mu_1 - \beta}{1 - \beta\mu_1}, \quad (2.80)$$

we get

$$j(\nu_1, \mu_1) = \frac{3\sigma_T I(\nu_0) n(\gamma)}{8\gamma^2 \beta \nu_0} \left(\frac{\nu_1}{\nu_0}\right)^2 \left[1 + \frac{(\mu_1 - \beta)^2}{(1 - \beta\mu_1)^2}\right] \times \\ S\left(\nu_1; \frac{\nu_0}{\gamma^2(1 + \beta)(1 - \beta\mu_1)}, \frac{\nu_0}{\gamma^2(1 - \beta)(1 - \beta\mu_1)}\right) \quad (2.81)$$

ϵ	10^{-1}	10^{-2}	10^{-3}	10^{-4}	10^{-5}	10^{-6}
$\gamma_{\text{a-min}}$	4.41	14.12	44.72	141.42	316.23	1414.21

Table 2.1: The minimum Lorentz factor required to achieve a certain ϵ accuracy.

where S is the interval function (2.62).

In the following we consider only in an emissivity average over scattering angle θ_1 , because we are interested only in those distributions of electrons whose velocity field is isotropic. Using the substitution $\eta_1 \equiv 1 - \beta\mu_1$ the integration is performed easily,

$$j(\nu_1, \gamma) = \frac{3\sigma_{\text{T}}}{16} \frac{n(\gamma)}{\gamma^2 + \gamma^{-2} - 2} \frac{I(\nu_0) \nu_1}{\nu_0 \nu_0} \times \begin{cases} \frac{\beta^+ \frac{\nu_1}{\nu_0} - \beta^-}{(2 - \gamma^{-2})^{-1}} - \frac{2\nu_1}{\gamma^2 \nu_0} \ln \left(\frac{\beta^+ \nu_1}{\beta^+ \nu_0} \right) - \frac{\beta^- \frac{\nu_1}{\nu_0} - \beta^+ \left(\frac{\nu_1}{\nu_0} \right)^2}{\gamma^2} & \text{if } \frac{\beta^-}{\beta^+} \leq \frac{\nu_1}{\nu_0} \leq 1 \\ \frac{\beta^+ - \beta^- \frac{\nu_1}{\nu_0}}{(2 - \gamma^{-2})^{-1}} + \frac{2\nu_1}{\gamma^2 \nu_0} \ln \left(\frac{\beta^- \nu_1}{\beta^+ \nu_0} \right) - \frac{\beta^- \left(\frac{\nu_1}{\nu_0} \right)^2 - \beta^+ \frac{\nu_1}{\nu_0}}{\gamma^2} & \text{if } 1 < \frac{\nu_1}{\nu_0} \leq \frac{\beta^+}{\beta^-} \\ 0 & \text{otherwise} \end{cases}, \quad (2.82)$$

where $\beta^+ \equiv 1 + \beta$ and $\beta^- \equiv 1 - \beta$. In case of ultra-relativistic electrons, the expressions in (2.82) can be simplified. We define the minimum $\gamma_{\text{a-min}}$ above which the expression $\gamma^2 + \gamma^{-2} - 2$ can be approximated by γ^2 up to some desired degree of accuracy $\epsilon < 1$ so that

$$1 - \frac{\gamma_{\text{a-min}}^2 + \gamma_{\text{a-min}}^{-2} - 2}{\gamma_{\text{a-min}}^2} = \epsilon$$

with the solution

$$\gamma_{\text{a-min}} = \sqrt{\frac{1 + \sqrt{1 - \epsilon}}{\epsilon}}. \quad (2.83)$$

Some typical values are shown in Table 2.2.1. If the ultrarelativistic approximation is valid, then the equation (2.82) becomes

$$j(\nu_1, \gamma) = 3\sigma_{\text{T}} n(\gamma) \frac{I(\nu_0)}{\nu_0} \mathcal{F} \left(\frac{\nu_1}{4\gamma^2 \nu_0}, \gamma \right), \quad (2.84)$$

where the function \mathcal{F} is (neglecting terms of order γ^{-4} and smaller)

$$\mathcal{F}(x, \gamma) = x \times \begin{cases} \frac{8\gamma^4 - 4\gamma^2 - 1}{2\gamma^2}x - \frac{1}{4\gamma^2} - 2x \ln(16\gamma^4 x) + 8\gamma^2 x^2 & \text{if } \frac{1}{16\gamma^4} \leq x \leq \frac{1}{4\gamma^2} \\ 1 - \frac{1}{2\gamma^2} + x \left(1 + \frac{1}{2\gamma^2}\right) + 2x \ln x - 2x^2 & \text{if } \frac{1}{4\gamma^2} < x \leq 1 \\ 0 & \text{otherwise} \end{cases} \quad (2.85)$$

If the scattering cross section is assumed to be isotropic, the emissivity would have the same form as (2.84), except for the function \mathcal{F} , which would have to be replaced by

$$\mathcal{F}^{\text{ISO}}(x, \gamma) = x \begin{cases} 4\gamma^2 x - \frac{1}{4\gamma^2} & \text{if } \frac{1}{16\gamma^4} \leq x \leq \frac{1}{4\gamma^2} \\ 1 - x & \text{if } \frac{1}{4\gamma^2} < x \leq 1 \\ 0 & \text{otherwise} \end{cases} \quad (2.86)$$

Figure 2.3 shows the generic shape of the emissivity. More insight is ob-

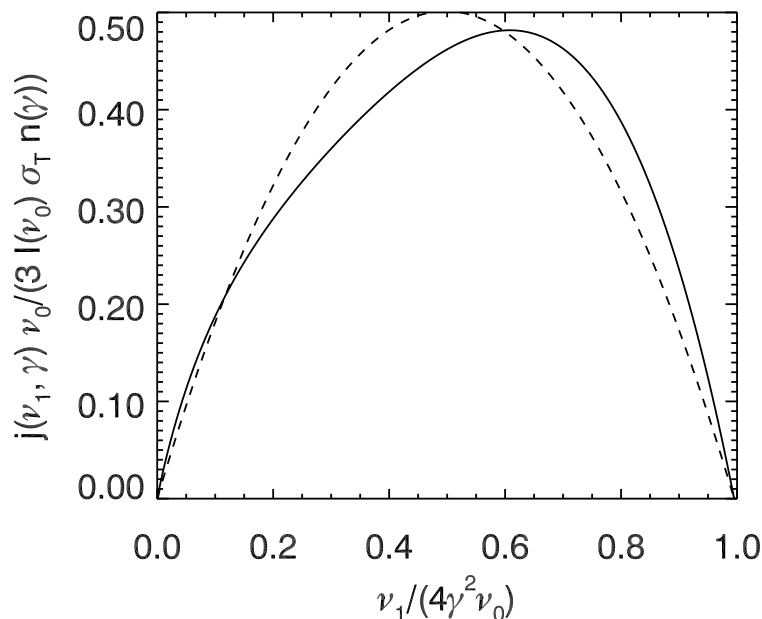


Figure 2.3: Generic shape of the emissivity for anisotropic (solid line) and isotropic (dashed line) scattering in the electron rest frame.

tained, if one plots the x -axis in logarithmic scale (Fig. 2.4). As we can see,

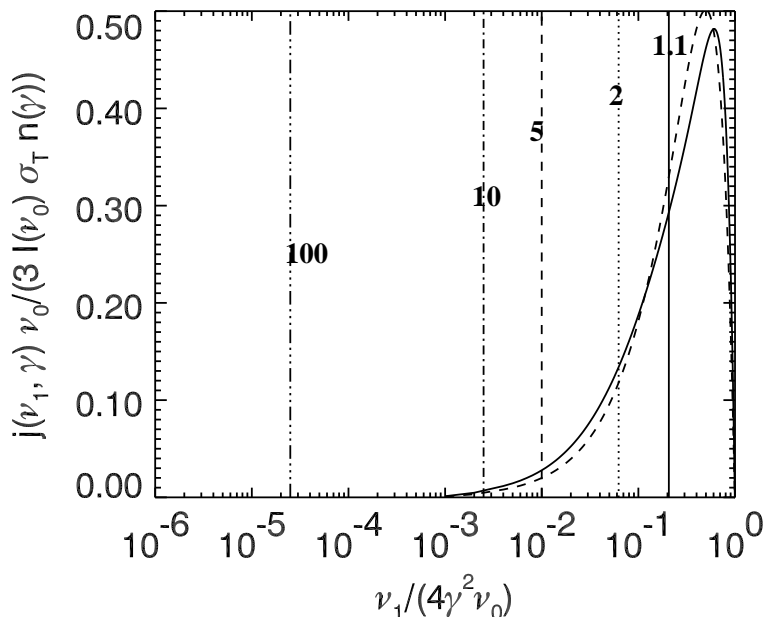


Figure 2.4: Generic shape of the emissivity for anisotropic (full line) and isotropic (dashed line) scattering, using a logarithmic x -axis. The vertical lines show frequencies at which $\nu_1 = \nu_0$, which are also the limits between two cases in the emissivity formulas. From right to left the limits are given for $\gamma = 1.1, 2, 5, 10, 100$,

for $\gamma > 10$ the dominant contribution comes from the frequencies $\nu_1 \geq \nu_0$ (which is, indeed, expected for an inverse Compton scattering process where photons get scattered to higher frequencies). Therefore, in the further considerations we limit ourselves to the case $\gamma > 10$. The emissivity has then the form

$$j(\nu_1, \gamma) = 3\sigma_{\text{T}}n(\gamma)\frac{I(\nu_0)}{\nu_0}f\left(\frac{\nu_1}{4\gamma^2\nu_0}, \gamma\right), \quad (2.87)$$

where (neglecting terms of order γ^{-2} and smaller)

$$f(x, \gamma) = (x + x^2 + 2x^2 \ln x - 2x^3)S\left(x; \frac{1}{4\gamma^2}, 1\right). \quad (2.88)$$

To proceed further, we compute the emissivity produced by the scattering of monochromatic radiation off a power law distribution of electrons (2.61). To simplify the notation, the following definitions will be useful: the dimensionless frequency

$$w \equiv \frac{\nu_1}{4\nu_0}, \quad (2.89)$$

the power law integral

$$P(a, b, p) \equiv \int_a^b dx x^p = \begin{cases} \frac{b^{p+1} - a^{p+1}}{p+1} & \text{if } p \neq -1 \\ \ln\left(\frac{b}{a}\right) & \text{if } p = -1 \end{cases}, \quad (2.90)$$

and the power law integral with a logarithm

$$Q(a, b, p) \equiv \int_a^b dx x^p \ln x = \begin{cases} \frac{b^{p+1} \ln b - a^{p+1} \ln a - P(a, b, p)}{p+1} & \text{if } p \neq -1 \\ \frac{1}{2} \ln(ab) P(a, b, p) & \text{if } p = -1 \end{cases}. \quad (2.91)$$

The total emissivity at a frequency ν_1 for a general distribution of electrons $n(\gamma)$ is

$$j(\nu_1) = 3\sigma_T \frac{I(\nu_0)}{\nu_0} \int_1^\infty d\gamma n(\gamma) f\left(\frac{\nu_1}{4\gamma^2\nu_0}, \gamma\right). \quad (2.92)$$

Specifying to the power law distribution (2.61) and using (2.89), (2.90) and (2.91) in (2.92) we get the emissivity

$$j(\nu_0, \nu_1) = \frac{3}{2} \sigma_T \frac{I(\nu_0)}{\nu_0} n(\gamma_1) \gamma_1^p w^{(1-p)/2} \times \begin{cases} \left. \begin{aligned} &P\left(\frac{w}{\gamma_2^2}, \frac{w}{\gamma_1^2}, \frac{p-1}{2}\right) + P\left(\frac{w}{\gamma_2^2}, \frac{w}{\gamma_1^2}, \frac{p+1}{2}\right) - \\ &2P\left(\frac{w}{\gamma_2^2}, \frac{w}{\gamma_1^2}, \frac{p+3}{2}\right) + 2Q\left(\frac{w}{\gamma_2^2}, \frac{w}{\gamma_1^2}, \frac{p+1}{2}\right) \end{aligned} \right\} & \text{if } \frac{1}{4} \leq w \leq \gamma_1^2 \leq \gamma_2^2 \\ \left. \begin{aligned} &P\left(\frac{w}{\gamma_2^2}, 1, \frac{p-1}{2}\right) + P\left(\frac{w}{\gamma_2^2}, 1, \frac{p+1}{2}\right) - \\ &2P\left(\frac{w}{\gamma_2^2}, 1, \frac{p+3}{2}\right) + 2Q\left(\frac{w}{\gamma_2^2}, 1, \frac{p+1}{2}\right) \end{aligned} \right\} & \text{if } \gamma_1^2 < w \leq \gamma_2^2 \\ 0 & \text{otherwise} \end{cases}, \quad (2.93)$$

where γ_1 and γ_2 are substituted for γ_{\min} and γ_{\max} in (2.61).

If the cross section is isotropic, the emissivity is

$$j^{\text{ISO}}(\nu_1) = \sigma_T \frac{I(\nu_0)}{\nu_0} n(\gamma_1) \gamma_1^p w^{(1-p)/2} \times \begin{cases} \left. \begin{aligned} &P\left(\frac{w}{\gamma_2^2}, \frac{w}{\gamma_1^2}, \frac{p-1}{2}\right) - P\left(\frac{w}{\gamma_2^2}, \frac{w}{\gamma_1^2}, \frac{p+1}{2}\right) \end{aligned} \right\} & \text{if } \frac{1}{4} \leq w \leq \gamma_1^2 \leq \gamma_2^2 \\ \left. \begin{aligned} &P\left(\frac{w}{\gamma_2^2}, 1, \frac{p-1}{2}\right) - P\left(\frac{w}{\gamma_2^2}, 1, \frac{p+1}{2}\right) \end{aligned} \right\} & \text{if } \gamma_1^2 < w \leq \gamma_2^2 \\ 0 & \text{otherwise} \end{cases} \quad (2.94)$$

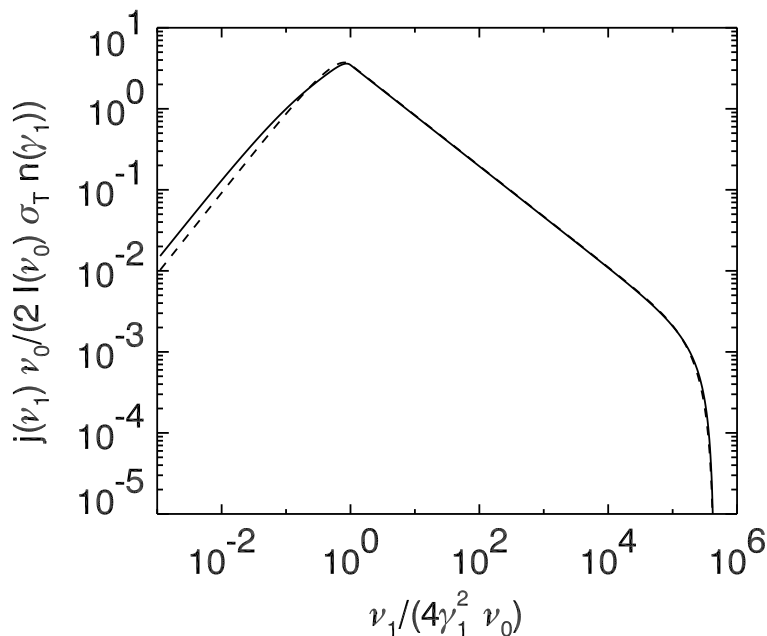


Figure 2.5: Emissivity for a power law electron distribution with parameters $\gamma_1 = 15$, $\gamma_2 = 10^4$, $p = 2.25$. The full line is the emissivity for non-isotropic scattering, and the dashed line corresponds to the emissivity for isotropic scattering.

Figure 2.5 shows an example for a typical power law index of 2.25 and the typical limiting Lorentz factors (in case of blazars) of the power law distribution.

2.2.2 Scattering of radiation whose intensity per unit frequency is a power law

In this subsection we derive the formulas for the scattering of incoming radiation distributed as a power law in frequency off a power law distribution of electrons. We assume that the incoming radiation field is isotropic and has the spectral shape

$$I(\nu) = I(\nu_1) \left(\frac{\nu}{\nu_1} \right)^{-q} S(\nu; \nu_1, \nu_2) \quad (2.95)$$

where ν_1 and ν_2 are the lower and upper limits of the spectrum. We will use equation (2.93), but we change the incoming frequency from ν_0 to ν and the scattering frequency from ν_1 to ν_s , to avoid confusion. The emissivity per unit of scattering frequency is obtained by integrating (2.93) over the frequency of the incoming photons. The notation simplifies when one

introduces the following symbols

$$R(a, b, c, d, \alpha, \beta) \equiv \int_c^d dx x^\beta P(xa, xb, \alpha) = P(a, b, \alpha)P(c, d, \alpha + \beta + 1), \quad (2.96)$$

$$\mathcal{S}(a, b, c, d, \alpha, \beta) \equiv \int_c^d dx x^\beta P(xa, b, \alpha) = \begin{cases} \frac{b^{\alpha+1}P(c, d, \beta) - a^{\alpha+1}P(c, d, \alpha + \beta + 1)}{\alpha + 1} & \text{if } \alpha \neq -1 \\ \ln\left(\frac{b}{a}\right)P(c, d, \beta) - Q(c, d, \beta) & \text{if } \alpha = -1 \end{cases}, \quad (2.97)$$

$$T(a, b, c, d, \alpha, \beta) \equiv \int_c^d dx x^\beta Q(xa, xb, \alpha) = Q(a, b, \alpha)P(c, d, \alpha + \beta + 1) + P(a, b, \alpha)Q(c, d, \alpha + \beta + 1) \quad (2.98)$$

and

$$U(a, b, c, d, \alpha, \beta) \equiv \int_c^d dx x^\beta Q(xa, b, \alpha) = \begin{cases} \frac{1}{\alpha + 1} \left[b^{\alpha+1} \ln(b)P(c, d, \beta) - a^{\alpha+1} \ln(a)P(c, d, \alpha + \beta + 1) - a^{\alpha+1}Q(c, d, \alpha + \beta + 1) - S(a, b, c, d, \alpha, \beta) \right] & \text{if } \alpha \neq -1 \\ \begin{cases} Q(a, b, \alpha)P(c, d, \beta) - \ln(a)Q(c, d, \beta) - \frac{1}{2} \frac{(d^{\beta+1} \ln^2(d) - c^{\beta+1} \ln^2(c)) - Q(c, d, \beta)}{\beta + 1} & \text{if } \beta \neq -1 \\ \frac{1}{6} [\ln^3(d) - \ln^3(c)] & \text{if } \beta = -1 \end{cases} & \text{if } \alpha = -1 \end{cases}. \quad (2.99)$$

Since functions (2.96)-(2.99) always occur in certain combinations, we define

$$G_1(a, b, c, d, \alpha, \beta) \equiv R(a, b, c, d, \alpha, \beta) + R(a, b, c, d, \alpha + 1, \beta) - 2R(a, b, c, d, \alpha + 2, \beta) + 2T(a, b, c, d, \alpha + 1, \beta), \quad (2.100)$$

and

$$G_2(a, b, c, d, \alpha, \beta) \equiv S(a, b, c, d, \alpha, \beta) + S(a, b, c, d, \alpha + 1, \beta) - 2S(a, b, c, d, \alpha + 2, \beta) + 2U(a, b, c, d, \alpha + 1, \beta). \quad (2.101)$$

The emissivity of the scattering of radiation distributed according to a power law spectrum off a power law electron distribution is

$$j(\nu_s) = \frac{3}{2} \sigma_T n(\gamma_1) I(\nu_1) \gamma_1^p (4\nu_1)^q \nu_s^{-q} \times \begin{cases} G_1 \left(\gamma_2^{-2}, \gamma_1^{-2}, w_2, w_1, \frac{p-1}{2}, \frac{2q-p-1}{2} \right) & \text{if } \frac{1}{4} \leq \frac{\nu_s}{4\nu_1} \leq \gamma_1^2 \\ \left. \begin{array}{l} G_1 \left(\gamma_2^{-2}, \gamma_1^{-2}, w_2, \gamma_1^2, \frac{p-1}{2}, \frac{2q-p-1}{2} \right) + \\ G_2 \left(\gamma_2^{-2}, 1, \gamma_1^2, w_1, \frac{p-1}{2}, \frac{2q-p-1}{2} \right) \end{array} \right\} & \text{if } \frac{\nu_s}{4\nu_2} \leq \gamma_1^2 \leq \frac{\nu_s}{4\nu_1}, \\ G_2 \left(\gamma_2^{-2}, 1, w_2, w_1, \frac{p-1}{2}, \frac{2q-p-1}{2} \right) & \text{if } \gamma_1^2 < \frac{\nu_s}{4\nu_2} \leq \gamma_2^2 \\ 0 & \text{otherwise} \end{cases} \quad (2.102)$$

where

$$w_1 \equiv \min \left(\frac{\nu_s}{4\nu_1}, \gamma_2^2 \right), \quad (2.103)$$

and

$$w_2 \equiv \max \left(\frac{\nu_s}{4\nu_2}, \frac{1}{4} \right), \quad (2.104)$$

Analogously, the emissivity for an isotropic cross section of interaction between electrons and photons is

$$j^{\text{ISO}}(\nu_s) = \sigma_T n(\gamma_1) I(\nu_1) \gamma_1^p (4\nu_1)^q \nu_s^{-q} \times \begin{cases} G_1^{\text{ISO}} \left(\gamma_2^{-2}, \gamma_1^{-2}, w_2, w_1, \frac{p-1}{2}, \frac{2q-p-1}{2} \right) & \text{if } \frac{1}{4} \leq \frac{\nu_s}{4\nu_1} \leq \gamma_1^2 \\ \left. \begin{array}{l} G_1^{\text{ISO}} \left(\gamma_2^{-2}, \gamma_1^{-2}, w_2, \gamma_1^2, \frac{p-1}{2}, \frac{2q-p-1}{2} \right) + \\ G_2^{\text{ISO}} \left(\gamma_2^{-2}, 1, \gamma_1^2, w_1, \frac{p-1}{2}, \frac{2q-p-1}{2} \right) \end{array} \right\} & \text{if } \frac{\nu_s}{4\nu_2} \leq \gamma_1^2 \leq \frac{\nu_s}{4\nu_1}, \\ G_2^{\text{ISO}} \left(\gamma_2^{-2}, 1, w_2, w_1, \frac{p-1}{2}, \frac{2q-p-1}{2} \right) & \text{if } \gamma_1^2 < \frac{\nu_s}{4\nu_2} \leq \gamma_2^2 \\ 0 & \text{otherwise} \end{cases} \quad (2.105)$$

where

$$G_1^{\text{ISO}}(a, b, c, d, \alpha, \beta) \equiv R(a, b, c, d, \alpha, \beta) - R(a, b, c, d, \alpha + 1, \beta), \quad (2.106)$$

and

$$G_2^{\text{ISO}}(a, b, c, d, \alpha, \beta) \equiv S(a, b, c, d, \alpha, \beta) - S(a, b, c, d, \alpha + 1, \beta). \quad (2.107)$$

Figure 2.6 shows an example of a typical electron distribution and radiation spectrum with a power law index typically used in applications involving synchrotron radiation. The actual value is taken from the results of Bednarz & Ostrowski (1998).

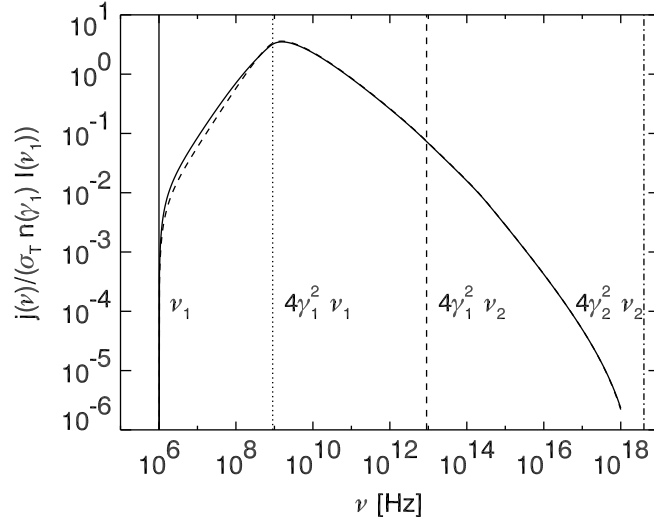


Figure 2.6: Comparison of emissivities for the anisotropic (full line) and isotropic (dashed line) scattering with parameters $\gamma_1 = 15$, $\gamma_2 = 10^4$, $p = 2.25$, $\nu_1 = 10^6$ Hz, $\nu_2 = 10^{10}$ Hz, and $q = 0.7$. The vertical lines denote the frequencies separating intervals in equations (2.102) and (2.105).

Figure 2.7 shows how the scattered radiation depends on the electron distribution index p .

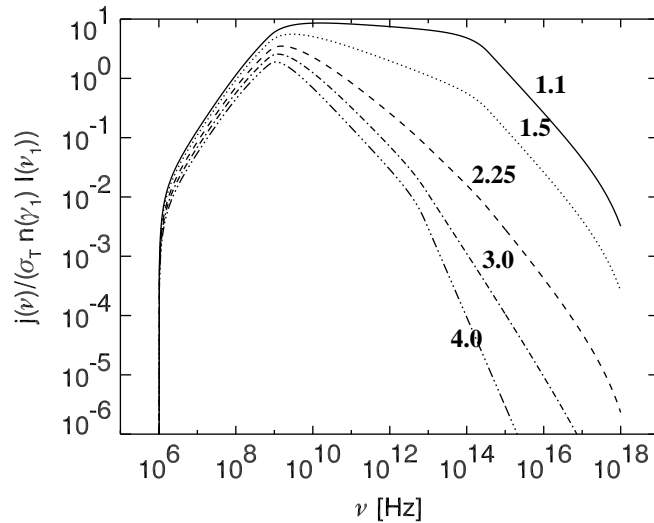


Figure 2.7: Dependence of the emissivity of the inverse Compton scattering on the electron distribution power law index for $\gamma_1 = 15$, $\gamma_2 = 10^4$, $\nu_1 = 10^6$ Hz, $\nu_2 = 10^{10}$ Hz and $q = 0.7$. The power law indices p of the electron distribution are (from top to bottom): 1.1, 1.5, 2.25, 3.0 and 4.0.

Chapter 3

Non-thermal particles

In this chapter the properties, the creation and the evolution of non-thermal particles are discussed. Non-thermal particles are considered to be those particles whose energy distribution does not correspond to a thermal distribution. In many cases, non-thermal particles are distributed according to simple power laws or to a “piecewise superposition” of several power law distributions.

3.1 Acceleration of particles at the shock fronts

The observations of cosmic rays arriving at Earth clearly show that their energy spectrum has the following form (Berezinskii et al. 1990, eqs. 2.27 and 2.28),

$$I_{\text{c.r.}}(> E) = \begin{cases} E^{-1.7} \text{cm}^{-2} & \text{if } 10 \text{ GeV} < E < 3 \times 10^6 \text{ GeV} \\ 3 \times 10^{-10} \left(\frac{E}{10^6} \right)^{-2.1} & \text{if } E > 3 \times 10^6 \text{ GeV} \end{cases}, \quad (3.1)$$

where $I_{\text{c.r.}}(> E)$ is the number of cosmic rays with energy (in GeV) greater than E per unit solid angle passing through a unit area perpendicular to the direction of observation in a unit of time. One sees that the (integral) energy spectrum of cosmic rays is a “broken” power law. Fermi (1949) was one of the first to point out that a power law distribution in energy can be achieved through interaction of particles with moving magnetic fields. In this section we first briefly outline the work of Bell (1978) which describes the acceleration of particles at non-relativistic shock fronts, and then we will give an overview about the acceleration of particles at relativistic shock fronts.

3.1.1 Non-relativistic shocks

We consider a shock propagating through a fluid parallel to the field lines of magnetic field, as sketched on Fig. 3.1. The thickness of the shock is

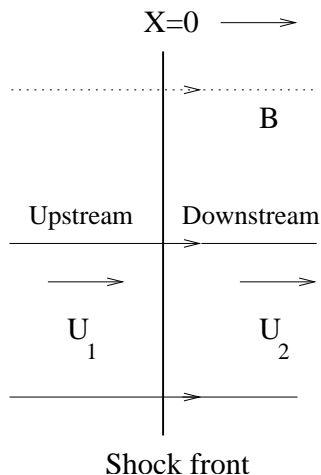


Figure 3.1: A shock propagating parallel to the magnetic field lines seen in the frame in which it is stationary.

assumed to be much smaller than the typical gyro-radius (2.5), and the particles are assumed to be able to pass freely between the regions upstream and downstream of the shock. Upstream (downstream) of the shock we assume the existence of scattering centers (Bell 1978) moving with velocities u_1 (u_2) relative to the shock, taken to be constant in their respective regions and *non-relativistic*. Due to scattering all the particles which enter the upstream region eventually have to return to the downstream region. The converse is not true and thus there is a certain probability η that a particle will be advected downstream after crossing the shock from upstream. This probability is (Bell 1978)

$$\eta = 4 \frac{u_2}{v}, \quad (3.2)$$

where v is the particle velocity relative to the shock. For ultra-relativistic particles ($v \approx c$) this probability is independent of the kinetic energy of the scattered particle, $\eta = 4u_2/c$. In this case, the velocity distribution of particles is assumed to be isotropic, although, due to their relativistic nature this is not true, and this assumption introduces an error of the order of $u_2/v \ll 1$.

Since it is mostly assumed that the scattering is caused by the interaction with magnetic fields, the energy of the particle in the rest frame of the upstream or downstream scattering centers does not change until it crosses from one to another region. Applying the suitable Lorentz transformations after each crossing of a particle it is possible to obtain the energy of the particle in the rest frame of the new region. A particle with energy E_k which has performed k cycles passing from upstream to downstream and back to upstream has, upon performing one more cycle, an energy

$$E_{k+1} = E_k \left(\frac{1 + v_{k,1}(u_1 - u_2) \cos \theta_{k,1}/c^2}{1 + v_{k,2}(u_1 - u_2) \cos \theta_{k,2}/c^2} \right), \quad (3.3)$$

where $v_{k,1}$ is the velocity at which the particle comes from upstream to downstream at an angle $\theta_{k,1}$ with respect to the shock normal, while $v_{k,2}$

and $\theta_{k,2}$ are the velocity and angle at which the particle returns to the upstream region, all measured in the rest frame of the upstream fluid. If the initial (injection) energy E_0 is such that $\gamma_0 = E_0/mc^2 \gg 1$, then we can approximate $v_{k,1} \approx v_{k,2} \approx c$ and we get after l shock crossings

$$\ln \left(\frac{E_l}{E_0} \right) = \sum_{k=0}^{l-1} \ln \left[1 + \frac{u_1 - u_2}{c} \cos \theta_{k,1} \right] - \sum_{k=0}^{l-1} \ln \left[1 + \frac{u_1 - u_2}{c} \cos \theta_{k,2} \right]. \quad (3.4)$$

To increase the initial energy significantly, $l \geq c/(u_1 - u_2)$. The distribution of $\ln(E_l/E_0)$ will be concentrated around the mean (due to the central limit theorem, since the energy *increase* in each cycle is independent of that in the previous cycle). Then we can assume that all particles have increased their energy by the same amount,

$$\ln \left(\frac{E_l}{E_0} \right) = l \left[\left\langle \ln \left(1 + \frac{u_1 - u_2}{c} \cos \theta_{k,1} \right) \right\rangle - \left\langle \ln \left(1 + \frac{u_1 - u_2}{c} \cos \theta_{k,2} \right) \right\rangle \right], \quad (3.5)$$

where $\langle \dots \rangle$ denotes the average over all particles. Since the velocity distribution of the particles is nearly isotropic (due to $u_1 - u_2 \ll c$), the number of particles crossing the shock front per unit of area at an angle in the range $[\theta, \theta + d\theta]$ is proportional to $(2\pi \sin \theta d\theta) \cos \theta$. The average of the first term in (3.5) is computed by averaging over θ from 0 to π , while that of the second term in (3.5) is computed with θ from π to 2π . The result is

$$\ln \left(\frac{E_l}{E_0} \right) = \frac{4}{3} l \frac{u_1 - u_2}{c}. \quad (3.6)$$

We can compute the probability P_l that a particle will complete at least l cycles. From (3.2) and (3.6) and taking into account that in a non-relativistic downstream medium ($u_2 \ll c$) $\eta \ll 1$ we have

$$\ln P_l = l \ln(1 - \eta) = l \ln \left(1 - \frac{4u_2}{c} \right) = -\frac{3u_2}{u_1 - u_2} \ln \left(\frac{E_l}{E_0} \right). \quad (3.7)$$

Thus the differential energy spectrum is (Bell 1978)

$$N(E)dE = \frac{\mu - 1}{E_0} \left(\frac{E}{E_0} \right)^{-\mu} dE, \quad (3.8)$$

where $\mu = (2u_2 + u_1)/(u_1 - u_2)$ is the power law index of the energy distribution. In general μ depends on the details of the model.

3.1.2 Relativistic shocks

In the case of relativistic shocks, i.e. when the shock velocity is very close to the speed of light, the anisotropies in the angular distribution of the particles are large and the theory becomes much more complex. We briefly outline the basic features of acceleration of particles at relativistic shocks (Achterberg et al. 2001).

When the shock front is ultra-relativistic in the upstream rest frame (URF), one can write for the shock velocity

$$v_s = \beta_s c \approx c \left(1 - \frac{1}{2\Gamma_s^2} \right), \quad (3.9)$$

where $\Gamma_s \gg 1$ is the shock Lorentz factor in the URF. The relative velocity between upstream and downstream fluid is

$$\beta_{\text{rel}} = \frac{\beta_u - \beta_d}{1 - \beta_u \beta_d} \quad (3.10)$$

where $\beta_u c$ and $\beta_d c$ are the velocities of upstream and downstream fluid. In the limit of ultra-relativistic shocks the relative velocity in the URF satisfies

$$\beta_{\text{rel}} \approx 1 - \frac{1}{\Gamma_s^2}, \quad (3.11)$$

which comes from the fact that $\Gamma_{\text{rel}} \approx \Gamma_s / \sqrt{2}$ (Blandford & McKee 1976). In the downstream rest frame (DRF) we have that the upstream fluid has a velocity $\bar{\beta}_u = -\beta_{\text{rel}}$.

We assume that all particles are relativistic in each of the three reference frames (URF, DRF, shock rest frame [SRF]). The particle motion relative to the shock is determined by the shock speed and the angle between the shock normal and the particle momentum. We denote the cosine of that angle in the URF by

$$\mu \equiv \cos \theta \approx \beta_{\parallel}, \quad (3.12)$$

where $\beta_{\parallel} c$ is the component of the particle velocity βc along the shock normal, where the magnitude of the particle velocity is assumed to be c , i.e. $\beta = 1$. Now, if we consider a cycle during which a particle crosses from upstream to downstream with an energy E_i and direction cosine $\mu_{\rightarrow d}$, elastically scatters in the downstream medium (energy \bar{E} remains constant) and then re-crosses into the upstream medium with an energy E_f and the direction $\mu_{\rightarrow u}$, we can relate the two energies (using transformations for the angles in different inertial systems, see e.g. Rybicki & Lightman 1979),

$$\frac{E_f}{E_i} = \frac{1 - \beta_{\text{rel}} \mu_{\rightarrow d}}{1 - \beta_{\text{rel}} \mu_{\rightarrow u}} = \frac{1}{2} \Gamma_s^2 (1 - \beta_{\text{rel}} \mu_{\rightarrow d}) (1 + \beta_{\text{rel}} \bar{\mu}_{\rightarrow u}). \quad (3.13)$$

where $\bar{\mu}_{\rightarrow u}$ is the cosine of the angle that a particle crossing from downstream to upstream forms with the shock normal measured in DRF.

We can see that the particle energy gain is $E_f/E_i \propto \Gamma_s^2$. However, we need to consider the relativistic effects, in particular the fact that all the particles with $-1 < \beta\mu < \beta_s$ in the upstream part can be overtaken by the shock. After initial shock encounter (particles being ‘‘swept’’ over by the shock) all particles become highly relativistic in the DRF and those re-crossing into the upstream region satisfy the following constraints (Achterberg et al. 2001)

$$\bar{\mu} > \bar{\beta}_s \approx \frac{1}{3}, \quad \mu > \beta_s. \quad (3.14)$$

Thus, equation (3.14) defines the *loss cone* with an opening angle θ_c around the shock normal in the URF,

$$\sin \theta_c = \frac{1}{\Gamma_s}, \quad (3.15)$$

so that all the particles which cross into the upstream region have to pass through the loss cone (Fig. 3.2). This is due to the relativistic beaming. For large Γ_s we have the condition for crossing into the upstream region,

$$\theta_{\rightarrow u} < \theta_c \approx \frac{1}{\Gamma_s}. \quad (3.16)$$

Scattering or deflection must change the flight angle by a value $\theta > \theta_c$ for the new shock crossing cycle to begin.

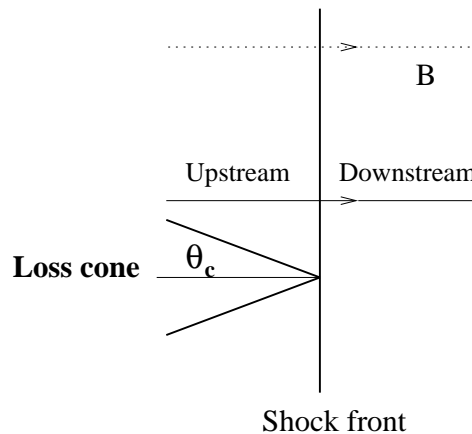


Figure 3.2: A sketch of the relativistic shock with the loss cone with the half-opening angle θ_c in the URF.

This fact makes the situation more complicated than in the non-relativistic case, since now we cannot assume that the particle velocity distribution is nearly isotropic in the URF or the DRF. Furthermore, once the particle has encountered the shock initially, its energy gain is much smaller than $\propto \Gamma_s^2$ and, in fact, is only around 2 (Gallant & Achterberg 1999). Therefore, the power law index of the particle energy distribution cannot be determined in a straightforward manner as in the non-relativistic case. However, a number of numerical simulations have been performed (Bednarz & Ostrowski 1998; Achterberg et al. 2001) showing the existence of a universal power law index 2.2, which agrees with the analytical results of Kirk et. al (2000).

Unfortunately, apart from the universal power law index, there is little else known about the energy distribution with certainty. In particular, the connection between the shock properties and the low- and high-energy cutoffs of the energy distribution remains unknown. As will be shown in section 4.2.3, we had to use a simple model to determine these cutoffs from the fluid properties.

3.2 Evolution of non-thermal particles

In the previous section we have seen that the energy distribution of the high-energetic particles near the shock is of the form (2.61) a value $p \approx 2.2$ is being supported by the numerical simulations and the analytical modeling. However, due to their high velocities and the presence of magnetic fields these particles are subject to energy losses. In this section we will, following the works of Kardashev (1962) and Gratton (1972), discuss the evolution of the particle energy distribution.

3.2.1 Kinetic equation

We are interested in the study of the temporal and spatial evolution of a distribution of particles in the presence of magnetic field. To this end we first define the number density $n(\gamma, \mathbf{r}, t)$ of particles at a time t , position \mathbf{r} and Lorentz factor γ . The evolution of these particles in the phase space (\mathbf{r}, γ) is governed by the following equation (Gratton 1972)

$$\frac{\partial n}{\partial t} - D\nabla^2 n + \frac{\partial}{\partial \gamma} (\dot{\gamma}n) = Q, \quad (3.17)$$

where D is a diffusion coefficient, $\dot{\gamma}$ are the radiation losses of a particle with Lorentz factor γ , and Q is a source term that can account, e.g. for the injection of new particles into the system. We will simplify this equation by considering a spatially piecewise uniform distribution of particles. This simplification is motivated by numerical reasons, because we will assume that the particle distribution is spatially homogeneous within a cell of the numerical grid (see chapter 4).

With this simplification, the kinetic equation reads

$$\frac{\partial n(\gamma, t)}{\partial t} + \frac{\partial}{\partial \gamma} [\dot{\gamma}n(\gamma, t)] = Q(\gamma, t), \quad (3.18)$$

where $n(\gamma, t)d\gamma$ is the number density of particles at time t with Lorentz factors in the interval $[\gamma, \gamma + d\gamma]$.

Since we are considering only synchrotron and inverse-Compton losses, we can write the radiation loss term in the form (Rybicki & Lightman 1979)

$$\dot{\gamma} \equiv \frac{d\gamma}{dt} = -q_L \gamma^2, \quad (3.19)$$

where $q_L > 0$ depends on the magnetic field energy density (in case of the synchrotron emission), or on the radiation field energy density (in case of the inverse Compton scattering). The solution of (3.19) is

$$\gamma(t) = \frac{\gamma(0)}{1 + q_L \gamma(0)t}, \quad (3.20)$$

where $\gamma(0)$ is the Lorentz factor of a particle at $t = 0$. We change variables

to (Gratton 1972)

$$\tau \equiv t + \frac{1}{q_L \gamma}; \tau > 0 \quad (3.21)$$

$$\Psi(\tau) \equiv q_L \gamma^2 n(\gamma, t) \quad (3.22)$$

$$J(\tau) \equiv q_L \gamma^2 Q(\gamma, t), \quad (3.23)$$

where γ now depends on t through the equation (3.20). Now the equation (3.18) takes the form

$$\frac{d\Psi(\tau)}{d\tau} = J(\tau). \quad (3.24)$$

We consider first the case when $J(\tau) = 0$. The solution is simply

$$\Psi(\tau) = \begin{cases} \Psi_0 & \text{if } \tau > 0 \\ 0 & \text{if } \tau \leq 0 \end{cases}, \quad (3.25)$$

where Ψ_0 is a constant determined by the initial energy distribution. If the initial energy distribution is of the form (2.61), then

$$\Psi_0 = n(\gamma_{\min}) \gamma_{\min}^p q_L \gamma^{2-p} S(\gamma; \gamma_{\min}, \gamma_{\max}). \quad (3.26)$$

Taking into account that the limiting Lorentz factors of the distribution function evolve according to the equation (3.20), and inserting (3.26) into (3.25), we obtain the so-called Kardashev solution (Kardashev 1962),

$$n(\gamma, t) = n(\gamma_{\min}) \left(\frac{\gamma}{\gamma_{\min}} \right)^{-p} (1 - q_L \gamma t)^{p-2} S \left(\gamma; \frac{\gamma_{\min}}{1 + q_L \gamma_{\min} t}, \frac{\gamma_{\max}}{1 + q_L \gamma_{\max} t} \right). \quad (3.27)$$

Note that from solution (3.25) there is an additional constraint to the homogeneous solution, $\gamma < 1/(q_L t)$, but since we are dealing with a distribution with finite limiting Lorentz factors, this condition is automatically fulfilled by the upper limit of the interval function in (3.27). It is nevertheless interesting to point out that if the initial distribution is extending to infinity,

$$\lim_{\gamma_{\max} \rightarrow \infty} \frac{\gamma_{\max}}{1 + q_L \gamma_{\max} t} = \frac{1}{q_L t} \quad (3.28)$$

we recover the condition $\gamma < 1/(q_L t)$. The fact that each energy distribution has an upper cutoff $1/(q_L t)$ even after a very short time t is the consequence of the quadratic nature of the loss term (3.19) (Kardashev 1962).

Figure 3.3 shows an example for an initial electron distribution with $\gamma_{\min} = 10^2$ and $\gamma_{\max} = 10^5$, and with a typical power law index $p = 2.2$. The sharp cutoff at $\gamma = 1/(q_L t)$ can be seen easily.

We now consider a time-independent power-law source term

$$Q(\gamma) = Q(\gamma_{\min}) \left(\frac{\gamma}{\gamma_{\min}} \right)^{-p} S(\gamma; \gamma_{\min}, \gamma_{\max}), \quad (3.29)$$

and assume that $n(\gamma, 0) = 0$. From (3.29) we get

$$J(\tau) = q_L^{p-1} (\tau - t)^{p-2} Q(\gamma_{\min}) \gamma_{\min}^p S \left(\frac{1}{q_L (\tau - t)}; \gamma_{\min}, \gamma_{\max} \right), \quad (3.30)$$

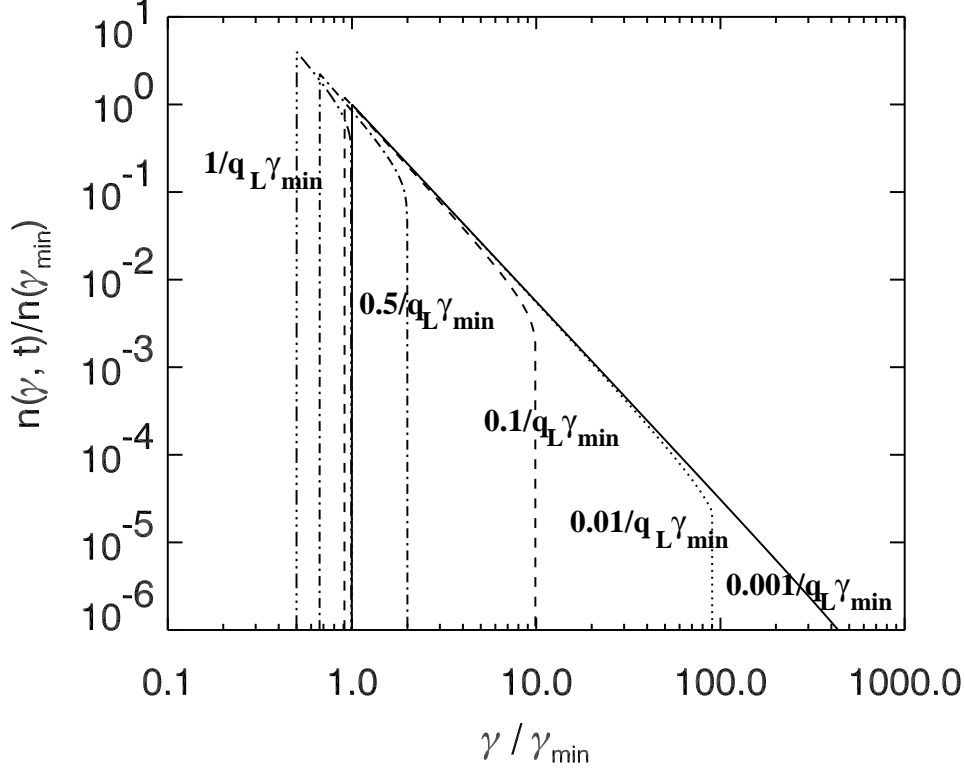


Figure 3.3: The evolution of an initial electron distribution with $\gamma_{\min} = 10^2$, $\gamma_{\max} = 10^5$, and power law index $p = 2.2$. The five curves show $n(\gamma, t)/n(\gamma_{\min})$ for times $10^{-3}/(q_L \gamma_{\min})$ (full line), $10^{-2}/(q_L \gamma_{\min})$ (dotted line), $10^{-1}/(q_L \gamma_{\min})$ (dashed line), $0.5/(q_L \gamma_{\min})$ (dot-dashed line) and $1/(q_L \gamma_{\min})$ (triple dot-dashed line).

where t is to be considered a parameter, so that for a certain value of τ $J(\tau)$ actually gives the value of the source term for a corresponding $\gamma = [q_L(\tau - t)]^{-1}$. Now equation (3.24) can be integrated, but care must be taken when considering the lower and upper limits of the integration. For the lower limit we have two conditions,

$$\tau \geq \frac{1}{q_L \gamma} \quad \text{and} \quad \tau \geq \frac{1}{q_L \gamma_{\max}} + t,$$

and for the upper limit

$$\tau \leq \frac{1}{q_L \gamma} + t \quad \text{and} \quad \tau \leq \frac{1}{q_L \gamma_{\max}} + t.$$

Taking into account these constraints, the solution of the equation (3.18) for the case of the time-independent power law source term (3.29) is given by

$$n(\gamma, t) = \frac{Q(\gamma_{\min})}{q_L(p-1)} \gamma_{\min}^p \gamma^{-2} (\gamma_{\text{low}}^{1-p} - \gamma_{\text{high}}^{1-p}) S \left(\gamma; \frac{\gamma_{\min}}{1 + q_L \gamma_{\min} t}, \gamma_{\max} \right), \quad (3.31)$$

where γ_{low} and γ_{high} have four different values

- *region 1:*
for $\frac{\gamma_{\max}}{1 + q_L \gamma_{\max} t} \leq \gamma \leq \gamma_{\min} \Rightarrow \gamma_{\text{low}} = \gamma_{\min}$ and $\gamma_{\text{high}} = \gamma_{\max}$
- *region 2:*
for $\frac{\gamma_{\min}}{1 + q_L \gamma_{\min} t} \leq \gamma \leq \gamma_{\min} \Rightarrow \gamma_{\text{low}} = \gamma_{\min}$ and $\gamma_{\text{high}} = \frac{\gamma}{1 - q_L \gamma t}$
- *region 3:*
for $\gamma_{\min} \leq \gamma \leq \frac{\gamma_{\max}}{1 + q_L \gamma_{\max} t} \Rightarrow \gamma_{\text{low}} = \gamma$ and $\gamma_{\text{high}} = \frac{\gamma}{1 - q_L \gamma t}$
- *region 4:*
for $\frac{\gamma_{\max}}{1 + q_L \gamma t} \leq \gamma \leq \gamma_{\max} \Rightarrow \gamma_{\text{low}} = \gamma$ and $\gamma_{\text{high}} = \gamma_{\max}$

When $\gamma_{\max} \rightarrow \infty$ (3.28) only regions 3 and 4 remain, the boundary being located at $1/q_L t$ (Kardashev 1962). Only one of the regions 1 and 2 can be present in the solution, region 2 for $t \leq \frac{1}{q_L} \left(\frac{1}{\gamma_{\min}} - \frac{1}{\gamma_{\max}} \right)$, and region 1 for the later times.

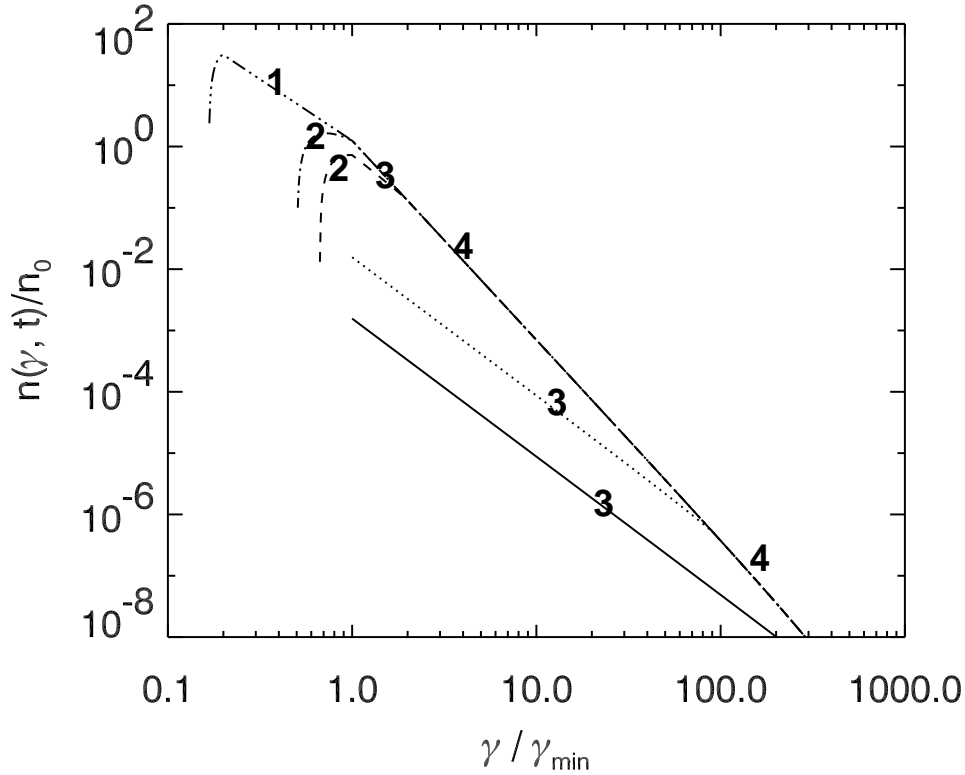


Figure 3.4: The electron distribution of five different times (from bottom to top curve): $10^{-3}/(q_L \gamma_{\min})$, $10^{-2}/(q_L \gamma_{\min})$, $0.5/(q_L \gamma_{\min})$, $0.99(1 - \gamma_{\min}/\gamma_{\max})/(q_L \gamma_{\min})$ and $0.5/(q_L \gamma_{\min})$, respectively. The numbers denote different regions of the solution (3.31) which appear as time progresses (see text for detailed explanation). The number density has been normalized to $n_0 \equiv Q(\gamma_{\min})/(q_L \gamma_{\min})$. The power law index of injection is $p = 2.2$.

Figure 3.4 shows five characteristic stages of power law injection. During

the early stage only region 3 appears in the solution (full curve). When $t > 1/(q_L \gamma_{\max})$, region 4 appears (dotted curve). Gradually region 2 appears as time progresses. Finally, after $t > \frac{1}{q_L} \left(\frac{1}{\gamma_{\min}} - \frac{1}{\gamma_{\max}} \right)$, region 1 replaces region 2, region 3 disappears and only region 4 remains for $\gamma > \gamma_{\min}$ (triple-dot-dashed curve).

Chapter 4

Numerical method

Next we describe two main building blocks of the numerical method, namely, the one dealing with the hydrodynamic evolution of the thermal content of the system and the part which considers the radiation produced by the non-thermal particles coupled to the thermal plasma by means of the magnetic field. The reason for splitting the problem in two parts is to exploit the existing code GENESIS (Aloy et al. 1999) to integrate the relativistic hydrodynamics (RHD) equations (see section 4.1.2). In essence, the non-thermal particles are considered as a set of tracer species advected by the thermal fluid, each tracer species representing a single energy bin of the non-thermal particle energy distribution. For this model to be applicable, the non-thermal particle distribution within a numerical cell must not change significantly solely due to the hydrodynamic evolution. This implies that there is a minimum magnetic field, or, conversely, a maximum allowed Larmor radius such that particles are contained within a cell during a time step.

In section 4.1 the equations of ideal RHD are given and the numerical scheme used to integrate them is presented. Section 4.2 explains in detail how the non-thermal particles are treated numerically. In section 4.3 the calculation of the non-thermal radiation emitted by the abovementioned non-thermal particles is explained. Finally, section 4.4 is devoted to the validation of the numerical method.

4.1 Numerical RHD

In this section we outline the numerical method used to solve the equations of ideal RHD. First we discuss the applicability of ideal RHD to the physics of jets in 4.1.1, then present the equations of RHD in section 4.1.2 and finally outline the numerical method used to integrate them (section 4.1.3).

4.1.1 Applicability of the ideal RHD approximation

Following the argument of Begelman et al. (1984), we consider a one-dimensional flow of plasma along a channel embedded in an external medium. This model is probably reasonable to describe jets since almost all well-

observed jets are collimated with opening angles less than 15 degrees. The mean free path for Coulomb collisions within the plasma is typically larger than the width of a jet, a fact which would make the ideal RHD approximation invalid. However, since we observe synchrotron radiation there should also be magnetic fields within the jet and the associated Larmor radii of the electrons and ions can be, at least, 8 orders of magnitude smaller than the jets width for the assumed magnetic field strengths (Blandford & Ress 1974). The coupling provided by the magnetic field allows to consider jets as fluid-like flows and essentially charge-neutral. In this work we assume that the magnetic field is dynamically unimportant, its field energy density is proportional to the fluid internal energy density and that it is entangled. Thus, we can describe the system with the equations of ideal RHD, neglecting the magnetic field in the hydrodynamic evolution of the fluid.

4.1.2 Equations of ideal RHD

The units used in this section are such that the speed of light c is set equal to 1. The metric which we use is $g^{\alpha\beta} = \text{diag}(-1, 1, 1, 1)$. The velocity four vector is defined as

$$u^\alpha = \Gamma(1, v^x, v^y, v^z), \quad (4.1)$$

where Greek indices run from 0 to 3, \mathbf{v} is the velocity measured in the laboratory frame and $\Gamma \equiv \sqrt{1 - \mathbf{v}^2}$ is the fluid Lorentz factor. The state of the fluid is described by its rest-mass density ρ , pressure P (both measured in the comoving frame of the fluid) and velocity \mathbf{v} . We define the specific enthalpy $h \equiv 1 + \varepsilon + P/\rho$, where ε is the specific internal energy. For an ideal gas with an adiabatic index γ_{ad} we have

$$h = 1 + \frac{\gamma_{\text{ad}}}{\gamma_{\text{ad}} - 1} \frac{P}{\rho}. \quad (4.2)$$

The conservation laws which describe the evolution of an ideal relativistic fluid are the conservation of mass

$$\sum_{\alpha=0}^3 \frac{\partial(\rho u^\alpha)}{\partial x^\alpha} = 0, \quad (4.3)$$

and the conservation of the total energy-momentum

$$\sum_{\beta=0}^3 \frac{\partial T^{\alpha\beta}}{\partial x^\beta} = 0, \quad (4.4)$$

where $T^{\alpha\beta}$ is the energy momentum tensor, which, in the case of a perfect fluid reads

$$T^{\alpha\beta} = \rho h u^\alpha u^\beta + p g^{\alpha\beta}. \quad (4.5)$$

The equations of ideal RHD can be cast in a system of conservation laws (Marti et al. 1994)

$$\frac{\partial \mathbf{U}}{\partial t} + \sum_{k=1}^3 \frac{\partial \mathbf{F}^k}{\partial x^k} = 0 \quad (4.6)$$

where \mathbf{U} and \mathbf{F}^k are the vector of conserved variables and the fluxes, respectively. In this work we are working with axisymmetric jets and the equation (4.6) in cylindrical coordinates (r, z) reads

$$\frac{\partial \mathbf{U}}{\partial t} + \frac{1}{r} \frac{\partial r \mathbf{F}}{\partial r} + \frac{\partial \mathbf{G}}{\partial z} = \mathbf{S}, \quad (4.7)$$

where

$$\mathbf{U} = \begin{pmatrix} \rho \Gamma \\ \rho h \Gamma^2 v_r \\ \rho h \Gamma^2 v_z \\ \rho h \Gamma^2 - P - \rho \Gamma \\ \rho \mathbf{X} \Gamma \end{pmatrix}, \quad (4.8)$$

is the vector of conserved quantities,

$$\mathbf{F} = \begin{pmatrix} \rho \Gamma v_r \\ \rho h \Gamma^2 v_r^2 + P \\ \rho h \Gamma^2 v_z v_r \\ \rho h \Gamma^2 v_r - \rho \Gamma v_r \\ \rho \mathbf{X} \Gamma v_r \end{pmatrix}, \quad (4.9)$$

and

$$\mathbf{G} = \begin{pmatrix} \rho \Gamma v_z \\ \rho h \Gamma^2 v_r v_z \\ \rho h \Gamma^2 v_z^2 + P \\ \rho h \Gamma^2 v_z - \rho \Gamma v_z \\ \rho \mathbf{X} \Gamma v_z \end{pmatrix}, \quad (4.10)$$

are the corresponding flux vectors in r and z direction, respectively. Here v_r is the radial component of the velocity, v_z the longitudinal component and $\Gamma = \sqrt{1 - v_r^2 - v_z^2}$. The symbol \mathbf{X} denotes an N -component vector representing N non-thermal species passively advected with the hydrodynamic fluid (see 4.2.1). The source \mathbf{S} is, in cylindrical coordinates,

$$\mathbf{S} = \begin{pmatrix} 0 \\ P/r \\ 0 \\ 0 \\ \mathbf{0} \end{pmatrix}. \quad (4.11)$$

4.1.3 RHD numerical scheme

In the following we outline the RHD numerical scheme used in the GENESIS code (Aloy et al. 1999) which was the basis for the code R-GENESIS, developed during this PhD work.

In order to solve system (4.7), one has to discretize the state vector \mathbf{U} within computational cells (zones). We use a two dimensional grid, whose zone-center positions are denoted by (i, j) and correspond to coordinates (r_i, z_j) in cylindrical geometry. Time is discretized into steps denoted by

an integer n so that the average of vector \mathbf{U} in grid zone (i, j) at time t^n is denoted by $\mathbf{U}_{i,j}^n$. Cell interfaces are denoted by half-integers, i.e. the interface between the zone (i, j) and $(i+1, j)$ is denoted by $(i+1/2, j)$. The fluxes are defined at cell interfaces so that the flux $\mathbf{F}(r_{i+1/2}, z_j, t^n)$ across the interface $(i+1/2, j)$ at time t^n is denoted by $\mathbf{F}_{i+1/2, j}^n$.

The discretization of (4.7) can be expressed following the method of lines (Le Veque 1991), so that the time variation of the state vector \mathbf{U} within a numerical zone (i, j) is obtained by integration of the system of semi-discrete ordinary differential equations

$$\frac{d\mathbf{U}_{i,j}^n}{dt} = -\frac{2\left(r_{i+1}\tilde{\mathbf{F}}_{i+1/2, j}^n - r_i\tilde{\mathbf{F}}_{i-1/2, j}^n\right)}{r_{i+1}^2 - r_i^2} - \frac{\tilde{\mathbf{G}}_{i, j+1/2}^n - \tilde{\mathbf{G}}_{i, j-1/2}^n}{z_{j+1} - z_j} + \mathbf{S}_{i,j}^n \equiv L(\mathbf{U}), \quad (4.12)$$

where $L(\mathbf{U})$ is the spatial operator of the method.

The numerical fluxes $\tilde{\mathbf{F}}_{i+1/2, j}$ and $\tilde{\mathbf{G}}_{i, j+1/2}$ between adjacent cells are obtained by solving the appropriate one-dimensional Riemann problems along the sweeps directions. We have used Marquina's flux formula (Donat et al. 1998) to compute the numerical fluxes at the cell interfaces.

The piecewise parabolic method (PPM) (Colella & Woodward 1984) was used to approximate the spatial distribution of the variables within numerical zones up to third order accuracy (Marti & Mueller 1996).

Using a Runge-Kutta (RK) method with a third order accuracy in time (Shu & Osher 1988). There are three integration steps performed in each numerical cell:

1. $\mathbf{U}^{(1)} = \mathbf{U}^n + \Delta t L(\mathbf{U})$,
2. $\mathbf{U}^{(2)} = \frac{1}{4} [3\mathbf{U}^n + (\mathbf{U}^{(1)} + \Delta t L(\mathbf{U}^{(1)}))]$,
3. $\mathbf{U}^{n+1} = \frac{1}{3} [\mathbf{U}^n + 2(\mathbf{U}^{(2)} + \Delta t L(\mathbf{U}^{(2)}))]$.

Here we have omitted the indices (i, j) to prevent the formulae to be cluttered with indices.

Due to the multidimensional nature of the equations, GENESIS performs the integration of the RHD system employing a directional splitting approach. First, all fluxes in the radial direction are computed (radial sweep) fixing the variation of the primitive variables (ρ , P and \mathbf{v}) in the z -direction. Then, all fluxes in the axial (longitudinal, z) direction (axial sweep) are calculated keeping the variation of the primitive variables in the radial direction constant. This procedure reduces the two-dimensional problem to a series of one-dimensional problems. The hydrodynamic conserved quantities \mathbf{U} are updated once all fluxes from different directions are added simultaneously at the end of each RK sub-step.

4.2 Treatment of the non-thermal particles

One of the most important achievements of this PhD project is the efficient and accurate treatment of the transport and evolution of non-thermal particles coupled to thermal plasma. In section 4.2.1 it is explained how non-thermal particles are advected with the fluid. The kinetic equation solver used to follow the temporal evolution of non-thermal particles is presented in section 4.2.2. The non-thermal electron injection models and power-law-like source terms are discussed in section 4.2.3.

4.2.1 Spatial transport: non-thermal particles as tracers

As mentioned in Section 4.1.2, a N -component vector \mathbf{X} is advected along with the thermal fluid. The components of this vector are the mass fractions of the tracer species, i.e. for species i

$$X_i = \frac{n_i m_e}{\rho}, \quad i = 1, \dots, N, \quad (4.13)$$

where m_e is the electron mass and n_i the number density of species i .

Each species represents the number density of electrons within a single energy (or, equivalently, Lorentz factor) bin. Thereby, the electron energy distribution in each zone is represented by a sum of power laws in N Lorentz factor intervals of the form

$$n(\gamma) = \sum_{i=1}^N n_0^i \gamma^{-p_i} S(\gamma; \gamma_{i-1}, \gamma_i), \quad (4.14)$$

where γ_{i-1} and γ_i are the lower and upper boundaries (limiting Lorentz factors) of the i th power law distribution which is normalized to n_0^i and has a power law index p_i . The limiting Lorentz factors γ_i are logarithmically distributed according to

$$\gamma_i = \gamma_0 \left(\frac{\gamma_N}{\gamma_0} \right)^{(i-1)/(N-1)}, \quad i = 1, \dots, N, \quad (4.15)$$

where γ_0 and γ_N are the limiting Lorentz factors of the whole energy interval considered for the non-thermal electron population. The mass fractions are computed using $n_0^i \gamma_i^{-p_i}$ instead of n_i in (4.13).

It is important to note that the spatial transport of non-thermal particles is assumed to keep their energy distribution 'frozen', i.e. each species is passively advected by the fluid.

4.2.2 The kinetic equation solver

Using the solutions (3.27) and (3.31) of the kinetic equation (3.18) derived in Section 3.2.1, we have constructed an efficient and accurate numerical

scheme to tackle the temporal evolution of the energy distribution of non-thermal electrons.

First we note that equation (3.18) is linear in $n(\gamma, t)$, i.e., we can solve the equation for each of the power law segments in (4.14) separately. Since this has to be done for each zone (several tens of thousands) and for each segment (several tens) in each iteration, the analytical solutions (3.27) and (3.31) greatly improve the efficiency of the code.

Second, we limit our model to source terms which are of the form of simple a power law (3.29) and constant within a time step.

The general solver algorithm is applied to each zone and has four steps:

1. **Power law approximation:** The vector \mathbf{X} is multiplied by the local fluid density ρ and divided by the electron mass m_e to obtain the $n_i^n \equiv n_0^i \gamma_i^{-p_i}$, $i = 1, \dots, N$. The power law index of the energy distribution within each power law segment i is computed according to the equation

$$p_i = -\frac{\ln n_{i+1}^n - \ln n_i^n}{\ln \gamma_i - \ln \gamma_{i+1}}, \quad i = 1, \dots, N, \quad (4.16)$$

and the power law normalization according to

$$n_0^i = n_i^n \gamma_i^{p_i}, \quad i = 1, \dots, N. \quad (4.17)$$

We note that solution (3.27) diverges for $p < 2$. Since the power law index of injection for relativistic shocks is $p \geq 2$ (see Section 3.1.2 we limit the power law index computed by (4.16) to be ≥ 2 .

2. **Solution of the homogeneous part:** For each γ_i the homogeneous solution (3.27) is used to compute $n_i^{n+1} = n(\gamma_i)$, the value for the $(n + 1)$ -th iteration,

$$n_i^{n+1} = \sum_{j=i}^N n_0^j \gamma_i^{-p_j} (1 - q_L \gamma_i \Delta t)^{p_j - 2} S \left(\gamma_i; \frac{\gamma_{j-1}}{1 + q_L \gamma_{j-1} \Delta t}, \frac{\gamma_j}{1 + q_L \gamma_j \Delta t} \right), \quad (4.18)$$

where Δt is the time step of the current iteration n . In practice, the interval function S is non-zero only for a handful of terms in the sum, so that the solver is computationally efficient.

3. **Solution of the particular part:** For each γ_i the particular solution (3.31) is added to the n_i^{n+1} computed in step 2,

$$n_i^{n+1} = n_i^{n+1} + \frac{Q(\gamma_{\min})}{q_L(p-1)} \gamma_{\min}^p \gamma_i^{-2} (\gamma_{\text{low}}^{1-p} - \gamma_{\text{high}}^{1-p}) S \left(\gamma; \frac{\gamma_{\min}}{1 + q_L \gamma_{\min} \Delta t}, \gamma_{\max} \right), \quad (4.19)$$

where p is the power law index of injection, Q_0 the source term normalization, γ_{\min} and γ_{\max} lower and upper boundaries, and γ_{low} and γ_{high} are determined from the region where γ_i resides with respect to γ_{\min} and γ_{\max} (see section 3.2.1), replacing γ by γ_i and t by Δt .

4. **Compute new tracer values:** For each power law segment compute the new tracer mass fraction X_i ,

$$X_i = \frac{n_i^{n+1} m_e}{\rho}, \quad i = 1, \dots, N. \quad (4.20)$$

The most important property of the solver is the accuracy with which it captures the characteristic sharp decrease of the electron distribution at $\gamma = 1/(q_L \Delta t)$. These property will be discussed in Section 4.4.1.

4.2.3 The treatment of the source term

Initially, the number density of non-thermal electrons is set to zero everywhere. The only way to inject electrons is via the source term $Q(\gamma)$ at shocks. Shocks are detected using the standard criterion in PPM (Colella & Woodward 1984) applied to the thermal fluid.

As discussed in section 3.1.2, the acceleration of electrons at relativistic shocks is a very complex problem which has not yet been completely solved. Furthermore, the acceleration time scale (Bednarz & Ostrowski 1996) is much smaller than the hydrodynamic time scale. Using similar arguments as Jones et al. (1999), we do not treat the shock acceleration process microscopically, but instead provide macroscopic models which describe the effects of the electron injection averaged over a hydrodynamic time step. Of course, this means that the same hydrodynamical evolution might give rise to different particle (and observed radiation) energy spectra, depending on the parameterization of the shock acceleration. However, in this way we can also compare the computed spectral and temporal properties of the radiation field with observations, and thus at least disregard those models which are in disagreement with the observed data.

In the following two subsections two electron injection models are discussed.

4.2.3.1 INJECTION MODEL OF TYPE-E

Once a shock is detected, we compute $\dot{\epsilon}$, the change of the internal energy of the thermal fluid per unit of time behind a shock. The crucial assumption is that $\dot{\epsilon}_{\text{acc}}$, the energy density available per unit of time to accelerate non-thermal electrons is a fraction α_e of $\dot{\epsilon}$ (Daigne & Mochkovitch 1998; Bykov & Meszaros 1996). Since in this work we are using an ideal gas equation of state with the adiabatic index γ_{ad} , we can write

$$\dot{\epsilon}_{\text{acc}} = \alpha_e \dot{\epsilon} = \frac{\alpha_e}{\gamma_{\text{ad}} - 1} \dot{p}, \quad (4.21)$$

where \dot{p} denotes the temporal change in the fluid pressure behind the shock due to the hydrodynamic evolution. In the following we consider only those situations when $\dot{p} > 0$ and write, following the definition of the power-law

source term (3.29),

$$\dot{\epsilon}_{\text{acc}} = \int_{\gamma_{\text{min}}}^{\gamma_{\text{max}}} d\gamma \gamma m_e c^2 Q_0^{\text{E}}(\gamma_{\text{min}}) \left(\frac{\gamma}{\gamma_{\text{min}}} \right)^{-p_{\text{inj}}}, \quad (4.22)$$

here $Q_0^{\text{E}}(\gamma_{\text{min}})$ is the source term normalization and p_{inj} is the injection power law index. The back reaction of the energy loss due to particle acceleration is treated by decreasing the pressure in the zone(s) where the acceleration takes place during a time interval $\Delta\tilde{t}$. From (4.21) one gets

$$\Delta p = -\frac{\gamma_{\text{ad}} - 1}{\alpha_e} \dot{\epsilon}_{\text{acc}} \Delta\tilde{t}, \quad (4.23)$$

where $\Delta\tilde{t}$ is computed in the rest frame of the zone.

In this work we always assume that the power law index of injection is $p_{\text{inj}} = 2.2$, which is a value in good agreement with the numerical simulations of relativistic shock acceleration (Bednarz & Ostrowski 1998; Achterberg et al. 2001) and analytical modeling (Kirk et al. 2000).

That means that we still have to determine the two remaining parameters, γ_{min} and γ_{max} . We make a further assumption that the ratio $\eta \equiv \gamma_{\text{max}}/\gamma_{\text{min}}$ is a global constant, so that now only γ_{min} needs to be determined. In the injection model of type-E we assume that γ_{min} is a global constant as well, so that, using the definition of η , (4.21) and (4.22) we get

$$Q_0^{\text{E}}(\gamma_{\text{min}}) = \frac{\alpha_e (p_{\text{inj}} - 2) \gamma_{\text{min}}^{-2} \dot{p}}{m_e c^2 (\gamma_{\text{ad}} - 1) (1 - \eta^{2-p_{\text{inj}}})} = \frac{\alpha_e \gamma_{\text{min}}^{-2}}{1 - \eta^{-0.2}} \left(\frac{\dot{p}}{1.36 \times 10^{-6} \text{erg cm}^{-3} \text{s}^{-1}} \right) \text{cm}^{-3} \text{s}^{-1}. \quad (4.24)$$

Therefore, the injection model of type-E has three free parameters, namely α_e , η and γ_{min} .

4.2.3.2 INJECTION MODEL OF TYPE-N

This model is similar to the type-E model, i.e., $Q_0^{\text{N}}(\gamma_{\text{min}})$ satisfies equation (4.24), but the difference is that instead of assuming that γ_{min} is a global constant we assume that the number density of electrons n_e^{acc} accelerated within a time step Δt is a fraction ζ of the number of thermal electrons within a zone,

$$n_e^{\text{acc}} = \zeta \frac{\rho}{m_p}, \quad (4.25)$$

where we have assumed that the ideal gas is the mono-atomic hydrogen gas and m_p is the proton mass. ζ is a global constant in this model. Using the definition of the power law source term (3.29) we can write

$$n_e^{\text{acc}} = \Delta t \int_{\gamma_{\text{min}}}^{\gamma_{\text{max}}} d\gamma Q_0^{\text{N}}(\gamma_{\text{min}}) \left(\frac{\gamma}{\gamma_{\text{min}}} \right)^{-p_{\text{inj}}} = \frac{\Delta t Q_0^{\text{N}}(\gamma_{\text{min}}) \gamma_{\text{min}} (1 - \eta^{1-p_{\text{inj}}})}{p_{\text{inj}} - 1}, \quad (4.26)$$

and then use it together with (4.24) (with $Q_0^E(\gamma_{\min})$ replaced by $Q_0^N(\gamma_{\min})$) and (4.25) to obtain

$$\begin{aligned} \gamma_{\min} &= \frac{p_{\text{inj}} - 2}{p_{\text{inj}} - 1} \frac{\alpha_e}{\zeta} \frac{1 - \eta^{1-p_{\text{inj}}}}{1 - \eta^{2-p_{\text{inj}}}} \frac{m_p}{m_e c^2} \frac{\dot{p} \Delta t}{(\gamma_{\text{ad}} - 1) \rho} = \\ &= \frac{\alpha_e}{\zeta} \frac{1 - \eta^{-1.2}}{1 - \eta^{-0.2}} \left(\frac{\dot{p} \Delta t}{1.36 \times 10^{-6} \text{erg cm}^{-3}} \right) \left(\frac{\rho}{1.39 \times 10^{-24} \text{g cm}^{-3}} \right)^{-1}. \end{aligned} \quad (4.27)$$

Inserting (4.27) into (4.24) we get the normalization of the source term

$$Q_0^N(\gamma_{\min}) = \frac{\alpha_e \gamma_{\min}^{-2}}{1 - \eta^{-0.2}} \left(\frac{\dot{p}}{1.36 \times 10^{-6} \text{erg cm}^{-3} \text{s}^{-1}} \right) \text{cm}^{-3} \text{s}^{-1}, \quad (4.28)$$

where γ_{\min} satisfies (4.27).

The injection model of type-N has three free parameters, namely α_e , η and ζ .

4.2.3.3 COMPARISON OF TYPE-E AND TYPE-N MODELS

Both type-E and type-N models inject the same amount of energy into the accelerated electrons (due to the assumption (4.21)). However, since they have different assumptions about γ_{\min} , the *number* of accelerated electrons and their energy distribution is different. Since both γ_{\min} and the number of accelerated electrons are affecting the observed radiation (see section 4.3.1.1), here we examine the behavior of the two models assuming the same underlying hydrodynamics.

We assume the following hydrodynamic situation: $\dot{p} = \dot{p}_0 = 1.36 \times 10^{-4} \text{erg cm}^{-3} \text{s}^{-1}$, $\Delta t = 10 \text{s}$, $\rho = 10^{-18} \text{g cm}^{-3}$.

For both type-E and type-N models we assume $\alpha_e = 0.05$ and $\eta = 10^4$. For the type-E model we assume $\gamma_{\min} = 50$ and then compute ζ from (4.27) such that γ_{\min} for the type-N model is the same as the one for type-E model and $\dot{p} = \dot{p}_0$, assuming that $p_{\text{inj}} = 2.2$. The result is $\zeta = 1.65 \times 10^{-6}$.

If \dot{p} is varied, the models show different behavior. To quantify it, we use the definition of n_e^{acc} (4.26) and of the average Lorentz factor

$$\bar{\gamma} \equiv \frac{\int_{\gamma_{\min}}^{\gamma_{\max}} d\gamma \gamma^{1-p_{\text{inj}}}}{\int_{\gamma_{\min}}^{\gamma_{\max}} d\gamma \gamma^{-p_{\text{inj}}}} = \frac{p_{\text{inj}} - 1}{p_{\text{inj}} - 2} \frac{1 - \eta^{2-p_{\text{inj}}}}{1 - \eta^{1-p_{\text{inj}}}} \gamma_{\min} = 6 \frac{1 - \eta^{-0.2}}{1 - \eta^{-1.2}} \gamma_{\min}, \quad (4.29)$$

and compute n_e^{acc} and $\bar{\gamma}$ for several different values of \dot{p} . The results are summarized in Table 4.1. Figures 4.1 and 4.2 show plots of the injected electron energy distribution corresponding to the values in the Table 4.1.

As one can see, increasing the energy injection rate in type-E model produces an increased number of accelerated electrons, keeping the shape of their energy distribution unchanged. For model type-N the energy injection rate increase does not produce more electrons but shifts the electron

$\frac{\dot{p}}{\dot{p}_0}$	$\gamma_{\min \text{ E}}$	$n_e^{\text{acc E}}$	$\bar{\gamma} \text{ E}$	$\gamma_{\min \text{ N}}$	$n_e^{\text{acc N}}$	$\bar{\gamma} \text{ N}$
0.1	50	0.099	252.5	5	0.99	25.25
1	50	0.99	252.5	50	0.99	252.5
10	50	9.9	252.5	500	0.99	2525
100	50	99	252.5	5000	0.99	25252

Table 4.1: γ_{\min} , n_e^{acc} and $\bar{\gamma}$ for different \dot{p} and two different injection models.

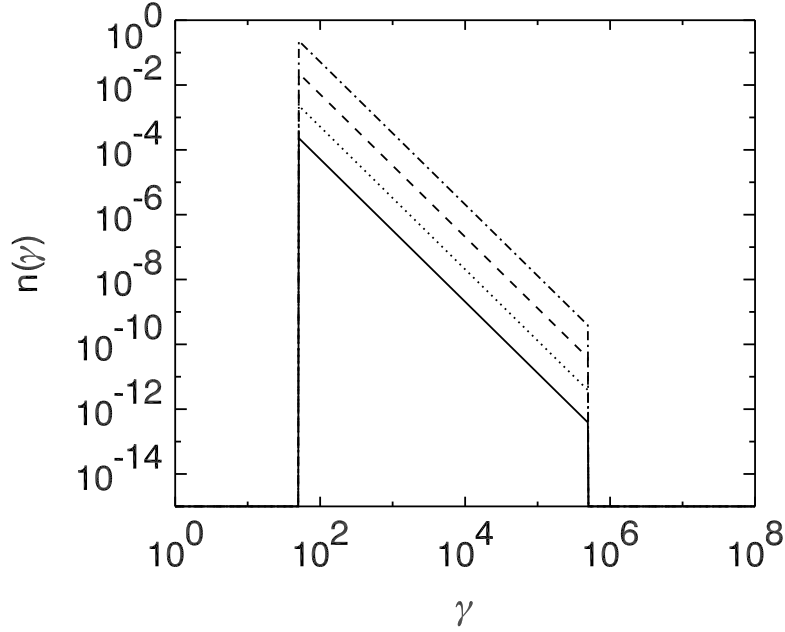


Figure 4.1: The energy distribution of the injected electrons for the injection model of type-E. Solid line is corresponding to $\dot{p} = 0.1\dot{p}_0$, dotted line to $\dot{p} = \dot{p}_0$, dashed line to $\dot{p} = 10\dot{p}_0$ and dot-dashed line to $\dot{p} = 100\dot{p}_0$, respectively

distribution to higher energies. As we will see in Section 4.3.1.1, the difference in behavior is expected to leave a signature in the observed radiation spectrum.

4.3 Non-thermal radiation

4.3.1 Treatment of the synchrotron radiation

As discussed in Section 4.2.1, we assume that the spatial distribution of the non-thermal particles is homogeneous within a numerical cell. Furthermore, since the energy distribution within each cell is represented by a sum of

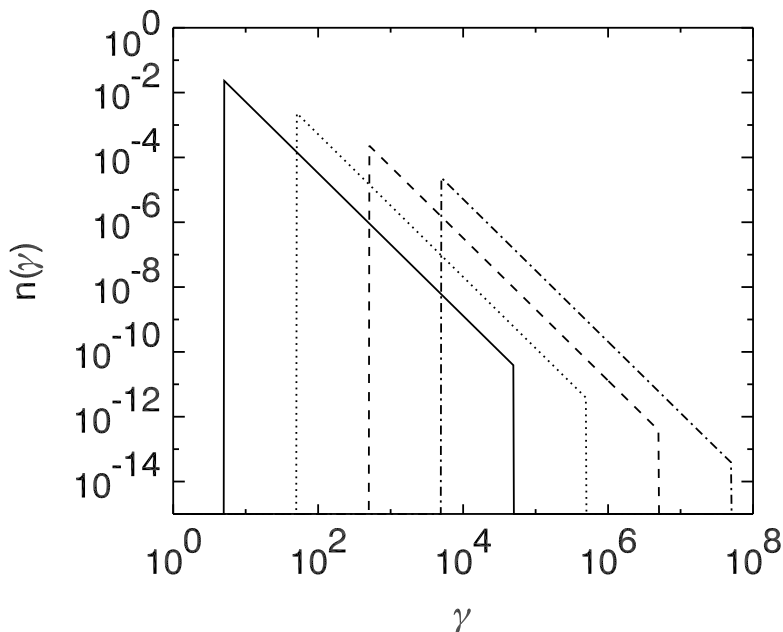


Figure 4.2: The energy distribution of the injected electrons for the injection model of type-N. The solid line corresponds to $\dot{p} = 0.1p_0$, the dotted line to $\dot{p} = p_0$, the dashed line to $\dot{p} = 10p_0$ and the dot-dashed line to $\dot{p} = 100p_0$, respectively.

connected power-laws (4.14), we can apply the formulae derived in section 2.1.3 to accurately compute the synchrotron radiation produced by this electron distribution.

Combining equations (2.69) and (4.14) we can write the emissivity in the rest frame of the numerical cell

$$j_{\text{syn}}(\nu) = \frac{\sqrt{3}B}{8\pi m_e c^2} \sum_{i=1}^N n_0^i \gamma_{i-1}^{(2-3p_i)/2} \left(\frac{\nu}{\nu_0}\right)^{(1-p_i)/2} H_1\left(\frac{\nu}{\nu_0 \gamma_{i-1}^2}, p_i, \frac{\gamma_i}{\gamma_{i+1}}\right), \quad (4.30)$$

where the magnetic field B is assumed to be randomly oriented in the cell rest frame, and its strength being constant, $\nu_0 = 3eB/4\pi m_e c$, H_1 are given by equation (2.70).

Due to the fact that the γ_i are distributed logarithmically, the ratio γ_i/γ_{i-1} is constant for all $i = 1, \dots, N$. We have tabulated H_1 as a function of two variables, $x \equiv \nu/\nu_0 \gamma^2$ and p . In such a way it is computationally efficient to perform the summation in (4.30) for each zone in each time step.

Once the rest frame emissivities for all zones are computed, they are transformed into the frame which is at rest with respect to the observer (we neglect cosmological effects; see the end of this section for discussion). If ν_{obs} is the frequency at which the observer measures emissivity we can

write, using (2.78) and (2.79),

$$j_{\text{obs}}(\nu) = \frac{j_{\text{syn}}(\gamma(1 - \beta\mu)\nu_{\text{obs}})}{(\gamma(1 - \beta\mu))^2}, \quad (4.31)$$

where γ and βc are the Lorentz factor and the velocity of the zone, and μ is the cosine of the angle between the velocity and the line of sight towards the observer (i.e., $\mu = 1$, if the zone is moving towards the observer parallel to the line of sight).

4.3.1.1 DIFFERENCES BETWEEN RADIATION PRODUCED BY TYPE-E AND TYPE-N MODELS

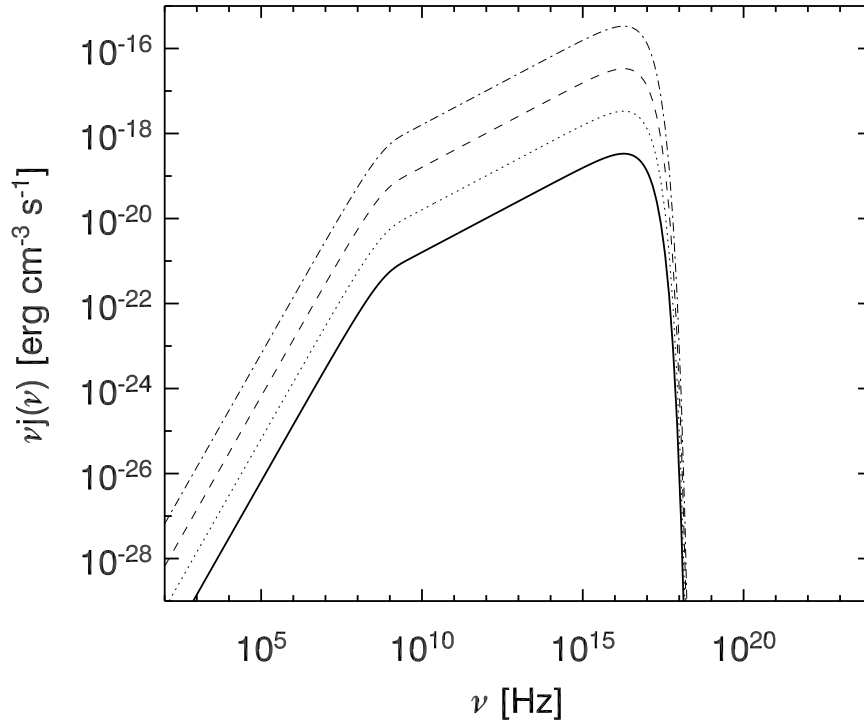


Figure 4.3: The synchrotron emissivity for type-E electron distributions from Figure 4.1.

Figures 4.3 and 4.4 show the synchrotron emissivity produced by the electron distribution used as an example in section 4.2.3.3. As we can see from Fig. 4.3, increasing the amount of dissipation within the type-E model changes only the amount of the emitted energy, while the spectral shape remains unchanged. On the other hand, increasing the dissipation within type-N model shifts the spectrum to higher frequencies, keeping the emitted energy constant (see Fig. 4.4).

4.3.2 Light curve computation

We assume that the observer is located at a distance z_{obs} from the origin (see Fig. 4.5). For simplicity we assume that the z -axis of the jet is parallel

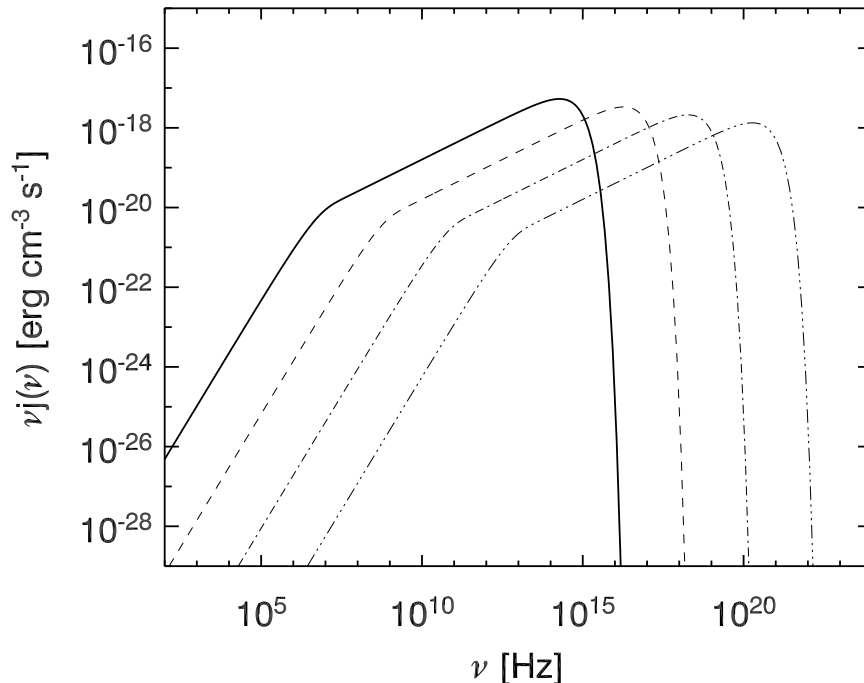


Figure 4.4: The synchrotron emissivity for type-N electron distributions from Figure 4.2.

to the line of sight. The radiation from the zone whose center is located at a position z_i at a time T_n arrives to the observer located at z_{obs} at a time (Fig. 4.5).

$$t_{\text{obs}}(z_i, T_n) = \frac{z_{\text{obs}} - z_i}{c} + T_n. \quad (4.32)$$

The light curve is discretized in segments of width t_{disc} . In principle, from every point (r_j, z_i) at every time T_n , one should have a contribution to the light curve. However, consistent with the numerical discretization, we assume that the radiation from whole hydrodynamic cell arrives at the same instant at the observer, so that the intensity of the radiation measured by the observer is $j_{\text{obs}}(\nu)\Delta z_{\text{obs}}$, where Δz_{obs} is the length of the cell in the observer frame parallel to the line of sight. We then assume that the cell is radiating constantly during a time step ΔT , so that the contribution to the light curve segment whose duration is t_{disc} is simply the total energy per unit of surface radiated during a time step $j_{\text{obs}}(\nu)\Delta z_{\text{obs}}\Delta T$ averaged over the size of the light curve segment,

$$\Delta I(\nu, t_{\text{obs}}(z_i, T_n)) = j_{\text{obs}}(\nu)\Delta z_{\text{obs}} \frac{\Delta T}{t_{\text{disc}}}, \quad (4.33)$$

where j_{obs} is computed according to (4.31). Due to the discretization it is possible (and in fact very probable) that a single light curve segment accumulates radiation from several zones during several time steps, so that, as sketched in Fig. 4.5, one has to wait until the end of the simulation to obtain the final light curve.

The light curve is computed at a number of discrete frequencies, and is integrated in different frequency bands in a post-processing phase assuming

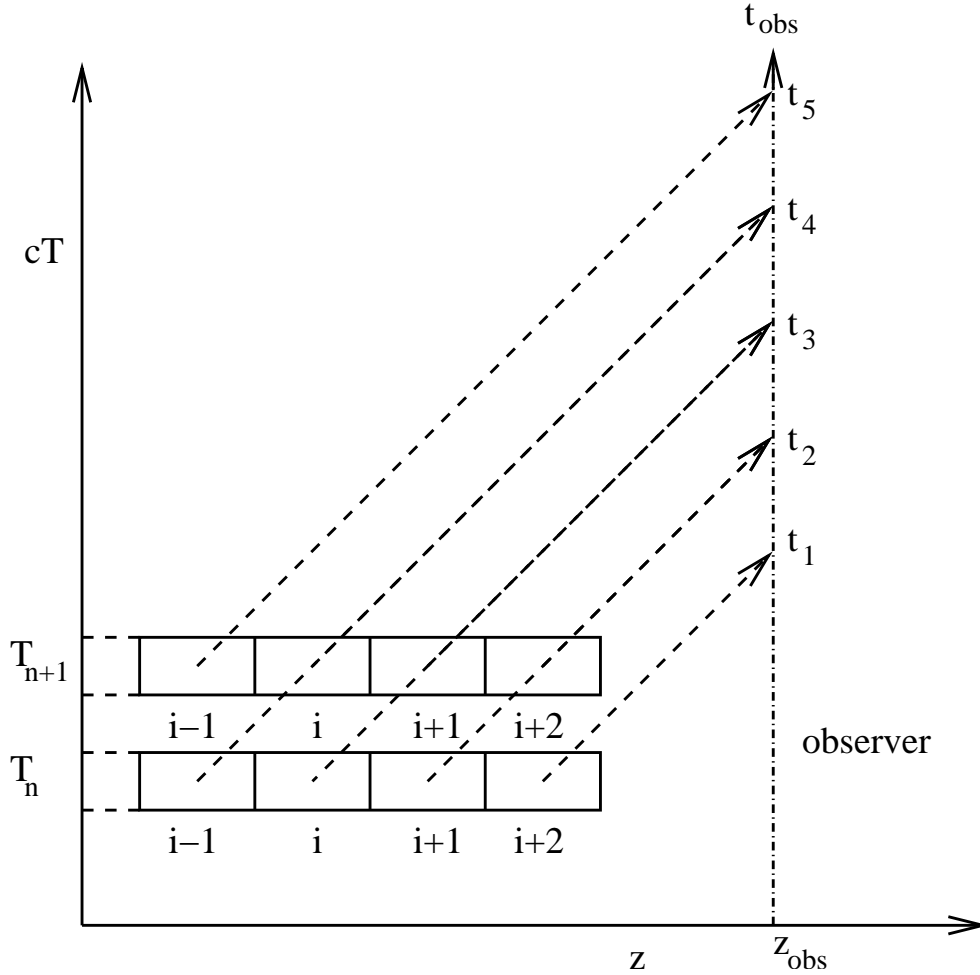


Figure 4.5: Scheme showing how the light curve is computed: an observer located at z_{obs} sees radiation emitted simultaneously from different zones arriving at different times (dashed vectors). Also, radiation from different zones in different time-steps may arrive at the same time (i.e., from zone $i - 1$ at T_n and from zone i at T_{n+1}). The final light curve depends on the radiation from *all* zones at *all* time steps!

that the spectrum between two neighboring frequencies is a power law. In order to compare with the observed light curves, it is necessary to convert the intensity of the observed radiation into (normalized) photon counts per second $s(t)$ in a certain frequency band $\nu_1 - \nu_2$. This is done easily using the formula

$$s(t) = \int_{\nu_1}^{\nu_2} d\nu \frac{I(\nu, t)}{h\nu}, \quad (4.34)$$

where h is Planck constant. If the intensity distribution between ν_1 and ν_2

is a power law of the form (2.95) we obtain

$$s(t) = \begin{cases} \frac{I(\nu_1)}{hq} \left[1 - \left(\frac{\nu_2}{\nu_1} \right)^{-q} \right] & \text{if } q \neq 0 \\ \frac{I(\nu_1)}{h} \ln \left(\frac{\nu_2}{\nu_1} \right) & \text{if } q = 0 \end{cases}. \quad (4.35)$$

Any frequency interval can be represented as the superposition of several power law intervals so that (4.35) can be used for an efficient light curve integration.

It is important to stress that we neglect cosmological effects on the properties of the observed radiation. The error we make is of the order of a few percent in the observed frequency, intensity, and time scales since the typical redshift of the best-studied blazars is about 0.1 (Fossati et al. 1998). In fact, the best studied blazar, Mrk 421, is located at $z = 0.03$.

4.4 Method validation

The relativistic hydrodynamics code *GENESIS* has been thoroughly tested in the past (Aloy et al. 1999), so that in this section we focus on testing the non-thermal part of the code. First, in section 4.4.1 the kinetic equation solver is tested. Then, the synchrotron radiation algorithm is validated. (section 4.4.2).

4.4.1 Tests of the kinetic-equation solver

We make two tests, both of which have known analytic solutions. Both cases are not just pure academic examples, but they occur frequently in applications involving the simulation of radiation coming from blazars.

THE EFFICIENCY OF THE KINETIC EQUATION (KE) SOLVER

The advantage of our KE solver compared to that of Chang & Cooper (1970) is that no iterative procedure is required, i.e. the solution is evaluated immediately from the initial electron distribution.

In an RHD simulation where one typically deals with tens of thousands of numerical cells and 50-100 energy bins per cell, iterative procedures can be quite expensive. The use of the analytic solver makes the electron transport scheme only as expensive as the hydrodynamic evolution, i.e. the code is only two times slower with respect to the pure RHD code.

INITIAL POWER-LAW DISTRIBUTION WITHOUT A SOURCE TERM

We consider an initial electron distribution of the form (2.61) with the parameters $\gamma_{\min} = 50$, $\gamma_{\max} = 5 \cdot 10^5$, $n(\gamma_{\min}) = 1 \text{ cm}^{-3}$, $p = 2.2$. The

N	10 s	5×10^5 s	10^7 s
24	0.0975	1.7278	32.5924
48	0.0419	1.5750	29.8560
96	0.0195	1.5179	29.5497
192	0.0094	1.4934	29.4242

Table 4.2: $\Delta(N, t)/10^{-4}$ for the test without a source term as a function of the number of energy bins (rows) and the time of integration (columns).

electrons are then assumed to emit synchrotron radiation in a magnetic field whose strength is $B = 0.05$ G. The analytic solution for the temporal evolution of the distribution function (3.27), reads in this case (with $q_L = 4.9 \times 10^{-12} \text{ s}^{-1}$)

$$n(\gamma, t) = \left(\frac{\gamma}{50}\right)^{-2.25} \times (1 - 4.9 \times 10^{-12} \text{ s}^{-1} \gamma t)^{0.25} S\left(\gamma; \frac{50}{1 + 4.9 \times 10^{-12} \text{ s}^{-1} \gamma t}, \frac{5 \times 10^5}{1 + 4.9 \times 10^{-12} \text{ s}^{-1} \gamma t}\right). \quad (4.36)$$

The results are shown on Fig. 4.6 for 24, 48, 96 and 192 energy bins. A convergence study for different times has been performed. Since we know the total number of electrons from the analytic solution ($n_e = 41.67 \text{ cm}^{-3}$), we can define the error of the numerical solution with N energy bins after time t as

$$\Delta(N, t) \equiv \frac{|n_e - n_e^{N,t}|}{n_e},$$

where $n_e^{N,t}$ is the total number of electrons after the solver has been called with N energy bins for a time interval t . Table 4.2 shows the dependence of $\Delta(N, t)$ on the number of bins and the time of integration. One sees that, especially for smaller t , it is necessary to use more than only 24 energy bins.

Figure 4.7 shows what happens when the solver is called repeatedly with very small time intervals, using the same parameters as in Fig. 4.6. Table 4.3 shows the behavior of $\Delta(N, t)$ as a function of the number of calls and the number of energy bins.

We point out that the kinetic equation is a first order partial differential equation. The integration of such an equation by means of standard conservative numerical methods produces excessive amounts of numerical viscosity that degrade the quality of the solution, particularly in those energy bins around the high-energy end of the distribution function. Capturing with sufficient sharpness this high-energy end of the distribution function is of relevance in order to compute correctly the spectra and the light curves of blazars. In fact, for sufficiently large integration time steps

$$\Delta t > \Delta t_d = \frac{\gamma_N - \gamma_{N-1}}{\gamma_{N-1} \gamma_N q_L}, \quad (4.37)$$

the KE solver accurately follows the high-energy break of the distribution function even with a moderate number of energy bins (Fig. 4.6). This

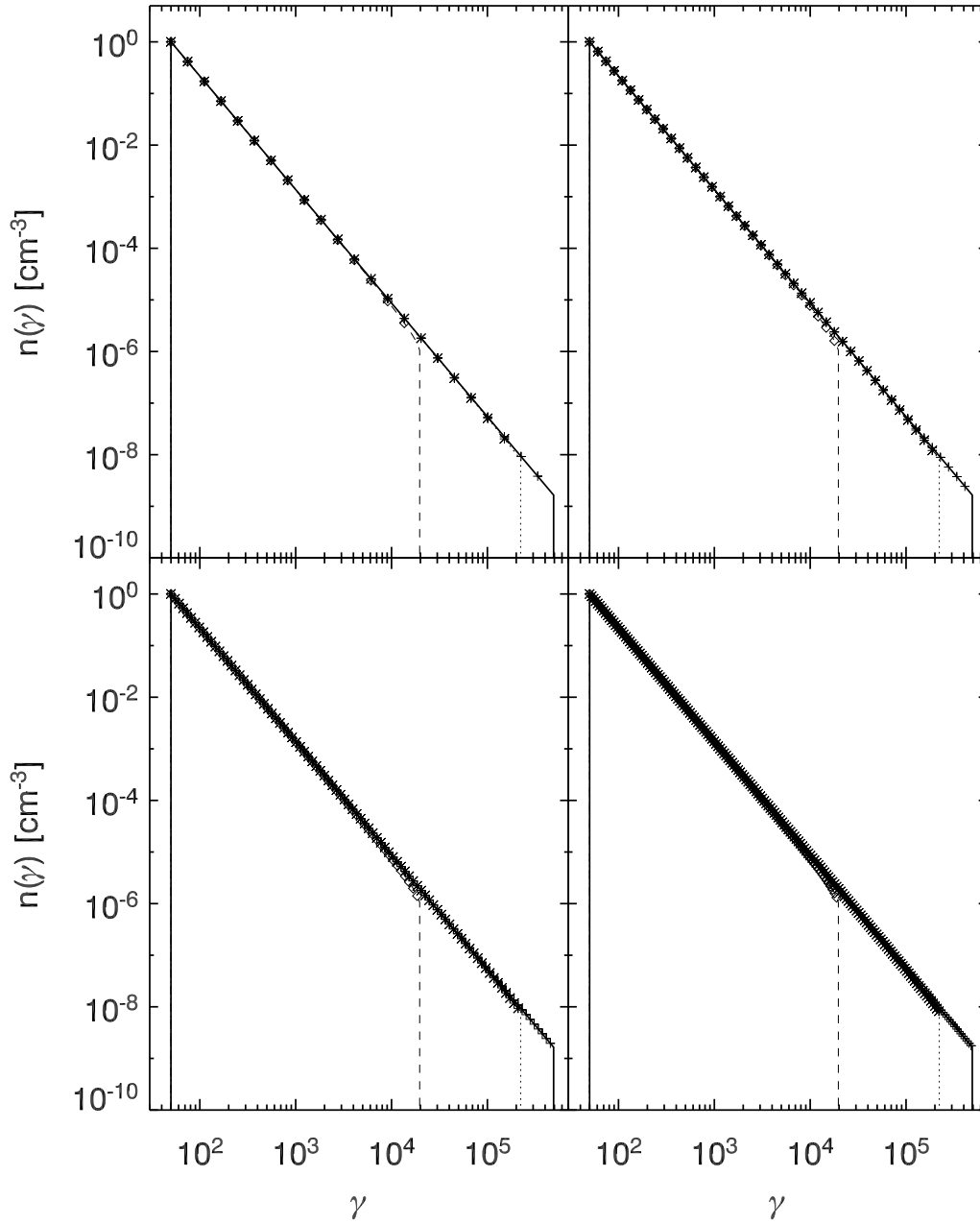


Figure 4.6: Test without source term: Analytic (lines) and numerical solutions (symbols) for 24 (upper left), 48 (upper right), 96 (lower left) and 192 (lower right panel) energy bins. The solid line corresponds to $t = 10$ s, the dotted line to $t = 5.1 \times 10^5$ s and the dashed line to $t = 10^7$ s, respectively. The KE solver was called only once to obtain the computed solutions.

restriction for the time step of the KE solver comes from the minimum time that electrons need to get transported between two consecutive energy bins γ_i and γ_{i-1} (obtained by integrating (3.19) between γ_i and γ_{i-1}). If the time is smaller than Δt_b , no electrons are transported to lower Lorentz factors. The net effect is an excess of electrons at higher Lorentz factors.

N	one call	100 calls	10^4 calls
24	3.4322	4.1546	4.1641
48	3.3833	3.2973	3.3046
96	3.0991	2.9614	2.9678
192	2.9730	2.8101	2.8162

Table 4.3: $\Delta(N, t)/10^{-5}$ as a function of the number of energy bins (rows) and the number of calls to the EK solver. The total integration time is 10^5 s and there is no source term present.

N	10 s	5×10^5 s	10^7 s
24	0.097611	0.577314	49.366889
48	0.039964	0.553605	49.388724
96	0.018643	0.547751	49.393972
192	0.008975	0.545921	49.395255

Table 4.4: $\Delta(N, t)/10^{-4}$ as a function of the number of energy bins (rows) and the integration time after calling the EK solver with source term.

But, as Fig. 4.7 shows, this effect is only critical at the very high end of the electron distribution. The other side effect is that the lower end of the electron distribution does not shift to lower frequencies (as expected from 4.36). However, this effect only becomes critical for very long evolutionary times.

SOURCE TERM WITHOUT ELECTRONS PRESENT INITIALLY

We consider the case when the initial electron distribution is equal to zero everywhere. The limits of the source term are $\gamma_{\min} = 50$ and $\gamma_{\max} = 5 \times 10^5$, its normalization $Q(\gamma_{\min}) = 10^{-5} \text{ cm}^{-3} \text{ s}^{-1}$, and the power law index $p = 2.2$. The magnetic field is $B = 0.05$ G. The comparison between analytic (lines) and numeric solutions (symbols) for three times $t = 10$ s, $t = 5.1, 10^5$ s and $t = 10^8$ s is shown on Fig. 4.8. The analytic solution was computed using equation (4.19) with $q_L = 4.9 \cdot 10^{-12} \text{ s}^{-1}$.

Table 4.4 shows $\Delta(N, t)$ as a function of the number of energy bins and the integration time. The reason for the worse performance with increased integration time can be seen in Fig. 4.9, where a zoom-in of the area around the break of the solution for $t = 10^7$ s is shown. Due to the finite number of points the break is not well resolved, which leads to an error in estimating the number of injected electrons when compared to the analytic solution (3.31).

In this section we have tested the performance of the KE solver for two typical cases which are found in application to internal shocks in blazar jets, (1) the injection of the electrons at the relativistic shocks and (2) the

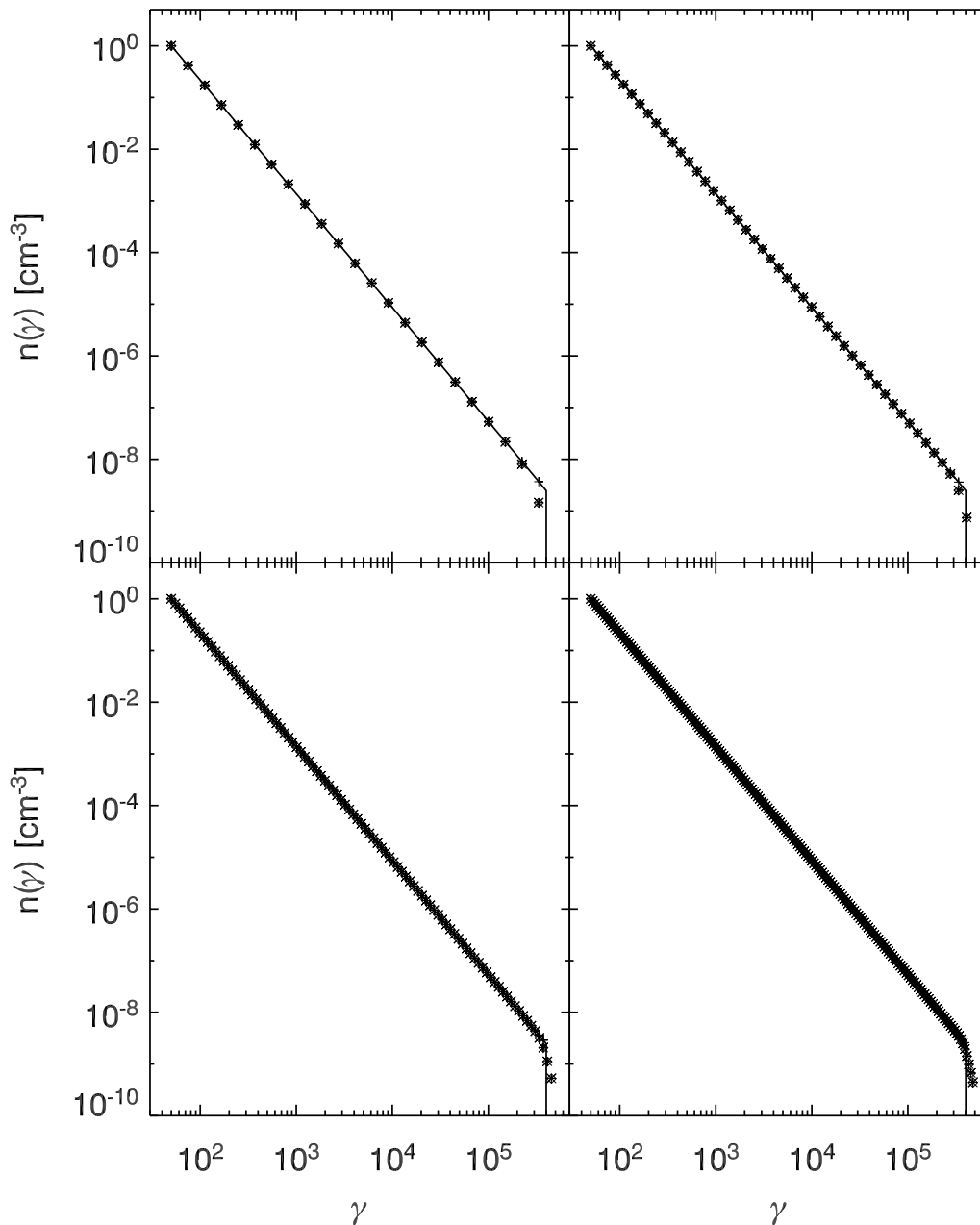


Figure 4.7: Test of the KE solver showing the errors in the high-energy end of the distribution if small time steps are used progressively to reach the final time $t = 10^5$ s. The solid line corresponds to analytic solution after $t = 10^5$ s. The plus, cross and diamond symbols show the numerical solution if the final time is reached after 1, 100 and 10000 calls to the KE solver. The upper left panel is the solution for 24 energy bins, the upper right for 48, the lower left for 96, and the lower right panel for 192 energy bins, respectively.

synchrotron cooling of the electrons in the presence of magnetic field. As tests show, it is possible to track the temporal evolution with reasonable accuracy with at least 50 Lorentz factor bins.

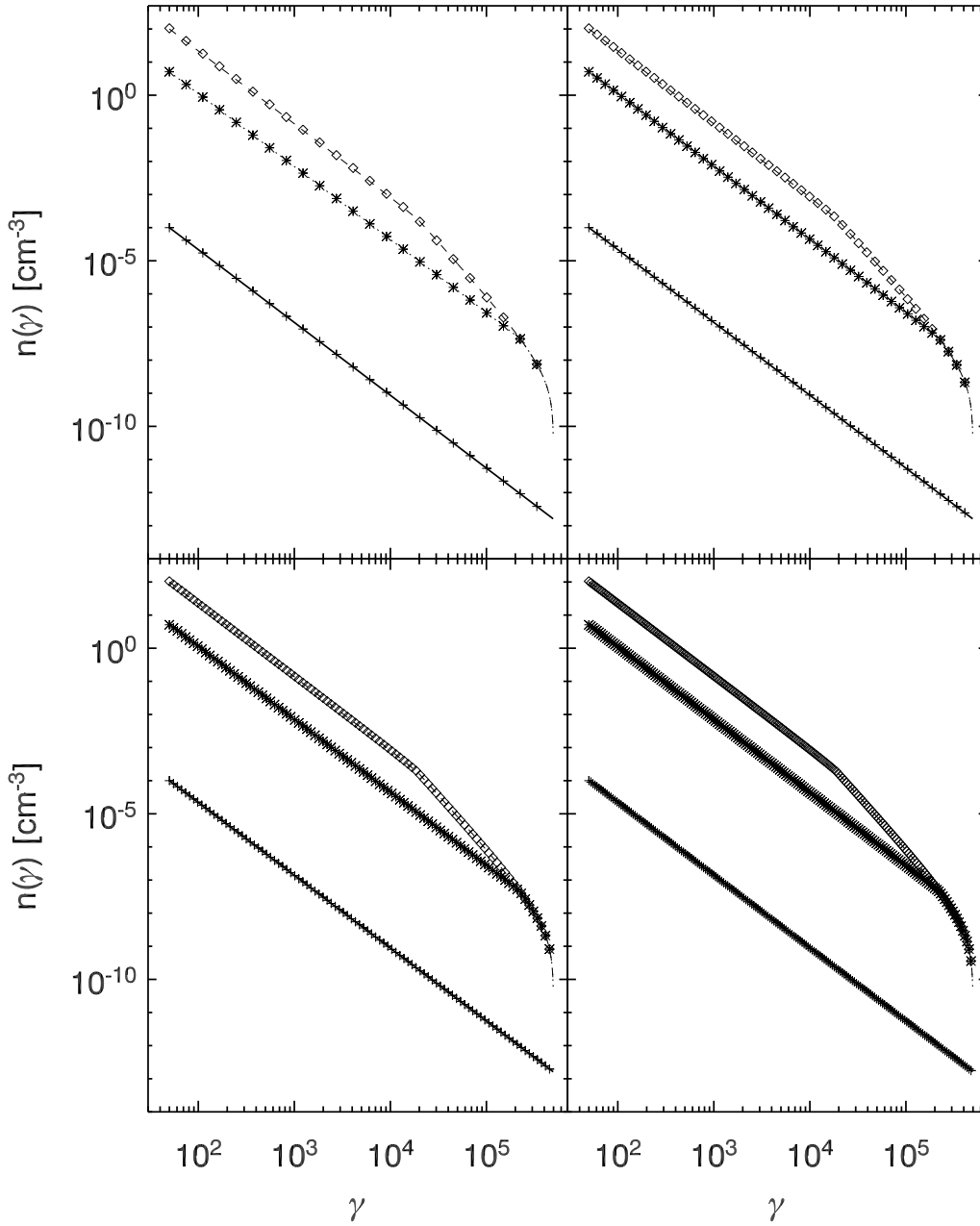


Figure 4.8: Test with source term: Analytic (lines) and numerical solutions (symbols) for 24 (upper left), 96 (upper right), 96 (lower left), and 192 (lower right panel) energy bins respectively. The solid line corresponds to $t = 10$ s, the dotted line to $t = 5.1 \times 10^5$ s and the dashed line to $t = 10^7$ s, respectively. Symbols give the corresponding numerical solution.

4.4.2 Test of the synchrotron radiation code

Figure 4.10 shows the results of a test problem where the evolution of the synchrotron emissivity for the same initial electron distribution and magnetic field as in section 4.4.1 is computed. The long-dashed line intersecting the dot-dashed line shows the synchrotron emissivity for the electron distri-

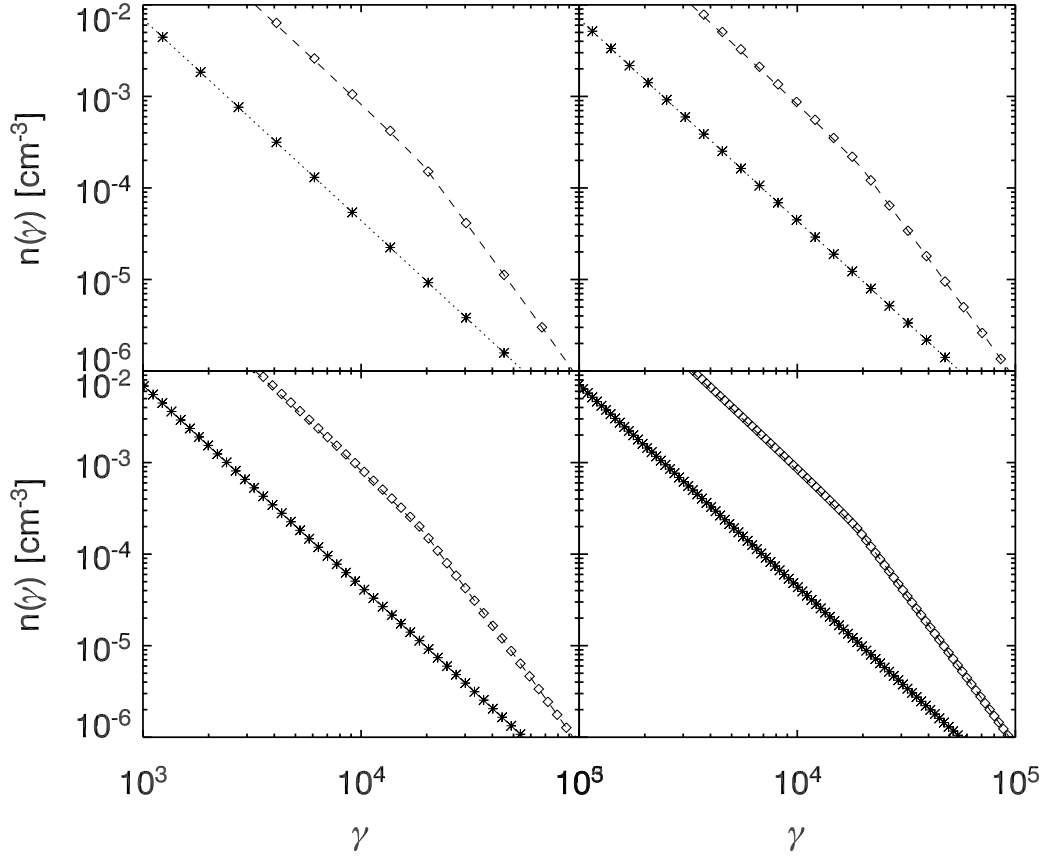


Figure 4.9: A zoom-in of the solution around the break in figure 4.7: Analytic (lines) and numerical solutions (symbols) for 24 (upper left), 96 (upper right), 96 (lower left), and 192 (lower right panel) energy bins, respectively. The solid line corresponds to $t = 10$ s, the dotted line to $t = 5.1 \cdot 10^5$ s and the dashed line to $t = 10^7$ s, respectively

bution resulting from 10^6 calls to the kinetic equation solver, each advancing the solution by 100 s, rather than just calling it once with $t = 10^8$ s (which was done in the case of the dot-dashed line). The area below the curves is $J_1 = 3.4927 \times 10^{-13}$ erg cm $^{-3}$ s $^{-1}$ for only one call to the KE solver, and $J_{10^6} = 3.0359 \cdot 10^{-13}$ erg cm $^{-3}$ s $^{-1}$ for 10^6 calls to the KE solver, i.e., a difference of $\approx 15\%$. It has to be pointed out, however, that in applications to blazars one expects far less (at least two orders of magnitude) calls to the KE solver for the *same* zone, so that the error in the treatment of the emissivity evolution is going to be smaller. The high-frequency spectral cut-off which develops as highly energetic electrons cool down and the electron distribution shifts to lower energies can also be seen.

In Fig. 4.11 the results of the test with the source term and no electrons present initially are shown. Again, the long dashed line shows the results of 10^6 calls to the kinetic equation solver with 100s time step in each call. The areas below curves for one and 10^6 calls to the KE solver are $J_1 = 1.2963 \times 10^{-9}$ erg cm $^{-3}$ s $^{-1}$ and $J_{10^6} = 1.2632 \times 10^{-9}$ erg cm $^{-3}$ s $^{-1}$, respectively. The relative difference is $\approx 2\%$, so that the radiation from the internal shocks (where injection takes place) is tracked with reasonable accuracy.

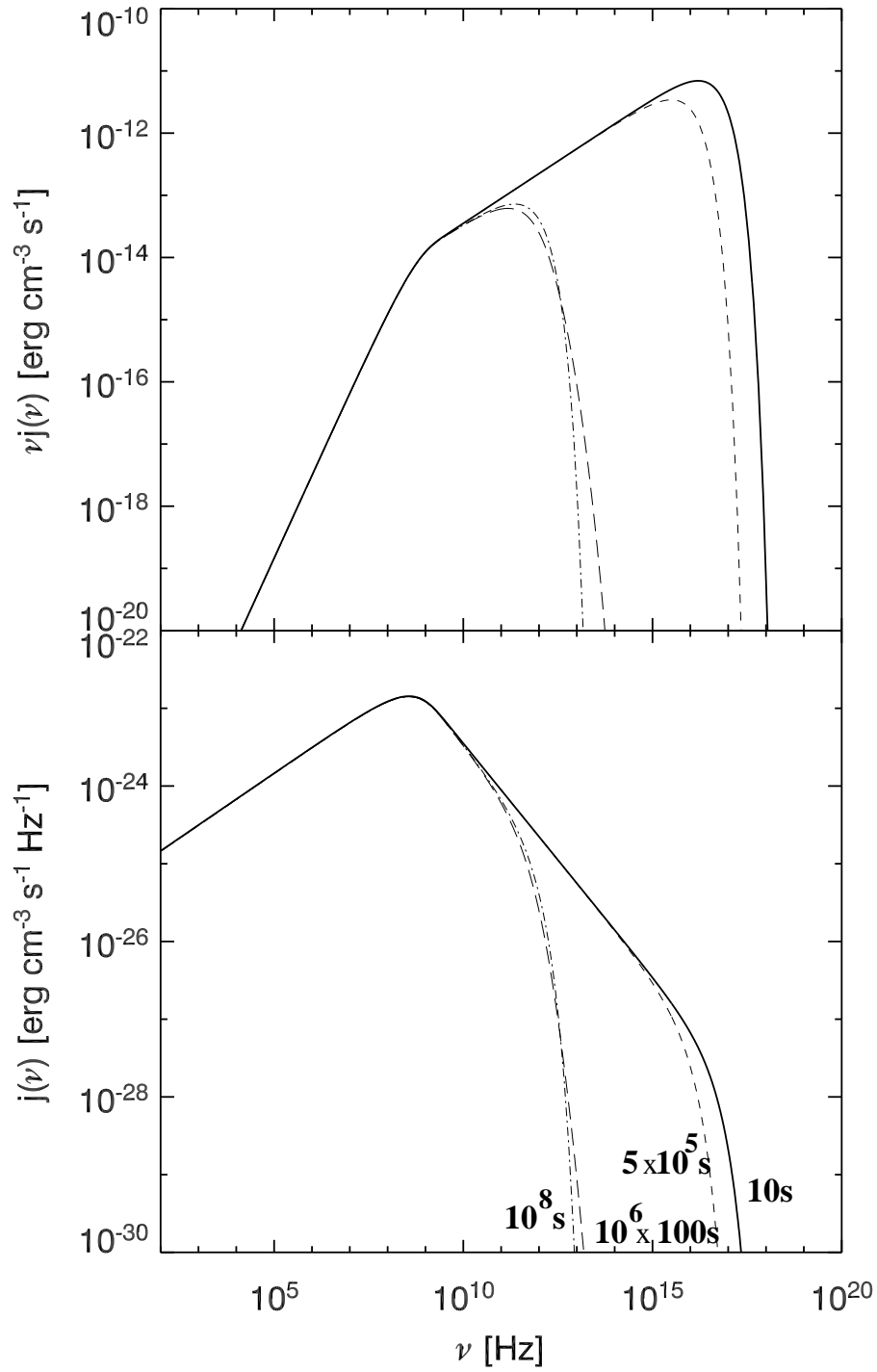


Figure 4.10: Synchrotron emissivity (lower panel) and spectral energy distribution (upper panel) for the same initial electron distribution as for the test of the KE solver without source term (see section 4.4.1). The full line is the synchrotron emissivity after the electrons have been radiating for 10 s, the dashed line for 5.1×10^5 s, dot-dashed line for 10^8 s and long-dashed line for 10^6 calls to the EK solver with $t = 100$ s. The number of electron bins is 48.

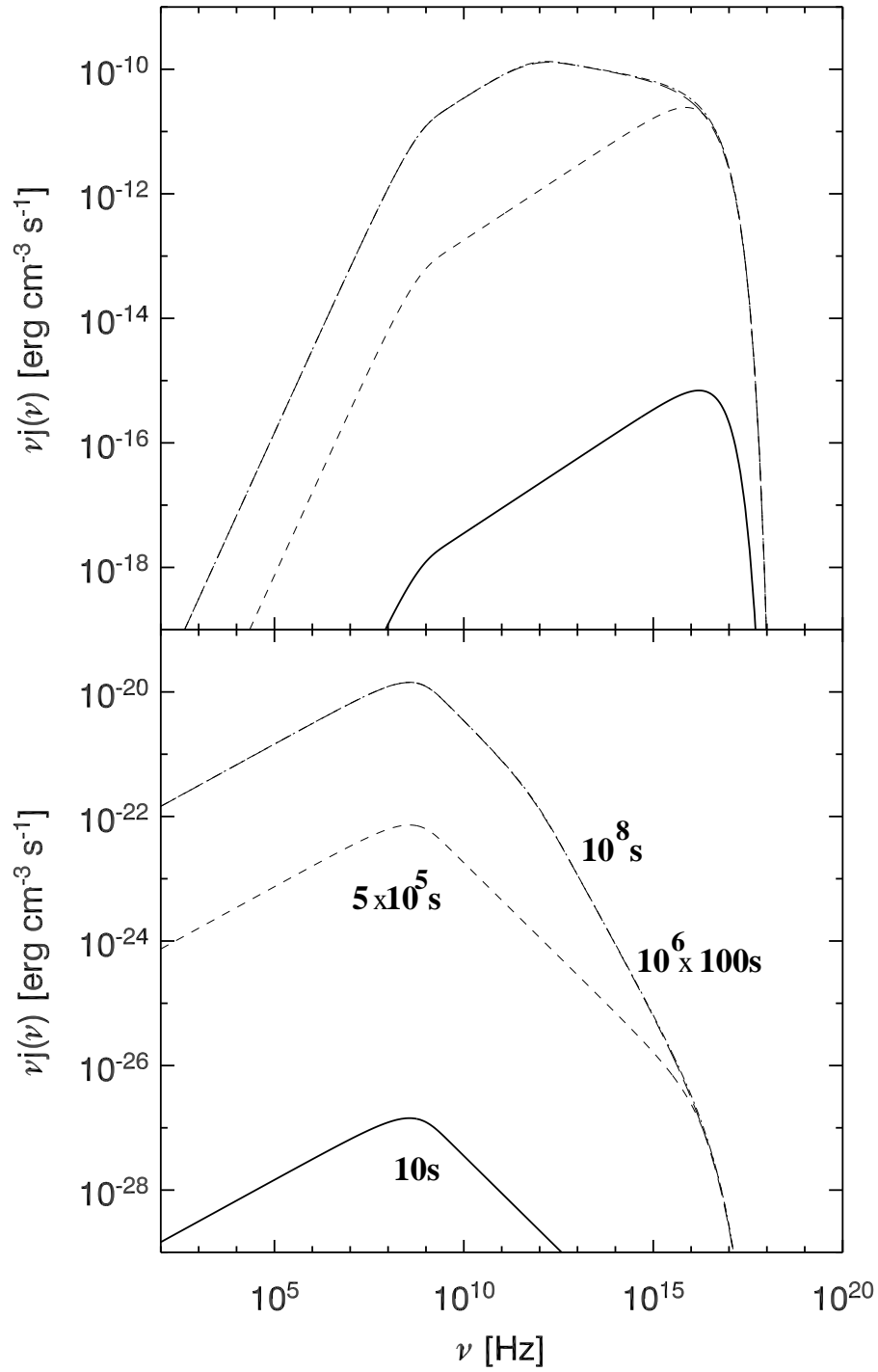


Figure 4.11: Synchrotron emissivity (lower panel) and spectral energy distribution (upper panel) for the same source of electrons as in the test of the KE solver with the source term and no electrons present initially (see section 4.4.1). The full line is the synchrotron emissivity after the source has been injecting electrons for 10 s, the dashed line for 5.1×10^5 s, dot-dashed line for 10^8 s. The long-dashed line (lying almost exactly on top of the dot-dashed line) is the synchrotron emissivity for the electron distribution which has been computed after 10^6 calls to the kinetic equation solver with a constant time step of 100 s. The number of electron bins is 48.

Chapter 5

Simulations of blazar flares

In this chapter the results of two- and one-dimensional simulations of blazar flares are presented. In section 5.1 an overview of the physical model and the numerical details of the simulations are given. Two-dimensional simulations have been used to study the interaction of two shells in great detail, in order to study the impact of the multidimensional geometry on synthetic light curves (section 5.2). One-dimensional simulations have been used to cover a large parameter space (section 5.3). In Section 5.4 an analytic nonthermal flare model is introduced. The comparison between our models and the observed blazar flares is discussed in Section 5.5. Finally, in Section 5.6 results of preliminary simulations of multiple collisions are shown.

5.1 Introduction to blazar simulations

5.1.1 The physical model

It is unknown in which form the energy of relativistic jets is transported, i.e., whether the energy is stored in kinetic energy of the moving plasma or in Poynting flux of some ordered magnetic field. Furthermore, the plasma composition (electrons and protons, or electron-positron pairs) is observationally still undetermined. It is also possible that both the composition and the energy transport mechanism vary along the jet.

We assume that a typical blazar jet at sub-parsec scales is composed of electrons and protons, consistent with estimates based on the minimum jet power and other constraints inferred from radio-to-X-ray spectra (Celotti 2003).

Most of the blazar jets seem to be pointing almost exactly towards the observer. For simplicity we assume that the jet axis is parallel to the line of sight, i.e., the jet is pointing *exactly* towards the observer.

We distinguish between the *background flow* (underlying jet), which we assume to have a uniform density ρ_{ext} and pressure p_{ext} , and that is moving with a velocity $v_{\text{ext}} = c\sqrt{1 - \Gamma_{\text{ext}}^{-2}}$ towards the observer, and the *shells* i , ($i = 1, 2$) which are cylinders of radius R_i , length L_i , Lorentz factor $\Gamma_i > \Gamma_{\text{ext}}$, density ρ_i and pressure p_i embedded into the external flow with an initial separation D_0 (Fig. 5.1). There are physical reasons to assume a

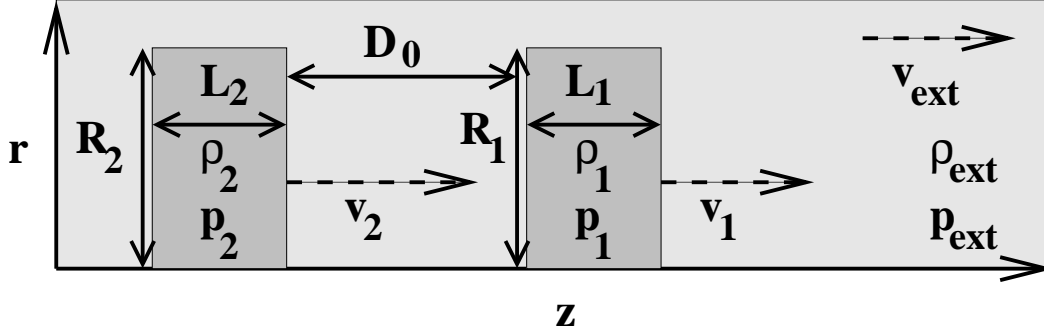


Figure 5.1: A model of a blazar jet: we assume that there exists an underlying homogeneous jet with density ρ_{ext} and pressure p_{ext} which is moving with velocity $v_{\text{ext}} = c(1 - \Gamma_{\text{ext}}^{-2})^{1/2}$ towards the observer. Two shells of density ρ_i , pressure p_i and velocity $v_i = c(1 - \Gamma_i^{-2})^{1/2} > v_{\text{ext}}$ are embedded in the underlying jet such that $v_2 > v_1$ and their initial separation is D_0 . The observer is located far to the right.

moving external medium: at parsec and kiloparsec scales AGN jets are observed as continuous channels of outflowing plasma, i.e., it is natural to assume that at subparsec scales the flow is continuous fluid, but there are density inhomogeneities (shells) of larger density embedded into the flow which move at different velocity.

If shell 2 is faster than the shell 1 (Fig. 5.1), they will collide approximately after

$$T_{\text{col}} = \frac{D_0}{v_2 - v_1} \approx 2D_0 \frac{\Gamma_1^2 \Gamma_2^2}{\Gamma_2^2 - \Gamma_1^2}, \quad (5.1)$$

where shells are assumed to be ultra-relativistic ($\Gamma_i \gg 1$). In the limit of a small relative velocity between the shells, we can write

$$T_{\text{col}} \approx D_0 \frac{\Gamma_1^3}{\Delta\Gamma}, \quad (5.2)$$

where it is assumed that $\Gamma_2 = \Gamma_1 + \Delta\Gamma$ and that $\Delta\Gamma \ll \Gamma_1$. It is important to point out that this estimate neglects any interaction of the shells with the external medium prior to the collision.

The interaction causes internal shocks which start to propagate through the shells. Non-thermal particles are accelerated at these shock fronts, and start emitting synchrotron radiation. In case of blazars we are mainly interested in the X-ray radiation in the range $10^{16} - 10^{19}$ Hz (corresponding to photon energies of 0.04 – 40 keV). With this set-up, our goal is to compute a multi-frequency light curve which is subsequently integrated in two frequency bands (soft band 0.1 – 1 keV; and hard band (2 – 10 keV) in order to compare directly with observations (of, e.g., *XMM-Newton*).

5.1.2 Numerical details of the simulations

When we model jets in 2D, they are assumed to be axisymmetric, while in the case of the 1D simulations the radial dependencies are neglected,

Δr	1.33×10^{14} cm
Δz	2×10^{12} cm
ν_{\min}	10^{16} Hz
ν_{\max}	10^{19} Hz
N_{freq}	21
γ_{\min}	1
γ_{\max}	10^8
N_{bins}	48

Table 5.1: Parameters used in the simulations: radial (Δr) and longitudinal (Δz) resolution, minimum (ν_{\min}) and maximum (ν_{\max}) frequency and number of frequencies (N_{freq}) distributed logarithmically between ν_{\min} and ν_{\max} , minimum (γ_{\min}) and maximum (γ_{\max}) Lorentz factor of the electron distribution function and the number of Lorentz factor of bins (N_{bins}).

although for the light curve computation we assume that the jet is cylindric¹. The jet axis coincides with the z -axis of the cylindrical coordinate system. In our numerical simulations we assume that the thermal fluid is made of mono-atomic hydrogen whose equation of state (EOS) corresponds to that of an ideal-gas with an adiabatic index $\gamma_{\text{ad}} = 4/3$. Table 5.1 shows the parameters used in all simulations of single flares. The energy spectrum of the electrons is covered from Lorentz factor 1 to Lorentz factor 10^8 in 48 logarithmically distributed energy bins.

In the two-dimensional simulations the radial size of the computational grid is 1.5×10^{16} cm, which is covered with 75 equidistant cells, i.e., with a spatial resolution of 1.33×10^{14} cm.

According to equation (5.1), the collision time is about two orders of magnitude larger than the light travel time across the initial separation of the shells for Lorentz factors of the order of 10. Since we need to resolve the initial separation *and* the full domain of interaction, using a uniform grid where the initial separation is resolved by about 100 zones, would imply that 10000 zones are needed to resolve the full domain of interaction *before* the time of collision. Therefore, at least two or three times as many zones are required to follow the full evolution of the collision. Performing a simulation with a phase space of $N_z \times N_r \times N_{\text{bins}} \times N_{\text{freq}} = 3.78 \times 10^9$ in each time step is not feasible with the available computational resources, so we have used a *re-mapping technique* to reduce the number of operations by two to three orders of magnitude (see also Fig. 5.2):

1. The shells are placed in a numerical grid with longitudinal boundaries at $z_{\min,0}$ and $z_{\max,0}$.
2. When the front part of the front shell reaches $z_{\max,0}$, new boundaries $z_{\min,1}$ and $z_{\max,1}$ are computed such that the back part of the back shell is located at some small distance away from $z_{\min,1}$ (Fig. 5.2) in order to avoid numerical problems due to interactions with the boundary.

¹In order to compute the observed radiation we have to assume that there is a certain emitting area. We consider that the jet is cylindric and for 1D models we further assume that for a fixed z all the points (with different radii) have the same properties.

3. The procedure is repeated when the front shell reaches $z_{\max,1}$.

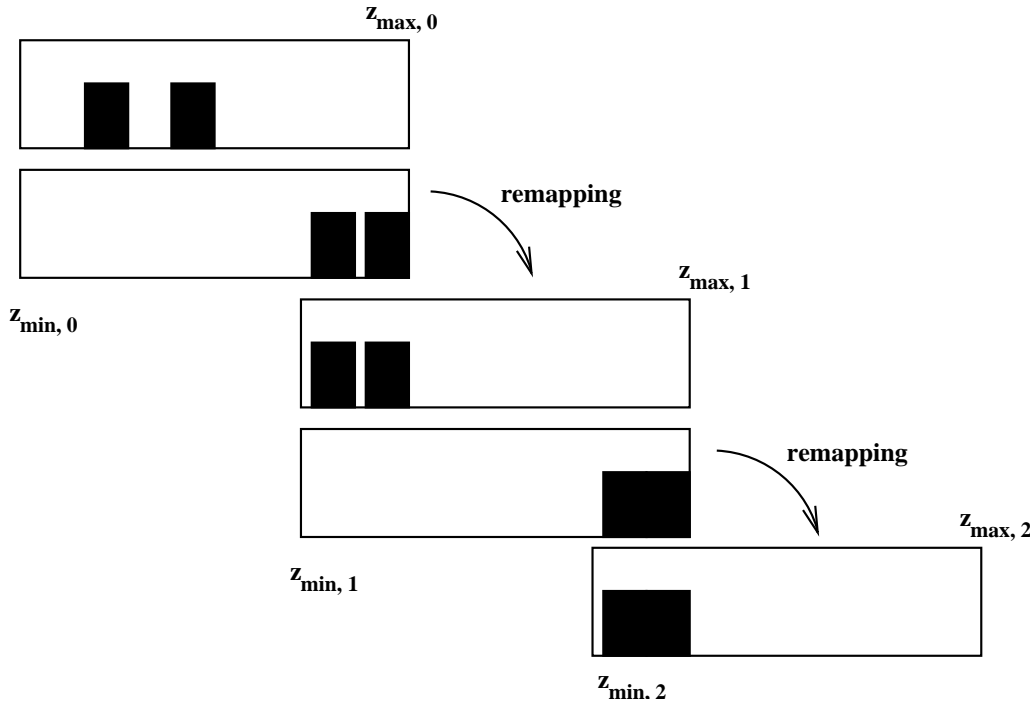


Figure 5.2: An illustration of the re-mapping procedure: the initial grid with longitudinal boundaries at $z_{\min,0}$ and $z_{\max,0}$ contains two shells which are moving to the right. When the front shell reaches $z_{\max,0}$ the boundaries are moved such that the back part of the back shell lies a little bit ahead of $z_{\min,1}$. The procedure is repeated every time the front shell reaches the end of the grid.

Due to the fact that the back shell is faster, the distance between the back part of the back shell and the front part of the front shell decreases, i.e., the whole structure becomes narrower. Hence, the distance which the front part of the front shell has to travel until the next re-mapping increases too. Consequently, the time interval between re-mappings becomes longer, making the procedure very effective until internal shocks break out of the shells, causing the interaction region to expand (see section 5.2.1), thereby decreasing the distance the shells can travel before another re-mapping is necessary.

The part of the grid which is added in front of the front shell during re-mapping is filled with the same homogeneous external medium the shells are initially embedded in. The distance from the grid to the observer decreases in each re-mapping. This effect has to be taken into account when computing light travel times.

In case of the two-dimensional simulations we used 500 cells in z direction, i.e., the numerical grid covers 10^{15} cm in longitudinal direction. The typical evolution of a shell collision lasts $\approx 1.5 \times 10^6$ s, and requires about 50 re-mappings.

In case of the one-dimensional simulations, we used 5000 cells in the z direction, and had to re-map only a few times during the whole evolution.

sim.	Γ_1	$\frac{\rho_1}{\rho_{\text{ext}}}$	$\frac{p_1}{\rho_1 c^2}$	$\frac{L_1}{10^{16} \text{cm}}$	Γ_2	$\frac{\rho_2}{\rho_{\text{ext}}}$	$\frac{p_2}{\rho_2 c^2}$	$\frac{L_2}{10^{16} \text{cm}}$
S0	3	10^4	5.56×10^{-6}	0.01	15	10^4	5.56×10^{-6}	0.01
D1	3	10^4	5.56×10^{-6}	0.01	15	10^3	5.56×10^{-6}	0.01
D2	3	10^3	5.56×10^{-6}	0.01	15	10^4	5.56×10^{-6}	0.01
P1	3	10^4	5.56×10^{-6}	0.01	15	10^4	5.56×10^{-7}	0.01
P2	3	10^4	5.56×10^{-7}	0.01	15	10^4	5.56×10^{-6}	0.01

Table 5.2: An overview of the shell properties for five two dimensional simulations. The initial distance between the shells is $D_0 = 3 \times 10^{14}$ cm and their thicknesses are L_1 and L_2 , respectively. The density, pressure and Lorentz factor of the external medium are $\rho_{\text{ext}} = 10^{-25}$ g cm $^{-3}$, $p_{\text{ext}} = 10^{-9}$ erg cm $^{-3}$ and $\Gamma_{\text{ext}} = 2.9$, respectively. The given ratio of pressure to density corresponds to a temperature 10^7 K of the external medium. The fraction of the internal energy density contained in the magnetic field is $\alpha_B = 10^{-3}$. The shock acceleration parameterization model used is type-E, with $\alpha_e = 10^{-2}$.

5.2 Two dimensional simulations

In this section the results of two dimensional simulations of colliding shells are presented. In total five simulations have been performed and their parameters are summarized in table 5.2. We use the type-E shock acceleration model in all of them. Section 5.2.1 contains a discussion of the hydrodynamic evolution of the shell interaction. In Section 5.2.2 we focus on the light curve of the prototype simulation S0. Sections 5.2.3 and 5.2.4 are concerned with the discussion of the influence of density and pressure variations in the shells on the observed light curves.

5.2.1 Hydrodynamic evolution

The hydrodynamic evolution of the shells prior to, during and after their collision has been presented by Mimica et al. (2004). The only difference between the model of Mimica et al. (2004) and the current ones is the presence of a moving background medium. The motion of the background medium does not change qualitatively the hydrodynamic evolution of the current set of models compared to the previous ones (Mimica et al. 2004). Our simulations show that the evolution of the shells can be divided into three typical stages: the evolution prior to the collision (Figs. 5.3 and 5.4, upper panels), the interaction phase (Figs. 5.3 and 5.4, lower left panels), and the post-collision evolution (Figs. 5.3 and 5.4, lower right panels).

Shells start with sharp discontinuities at their edges so that their pre-collision evolution can be predicted using an exact one-dimensional Riemann solver. In Fig. 5.5 the top two panels show the analytic evolution of the flow conditions. The leading discontinuity of each shell decays into a bow shock (for example, S1b of the leading shell) and a reverse shock (S1a and S2a) separated by a contact discontinuity (e.g., CD1R in the top right panel of Fig. 5.5). The trailing discontinuity of each shell develops into a rarefaction

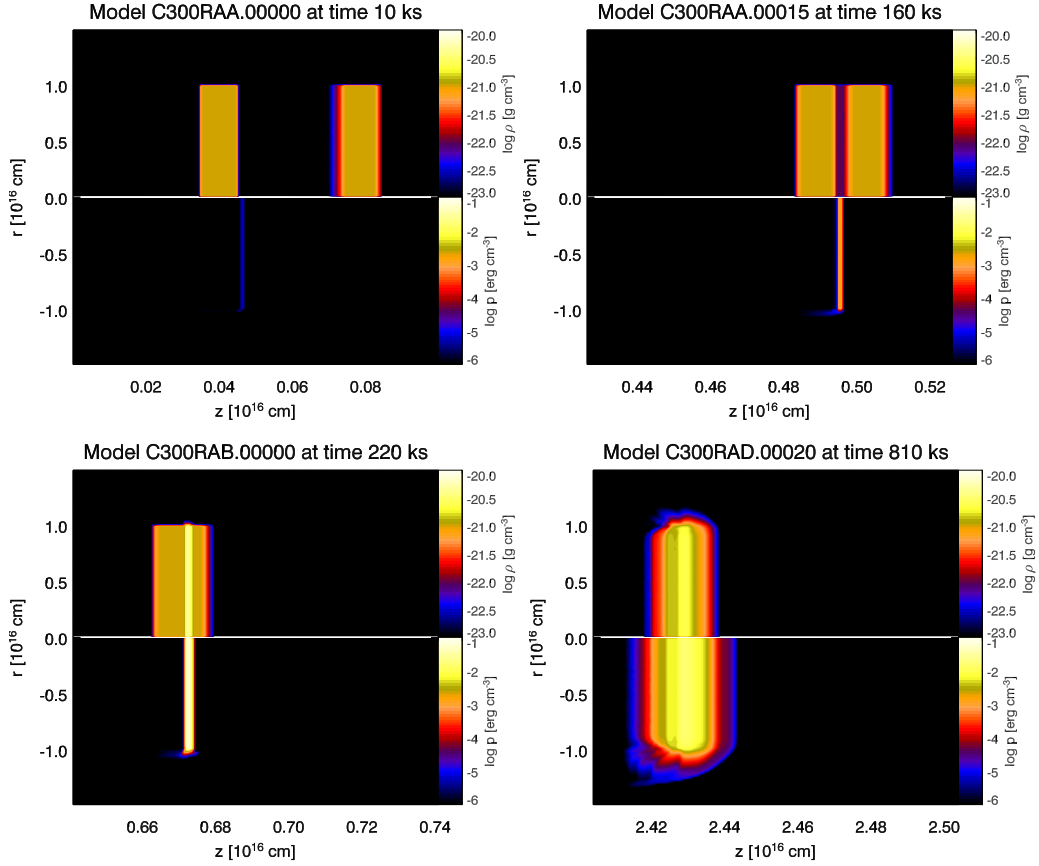


Figure 5.3: Four stages of the hydrodynamic evolution of shells collision: the pre-collision stage (upper left panel), the beginning of the collision (upper right panel), the formation of internal shocks (lower left panel) and close to the post-collision state (lower right panel). The upper half of each panel shows the logarithm of the rest-mass density, the lower half the logarithm of the pressure. For the purpose of visualization both the density and pressure have been cut-off at 10^{-23} g cm $^{-3}$ and 10^{-6} erg cm $^{-3}$, respectively.

(R1b and R2b) that connects the still unperturbed state inside the shell with a contact discontinuity separating shell matter from the external medium (CD1L in the top left panel of Fig. 5.5), and into a second rarefaction (*R1a* and *R2a*) that connects the state behind the contact discontinuity with the external medium.

The pre-collision evolution is qualitatively similar when instead of sharp discontinuities a more smooth transition between the shells and the external medium is assumed. The Riemann structure emerging from the edges of the shells will be quantitatively the same, i.e, it will consist of the same structure of shocks and rarefactions as with our set up. However, the exact values of the state variables in the intermediate states connecting the conditions in the shells with the external medium will be obviously different.

The pre-collision hydrodynamics has two direct consequences. On the one hand, each shell is heated by a reverse shock (*S1a* and *S2a*). On the other hand, both shells are spread in z direction as external medium shocked in the bow shocks (*S1b* and *S2b*) piles up in front of the shells. The latter

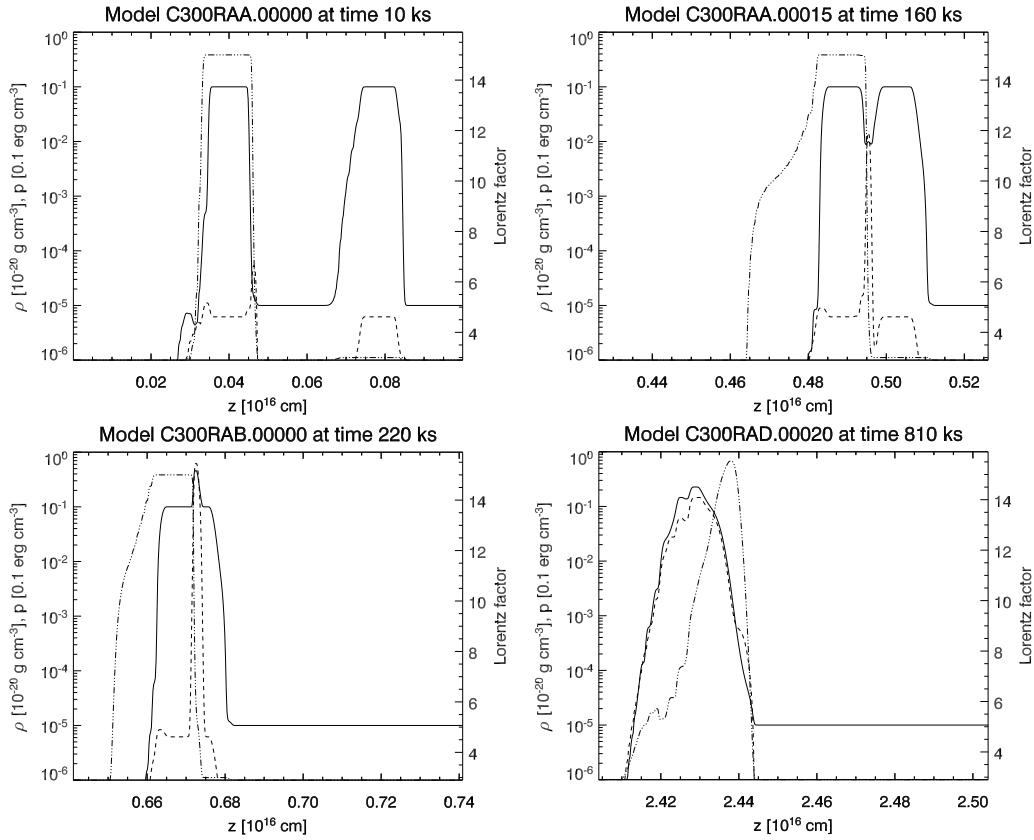


Figure 5.4: Four stages of the hydrodynamic evolution of shells collision: the pre-collision stage (upper left panel), the beginning of the collision (upper right panel), the formation of internal shocks (lower left panel) and near the post-collision state (lower right panel). Values at the jet axis of rest-mass density (full line), pressure (dashed line) and Lorentz factor of the fluid moving to the right (triple-dot-dashed line) are plotted.

effect is complicated in case of the faster trailing shell by the fact that its bow shock ($S2b$) soon starts to interact with the rarefaction ($R1a$) of the slower leading shell. Thereby the bow shock speeds up, and it eventually catches up with the slower leading shell. Our simulations show that the resulting interaction of the two shells occurs at a distance which is slightly smaller than the distance derived from an analytic estimate (see below). The accelerating bow shock $S2b$ drags along the whole Riemann structure. This explains why the state behind $S2b$ is not uniform (as in case of the slower leading shell), but shows a monotonically decreasing density and pressure distribution (Fig. 5.5). It further explains why the density behind the reverse shock of the faster shell ($S2a$) is always less than that behind the reverse shock ($S1a$) of the slower shell.

Before the bow shock $S2b$ of the faster trailing shell can enter the interior of the slower shell, it has to cross the rarefaction $R1b$, i.e., it has to propagate through a steadily increasing density. Hence, the emission produced by the shock will increase gradually during this epoch until it becomes an internal shock propagating through the slower shell (figs. 5.3 and 5.4, panels at times 160 ks and 220 ks). We point out that in analytic models (e.g., Spada

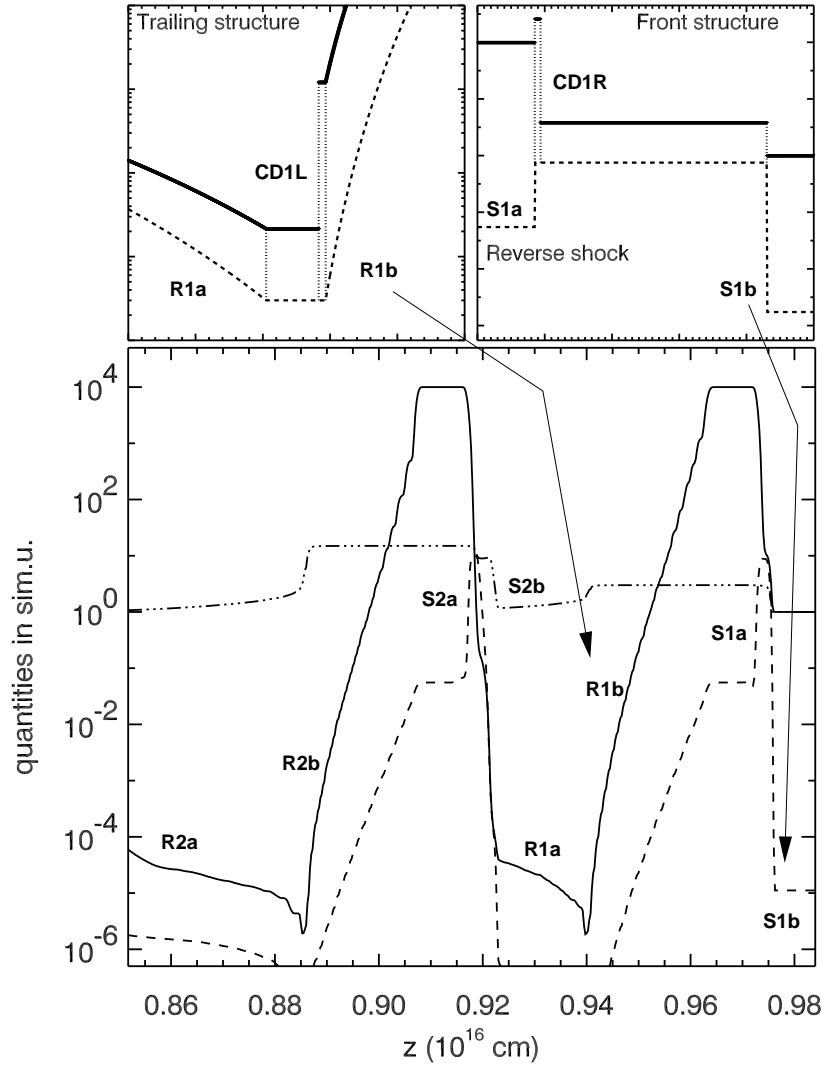


Figure 5.5: Snapshot illustrating the flow structure along the symmetry axis arising from the shell motion just before the two shells start to interact. The lower panel shows the density (solid line) and pressure (dashed line) distribution measured in units of ρ_{ext} and $\rho_{\text{ext}}c^2$, respectively. The dash-dotted line gives the Lorentz factor of the fluid which is moving towards the right. The upper left (right) panel displays the exact solution of the one dimensional Riemann problem defined by the trailing (leading) edge of the right shell. Labeled are the two bow shocks $S1b$ and $S2b$, the two reverse shocks $S1a$ and $S2a$, the four rarefactions $R1a$, $R1b$, $R2a$ and $R2b$, and (in the top panels only) the contact discontinuities $CD1L$ and $CD1R$.

et al. 2001) the internal shock does appear instantaneously when the two shells touch each other.

5.2.2 S0 light curve

The light curves and the instantaneous spectra of the prototype simulation S0 (see Tab. 5.2) are shown in Fig. 5.6. The soft (0.1-1 keV; full line

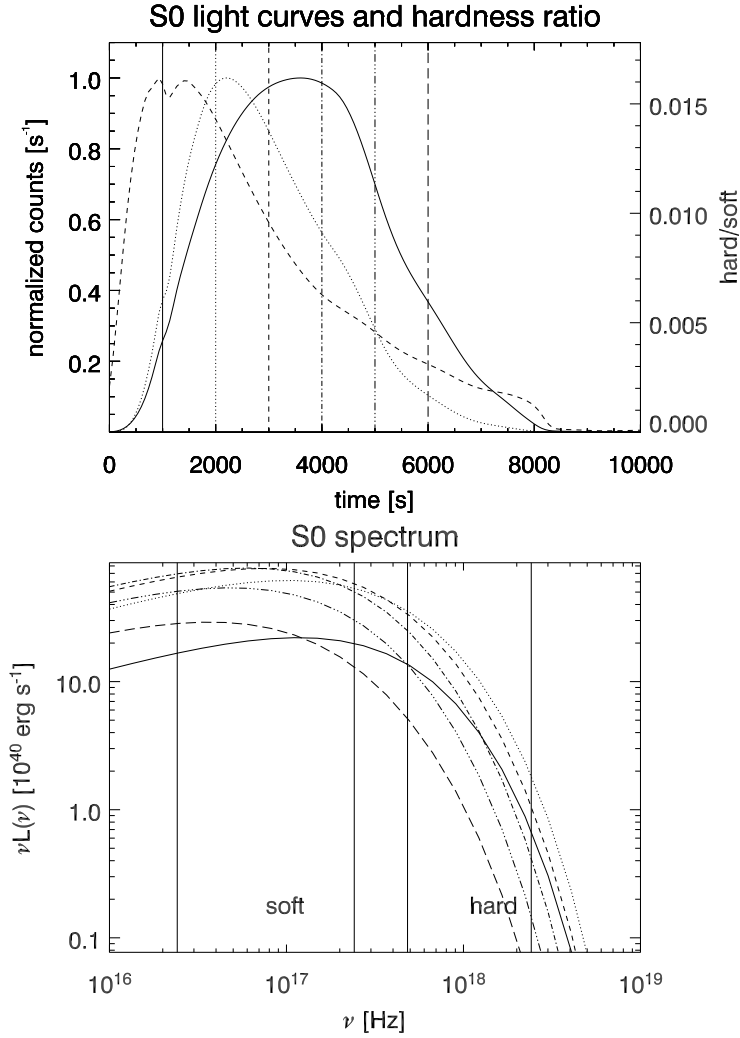


Figure 5.6: Light curves, hardness ratio (top panel) and spectra (bottom panel) resulting for model S0. The full line in the top panel is the normalized soft light curve, the dotted line is the hard light curve and the dashed line is the hardness ratio (the ratio between the number of counts per second in the soft and hard light curve). The vertical lines in the top panel mark the times at which the instantaneous spectra plotted in the bottom panel are computed. The vertical lines in the bottom panel denote the edges of the soft and hard frequency ranges. The shock acceleration and magnetic field parameters of this and all other two-dimensional models are: $\alpha_e = 0.01$, $\gamma_{\min} = 30$, $\eta = 7 \times 10^3$, $\alpha_B = 0.001$.

in the top panel) and hard (2-10 keV; dotted line) light curves have been normalized separately to their respective maxima. The dashed line gives the hardness ratio, i.e., the ratio between the number of counts per second in the hard and the soft band.

The bottom panel shows six (instantaneous) spectra corresponding to the observer times denoted by the vertical lines in the top panel. We can see that the decrease in the hardness ratio results from a shift of the spectrum towards lower frequencies with time (in the observer frame). This shift is the consequence of two effects: the cooling of the non-thermal particles which produce the observed radiation, and the decrease of the magnetic

field strength due to the decrease in pressure. The latter occurs as the internal shocks break out of the shells causing a faster cooling of the heated interaction region. In section 5.3 this effect will be discussed in more detail.

5.2.3 Influence of the density

Simulations D1 and D2 have the same parameters as S0 except that in both cases the density of one of the shells has been reduced by a factor of 10 compared to that of S0 (see Table 5.2). Figure 5.7 shows the comparison of the soft (top panel) and hard (bottom panel) light curves of S0 (full line), D1 (dotted line) and D2 (dashed line), respectively. Obviously the light curves have of D1 a more complex form, i.e., two peaks (soft) or a peak and a plateau (hard). On the other hand, the light curve of D2 shows a similar smooth structure as that of S0.

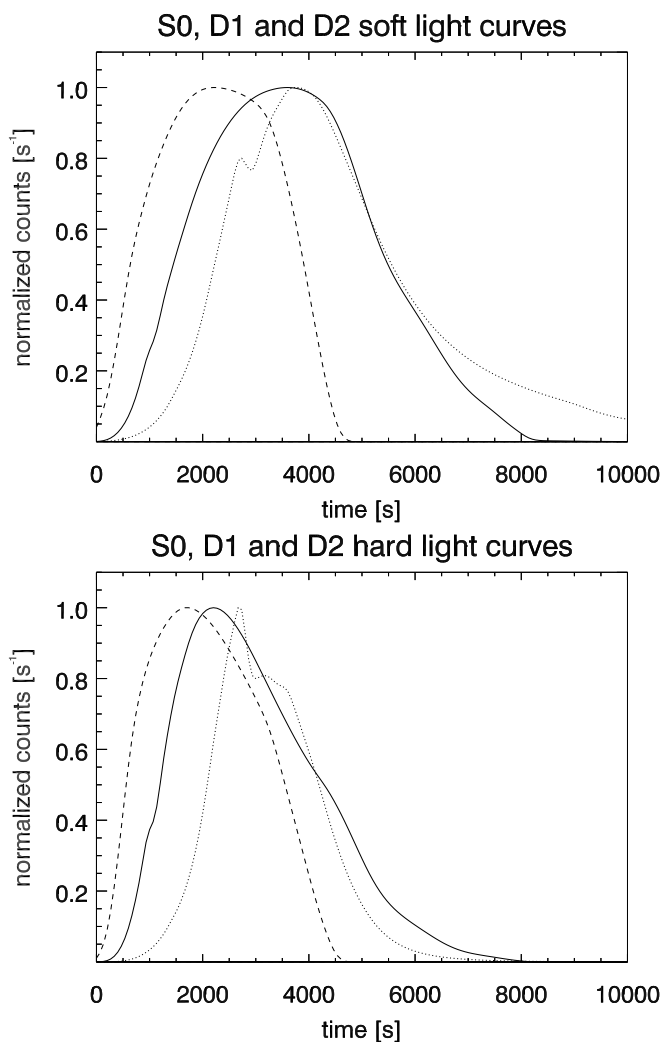


Figure 5.7: Soft (upper panel) and hard (lower panel) light curves of model S0 (full line), D1 (dotted line) and D2 (dashed line), respectively. Each light curve has been normalized separately.

Figure 5.8 shows the light curves on a logarithmic scale without any normalization, so that it is possible to compare the luminosity of the collisions. The D1 light curves are the least luminous ones, which leads to the conclusion that, all other parameters kept unchanged, the decrease of the density of the faster shell has a direct influence on the observed luminosity and the shape of the light curve. The D2 light curve is also less luminous than S0. However, in this case this is expected because since the slower shell is less dense, there are less electrons in the fluid to be accelerated, and there is less fluid to interact with, i.e., to dissipate kinetic into thermal energy.

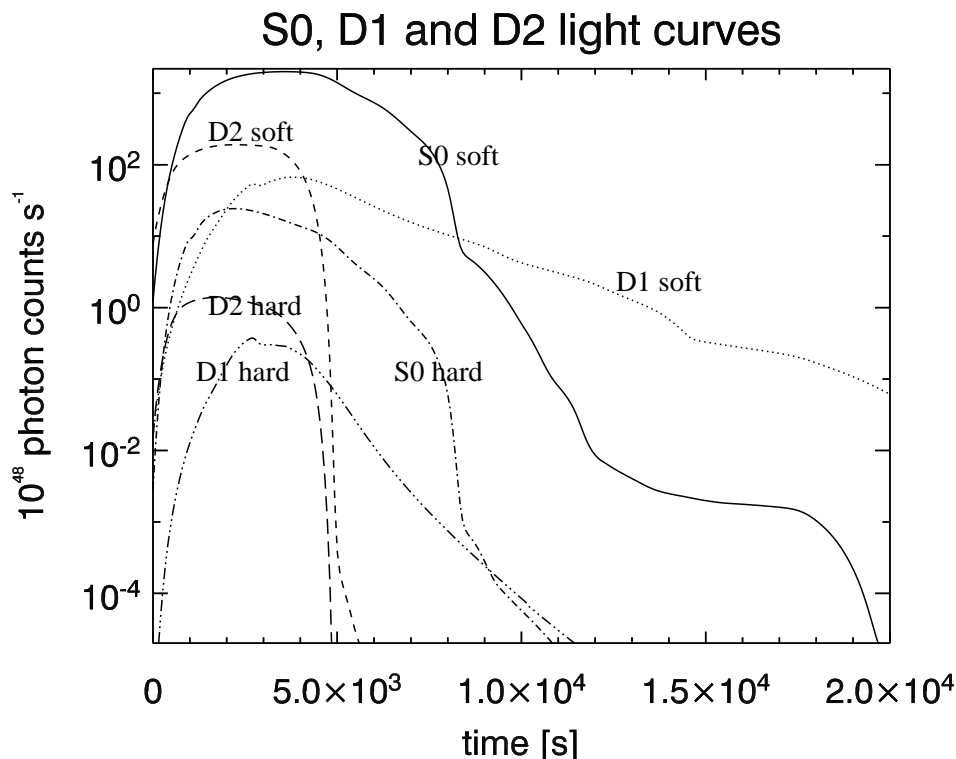


Figure 5.8: Soft and hard light curves of models S0, D1 and D2 plotted logarithmically. The photon counts are measured in the source frame, where 10^{48} photon counts per second correspond to an average luminosity of $2.88 \times 10^{21} \text{ erg s}^{-1} \text{ Hz}^{-1}$ in the soft and $4.12 \times 10^{21} \text{ erg s}^{-1} \text{ Hz}^{-1}$ in the hard band, respectively

5.2.4 Influence of the pressure

Figure 5.9 displays the results of the S0, P1 and P2 simulations. We find no significant influence on the light curve if the pressure of one of the shells is decreased 10 times. As most of the energy is initially in the form of kinetic energy (i.e., the shells are *cold*), which gets dissipated at internal shocks (see section 5.2.1), the initial value of the pressure has no large influence on the observed light curve, as long as the internal energy of the shells is much smaller than their kinetic energy.

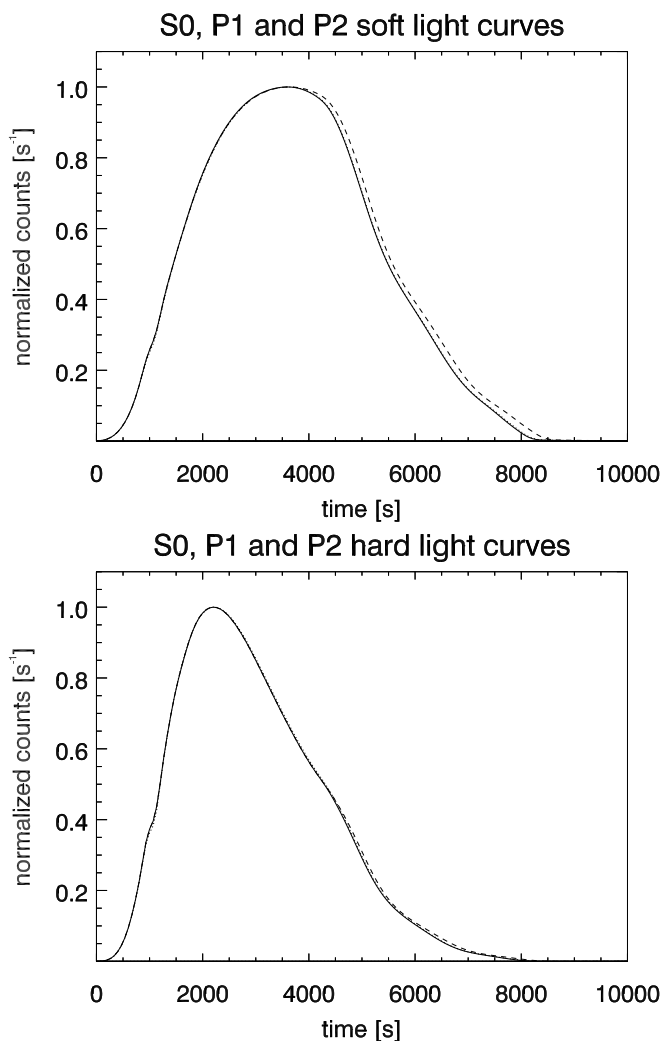


Figure 5.9: Soft (upper panel) and hard (lower panel) light curves of models S0 (full line), P1 (dotted line) and P2 (dashed line), respectively. Each light curve has been normalized separately.

5.3 One dimensional simulations

Motivated by the results of the high-resolution two dimensional simulations a larger number of one dimensional simulations has been performed, with the aim to better cover the parameter space. As we have seen in the previous section, the sideways expansion of the shells is negligible (see e.g. Fig. 5.3). Thus, a one-dimensional modeling of the interaction is well justified to discuss many qualitative features. In particular, we focus on the influence of the relative velocity and/or the length of the shells on the observed light curves. Also, due to the fact that one dimensional simulations are computationally less expensive, the number of re-mappings (see section 5.1.2) could be reduced by increasing the grid length ten times. Furthermore, both type-E and type-N models of shock acceleration were performed for each collision.

sim.	Γ_1	$\frac{L_1}{10^{16}\text{cm}}$	Γ_2	$\frac{L_2}{10^{16}\text{cm}}$
G0	3	0.01	15	0.01
G1	3	0.01	10	0.01
G2	5	0.01	15	0.01
G3	3	0.005	15	0.01
G4	3	0.01	15	0.005
G5	5	0.01	15	0.005
G6	5	0.005	15	0.01
G7	3	0.01	10	0.005
G8	3	0.005	10	0.01

Table 5.3: An overview of the shell properties (thickness L_1 and L_2 , and Lorentz factors Γ_1 and Γ_2) for nine one dimensional setups. The initial distance between the shells is $D_0 = 3 \times 10^{14}$ cm, the density of the external medium $\rho_{\text{ext}} = 10^{-25}$ g cm $^{-3}$, the pressure $p_{\text{ext}} = 10^{-9}$ erg cm $^{-3}$, and the Lorentz factor $\Gamma_{\text{ext}} = 2.9$. The density and the pressure of the shells is the same as in the case of the two dimensional simulation S0. The ratio of the energy density contained in the magnetic field and the fluid internal energy density is $\alpha_B = 10^{-3}$. The parameters of the shock acceleration models are: $\alpha_e = 10^{-2}$, $\gamma_{\text{min}} = 30$, $\eta = 7 \times 10^3$ (type-E), and $\alpha_e = 10^{-2}$, $\zeta = 5 \times 10^{-3}$, $\eta = 7 \times 10^3$ (type-N), respectively.

Table 5.3 shows the parameters of the 18 simulations performed (nine initial setups were simulated with both type-E and type-N shock acceleration models).

5.3.1 Spacetime analysis of the light curve

The radiation observed at a certain time in the observer frame is the sum of the radiation emitted at many different times from many different positions in the source frame all of which satisfy equation (4.32) for a fixed t_{obs} and an observer located at z_{obs} (see section 4.3.2). Therefore, features in the light curve might depend in a complex way on the evolution of the emissivity in time and space.

For simplicity we assume that the observer sees monochromatic radiation, so that the emissivity is only a function of z and T . The intensity observed at time t is, using (4.33),

$$I(t) = \int dz j \left(z, t + \frac{z_{\text{obs}} - z}{c} \right), \quad (5.3)$$

where $j(z, T)$ is assumed to be transformed into the observer frame using (4.31).

A significant simplification of the spacetime representation can be achieved by changing from the (z, T) coordinate system into the (x, y) coordinate

system (“observer-xy frame”², see Fig. 5.10), where

$$x \equiv \frac{-z + cT}{\sqrt{2}}, \quad (5.4)$$

$$y \equiv \frac{z + cT}{\sqrt{2}}. \quad (5.5)$$

The analysis in the observer-xy frame makes it possible to view simultaneously the light curve and the temporal and spatial evolution of the emissivity giving rise to the light curve, as we shall see in the following sections. The relation between x and t_{obs} is, using (4.32) and (5.4),

$$t_{\text{obs}}(z, T) = \frac{z_{\text{obs}} + \sqrt{2}x}{c}. \quad (5.6)$$

So we see that in the observer-xy frame the radiation emitted from lines of constant x arrives to the observer at the same t_{obs} . This means that the observed intensity at a time t is simply the emissivity $j_x(x, y)$ integrated along the y axis,

$$I(t) = \int dy j_x \left(\frac{t - z_{\text{obs}}/c}{\sqrt{2}}, y \right). \quad (5.7)$$

It is easy to verify that the integration in (5.3) is along the line

$$T = t - \frac{z_{\text{obs}}}{c} + \frac{z}{c},$$

which is, upon substituting (5.4) equal to integration along the line in observer-xy frame

$$x = \frac{ct - z_{\text{obs}}}{\sqrt{2}},$$

thus confirming that the integrals (5.3) and (5.7) are identical provided that

$$j_x(x, y) = j \left(\frac{-z + cT}{\sqrt{2}}, \frac{z + cT}{\sqrt{2}} \right). \quad (5.8)$$

If a particle is moving with a velocity βc towards the observer, its trajectory in the observer-xy frame is given by

$$y = x \frac{1 + \beta}{1 - \beta} \approx 4\Gamma^2 x, \quad (5.9)$$

where it was assumed that the particle starts from $z = 0$ at $T = 0$. The second expression is valid for ultra-relativistic particles. Figure 5.10 shows the trajectories of three different particles as seen in the laboratory and the observer-xy frame. From (5.9) we see that a particle at rest moves along the line $y = x$ (if it was located at $z = 0$ for $T = 0$). In the observer-xy frame the light propagates along lines $x = \text{const}$ (note that (5.9) is not valid for light since $\beta = 1$).

²We have chosen the name “observer-xy frame” instead of just “(x, y) frame” in order to make it clear that the particular choice of axes simplifies the computation of the observed light curve from the spacetime distribution of the emissivity.

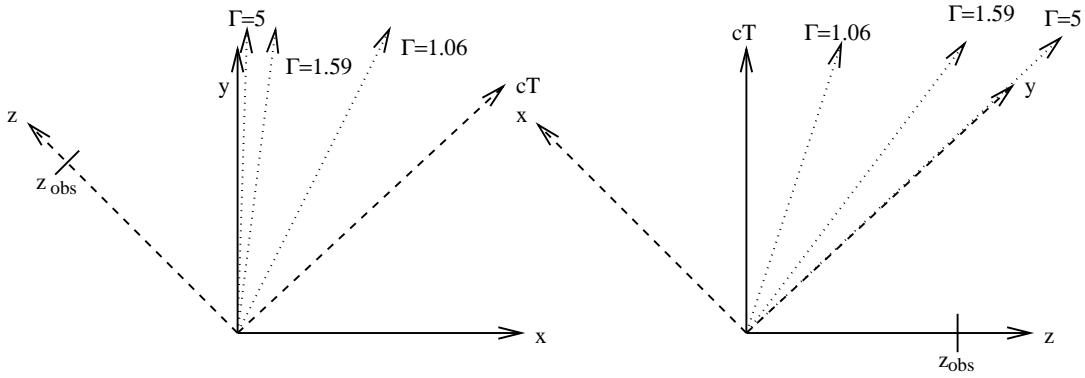


Figure 5.10: The relation between the (z, T) and the observer- xy coordinate systems. Also shown are the trajectories of three particles moving with different Lorentz factors towards the observer located at z_{obs} . The light emitted by the particles moves along trajectories parallel to the y axis.

5.3.2 Light curves of one-dimensional models

In this section we present the results of simulations with emission models type-E and type-N. We use the following naming convention: GiE and GiN denote model Gi ($i = 0, \dots, 8$) with a shock acceleration model type-E and type-N, respectively. All 18 models can be divided into three groups according to the Lorentz factors of the two shells. The prototypes of each group are the models $G0$ ($\Gamma_1 = 3$, $\Gamma_2 = 15$), $G1$ ($\Gamma_1 = 3$, $\Gamma_2 = 10$), and $G2$ ($\Gamma_1 = 5$, $\Gamma_2 = 15$). In these simulations both shells have the same width. In the remaining 6 models either the slower or the faster shell has a width two times smaller than that of the other shell. Figure 5.11 shows soft and hard light curves for these models, each light curve normalized to its maximum value to better see the influence of the Lorentz factors of the shells on the shape of the light curve (the influence of the Lorentz factors on the energetics of the light curve, and its normalization, is discussed later).

As can be seen for both soft and hard light curves, the width of the peaks generally decreases as the Lorentz factors of the shells increase. This is due to fact that when the Lorentz factor of the faster shell increases, the duration of the flare in the observer frame decreases, since the shell is moving closer to the speed of light (see section 5.3.3). The hard light curve has a shorter tail than the soft light curve, which is due to the decrease of the magnetic field in the post-collision phase, causing the synchrotron radiation spectral peak to shift to lower frequencies. The differences between type-E and type-N light curves can be attributed to the different behavior of the type-E and type-N shock acceleration models (see section 4.2.3.3). In general, the duration of flares of the type-N seems to be slightly smaller than that of type-E acceleration model. In Fig. 5.11 we also see that the initiation of the flare is delayed as the relative velocity $v_2 - v_1$ between the shells decreases, because the time of collision (5.1) increases as $v_2 - v_1$ decreases. Finally, we note the presence of a double peak or a non-smooth feature in the light curve of models $G1E$ and $G1N$ whose nature will be discussed later in the context of our analytic model (section 5.4).

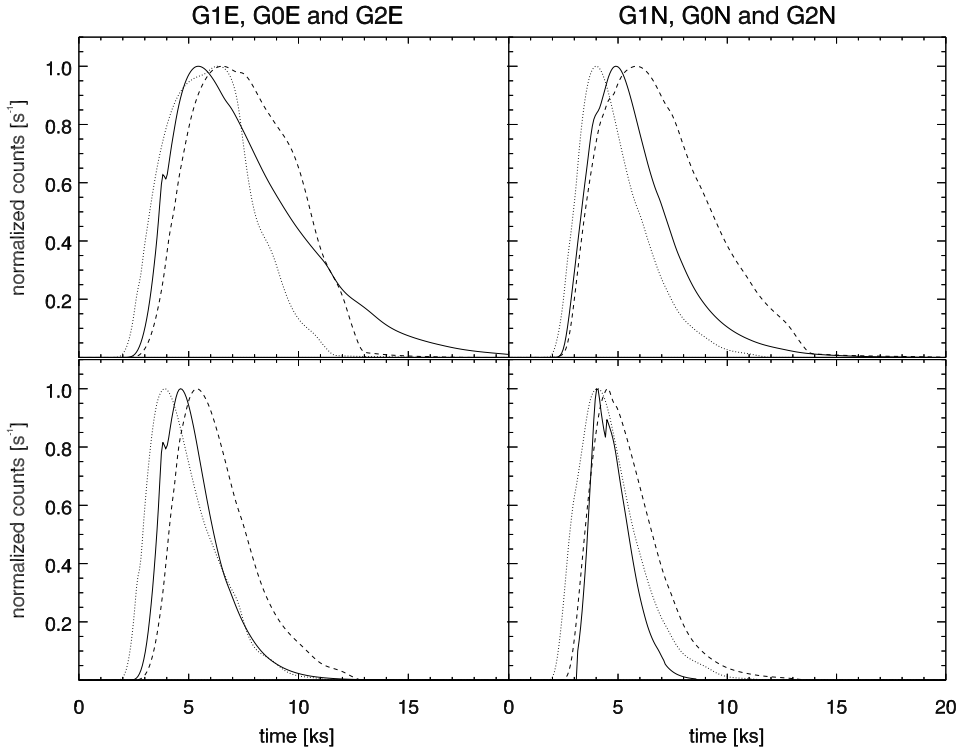


Figure 5.11: Soft (upper panels) and hard (lower panels) light curves of models $G1$ (full line), $G0$ (dotted line) and $G2$ (dashed line), each normalized separately. The models of type-E and type-N are shown on the left and right panels, respectively.

Figure 5.12 shows the light curves of the models $G8$, $G3$ and $G6$, where the width of the slower shell has been halved. Qualitatively the light curves have the same properties as the one displayed in Fig. 5.11, except that they are, in general, slightly shorter. This is easily understood since the duration of the light curve is determined by the time it takes the reverse shock to cross the faster shell (whose size was not changed with respect to that of the models $G1$, $G0$ and $G2$).

Figure 5.13 shows the light curves of models $G7$, $G4$ and $G5$, where the width of the faster shell has been halved and different combinations of Lorentz factors have been tested (Table 5.3). Obviously, the light curves are qualitatively different from those in Fig. 5.11, displaying a more complex shape with double-peaked structures in both soft and hard band. The peak luminosities are also shifted with respect to the counterpart models in Fig. 5.11.

In order to illustrate the differences when the width of the faster shell is decreased, but the relative velocity between the shells is kept constant, we plot the light curves of models $G1$, $G8$ and $G7$ in Fig. 5.14. In all three cases the shells have the same respective Lorentz factors. In case of $G8$ the width of slower shell has been halved, while in case of $G7$ the width of the faster shell has been halved. As we can clearly see, the light curve shape depends strongly on the width of faster shell, while it shows almost no dependence on the width of the slower shell.

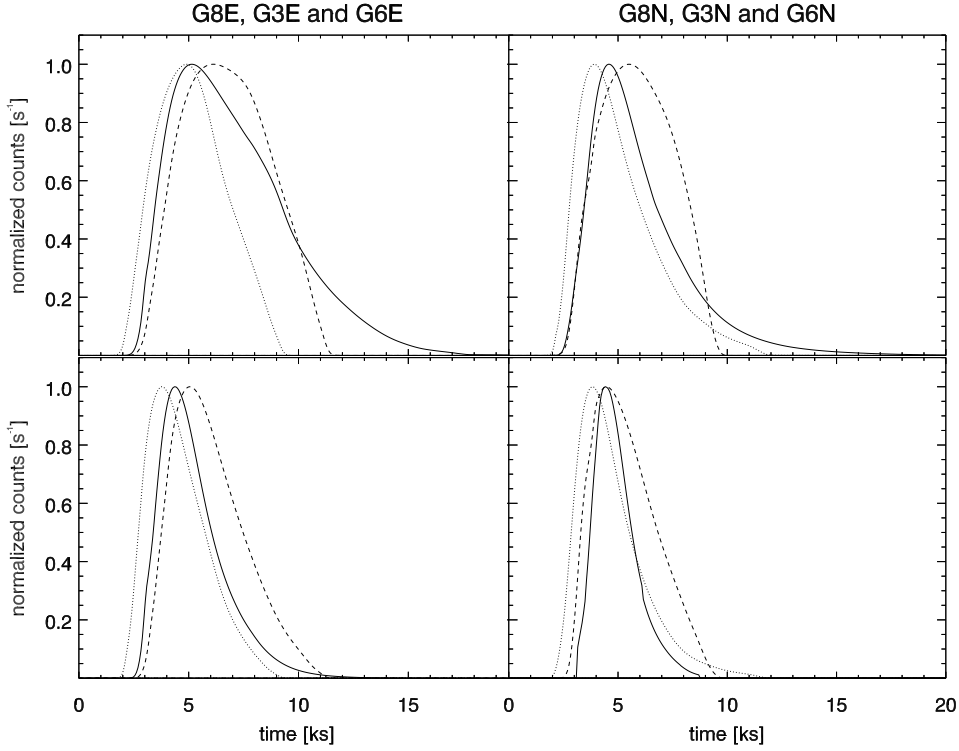


Figure 5.12: Same as Fig. 5.11, but for models *G8* (full line), *G3* (dotted line) and *G6* (dashed line), respectively.

Another important aspect to be considered is the energetics of the flares. What is particularly interesting is the fraction of the initial kinetic energy which is converted into radiation. To this end we define the following quantities:

1. the total initial rest mass of the shells

$$M = (L_1 + L_2)R_{\text{sh}}^2\pi\rho_{\text{sh}}, \quad (5.10)$$

2. the total mass of the shells

$$\mathcal{M} = \int_V d\mathbf{x} \rho(\mathbf{x})\Gamma(\mathbf{x}), \quad (5.11)$$

where Γ is the fluid Lorentz factor and the volume integration is performed in the laboratory frame over both shells,

3. the kinetic energy

$$E^K = \int d\mathbf{x} \rho(\mathbf{x})\Gamma(\mathbf{x})[\Gamma(\mathbf{x}) - 1]c^2, \quad (5.12)$$

4. the internal (thermal) energy

$$E^T = \int d\mathbf{x} \frac{p(\mathbf{x})}{\gamma_{\text{ad}} - 1} [\gamma_{\text{ad}}(\Gamma(\mathbf{x})^2 - 1) - 1], \quad (5.13)$$

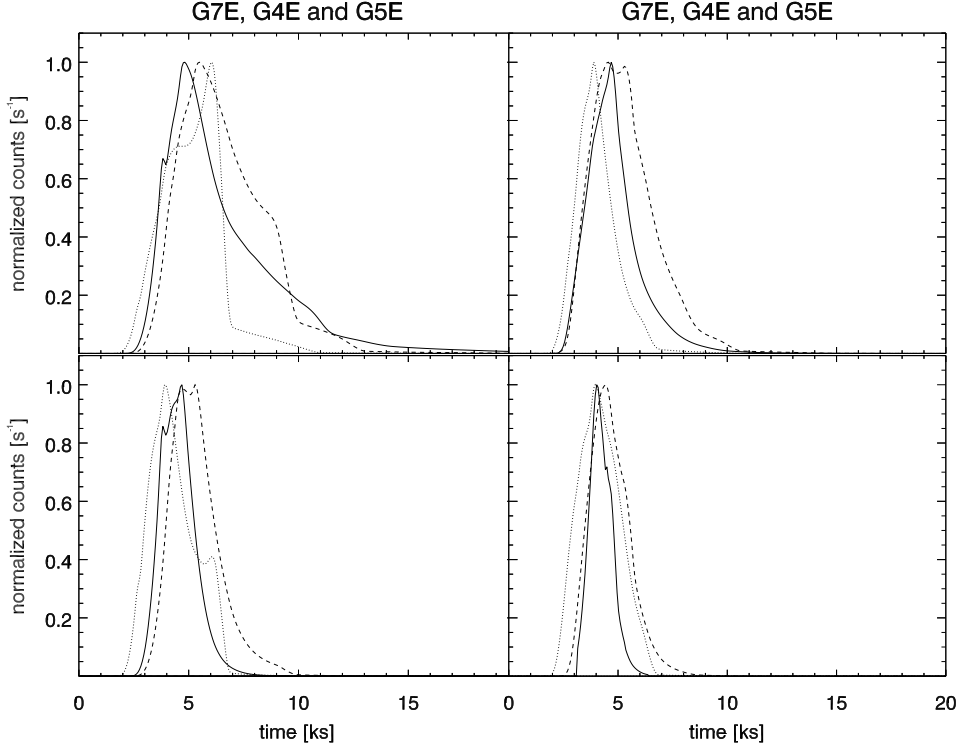


Figure 5.13: Same as Fig. 5.11, but for models *G7* (full line), *G4* (dotted line) and *G6* (dashed line), respectively.

where p and γ_{ad} are the pressure of the shell fluid and the adiabatic index, respectively,

5. the theoretical efficiency, ϵ^{KPS} , of conversion of kinetic into thermal energy computed by Kobayashi et al. (1997)

$$\epsilon^{\text{KPS}} \approx 1 - \frac{\mathcal{M}_1 + \mathcal{M}_2}{\sqrt{\mathcal{M}_1^2 + \mathcal{M}_2^2 + \mathcal{M}_1 \mathcal{M}_2 \left(\frac{\Gamma_1}{\Gamma_2} + \frac{\Gamma_2}{\Gamma_1} \right)}}, \quad (5.14)$$

where \mathcal{M}_i and Γ_i are the initial masses and the Lorentz factors of the shells,

6. the total radiated energy $E_{\text{total}}^{\text{E}}$ and $E_{\text{total}}^{\text{N}}$ in the observer frame for type-E and type-N models, respectively, computed by integrating each light curve in time over the full frequency range 10^{16} - 10^{19} Hz.

The shell radius has to be assumed in the 1D simulations since only the z -dependence of the variables is considered. We take a shell radius of 10^{16} cm.

Table 5.4 shows the abovementioned quantities for each model. The final values have been computed at the time when the reverse shock has completely passed through the faster shell. Comparison of ϵ^{KPS} with the fraction of initial kinetic energy converted into thermal energy (sixth row

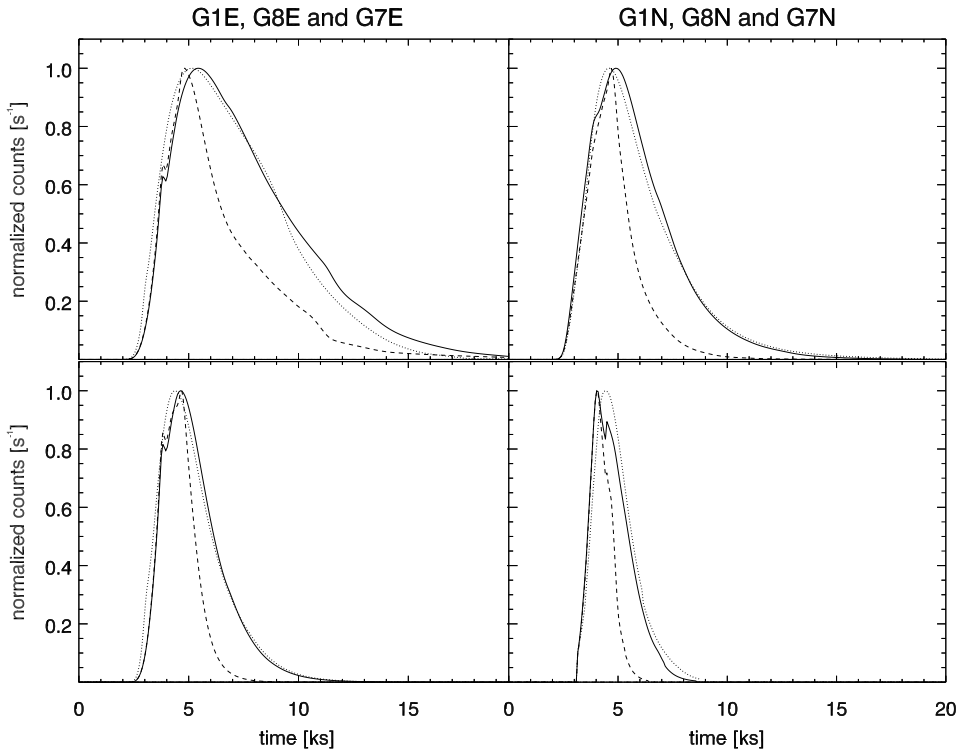


Figure 5.14: Same as Fig. 5.11, but for models $G1$ (full line), $G8$ (dotted line) and $G7$ (dashed line), respectively.

of table 5.4) shows a good agreement with the models (the maximum relative difference being $\approx 40\%$ for model $G1$). The discrepancy between the model of Kobayashi et al. (1997) and the results of our simulations is due to their assumption that the interaction of two shells produces instantly a merged shell, while in reality the internal shocks need some time to propagate through the shells. Furthermore, for the shells with comparable thickness, the time it takes for the forward shock to propagate through the slower shell is smaller than the time it takes the reverse shock to cross the faster shell.

A closer examination of the final thermal energy (row eight in Table 5.4) of the models reveals that the *absolute* final thermal energy is almost the same for the pairs of models with the same total initial rest-mass of the shells like, e.g., ($G3$, $G4$) and ($G7$, $G8$). This suggests that the collision of two shells with the same initial rest mass does not depend on the geometrical distribution of the mass, i.e., it does not matter whether we make one or the other shell smaller. The total kinetic energy dissipated into thermal energy will be very similar provided the initial rest mass is the same.

As can be seen from Table 5.4, models of type-E produce much more radiation than type-N acceleration schemes. This is due to the fact that in type-N models the number of electrons is fixed by the density of the fluid, while in the type-E models the number of electrons is larger for larger dissipation (proportional to the temporal change of pressure), regardless of

sim.	$G0$	$G1$	$G2$	$G3$	$G4$	$G5$	$G6$	$G7$	$G8$
$\frac{M}{10^{25}\text{g}}$	6.28	6.28	6.28	4.71	4.71	4.71	4.71	4.71	4.71
$\frac{\mathcal{M}}{10^{26}\text{g}}$	5.65	4.08	6.28	5.18	3.30	3.93	5.5	2.51	3.61
$\frac{E_{\text{ini}}^{\text{K}}}{10^{48}\text{erg}}$	6.09	2.71	6.49	6.01	3.13	3.53	6.21	1.44	2.65
$\frac{E_{\text{fin}}^{\text{K}}}{E_{\text{ini}}^{\text{K}}}$	0.77	0.83	0.85	0.85	0.7	0.86	0.90	0.78	0.87
$\frac{10^5 E_{\text{ini}}^{\text{T}}}{E_{\text{ini}}^{\text{K}}}$	3.21	3.06	3.16	3.18	3.93	3.82	3.19	3.63	3.06
$\frac{E_{\text{fin}}^{\text{T}}}{E_{\text{ini}}^{\text{K}}}$	0.23	0.17	0.15	0.15	0.3	0.14	0.09	0.21	0.12
ϵ_{KPS}	0.17	0.12	0.11	0.12	0.32	0.23	0.08	0.25	0.09
$\frac{E_{\text{fin}}^{\text{T}}}{10^{47}\text{erg}}$	14.01	4.56	9.45	9.30	9.36	4.68	5.59	3.05	3.07
$\frac{10^3 E_{\text{total}}^{\text{E}}}{E_{\text{ini}}^{\text{K}}}$	1.08	0.22	1.62	0.45	3.81	1.63	0.62	0.25	0.11
$\frac{10^6 E_{\text{total}}^{\text{N}}}{E_{\text{ini}}^{\text{K}}}$	5.80	0.03	0.92	6.06	7.23	1.34	0.66	0.04	0.04

Table 5.4: Characteristic quantities of the simulations: total initial rest mass of the shells M , conserved total mass of the shells \mathcal{M} , initial and final kinetic energy $E_{\text{ini}}^{\text{K}}$ and $E_{\text{fin}}^{\text{K}}$, initial and final thermal energy $E_{\text{ini}}^{\text{T}}$ and $E_{\text{fin}}^{\text{T}}$, total radiation emitted by the type-E and type-N models $E_{\text{total}}^{\text{E}}$ and $E_{\text{total}}^{\text{N}}$.

the fluid density. Since the relative change of the density in the region of interaction is larger, more electrons are accelerated in the type-E model. This is because the parameter ζ of type-N model was chosen such that the spectral maximum of the emitted radiation roughly (to an order of magnitude) corresponds to the spectral maximum of the type-E model.

The radiative efficiency of the models (last two rows in Table 5.4) seems to have a more complex relation to the dissipated kinetic energy than the simple proportionality often assumed in analytic models (i.e., Kobayashi et al. (1997), Spada et al. (2001)). On the one hand, it is the time evolution of the energy dissipation and the magnetic field which determine the total amount of emitted radiation and not just the final state of the interaction as is in analytic models. Type-N models are especially affected by this since their electron energy distribution strongly depends on the dissipation rate. On the other hand, what we have computed is the radiation in the observer frame, which is affected by relativistic effects, i.e., the emissivity of a fluid element is boosted by the square of the Doppler factor $\delta = [\Gamma(1 - \beta)]^{-1}$.

Hence, it is difficult to disentangle the emission properties which are due to the interaction of the shells alone and those that are simply the product of the relativistic velocities at which the shells propagate. In section 5.4 we will discuss an analytic model which provides some insight into the influence of the fluid properties on the observed light curve.

5.3.3 Spacetime evolution of the emissivity

Figures 5.15, 5.16 and 5.17 show the combined plots of the total light curves and the emissivity in the observer-xy frame. These plots are particularly useful in determining where each part of the light curve originates from (from which time and position), since, as shown in section 5.3.1, one simply needs to integrate the emissivity along the y (or $z + cT$) axis for fixed x (or t_{obs}) to obtain the observed radiation at chosen time instant in the observer frame.

The shape of the colored regions in figures 5.15, 5.16 and 5.17 is determined by the physical region where most of the radiation is produced, i.e., between the forward and the reverse shocks which originate when shells collide. More precisely, the bottom(top) edge of the colored region is determined by the world line of the reverse (forward) shock.

As we discussed in section 5.3.1 (Eq. [5.9]) and as is shown in Fig. 5.10, the slope of the particle trajectory in the observer-xy frame is proportional to the square of its Lorentz factor. Figures 5.16, 5.15 and 5.17 show that the duration of the flare decreases as the Lorentz factors of the shells increase.

Whether the light curve will display more than one peak or not depends on the distribution of the emissivity in the observer-xy frame. As we will see in section 5.4, it is possible to develop a simple model which connects the parameters of the interacting shells with the observed light curve and the distribution of emissivity which is able to account for the shape and duration of the observed light curves. Such a model allows us to deduce a number of physical parameters from observed light curves, whereas it is impossible to invert the one dimensional light curve to obtain the two dimensional spacetime distribution of the emissivity.

5.3.4 Spectral evolution

Figures 5.18, 5.19 and 5.20 show the spectral evolution of the observed light curves. The color coded contour plots show the logarithm of the light curve, i.e., the luminosity in the observer frame seen at 21 frequencies logarithmically spaced between 10^{16} and 10^{19} Hz for different observation times. The horizontal lines denote the frequency limits of the two light curve integration bands: S (soft from 0.1 to 1keV) and H (hard from 2 to 10keV). The overplotted black line shows the temporal evolution of the spectral maximum.

The observed duration of type-N flares is in general shorter than that of

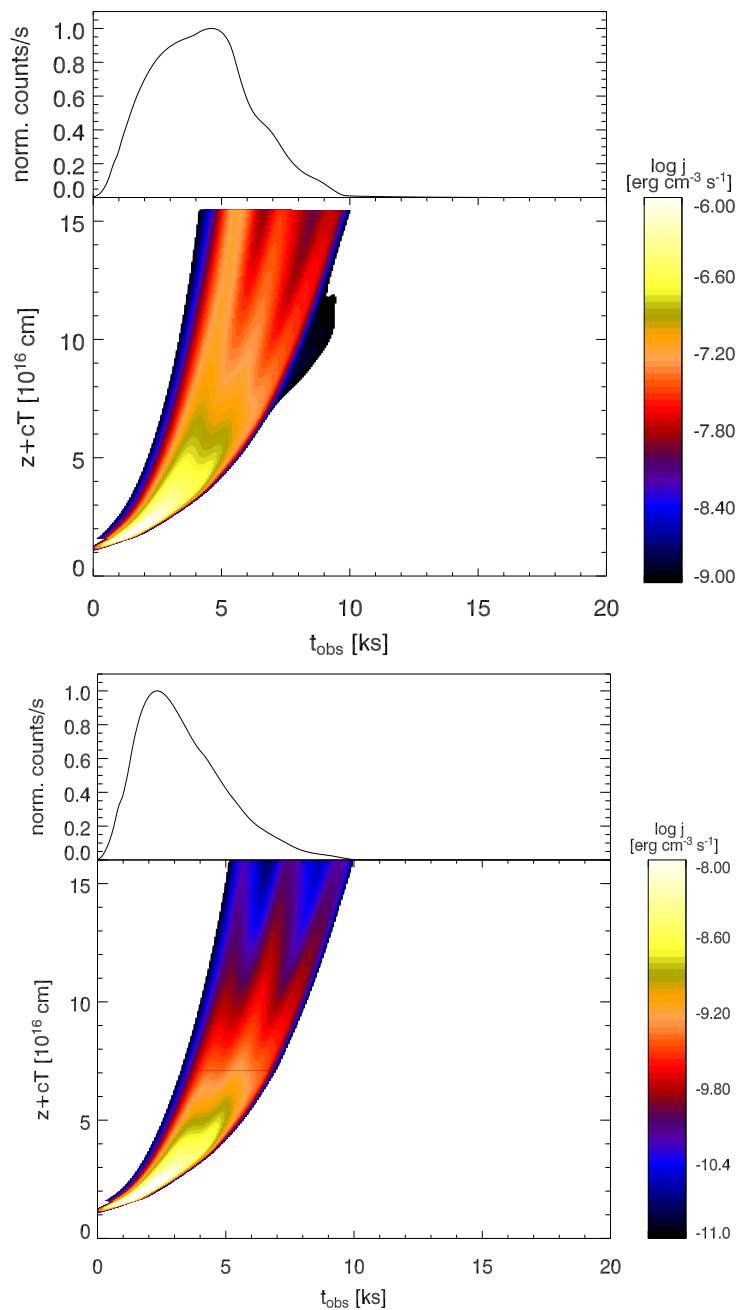


Figure 5.15: Light curves (top) and observer-xy plots (bottom) of models emissivity for the G0E (upper panel) and G0N (lower panel), respectively. Both light curves and the emissivity have been integrated in the frequency band $10^{16} - 10^{19}$ Hz. z is the distance along the jet axis and T is the time measured in the laboratory frame. t_{obs} is the time measured by the observer.

type-E models. This is because the spectral maximum of type-N models is generally a bit lower than in type-E models, so that the radiation is “lost” from the observational bands (soft and hard). The exception are models *G2N* (Fig. 5.18), *G5N* (Fig. 5.19) and *G6N* (Fig. 5.20) where the spectral

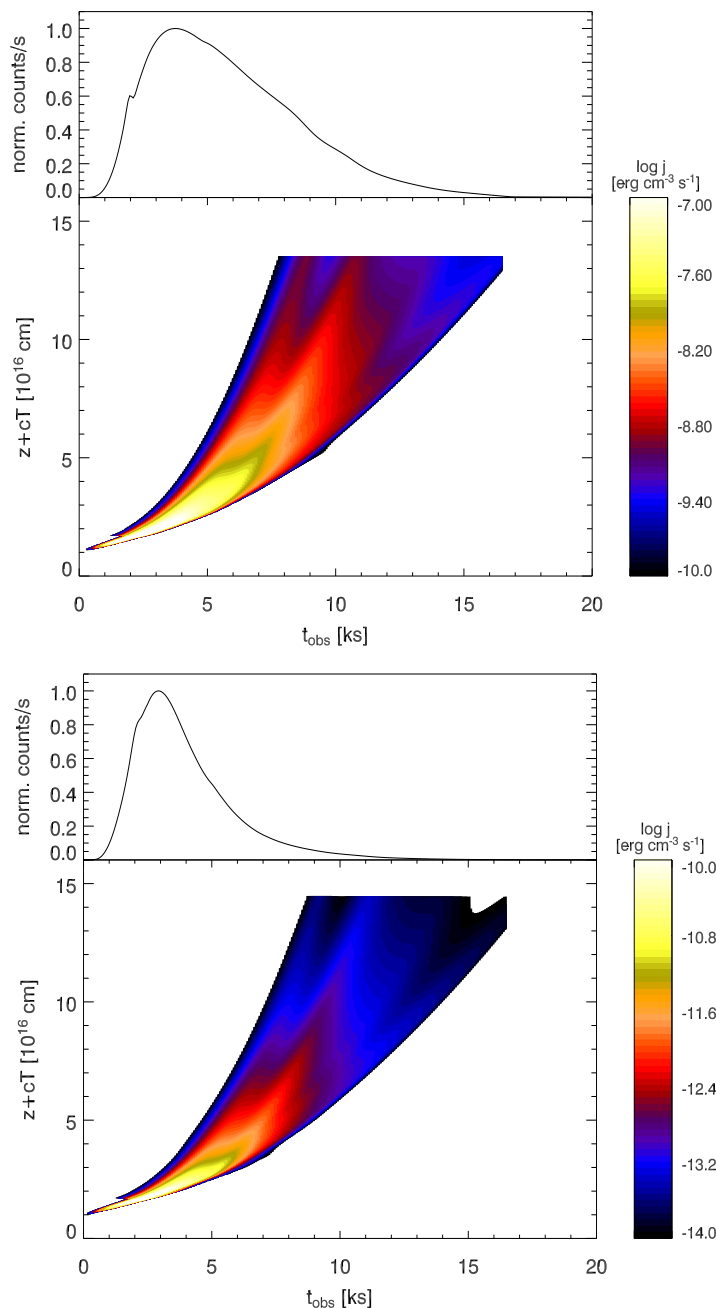


Figure 5.16: Same as Fig. 5.15, but for models *G1E* and *G1N*, respectively.

evolution has a similar behavior as in their type-E counterparts. These models have in common the Lorentz factors of the shells ($\Gamma_1 = 5$, $\Gamma_2 = 15$).

Models *G0N*, *G3N* and *G4N* ($\Gamma_1 = 3$, $\Gamma_2 = 15$) are the most luminous, although their spectral maxima always lie below 10^{16} Hz.

This can be explained by the property of the type-N model of accelerating only a fixed number of electrons (proportional to fluid density). Since the relative velocity between the shells in models *G0N*, *G3N* and *G4N* is higher than in *G2N*, *G5N* and *G6N*, there is more dissipation and, conse-

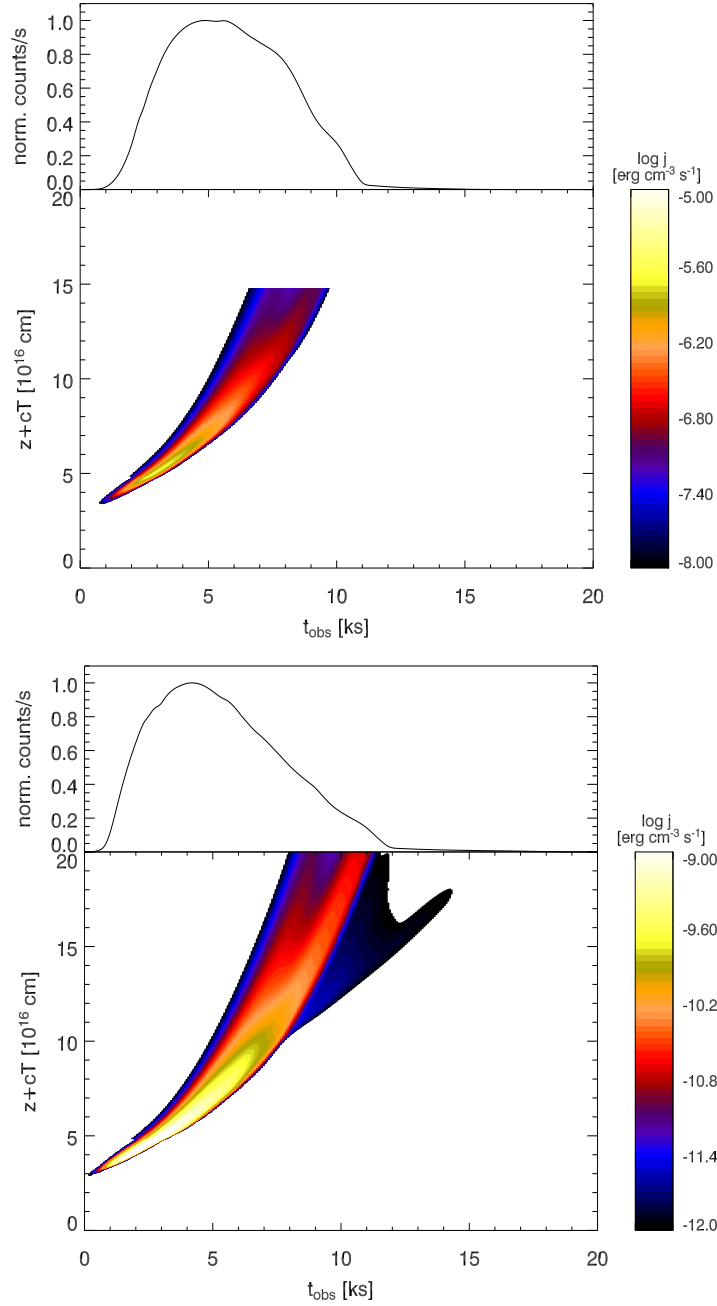


Figure 5.17: Same as Fig. 5.15, but for models *G2E* and *G2N*, respectively.

quently, electrons are being accelerated for longer time, i.e., the net effect is that more electrons have been accelerated than in the other three models. However, the Lorentz factor of the fluid in the region of interaction is higher in case of *G2N*, *G5N* and *G6N*, so that the radiation is more Doppler blueshifted than in the case of *G0N*, *G3N* and *G4N*. A rough estimate can be done by comparing the effective Doppler factors $\delta = [\Gamma_{\text{eff}}(1 - \beta_{\text{eff}})]^{-1}$ (where $\Gamma_{\text{eff}} = \sqrt{\Gamma_1 \Gamma_2}$) in both cases: $\delta = 13$ (for *G0N*, *G3N* and *G4N*) and $\delta = 17$ (for *G2N*, *G5N* and *G6N*). The frequency of the emitted radiation

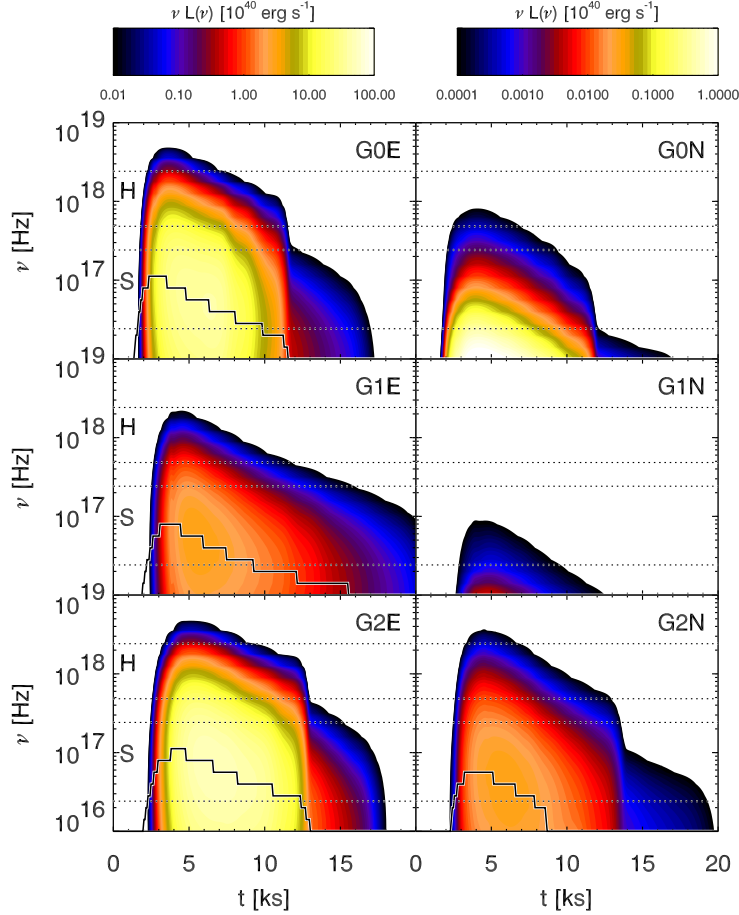


Figure 5.18: Spectral evolution of the light curves of models G0, G1 and G2, respectively. A color-coded contour plot of the logarithm of $\nu L(\nu, t)$ (where $L(\nu, t)$ is the luminosity in the observer frame, at a frequency ν at a time t) is shown. Four horizontal lines denote the two light curve integration bands, S (soft from 0.1 to 1keV) and H (hard from 2 to 10 keV). The overplotted black line shows the frequency of spectral maximum for a given time of observations. In case of models G0N and G1N the maximum in the frequency band under consideration has a frequency of 10^{16} Hz at all times. The line exhibits sharp jumps which are due to the finite number of frequency bins used in a simulation.

is being shifted by at least this factor (and probably by a larger factor since the region of interaction has a larger Lorentz factor than the slower shell), so that the ratio of the frequency maxima between models $G2N$, $G5N$, $G6N$ and $G0N$, $G3N$ and $G4N$ is > 1.3 , consistent with what is seen of Figs. 5.18, 5.19 and 5.20. For similar reasons the light curves of $G1N$, $G7N$ and $G8N$ are very weak in the frequency band 10^{16} - 10^{19} Hz.

Looking at the light curves of type-E models, we can see that the rise of the spectral maximum seems to be well correlated with the rise of the observed intensity. This is not surprising since, in type-E models, the increase of dissipation means that the number of electrons injected increases. Since their energy distribution has always the same limits, the frequency of the spectral maximum rises as the pressure (and thus magnetic field) rises in

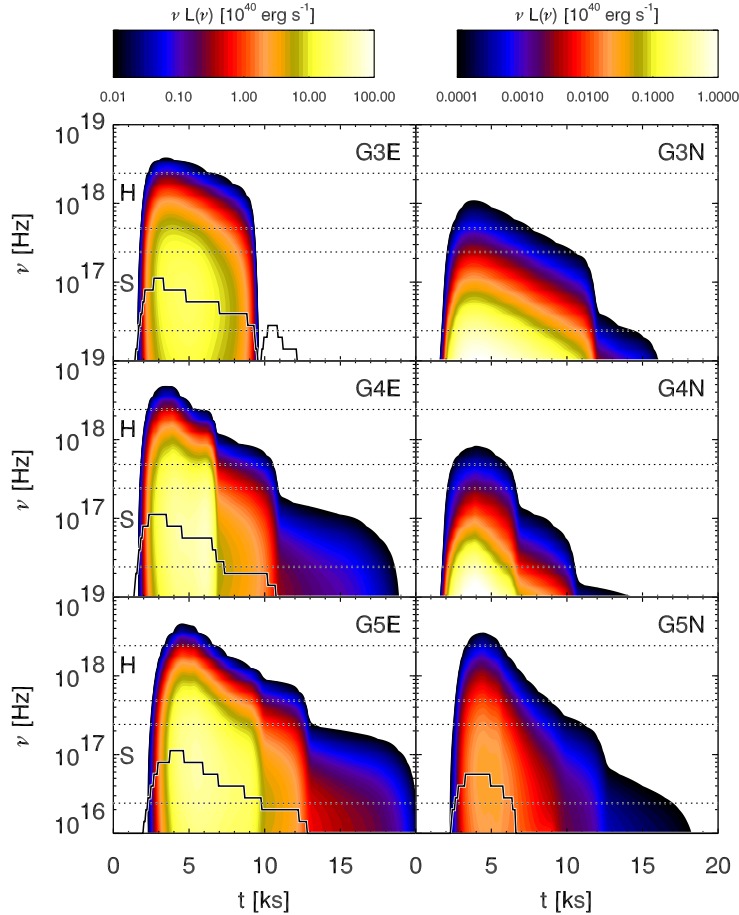


Figure 5.19: Same as Fig. 5.18, but for models G3, G4 and G5, respectively.

the region where a lot of kinetic energy is dissipated into thermal energy. However, the time of the observed maximum of the observed light curve does not coincide *exactly* with the time at which the maximum frequency of the spectral maximum is observed. This is due to the fact that, as the emitting region expands the magnetic field decreases, thus decreasing the frequency of the maximum. However, due to the expansion, more radiation arrives to the observer simultaneously. This means that the time at which the global spectral maximum is observed should be slightly ahead of the time when the global light curve maximum is observed, which is the case for all type-E models in Figs. 5.18, 5.19 and 5.20.

5.4 Analytic flare model

Motivated by the results of our simulations of shell collisions we propose a model for blazar X-ray flares. The basic idea is that the collision of the shells proceeds in three distinct phases:

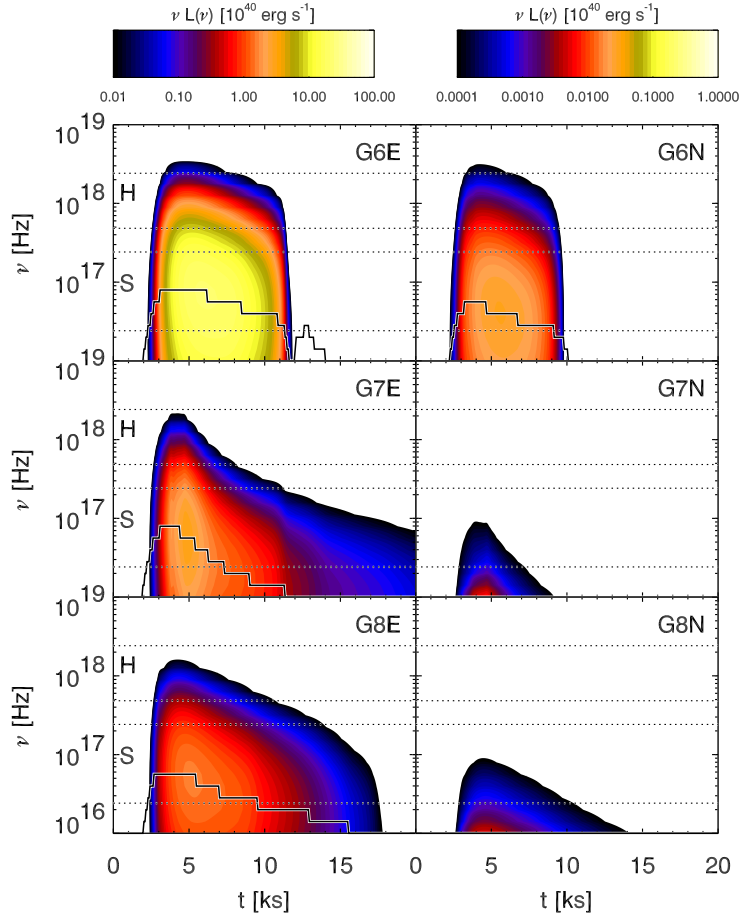


Figure 5.20: Same as Fig. 5.18, but for models G6, G7 and G8, respectively.

1. The start of the interaction between the shells is marked by the rise of the magnetic field (due to compression) and the injection of non-thermal electrons at internal shocks. We can idealize this phase by assuming that radiation is produced in an growing region where the emissivity is rising in time due to fluid compression. In Figures 5.15, 5.16 and 5.17 this phase corresponds to the part between the tip of the horn-shaped region of intense emission in Figures 5.15, 5.16 and 5.17 (we will call it horn in the rest of this section) and the point where the emissivity reaches its maximum (at $\approx 2 - 3$ ks).
2. The propagation of the internal shocks through the shells is marked by a slight decrease of the emissivity due to electron energy losses and an expansion of the emitting region causing the magnetic field to decrease. This phase corresponds to the region of the emissivity map (in the observer-xy frame) between the emissivity maximum and the turnover of the left edge of the brightest emission region in the center of the horn (e.g., in Fig. 5.16 this phase lasts from 2 to 8 ks).
3. The front shock breaks out of the slower shell, accelerates and causes

the emitting region to cool faster, thereby decreasing the magnetic field and the emissivity still faster. In the emissivity maps this phase corresponds to the region of the horn after the turnover of the left edge (after 8 ks in Fig. 5.16).

For simplicity we assume that the emissivity is uniform in space between two internal shocks at any time.

Thus, we need to compute the light curve of an expanding region of uniform emissivity. In Fig. 5.21 the situation is illustrated: in spacetime diagrams at T_i a region extending in space from $z_r(T_i)$ to $z_f(T_i) > z_r(T_i)$, starts expanding so that for $T_i \leq T \leq T_f$

$$z_r(T) = z_r(T_i) + \beta_r(T - T_i) \quad (5.15)$$

and

$$z_f(T) = z_f(T_i) + \beta_f(T - T_i), \quad (5.16)$$

where the velocities of the edges β_r and β_f obey the condition $1 \geq \beta_f > \beta_r \geq 0$. The observer is assumed to be located at large positive z (i.e., to the right). The uniform emissivity is assumed to vary as a power law with time, $j(T_i) = j_i$ and $j(T_f) = \eta j_i$, η being the factor by which the emissivity changes from T_i to T_f . The expression for the emissivity in lab frame reads

$$j(z, T) = j_i \left[1 - (1 - \eta) \left(\frac{T - T_i}{T_f - T_i} \right)^\theta \right] S(z; z_r(T), z_f(T)), \quad (5.17)$$

where $\theta > 0$ is the power law index of the emissivity change.

Using equations (5.4) and (5.5) we can write

$$j(x, y) = j_i \left\{ 1 - (1 - \eta) \left[\frac{x + y - \sqrt{2c}T_i}{\sqrt{2c}(T_f - T_i)} \right]^\theta \right\}, \quad (5.18)$$

where x and y need to fulfill conditions which are equivalent to $z_r(T) \leq z \leq z_f(T)$ for $T_i \leq T \leq T_f$. In the right panel of Fig. 5.21 the expanding region is plotted in the observer- xy frame. The condition for the emissivity to be nonzero at point (x, y) is equivalent to the requirement that the point lies within a quadrangle 1243, where corner 1 corresponds to the initial position of the rear edge, corner 2 to its final position, corner 3 to the initial position of the front edge, and corner 4 to its final position.

In order to compute the light curve, one needs to integrate the emissivity along the y axis for a fixed x . The general expression for the integral of equation (5.18) between the two limits a and b is found to be

$$I_a^b(x) \equiv \int_a^b dy j_x(x, y) = j_i \left[b - a - \frac{1 - \eta}{(\theta + 1)(\sqrt{2c}(T_f - T_i)^\theta)} \times \left\{ (b + x - \sqrt{2c}T_i)^{\theta+1} - (a + x - \sqrt{2c}T_i)^{\theta+1} \right\} \right]. \quad (5.19)$$

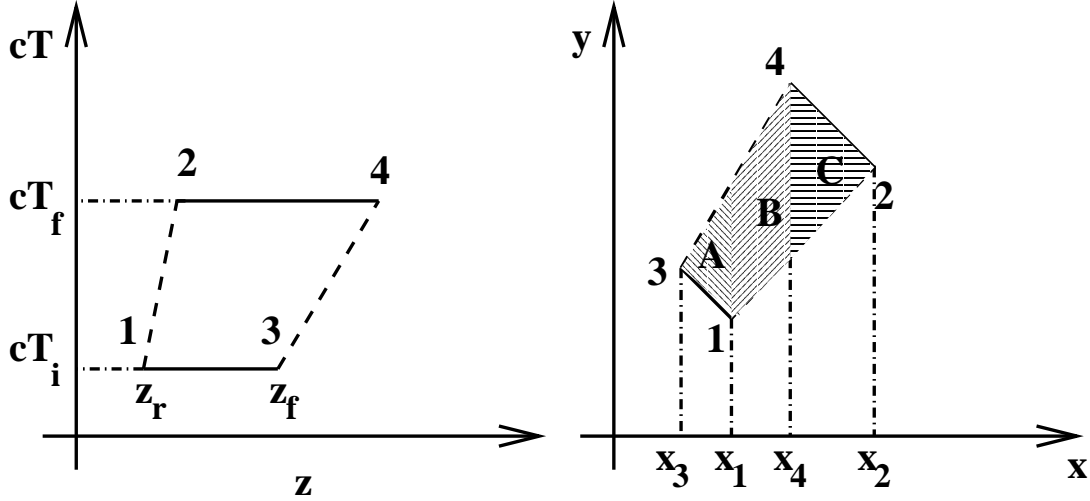


Figure 5.21: A space-time diagram of the expanding region in the laboratory frame (left panel) and the observer- xy system (right panel). Point 1 corresponds to the initial position of the rear edge, 2 corresponds to its final position, 3 marks the initial position of the front edge and 4 its final position. x_1 , x_2 , x_3 and x_4 denote the x coordinates of each point. Letters A, B and C denote three regions used in computation of the light curve (Eq. (5.26)).

The coordinates of the four corners 1, 2, 3 and 4 (Fig. 5.21) are easily computed

$$x_1 = \frac{-z_r + cT_i}{\sqrt{2}} \quad y_1 = \frac{z_r + cT_i}{\sqrt{2}} \quad (5.20)$$

$$x_2 = \frac{-z_r + (1 - \beta_r)cT_f + \beta_r cT_i}{\sqrt{2}} \quad y_2 = \frac{z_r + (1 + \beta_r)cT_f - \beta_r cT_i}{\sqrt{2}} \quad (5.21)$$

$$x_3 = \frac{-z_f + cT_i}{\sqrt{2}} \quad y_3 = \frac{z_f + cT_i}{\sqrt{2}} \quad (5.22)$$

$$x_4 = \frac{-z_f + (1 - \beta_f)cT_f + \beta_f cT_i}{\sqrt{2}} \quad y_4 = \frac{z_f + (1 + \beta_f)cT_f - \beta_f cT_i}{\sqrt{2}} \quad (5.23)$$

where $z_r \equiv z_r(T_i)$ and $z_f \equiv z_f(T_i)$. The equations of the straight lines $y_{ij}(x)$ connecting the points i and j are

$$y_{12}(x) = \frac{(1 + \beta_r)x + \sqrt{2}(z_r - \beta_r cT_i)}{1 - \beta_r} \quad y_{13}(x) = -x + \sqrt{2}cT_i \quad (5.24)$$

$$y_{34}(x) = \frac{(1 + \beta_f)x + \sqrt{2}(z_f - \beta_f cT_i)}{1 - \beta_f} \quad y_{24}(x) = -x + \sqrt{2}cT_f \quad (5.25)$$

To compute the light curve we divide the quadrangle 1234 in three parts (assuming $x_4 > x_1$ which holds as long as the region is expanding for sufficiently long time, i.e. $c(T_f - T_i) > (z_f - z_r)/(1 - \beta_f)$): part A between x_3 and x_1 , part B between x_1 and x_4 , and part C between x_4 and x_2 (right panel of Fig. 5.21). Using equations (5.24), (5.25) and (5.19) we obtain the

following expression for the light curve,

$$I(x; z_f, z_r, T_i, T_f, j_i, \eta, \theta, \beta_f, \beta_r) = \begin{cases} I_A(x; z_f, z_r, T_i, T_f, j_i, \eta, \theta, \beta_f, \beta_r) & \text{if } x_3 \leq x \leq x_1 \\ I_B(x; z_f, z_r, T_i, T_f, j_i, \eta, \theta, \beta_f, \beta_r) & \text{if } x_1 < x \leq x_4 \\ I_C(x; z_f, z_r, T_i, T_f, j_i, \eta, \theta, \beta_f, \beta_r) & \text{if } x_4 < x \leq x_2 \\ 0 & \text{otherwise} \end{cases}, \quad (5.26)$$

with

$$I_A(x; z_f, z_r, T_i, T_f, j_i, \eta, \theta, \beta_f, \beta_r) = j_i \sqrt{2} \frac{\sqrt{2}x + z_f - cT_i}{1 - \beta_f} \times \left[1 - \frac{1 - \eta}{\theta + 1} \left(\frac{\sqrt{2}x + z_f - cT_i}{(1 - \beta_f)c(T_f - T_i)} \right)^\theta \right], \quad (5.27)$$

$$I_B(x; z_f, z_r, T_i, T_f, j_i, \eta, \theta, \beta_f, \beta_r) = j_i \left[\frac{(1 + \beta_f)x + \sqrt{2}(z_f - \beta_f cT_i)}{1 - \beta_f} - \frac{(1 + \beta_r)x + \sqrt{2}(z_r - \beta_r cT_i)}{1 - \beta_r} - \sqrt{2}c(T_f - T_i) \frac{1 - \eta}{\theta + 1} \left\{ \left(\frac{\sqrt{2}x + z_f - cT_i}{(1 - \beta_f)c(T_f - T_i)} \right)^{\theta+1} - \left(\frac{\sqrt{2}x + z_r - cT_i}{(1 - \beta_r)c(T_f - T_i)} \right)^{\theta+1} \right\} \right], \quad (5.28)$$

$$I_C(x; z_f, z_r, T_i, T_f, j_i, \eta, \theta, \beta_f, \beta_r) = j_i \sqrt{2} \left[\frac{cT_f - \beta_r c(T_f - T_i) - \sqrt{2}x - z_r}{1 - \beta_r} - c(T_f - T_i) \frac{1 - \eta}{\theta + 1} \left\{ 1 - \left(\frac{\sqrt{2}x + z_r - cT_i}{(1 - \beta_r)c(T_f - T_i)} \right)^{\theta+1} \right\} \right]. \quad (5.29)$$

Fig. 5.22 shows a typical light curve obtained with the analytical model (5.26). Compared to the Kobayashi et al. (1997) light curve (Fig. 1.14 we see that our light curve has both convex and concave parts (while that of Kobayashi et al. is concave everywhere) and does not have a sharp peak at maximum.

We can now use expression (5.26) to construct our analytical flare model. As mentioned above, the evolution consists of three distinct phases, where the emissivity rises in the first phase and decreases during the second and third phase. In Fig. 5.23 the left panel illustrates the idea: two shocks (forward and reverse) start propagating from the same point 0 (which physically corresponds to the moment when the colliding shells touch). The reverse shock moves a bit slower than the forward shock, but both propagate towards the observer located to the right.

In the first phase between T_0 and T_1 the emissivity rises from j_0/η_{01} to j_0 ($\eta_{01} > 1$). From T_1 to T_2 the emissivity decreases from j_0 to $\eta_{12}j_0$ ($\eta_{12} < 1$).

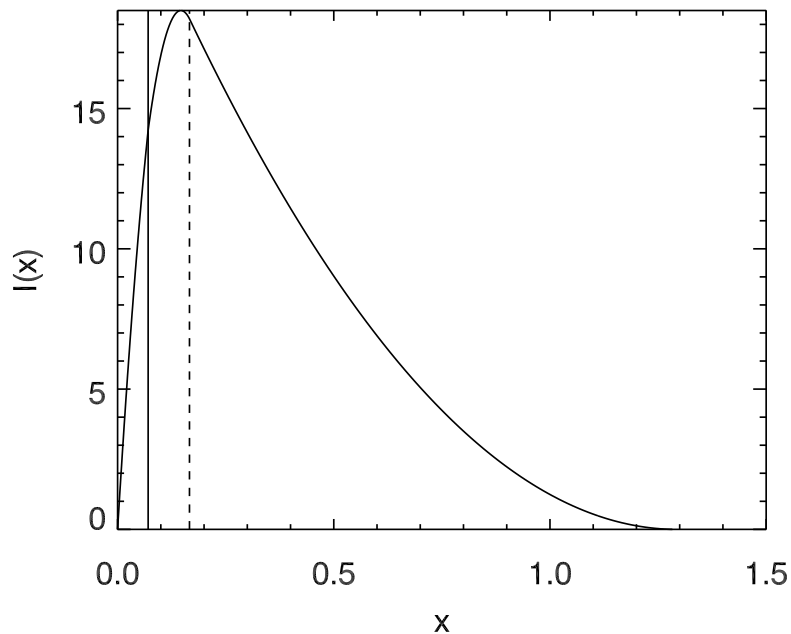


Figure 5.22: A typical light curve obtained with the analytic model corresponding to equation (5.26). The full vertical line indicates the position of x_1 , and the dashed vertical line the position of x_4 .

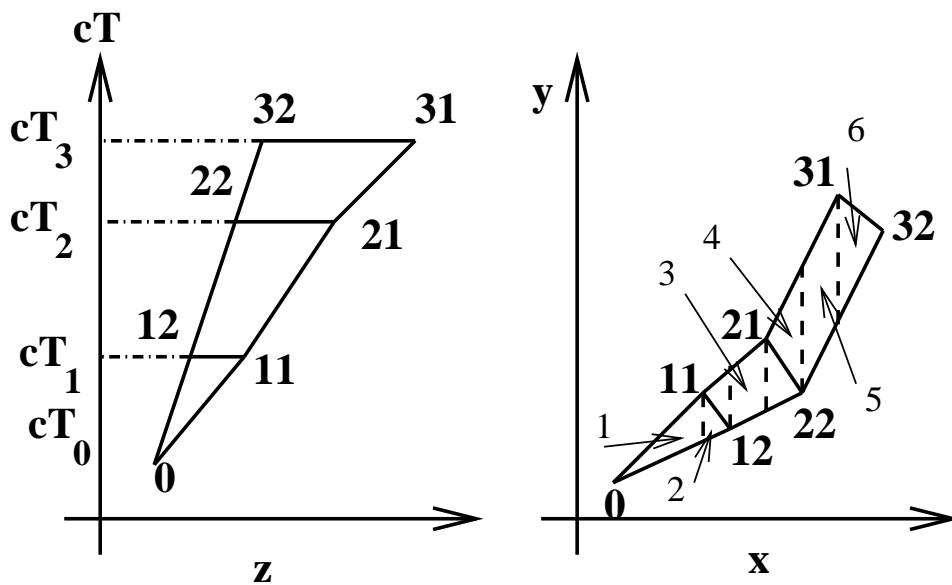


Figure 5.23: An illustration of the three different phases of the analytic flare model: the rising emissivity phase (between cT_0 and cT_1), the expansion until the forward shock crosses the slower shell (between cT_1 and cT_2), and the faster expansion after the shock breaks out of the slower shell (between cT_2 and cT_3). The right panel shows the model representation in the observer- xy frame. The numbers 1 to 6 in the right panel denote six regions in which the light curve is computed (Eq. (5.33)).

Finally, from T_2 to T_3 the emissivity decreases further from $\eta_{12}j_0$ to $\eta_{12}\eta_{23}j_0$ ($\eta_{23} < 1$). The rear edge moves with velocity $c\beta_r$ towards the observer between T_0 and T_2 , while the front edge moves with velocity $c\beta_f$ between T_0 and T_2 . At time T_2 the forward shock breaks out of the slower shell causing both shocks to progressively speed up their motion towards the observer. From T_2 to T_3 the reverse shock propagates with velocity $c\beta'_r > c\beta_r$, while the forward shock moves with velocity $c\beta'_f > c\beta_f$. In each phase the emissivity changes with power law indices θ_{01} , θ_{12} and θ_{23} , respectively. The locations of the rear (z_{j2}) and the front (z_{j1}) edges (shocks) at times T_j , and the corresponding values of the x coordinate are (assuming, for simplicity, that $z_0 = 0$ and $T_0 = 0$)

$$\begin{aligned}
z_{11} &= \beta_f c T_1 & x_{11} &= \frac{(1 - \beta_f) c T_1}{\sqrt{2}} \\
z_{12} &= \beta_r c T_1 & x_{12} &= \frac{(1 - \beta_r) c T_1}{\sqrt{2}} \\
z_{21} &= \beta_f c T_2 & x_{21} &= \frac{(1 - \beta_f) c T_2}{\sqrt{2}} \\
z_{22} &= \beta_r c T_2 & x_{22} &= \frac{(1 - \beta_r) c T_2}{\sqrt{2}} \\
z_{31} &= \beta_f c T_2 + \beta'_f c (T_3 - T_2) & x_{31} &= \frac{(1 - \beta'_f) c T_3 + (\beta'_f - \beta_f) c T_2}{\sqrt{2}} \\
z_{32} &= \beta_r c T_3 & x_{32} &= \frac{(1 - \beta'_r) c T_3 + (\beta'_r - \beta_r) c T_2}{\sqrt{2}}
\end{aligned} \tag{5.30}$$

We can now apply the expression (5.26) to each of the regions (0, 11, 12), (11, 12, 21, 22) and (21, 22, 31, 32) to obtain the total light curve. There are six parts of the light curve separated by x coordinates of the points 11, 12, 21, 22 and 31, respectively (right panel in Fig. 5.23). We use the following useful definitions

$$\Delta L_{i0} \equiv 2^{-3/2} c T_i, \tag{5.31}$$

$$\Delta L_{ij} \equiv 2^{-3/2} c (T_i - c T_j), \tag{5.32}$$

ΔL_{i0} and ΔL_{ij} are proportional to the distances that light crosses in the corresponding times T_i or $T_i - T_j$, respectively.

We note that when applying (5.26) to region (0, 11, 12) the expression for I_A is zero since both edges coincide at the beginning. The light curve is computed by using expressions for I_A , I_B and I_C for different regions. For those regions where parts of two different phases overlap (e.g., in right panel of Fig. 5.23 in region 2 first and second phase overlap) these expressions are summed (e.g, I_A and I_C in the region 2). After a simple, but tedious

calculation using (5.26) we find the following expression for the light curve

$$I(x) = \begin{cases} I_1(x) & \text{if } 0 \leq x \leq 2(1 - \beta_f)\Delta L_{10} \\ I_2(x) & \text{if } 2(1 - \beta_f)\Delta L_{10} < x \leq 2(1 - \beta_r)\Delta L_{10} \\ I_3(x) & \text{if } 2(1 - \beta_r)\Delta L_{10} < x \leq 2(1 - \beta_f)\Delta L_{20} \\ I_4(x) & \text{if } 2(1 - \beta_f)\Delta L_{20} < x \leq 2(1 - \beta_r)\Delta L_{20} \\ I_5(x) & \text{if } \begin{matrix} 2(1 - \beta_r)\Delta L_{20} < x \leq \\ 2[(1 - \beta'_f)\Delta L_{30} + (\beta'_f - \beta_f)\Delta L_{20}] \end{matrix} \\ I_6(x) & \text{if } \begin{matrix} 2[(1 - \beta'_f)\Delta L_{30} + (\beta'_f - \beta_f)\Delta L_{20}] < x \leq \\ 2[(1 - \beta'_r)\Delta L_{30} + (\beta'_r - \beta_r)\Delta L_{20}] \end{matrix} \\ 0 & \text{otherwise} \end{cases}, \quad (5.33)$$

where I_1 is computed from I_B ,

$$I_1(x) = I_B \left(x; 0, 0, 0, \sqrt{2^3} \frac{\Delta L_{10}}{c}, \frac{j_0}{\eta_{01}}, \eta_{01}, \theta_{01}, \beta_f, \beta_r \right) = \frac{4j_0}{\eta_{01}} \left\{ \frac{\beta_f - \beta_r}{2(1 - \beta_f)(1 - \beta_r)} x - \frac{1 - \eta_{01}}{1 + \theta_{01}} \Delta L_{10}^{-\theta_{01}} 2^{-(\theta_{01}+1)} \times x^{\theta_{01}+1} [(1 - \beta_f)^{-(\theta_{01}+1)} - (1 - \beta_r)^{-(\theta_{01}+1)}] \right\}. \quad (5.34)$$

I_2 is computed by combining I_A and I_C

$$I_2(x) = I_C \left(x; 0, 0, 0, \sqrt{2^3} \frac{\Delta L_{10}}{c}, \frac{j_0}{\eta_{01}}, \eta_{01}, \theta_{01}, \beta_f, \beta_r \right) + I_A \left(x; \sqrt{2^3} \beta_f \Delta L_{10}, \sqrt{2^3} \beta_r \Delta L_{10}, \sqrt{2^3} \frac{\Delta L_{10}}{c}, \sqrt{2^3} \frac{\Delta L_{20}}{c}, j_0, \eta_{12}, \theta_{12}, \beta_r, \beta_f \right) = 4j_0 \left\{ \frac{\Delta L_{10}}{\eta_{01}} - \frac{x}{2(1 - \beta_r)\eta_{01}} - \frac{(1 - \eta_{01})\Delta L_{10}}{\eta_{01}(1 + \theta_{01})} \left[1 - \left(\frac{x}{2(1 - \beta_r)\Delta L_{10}} \right)^{\theta_{01}+1} \right] + \left(\frac{x}{2(1 - \beta_f)} - \Delta L_{10} \right) \left[1 - \frac{1 - \eta_{12}}{1 + \theta_{12}} \left(\frac{x}{2(1 - \beta_f)\Delta L_{21}} - \frac{\Delta L_{10}}{\Delta L_{21}} \right)^{\theta_{12}} \right] \right\}. \quad (5.35)$$

I_3 is computed from I_B

$$\begin{aligned}
I_3(x) = & \\
I_B \left(\sqrt{2^3} \beta_f \Delta L_{10}, \sqrt{2^3} \beta_r \Delta L_{10}, \sqrt{2^3} \frac{\Delta L_{10}}{c}, \sqrt{2^3} \frac{\Delta L_{20}}{c}, j_0, \eta_{12}, \theta_{12}, \beta_f, \beta_r \right) = & \\
4j_0 \left\{ \frac{\beta_f - \beta_r}{2(1 - \beta_f)(1 - \beta_r)} x - \frac{1 - \eta_{12}}{1 + \theta_{12}} \Delta L_{21}^{-\theta_{12}} \times \right. & \\
\left. \left[\left(\frac{x}{2(1 - \beta_f)} - \Delta L_{10} \right)^{\theta_{12}+1} - \left(\frac{x}{2(1 - \beta_r)} - \Delta L_{10} \right)^{\theta_{12}+1} \right] \right\}, & \quad (5.36)
\end{aligned}$$

I_4 is computed from I_A and I_C ,

$$\begin{aligned}
I_4(x) = & \\
I_C \left(\sqrt{2^3} \beta_f \Delta L_{10}, \sqrt{2^3} \beta_r \Delta L_{10}, \sqrt{2^3} \frac{\Delta L_{10}}{c}, \sqrt{2^3} \frac{\Delta L_{20}}{c}, j_0, \eta_{12}, \theta_{12}, \beta_f, \beta_r \right) + & \\
I_A \left(\sqrt{2^3} \beta_f \Delta L_{20}, \sqrt{2^3} \beta_r \Delta L_{20}, \sqrt{2^3} \frac{\Delta L_{20}}{c}, \sqrt{2^3} \frac{\Delta L_{30}}{c}, j_0 \eta_{12}, \eta_{23}, \theta_{23}, \beta'_f, \beta'_r \right) = & \\
4j_0 \left\{ \Delta L_{20} - \frac{x}{2(1 - \beta_r)} - \frac{1 - \eta_{12}}{1 + \theta_{12}} \Delta L_{21} \left[1 - \left(\frac{x}{2(1 - \beta_r) \Delta L_{21}} - 1 \right)^{\theta_{12}+1} \right] + \right. & \\
\left(\frac{x}{2(1 - \beta'_f)} - \frac{1 - \beta_f}{1 - \beta'_f} \Delta L_{20} \right) \left[1 - \frac{1 - \eta_{23}}{1 + \theta_{23}} \times \right. & \\
\left. \left. \left(\frac{x}{2(1 - \beta'_f) \Delta L_{32}} - \frac{(1 - \beta_f) \Delta L_{20}}{(1 - \beta'_f) \Delta L_{32}} \right)^{\theta_{23}} \right] \right\}. & \quad (5.37)
\end{aligned}$$

I_5 is computed from I_B ,

$$\begin{aligned}
I_5(x) = & \\
I_B \left(\sqrt{2^3} \beta_f \Delta L_{20}, \sqrt{2^3} \beta_r \Delta L_{20}, \sqrt{2^3} \frac{\Delta L_{20}}{c}, \sqrt{2^3} \frac{\Delta L_{30}}{c}, j_0 \eta_{12}, \eta_{23}, \theta_{23}, \beta'_f, \beta'_r \right) = & \\
4j_0 \eta_{12} \left\{ \left(\frac{1 + \beta'_f}{1 - \beta'_f} - \frac{1 + \beta'_r}{1 - \beta'_r} \right) \frac{x}{4} - \right. & \\
\left. \left(\frac{1 - \beta_f}{1 - \beta'_f} + \frac{1 - \beta_r}{1 - \beta'_r} \right) \Delta L_{20} - \frac{1 - \eta_{23}}{1 + \theta_{23}} \Delta L_{32}^{-\theta_{23}} \times \right. & \\
\left. \left[\left(\frac{x}{2(1 - \beta'_f)} - \frac{1 - \beta_f}{1 - \beta'_f} \Delta L_{20} \right)^{\theta_{23}+1} - \left(\frac{x}{2(1 - \beta'_r)} - \frac{1 - \beta_r}{1 - \beta'_r} \Delta L_{20} \right)^{\theta_{23}+1} \right] \right\}, & \quad (5.38)
\end{aligned}$$

and $I_6(x)$ is computed using the same substitutions as for I_5 applied to I_C ,

$$\begin{aligned}
I_6(x) = & \\
I_C \left(\sqrt{2^3} \beta_f \Delta L_{20}, \sqrt{2^3} \beta_r \Delta L_{20}, \sqrt{2^3} \frac{\Delta L_{20}}{c}, \sqrt{2^3} \frac{\Delta L_{30}}{c}, j_0 \eta_{12}, \eta_{23}, \theta_{23}, \beta'_f, \beta'_r \right) = & \\
4j_0 \eta_{12} \left\{ \frac{\Delta L_{30} - \beta'_r \Delta L_{32} - \Delta L_{20} \beta_r}{1 - \beta'_r} - \frac{x}{2(1 - \beta'_r)} - \right. & \\
\left. \frac{1 - \eta_{23}}{1 + \theta_{23}} \left[\Delta L_{32} - \Delta L_{32}^{\theta_{23}} \left(\frac{x}{2(1 - \beta'_r)} - \frac{1 - \beta_r}{1 - \beta'_r} \Delta L_{20} \right)^{\theta_{23}+1} \right] \right\}. & \quad (5.39)
\end{aligned}$$

Fig. 5.24 shows an example of a light curve obtained with this model. The coordinates x_{11} , x_{12} , x_{21} , x_{22} , x_{31} and x_{32} are also shown by vertical lines. Choosing different values for times, velocities and η will change the shape of the light curve significantly, e.g., it may enhance or suppress the first (lower) peak of the light curve.

The above expressions for the light curve simplify significantly, if it is assumed that both the forward and reverse shocks are ultra-relativistic. In that case, assuming

$$\beta_r = \sqrt{1 - \Gamma_r^{-2}} \approx 1 - 2\Gamma_r^{-2} \quad (5.40)$$

$$\beta_f = \sqrt{1 - \Gamma_f^{-2}} \approx 1 - 2\Gamma_f^{-2} \quad (5.41)$$

$$\beta'_r = \sqrt{1 - \Gamma_r'^{-2}} \approx 1 - 2\Gamma_r'^{-2} \quad (5.42)$$

$$\beta'_f = \sqrt{1 - \Gamma_f'^{-2}} \approx 1 - 2\Gamma_f'^{-2} \quad (5.43)$$

we can write

$$I^U(x) = \begin{cases} I_1^U(x) & \text{if } 0 \leq x \leq \Gamma_f^{-2} \Delta L_{10} \\ I_2^U(x) & \text{if } \Gamma_f^{-2} \Delta L_{10} < x \leq x \Gamma_r^{-2} \Delta L_{10} \\ I_3^U(x) & \text{if } \Gamma_r^{-2} \Delta L_{10} < x \leq \Gamma_f^{-2} \Delta L_{20} \\ I_4^U(x) & \text{if } \Gamma_f^{-2} \Delta L_{20} < x \leq \Gamma_r^{-2} \Delta L_{20} \\ I_5^U(x) & \text{if } \Gamma_r^{-2} \Delta L_{20} < x \leq \Gamma_f'^{-2} \Delta L_{32} + \Gamma_f^{-2} \Delta L_{20} \\ I_6^U(x) & \text{if } \Gamma_f'^{-2} \Delta L_{32} + \Gamma_f^{-2} \Delta L_{20} < x \leq \Gamma_r'^{-2} \Delta L_{32} + \Gamma_r^{-2} \Delta L_{20} \\ 0 & \text{otherwise} \end{cases}, \quad (5.44)$$

with the ultrarelativistic approximation of the functions I_1 through I_6 :

$$I_1^U(x) = \frac{4j_0}{\eta_{01}} \left\{ (\Gamma_f^2 - \Gamma_r^2)x - \frac{1 - \eta_{01}}{1 + \theta_{01}} \Delta L_{10}^{-\theta_{01}} x^{\theta_{01}+1} \left[\Gamma_f^{2(\theta_{01}+1)} - \Gamma_r^{2(\theta_{01}+1)} \right] \right\}, \quad (5.45)$$

$$\begin{aligned}
I_2^U(x) = 4j_0 \left\{ \frac{\Delta L_{10}}{\eta_{01}} - \frac{\Gamma_r^2}{\eta_{01}} x - \frac{1 - \eta_{01}}{1 + \theta_{01}} \left[\Delta L_{10} - \Delta L_{10}^{-\theta_{01}} \Gamma_r^{2(\theta_{01}+1)} x^{\theta_{01}+1} \right] + \right. & \\
\left. (\Gamma_f^2 x - \Delta L_{10}) \left[1 - \frac{1 - \eta_{12}}{1 + \theta_{12}} \Delta L_{21}^{-\theta_{12}} (\Gamma_f^2 x - \Delta L_{10})^{\theta_{12}} \right] \right\}, & \quad (5.46)
\end{aligned}$$

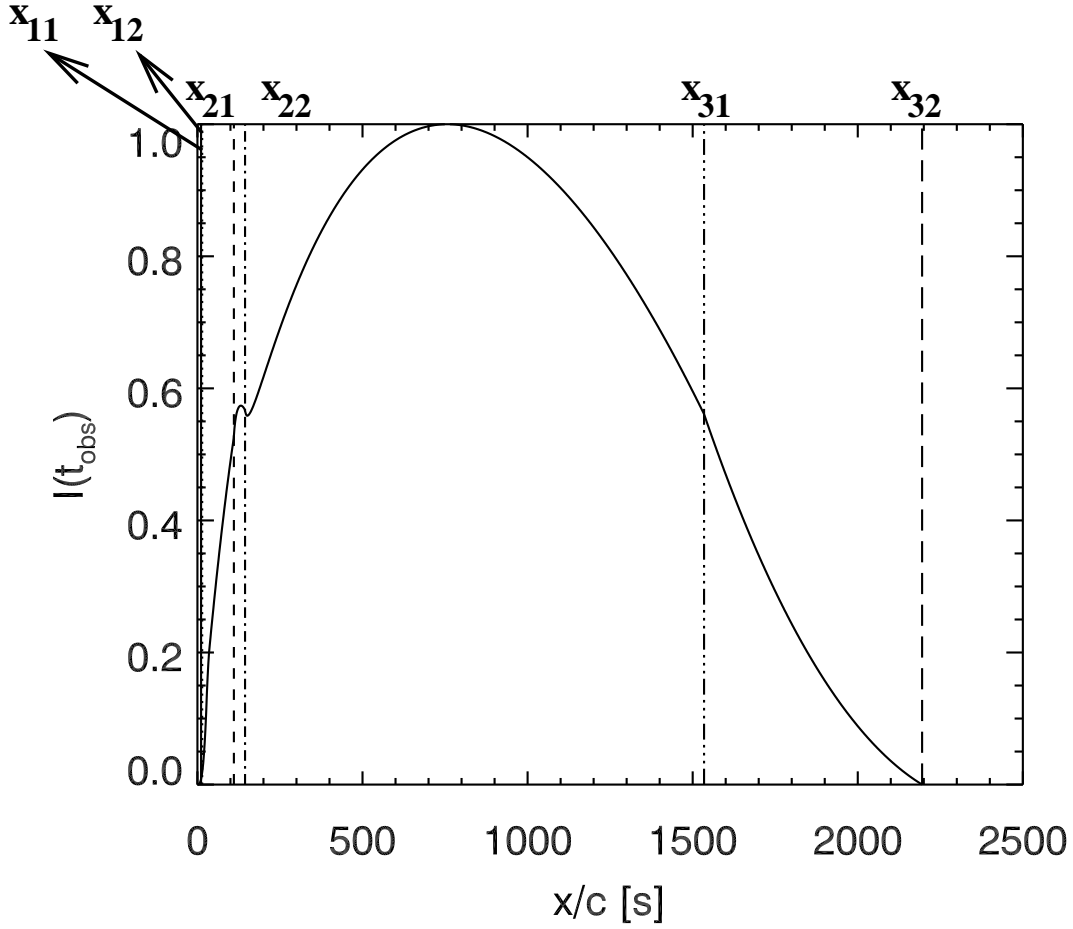


Figure 5.24: An example of the light curve produced by the analytic model (5.32). The parameters of the model are: $\theta_{01} = 2$, $\theta_{12} = 1$, $\theta_{23} = 0.1$, $\beta_r = 0.9897$, $\beta_f = 0.9922$, $\beta'_r = 0.9950$, $\beta'_f = 0.9965$, $T_1 = 2$ ks, $T_2 = 20$ ks, $T_3 = 600$ ks, $j_0 = 1$, $\theta = 1$, $\eta_{01} = 100$, $\eta_{12} = 0.8$ and $\eta_{23} = 0.01$. The coordinates of the six points determining the model are shown on the plot by vertical lines. They are: $x_{11}/c = 11.08$ s, $x_{12}/c = 14.43$ s, $x_{21}/c = 110.49$ s, $x_{22}/c = 144.31$ s, $x_{31}/c = 1534.52$ s and $x_{32}/c = 2194.92$ s.

$$I_3^U(x) = 4j_0 \left\{ (\Gamma_f^2 - \Gamma_r^2)x - \frac{1 - \eta_{12}}{1 + \theta_{12}} \Delta L_{21}^{-\theta_{12}} \times \right. \\ \left. [(\Gamma_f^2 x - \Delta L_{10})^{\theta_{12}+1} - (\Gamma_r^2 x - \Delta L_{10})^{\theta_{12}+1}] \right\}, \quad (5.47)$$

$$I_4^U(x) = 4j_0 \left\{ \Delta L_{20} - \Gamma_r^2 x - \right. \\ \frac{1 - \eta_{12}}{1 + \theta_{12}} \Delta L_{21} \left[1 - \Delta L_{21}^{-(\theta_{12}+1)} (\Gamma_r^2 x - \Delta L_{10})^{\theta_{12}+1} \right] + \\ \eta_{12} \left(\Gamma_f^2 x - \frac{\Gamma_f^2}{\Gamma_f^2} \Delta L_{20} \right) \left[1 - \right. \\ \left. \frac{1 - \eta_{23}}{1 + \theta_{23}} \Delta L_{23}^{-\theta_{23}} \left(\Gamma_f^2 x - \frac{\Gamma_f^2}{\Gamma_f^2} \Delta L_{20} \right)^{\theta_{23}} \right] \left. \right\}, \quad (5.48)$$

$$I_5^U(x) = 4j_0\eta_{12} \left\{ (\Gamma_f'^2 - \Gamma_r'^2)x - \left[\frac{\Gamma_f'^2}{\Gamma_f'^2} - \frac{\Gamma_r'^2}{\Gamma_r'^2} \right] \Delta L_{20} - \frac{1 - \eta_{23}}{1 + \theta_{23}} \left[\Delta L_{32} - \Delta L_{32}^{-\theta_{23}} \left(\Gamma_r'^2 x - \frac{\Gamma_r'^2}{\Gamma_r'^2} \Delta L_{20} \right)^{\theta_{23}+1} \right] \right\}, \quad (5.49)$$

$$I_6^U(x) = 4j_0\eta_{12} \left\{ \Delta L_{30} + \left(\frac{\Gamma_r'^2}{\Gamma_r'^2} - 1 \right) \Delta L_{20} - \Gamma_r'^2 x - \frac{1 - \eta_{23}}{1 + \theta_{23}} \left[\Delta L_{32} - \Delta L_{32}^{-\theta_{23}} \left(\Gamma_r'^2 x - \frac{\Gamma_r'^2}{\Gamma_r'^2} \Delta L_{20} \right)^{\theta_{23}+1} \right] \right\}. \quad (5.50)$$

The analytic model has 13 free parameters (excluding j_0 which is a normalization constant): θ_{01} , θ_{12} , θ_{23} , Γ_r , Γ_f , Γ_r' , Γ_f' , ΔL_{10} , ΔL_{20} , ΔL_{30} , η_{01} , η_{12} and η_{23} . However, if one knows the duration Δt_f of the flare in the observer frame, then ΔL_{30} is no longer independent parameter. It can be computed from the equation for x_{32} (Eq. (5.30); $\Delta t_f = \sqrt{2}x_{32}$ in the analytic model):

$$\Delta L_{30} = \Gamma_r'^2 \frac{\Delta t_f}{\sqrt{2}} + \Delta L_{20} \left(1 - \frac{\Gamma_r'^2}{\Gamma_r'^2} \right). \quad (5.51)$$

This leaves us with the 12 independent parameters which should be fitted to the observed light curve.

5.4.1 Application to models G0E, G1E and G2E

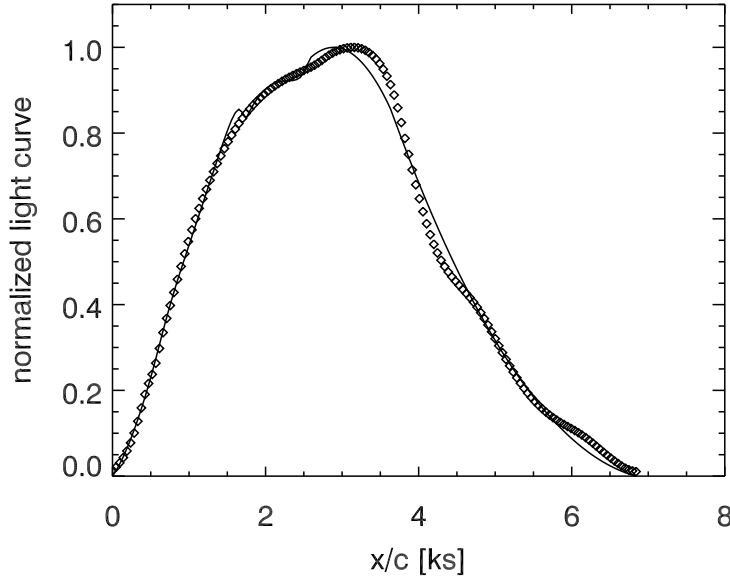


Figure 5.25: Total light curve of model G0E (diamonds) and the fit obtained with the analytic model (full line).

model	G0E	G1E	G2E
θ_{01}	0.8 ± 1	3 ± 1	2.1 ± 1
θ_{12}	14 ± 3	2 ± 1	0.08 ± 1
θ_{23}	0.9 ± 0.1	0.05 ± 0.01	0.07 ± 0.01
Γ_r	4 ± 1	4 ± 1	4 ± 2
Γ_r^{sim}	5.28 ± 0.03	4.75 ± 0.03	7.1 ± 0.2
Γ_r^{KPS}	10.24	6.58	10.64
Γ_f	5 ± 2	5 ± 2	7 ± 2
Γ_f^{sim}	6.94 ± 0.08	5.63 ± 0.04	9.1 ± 0.5
Γ_f^{KPS}	13.08	8.5	12.71
Γ_r'	10 ± 3	10 ± 3	10 ± 3
$\Gamma_r'^{\text{sim}}$	6.7 ± 0.03	5.63 ± 0.04	7.7 ± 0.2
Γ_f'	15 ± 3	16 ± 3	11 ± 3
$\Gamma_f'^{\text{sim}}$	10.9 ± 0.1	7.8 ± 0.06	9.4 ± 0.3
$\Delta L_{10}/c$ [ks]	21 ± 0.4	12 ± 0.3	41 ± 0.1
$\Delta L_{20}/c$ [ks]	60 ± 0.4	54 ± 3	86.6 ± 0.06
$\Delta L_{30}/c$ [ks]	7700 ± 400	1900 ± 700	191 ± 700
η_{01}	2 ± 2	2.2 ± 0.2	2.6 ± 0.2
η_{12}	0.14 ± 0.02	0.30 ± 0.02	0.84 ± 0.02
η_{23}	0.07 ± 0.01	0.01 ± 0.01	0.15 ± 0.01

Table 5.5: Results of the fit of the ultrarelativistic version of the analytic model to the total light curves of models G0E, G1E and G2E, respectively. The parameters with the superscript “sim” are the values obtained from the simulations, while those with the superscript “KPS” are computed using the model of Kobayashi et al. (1997) (see text for details). The errors shown are those defined in Appendix A.

We use the algorithm described in Appendix A to fit the parameters of the ultrarelativistic analytic model (5.44) to the total light curves. The fit was obtained with with $5 \cdot 10^5$ iterations.

Table 5.5 shows the resulting fit parameters of several models. Parameters without superscripts refer to the analytic model. The errors provided in the table have been computed as described in Appendix A. The Lorentz factor with the superscript “sim” are obtained from the hydrodynamic data. Γ_r^{KPS} and Γ_f^{KPS} are the Lorentz factors of the forward and reverse shocks obtained with the model of Kobayashi et al. (1997).

Figures 5.25, 5.26 and 5.27 show the synthetic light curves computed from the simulation (diamonds) and the best-fit model light curves (solid line) that are obtained with our analytic model (5.44).

As one can see, the model light curves are in a good agreement with the simulated light curves. The fitted initial shock velocities are consistent with those from the simulation, while the model of Kobayashi et al. (1997) overestimates shock velocities (Tab. 5.5., rows 4-7). The shock velocities after the forward (Γ_f') or the reverse (Γ_r') shock has broken out of the faster or the slower shell, are systematically larger (on average about 50%) than in the actual hydrodynamic evolution. However, considering the lower limits the fitted values predict very well the hydrodynamic data (with an average

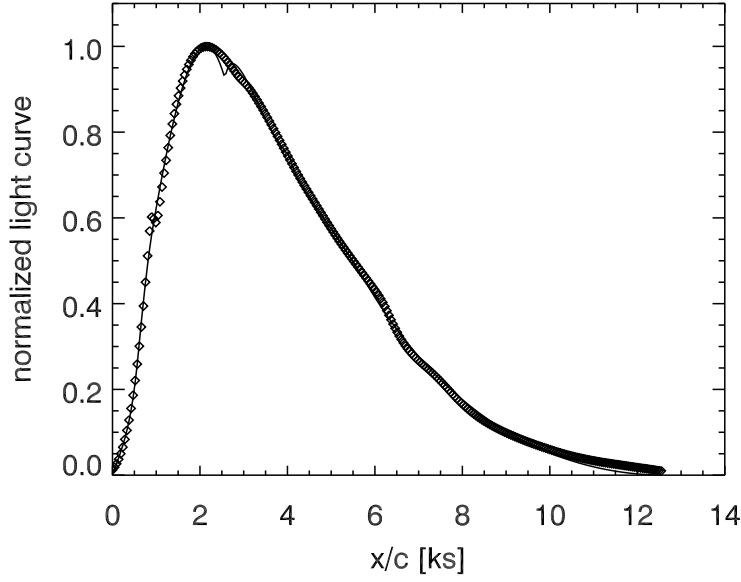


Figure 5.26: Same as Fig. 5.25, but for model G1E.

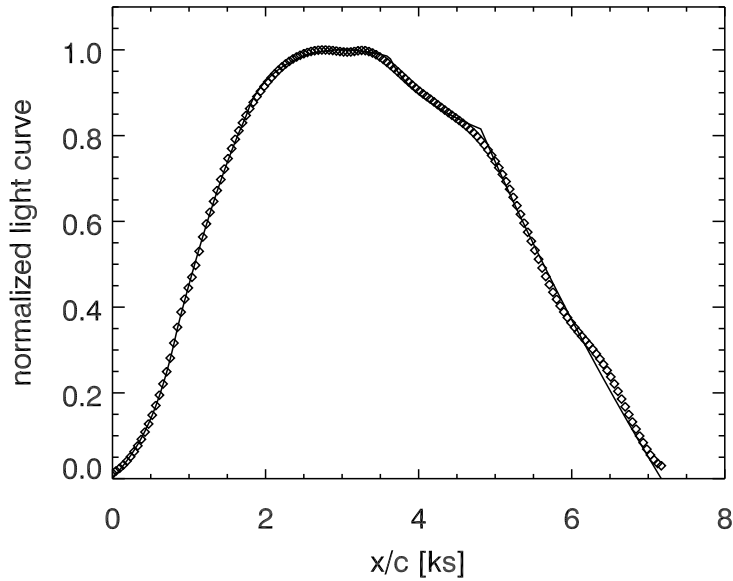


Figure 5.27: Same as Fig. 5.25, but for model G2E.

deviation of $\approx 7\%$ for Γ'_r and 21% for Γ'_f).

The power law indices of the temporal change of the emissivity (Tab. 5.5, rows 1-3) show a trend which is compatible with what is seen in the simulations (Fig. 5.28): a rapid rise, a slow decline followed by an even slower decline of the emissivity. The values of ΔL_{10} and ΔL_{20} are small compared to ΔL_{30} , a feature also seen in Fig. 5.28 (L_{10} corresponds to time interval between 0 and the time when the emissivity reaches maximum, L_{20} corresponds roughly to the time interval where the emissivity decreases

faster, and L_{30} to the time interval where the emissivity decreases slower). We can also see that the values of η_{12} and η_{23} seem to reproduce quite well the ratios seen in Fig. 5.28, because the emissivity decreases by one to two orders of magnitude from its maximum during the course of the evolution. The final emissivity of our model is $j_0\eta_{12}\eta_{23} \approx 0.02j_0$.

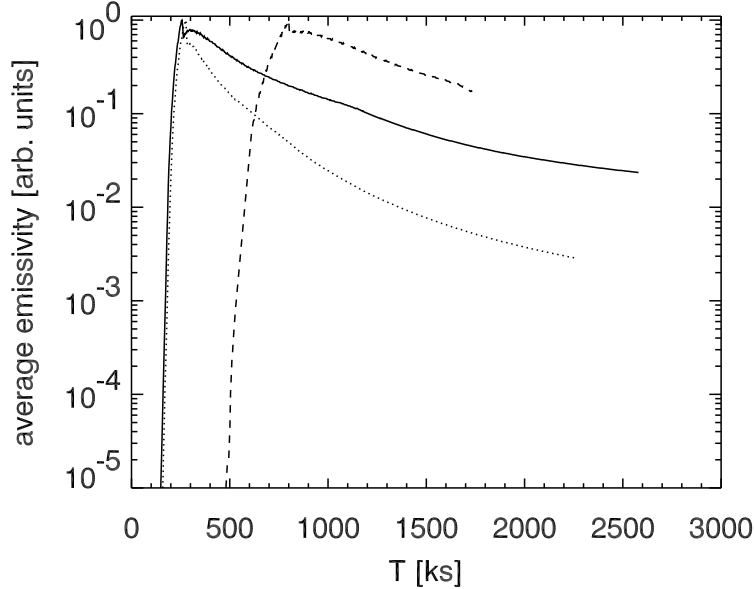


Figure 5.28: The average emissivity of models *G0E* (solid line), *G1E* (dotted line) and *G2E* (dashed line), respectively, as a function of the time T in the simulation frame. Each curve has been normalized to its maximum.

As we have demonstrated, the parameters of our analytic model obtained by fitting the synthetic light curves are consistent with the hydrodynamic data produced by the time-dependent RHD-simulations. These preliminary results give us confidence that the analytic model for the blazar flares is able to reproduce the essentials of the physics of internal shocks, and that it can be applied to observed blazar light curves in order to estimate physical parameters of the underlying jets with a known and reasonable degree of accuracy.

5.5 Comparison with observations of blazar flares

Figures 5.29 and 5.30 show two flares of the source Mrk 421 observed by the *XMM-Newton* satellite (Brinkmann et al. 2003). The pink line is the soft light curve, and the black line is the hard one, both normalized separately.

The light curve in Fig. 5.29 is very similar to the synthetic light curves of the models with the type-E electron acceleration (see, e.g., sections 5.3.2 and 5.3.4) in that both soft and hard bands show similar properties. On the other hand, the light curve in Fig. 5.30 is more similar to synthetic light

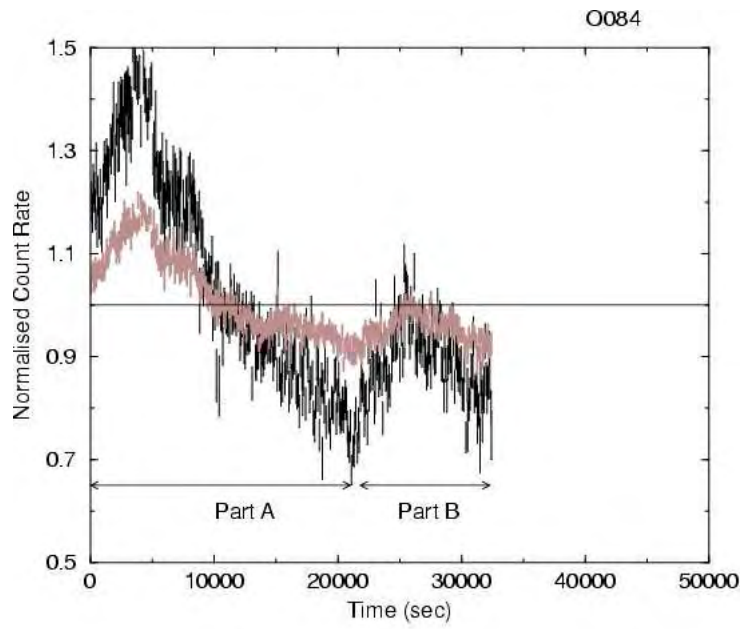


Figure 5.29: Normalized soft (pink line) and hard (black line) light curve of the source Mrk 421 observed by *XMM-Newton* during its orbit 084 (Brinkmann et al. 2003).

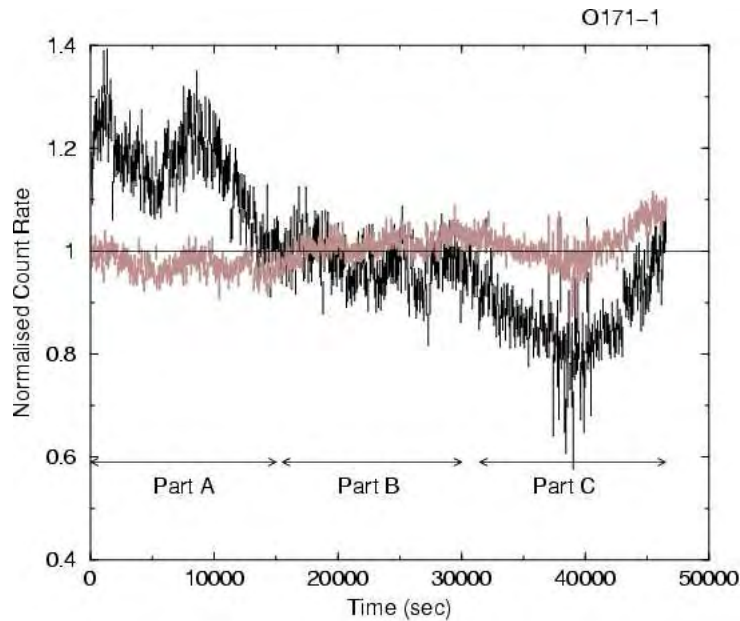


Figure 5.30: Normalized soft (pink line) and hard (black line) light curve of the source Mrk 421 observed by *XMM-Newton* during its orbit 171 – 1 (Brinkmann et al. 2003).

curves of type-N models since the hard light curve seems to vary with larger amplitude than the soft one. However, it has to be pointed out that the observed light curves show smaller variations around the mean value than the synthetic light curves do. This might be also due to the presence of a background source of luminosity (unrelated to flares), which is not present

in our simulations.

5.6 Simulations of multiple collisions

Up to this point, we have gained some insight in the physics of blazar flares by considering them as the result of “two-shell” interactions. However, typical light curves of blazars display a complex morphology which cannot be attributed to a single “two-shell” interaction, but, instead, to the dynamic interaction of “many shells”. Therefore, we model a blazar jet as an inhomogeneous flow emitted by the central engine. We point out that the results are not yet conclusive, because they are part of a work in progress.

5.6.1 A model of an inhomogeneous blazar jet

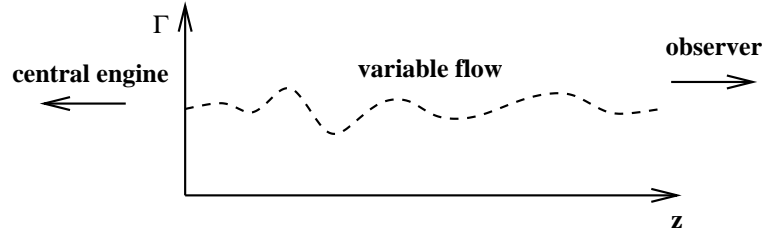


Figure 5.31: A model of an inhomogeneous onedimensional jet: a central engine (located to the left) emits a flow of variable Lorentz factor. The variable flow enters through the left grid boundary ($z = 0$) and propagates along the z axis (jet axis) towards the observer located to the right. The pressure and density of the incoming material are computed in such a way that the quantities $\rho\Gamma$ and p/ρ (proportional to the temperature) are constant (independent of Γ of the incoming material).

In Fig. 5.31 a schematic view of the proposed model is shown: variable flow emitted by a central engine enters through the left grid boundary at $z = 0$ and propagates along the z axis towards the observer. Density and pressure of the incoming material depend only on Γ in such a way that

$$\rho\Gamma = \rho_0\Gamma_0 = \text{const.}, \quad (5.52)$$

and

$$\frac{p}{\rho} = \frac{p_0}{\rho_0} = \text{const.}. \quad (5.53)$$

This means that the flow structure is completely determined by the temporal variations of the Lorentz factor, and two parameters ρ_0 and p_0 determine the mass flux and the temperature of the flow.

We assume the Lorentz factor of the flow to be a random variable distributed according to a Gaussian probability function

$$\mathcal{P}(\Gamma) = \frac{1}{\sigma_\Gamma\sqrt{2\pi}} \exp\left[-\frac{(\Gamma - \Gamma_0)^2}{2\sigma_\Gamma^2}\right], \quad (5.54)$$

where $\mathcal{P}(\Gamma)$ is the probability that a shell with a Lorentz factor Γ will be emitted, Γ_0 is the mean Lorentz factor of the flow and σ_Γ is the standard deviation of the Lorentz factor the around mean value.

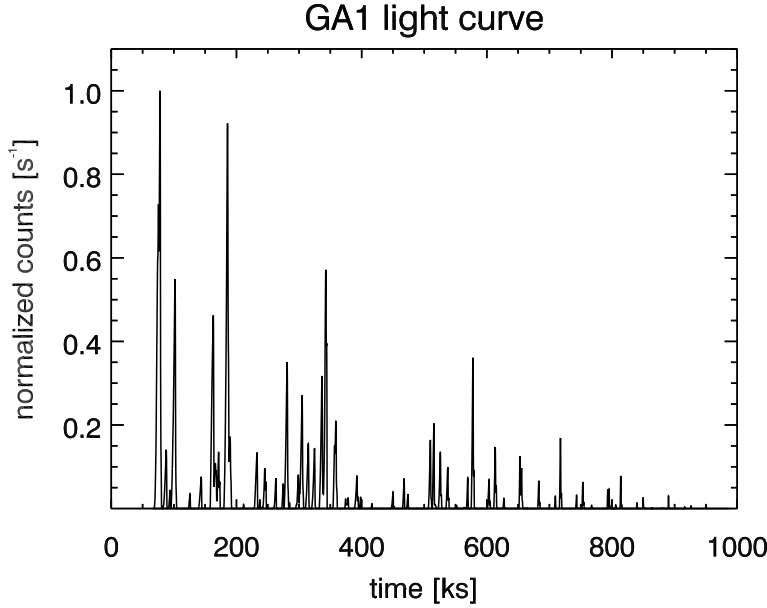


Figure 5.32: Soft light curve of model GA1. The parameters of the model are: $\Gamma_0 = 8$, $\sigma_\Gamma = 0.1$, $\Delta T_e = 2$ ks, $\rho_0 = 10^{-18}$ g cm $^{-3}$ and $p_0/\rho_0 c^2 = 10^{-4}$.

Finally, we assume that the engine is operating on a time scale ΔT_e , i.e., the flow has constant Lorentz factor, density and pressure for a period ΔT_e . Then a new random value of Γ is drawn, and the corresponding p and ρ are computed.

We have performed 3 long term simulations of inhomogeneous jets, *GA1*, *GA2* and *GA3* without remapping. The simulations have been stopped when the head of the jet reached a distance of roughly 3×10^{16} cm. Figures 5.32, 5.33 and 5.34 show soft light curves of the models *GA1*, *GA2* and *GA3*. All models have $\Gamma_0 = 8$, $\rho_0 = 10^{-18}$ g cm $^{-3}$ and $p_0/\rho_0 c^2 = 10^{-4}$. The only difference is in σ_Γ and ΔT_e : for *GA1* $\sigma_\Gamma = 0.1$ and $\Delta T_e = 2$ ks, for *GA2* $\sigma_\Gamma = 0.05$ and $\Delta T_e = 2$ ks, and for *GA3* $\sigma_\Gamma = 0.1$ and $\Delta T_e = 1$ ks. The acceleration model used is of type-E, with $\alpha_e = 0.05$, $\gamma_{\min} = 50$, and $\eta = 10^4$. The magnetic field proportionality constant is $\alpha_B = 10^{-4}$. The number of zones of the numerical grid is 20000, the number of non-thermal electron energy bins is 48, and the number of frequencies at which the radiation is computed is 21.

One sees that the light curve of model *GA1* (Fig. 5.32) is “denser” than that of model *GA2* (Fig. 5.33), a property related to σ_Γ . The larger σ_Γ , the shorter the time between the collisions, and thus the shorter the time between the peaks in the observed light curve. The light curve of model *GA3* (Fig. 5.34) is even denser than *GA1*, which is again related to the fact that for shorter ΔT_e the time between subsequent collisions is shorter.

We observe in all three light curves an almost monotonic trend: earlier peaks seem to be more luminous than later peaks. This can be interpreted

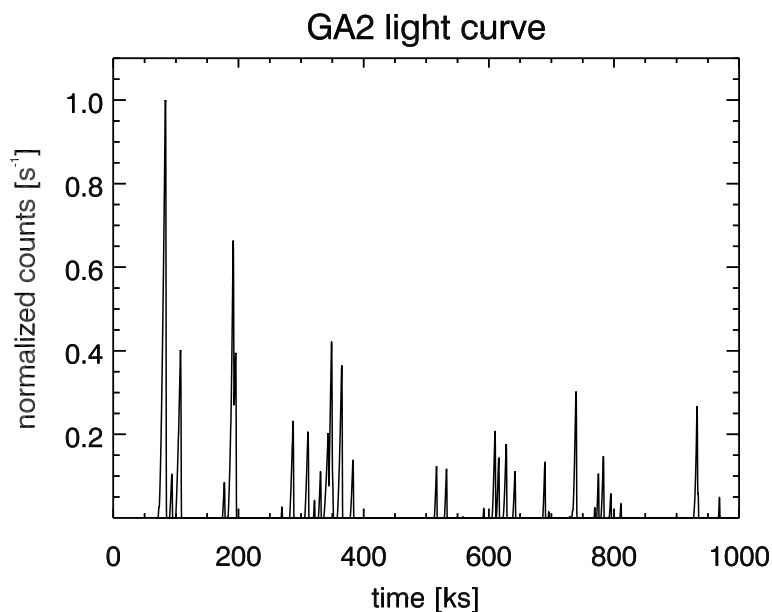


Figure 5.33: Soft light curve of model GA2. The parameters of the model are: $\Gamma_0 = 8$, $\sigma_\Gamma = 0.05$, $\Delta T_e = 2$ ks, $\rho_0 = 10^{-18}$ g cm⁻³ and $p_0/\rho_0 c^2 = 10^{-4}$.

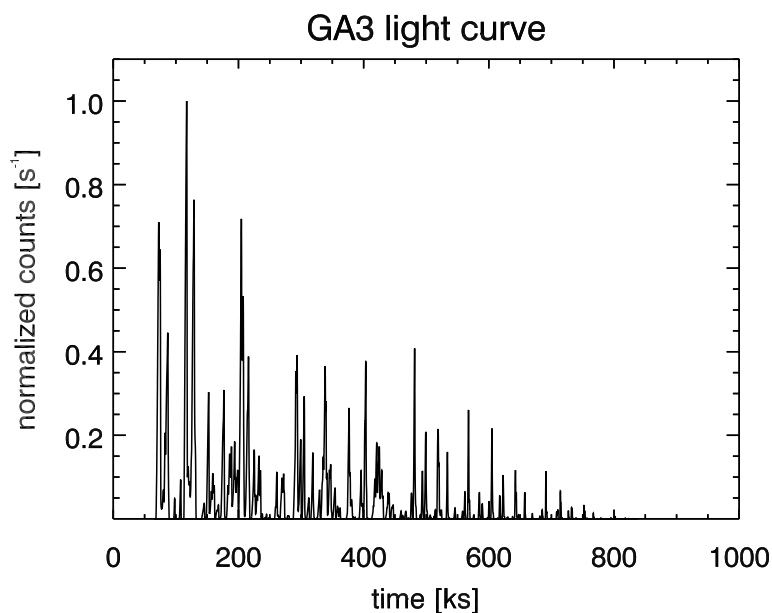


Figure 5.34: Soft light curve of model GA3. The parameters of the model are: $\Gamma_0 = 8$, $\sigma_\Gamma = 0.1$, $\Delta T_e = 1$ ks, $\rho_0 = 10^{-18}$ g cm⁻³ and $p_0/\rho_0 c^2 = 10^{-4}$.

by the fact that in an inhomogeneous jet model (Fig. 5.31) the internal shocks form immediately upon ejection of the fluid from the central engine. Hence, an observer collects more photons from those shocks which were formed at earlier times, and sees a monotonically decreasing light curve.

This trend is not seen in observations (Brinkmann et al. 2003), and we have to refine our model to account for this. Such a refinement consists

of adding a quiescence period when the central engine is ejecting a fluid of lower density. In the simplest extension of our model, we assume that the shells are ejected as described above, but with a quiescence period ΔT_e between subsequent shell ejections. The new parameter added here is ρ_1 , the density of the fluid ejected between shells. The Lorentz factor of that fluid is assumed to be Γ_0 , and its ratio of pressure to density to be the same as for the shells.

Accordingly, another two long-term models $T1$ and $T2$ have been computed, simulating a segment of a jet 5×10^{15} cm long. The use of the remapping technique (see section 5.1.2) has made it possible to follow the evolution up to a distance of more than 8×10^{16} cm. Figures 5.35 and 5.36 show the synthetic soft light curves of models $T1$ and $T2$ using the same shock acceleration parameters as in the models $GA1$, $GA2$ and $GA3$. The density of the fluid ejected during the latency period is half of the density of the shell fluid. The number of zones in the numerical grid is 3750, the number of non-thermal electron energy bins is 48, and the number of frequencies at which the radiation is computed is 21.

There is no monotonic trend in light curves of models $T1$ and $T2$. The light curves are the result of the collisions of denser shells separated by lighter fluid. The prominent peaks of the light curves originate from those collisions where the Lorentz factors and the relative velocity are large enough (see section 5.3.2 for discussion of the peak luminosity and the initial shell properties). One also recognizes that there is a “background” in each light curve originating from hundreds of less luminous collisions whose peaks, viewed in the observer frame, have merged. This can be one possible source of confusion when one applies the analytic model described in section 5.4, since it has to be clear that the observed flare originates from only one collision, and is not a structure formed from many merged flares, not resolved individually due to the limited time resolution of the instrument. However, the brightest peaks originate from single, very efficient collisions.

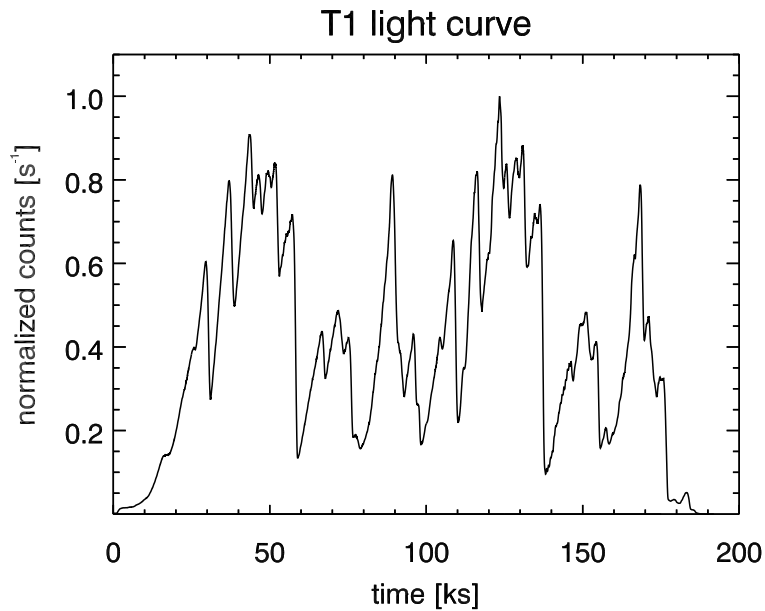


Figure 5.35: Soft light curve of model T1. The parameters of the model are: $\Gamma_0 = 8$, $\sigma_\Gamma = 0.1$, $\Delta T_e = 3$ ks, $\rho_0 = 10^{-19}$ g cm $^{-3}$ and $p_0/\rho_0 c^2 = 10^{-4}$, $\rho_1/\rho_0 = 0.5$.

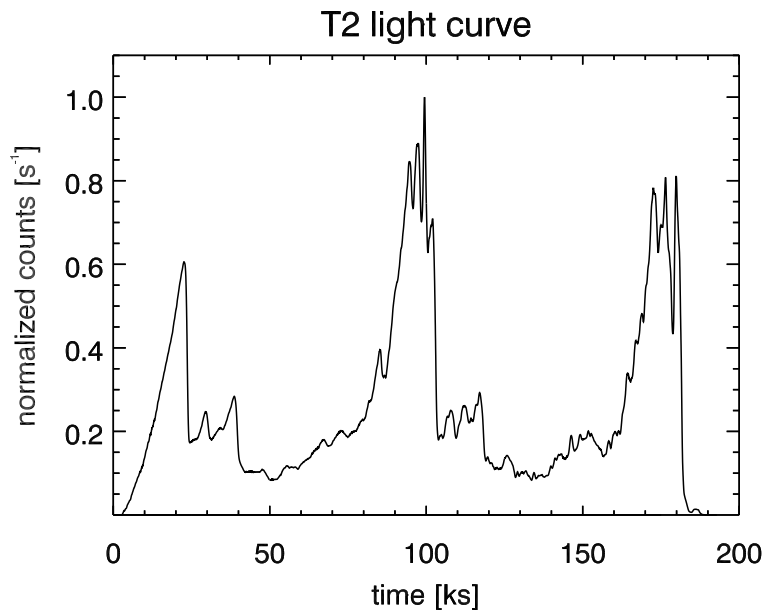


Figure 5.36: Soft light curve of model T2. The parameters of the model are: $\Gamma_0 = 8$, $\sigma_\Gamma = 0.05$, $\Delta T_e = 3$ ks, $\rho_0 = 10^{-19}$ g cm $^{-3}$ and $p_0/\rho_0 c^2 = 10^{-4}$, $\rho_1/\rho_0 = 0.5$.

Chapter 6

Summary and conclusions

6.1 Summary of the results

We have used a new numerical tool to investigate the internal shock model for blazar flares. In total five two dimensional axisymmetric and 18 one dimensional simulations of collisions of dense shells have been simulated. In addition, three long-term simulations of an inhomogeneous flow emitted by the central engine and two long-term simulations of an inhomogeneous flow with a certain quiescence period of the central engine have been performed.

The analysis of the results of the two dimensional simulations of shell collisions (see Fig. 5.1 for the schematic description of the initial setup) shows that the sideways (in the radial direction) expansion of the shells is negligible, and thus one is well justified to use one dimensional simulations (assuming that all shells have the same radius, see however section 6.2). The shell interaction is influenced by the background medium during the phase when the faster shell catches up with the slower one (as opposed to the analytic models where no background medium is considered). The rarefaction in the background medium caused by the motion of the slower shell causes the faster shell to speed up, so that the collision of two shells takes place earlier than estimated analytically. Instead of having only two internal shocks we have four shocks, two at the front and two at the back end of each shell. The interaction of these shocks with the shell material and with each other makes the collision dynamics very nonlinear.

A study of the energetics of one dimensional models shows that the analytic model developed by Kobayashi et al. (1997) predicts quite well the amount of kinetic energy dissipated into the internal energy of the fluid. However, the amount of *emitted* energy (in the observer frame) does not simply scale with the dissipated kinetic energy. This is due to two effects: (1) the evolution of the magnetic field and of the non-thermal electron energy distribution during the course of interaction is complex and difficult to model; (2) the relativistic effects (Doppler shift, relativistic beaming) make it difficult to deduce the “intrinsic” emission properties of the shell interaction.

We have introduced the observer-xy coordinate system to study the spacetime evolution of the emissivity. In this frame the emissivity distri-

bution has a characteristic horn-like shape, with the tip of the horn corresponding to the spacetime event where the shell interaction starts. Inspired by the shape of the horn we have constructed an analytic model for blazar flares. The model assumes that internal shocks start propagating through the shells with a constant velocity until the forward shock breaks out of the slower shell, at which point both shocks accelerate. Fitting a model to the light curves of three of the simulations we obtain shock velocities which are compared to the shock velocities computed from the simulations and those predicted by Kobayashi et al. (1997). We find that the analytic model predicts the values computed from simulations reasonably well (on average the deviation Lorentz factors differs by up to $\sim 35\%$), while the model of Kobayashi et al. (1997) overestimates the shock velocities. Our analytic model also provides information about changes in the shock velocities after the forward shock breaks out of the slower shell (this information is not provided by Kobayashi et al. '97 model). The final shock velocities of our analytic model are reasonable upper bounds of the actual shock velocities in the late stages of the shell collision (average deviation between 7% and 21%). The analytic model also provides the values for the power law indices of the temporal change of the emissivity (see Section 5.4.1) which are in a quite good agreement with the results of the simulations. The agreement is surprisingly good when one takes into account that the analytic model assumes an average homogeneous emissivity distribution in the region of interaction, which is not exactly the case in the hydrodynamic simulation.

Comparison of some of the observed light curves of the typical blazar Mrk 421 with the synthetic light curves shows that the latter exhibit variations of somewhat larger amplitude. However, this could be due to the fact that the observed blazar flares possibly involve radiation from a background source which we do not include in our model.

Finally, long-term simulations show that the model of an intermittently working central engine seems to produce results more similar to current observations of blazars, since the continuous outflow produces a light curve with a long-term trend which is not observed. These results are preliminary and part of work in progress.

6.2 Next steps

This work can be continued in several directions:

- A more complete parameter study of the shell interactions will be performed changing the initial mass and geometry (e.g, the radii of the shells can be different) of the shells as well as their separation and relative velocity. The goal of that project is the development of a more realistic analytic model for the flares which could be used to interpret observations.
- Long-term simulations are promising since they allow to compare the statistical properties of the synthetic light curves with those of the

observed light curves. Moreover, in a simulation one has a complete knowledge of the properties of the source of inhomogeneous flow. Thus, it may be possible to relate statistical properties of the light curve (average peak separation, width, height, etc.) to the properties of the source. That would be a big step forward in the understanding of the nature of variations of the central engine.

- The results of the long-term simulations can be used as initial models for large-scale jet simulations whose aim would be to produce radio maps of parsec or kiloparsec-scale jets. These two-step studies might shed some light on the connection between the morphology present in large scale jets and the variability characteristics of subparsec scale jets.
- The numerical method which treats non-thermal particles and their radiation can be coupled with the RMHD code developed from the RHD code *GENESIS* (Leismann 2004). Using the exact knowledge of the magnetic field structure the observational properties (particularly the polarization) of extragalactic jets can be studied more realistically.
- In order to study the emission of γ -rays from blazar jets the inverse-Compton process has to be implemented in a non-local manner in the code. That requires a large amount of computational power and sophisticated software development.
- An ultimate goal is to perform three-dimensional simulations, because then one could study non-axisymmetric flows (i.e., precessing jets, shells whose centers are misaligned, etc.). Although the code is fully operational in three dimensions, the computational power available at present does not make it possible to run these physically most interesting simulations. However, with the advent of new fast processors and parallel systems, it may come within reach within a couple of years.

Appendix A

The fitting algorithm

The analytic model (5.44) has 12 free parameters, assuming that one knows the duration of the flare and can therefore use equation (5.51) to compute ΔL_{30} from the other parameters. However, analyzing the results of our numerical simulations and due to the physical conditions in the “two-shell” model, not every combination of the parameters describes a valid model. The constraints are (see section 5.4 for the description of three-phase flare model):

$$\Gamma_r < \Gamma_f \tag{A.1}$$

$$\Gamma_r < \Gamma'_r \tag{A.2}$$

$$\Gamma'_r < \Gamma'_f \tag{A.3}$$

$$\Gamma_f < \Gamma'_f \tag{A.4}$$

$$\Delta L_{10} < \Delta L_{20} \tag{A.5}$$

$$\Delta L_{20} < \Delta L_{30} \tag{A.6}$$

$$\Gamma_r^{-2} \Delta L_{10} < \Gamma_f^{-2} \Delta L_{20} \tag{A.7}$$

$$\Gamma_r^{-2} \Delta L_{20} < \Gamma_f'^{-2} \Delta L_{32} + \Gamma_f^{-2} \Delta L_{20} \tag{A.8}$$

$$\theta_{01} > 0 \tag{A.9}$$

$$\theta_{12} > 0 \tag{A.10}$$

$$\theta_{23} > 0 \tag{A.11}$$

$$\eta_{01} > 1 \tag{A.12}$$

$$\eta_{12} < 1 \tag{A.13}$$

$$\eta_{23} < 1 \tag{A.14}$$

Obviously, the phase space of the valid combinations of parameters (those satisfying the constraints (A.1) - (A.14)) has a very complicated structure.

The idea is to minimize the square deviation of the model light curve with respect to the “observed” light curve (computed from the simulation). Using a nonlinear least-square fitting algorithm (Marquardt 1963) from a single initial guess does not guarantee success due to the complicated structure of the parameter space (it is very easy to get “stuck” in the local minimum). In order to overcome this difficulty, Marquardt’s algorithm can be used in combination with a Monte-Carlo-like approach as following:

1. The minimum (a_i^{\min}) and maximum (a_i^{\max}) value for each parameter i is guessed.

2. A random value a_i from the interval $[a_i^{\min}, a_i^{\max}]$ is drawn. If a_i^{\min} and a_i^{\max} are of the same order then

$$p_i = p_i^{\min} + u(p_i^{\max} - p_i^{\min}).$$

If the maximum value is much larger than the minimum value, then

$$p_i = p_i^{\min} \left(\frac{p_i^{\max}}{p_i^{\min}} \right)^u,$$

where u is a random number between 0 and 1.

3. If the combination of parameters is valid in the sense of equations (A.1) - (A.14) it is used as an initial guess for Marquardt's algorithm. If the algorithm terminates successfully, the square deviation of the model and the observed light curve is computed and, if it is smaller than the smallest value obtained so far, it is chosen as the new global minimum.
4. Steps 2-3 are repeated for a large number of iterations.

We note that this algorithm does not guarantee that the solution which corresponds to the global minimum of the square deviation will be found. However, with increasing number of iterations the probability that the values of the parameters are close to the solution rises. We have used this algorithm in our fits of the light curves of our simulations with satisfactory results. The typical number of iterations is 10^5 - 10^6 .

Tests of the algorithm

We have tested the fitting algorithm by producing a synthetic light curve using the analytic model (5.44) and then using the algorithm to recover the parameters. This is a minimum self-consistency test.

In Table A.1 one can see the results of the test: the synthetic light curve (Fig. A.1) was generated using parameters in the column "inp". The algorithm was applied to that light curve for three different number of iterations, 10^5 , 5×10^5 and 10^6 . For each fixed number of iterations several different seeds for the random number generator were used. The results shown are the statistical mean and the standard deviation of the results for each of these different seeds. The interval from which the random numbers were drawn is shown in the column "interval".

As one can see, the values of θ_{12} , θ_{23} , η_{12} and η_{23} are very well recovered. The parameter ΔL_{10} is also well recovered. The Lorentz factors and ΔL_{20} and ΔL_{30} are recovered with less accuracy. This is due to the fact that there is a certain degree of degeneracy in these parameters since they appear in combinations in the analytic model (5.44), thus making it possible to obtain very similar light curves with different values of these parameters. The values of θ_{01} and η_{01} are more uncertain since the part of the light curve

par.	inp.	interval	10^5 iter.	5×10^5 iter.	10^6 iter
θ_{01}	2	[1, 5]	7 ± 7	5 ± 3	4 ± 2
θ_{12}	1	[1, 5]	0.99 ± 0.05	1.01 ± 0.01	0.999 ± 0.001
θ_{23}	0.1	[0.001, 1]	0.12 ± 0.06	0.09 ± 0.04	0.1 ± 0.001
Γ_r	7	[4, 15]	8 ± 1	9 ± 1	9 ± 1
Γ_f	8	[4, 15]	9 ± 2	10 ± 1	10 ± 1
Γ'_r	10	[4, 15]	11 ± 2	12 ± 2	12 ± 2
Γ'_f	12	[4, 15]	13 ± 2	14 ± 2	15 ± 2
$\Delta L_{10}[ks]$	1.77	[0.5, 10]	1.9 ± 0.7	2.4 ± 0.8	2.7 ± 0.8
$\Delta L_{20}[ks]$	7.07	[1, 100]	9 ± 5	10 ± 3	11 ± 3
$\Delta L_{30}[ks]$	212.13	[100, 2000]	800 ± 600	900 ± 400	1000 ± 700
η_{01}	100	[10, 50000]	60 ± 100	6 ± 1	5 ± 2
η_{12}	0.5	[0.01, 1]	0.47 ± 0.09	0.50 ± 0.01	0.499 ± 0.001
η_{23}	0.01	[0.001, 0.1]	0.012 ± 0.005	0.01 ± 0.0001	0.01 ± 0.0001

Table A.1: Results of a test of the fitting algorithm: The synthetic light curve was generated using values shown in the column “inp.”. The algorithm was then applied to that light curve using the minimum and maximum values for the parameters shown in the column “interval”. Tests for 10^5 , 5×10^5 and 10^6 iterations have been performed, using several different sequences of random numbers for a fixed number of iterations. The results shown in the last three columns of the table are the statistical mean and the standard deviation of results for different random number sequences.

affected by these parameters is usually very short, i.e., only a very small number of measurements (corresponds to the part of the light curve before the first peak on Fig. 2.1) is used to constrain those parameters.

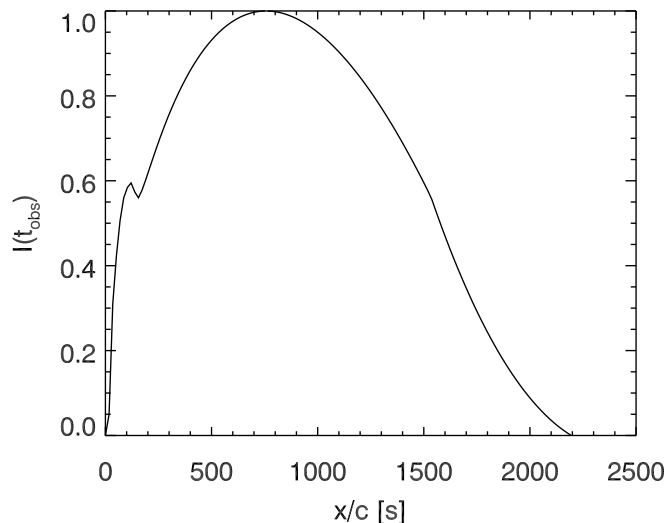


Figure A.1: A synthetic light curve used to test the fitting algorithm created using the analytic model (5.44) using parameters listed in Table A.1. All the fits recover the light curve completely, i.e., their light curves all lie on top of the synthetic light curve.

We can give an upper estimate on the errors of the fit by considering

that, when C is the number of iterations and M the number of parameters, one we can estimate the number of values between p_i^{\min} and p_i^{\max} which have been tried as $\approx C^{1/M}$. That means that the error in determining some parameter can roughly be estimated as $C^{-1/M}(p_i^{\max} - p_i^{\min})$. Except for θ_{12} , θ_{23} , η_{12} , and η_{23} this estimate seems to be a good upper limit on the errors shown in Table A.1.

List of Tables

2.1	The minimum Lorentz factor required to achieve desired accuracy	48
4.1	γ_{\min} , n_e^{acc} and $\bar{\gamma}$ for different \dot{p} and two different injection models	76
4.2	$\Delta(N, t)/10^{-4}$ as a function of the number of energy bins (rows) and the time of integration (columns)	82
4.3	$\Delta(N, t)/10^{-5}$ as a function of the number of energy bins (rows) and the number of calls to the EK solver	84
4.4	$\Delta(N, t)/10^{-4}$ as a function of the number of energy bins (rows) and the integration time after calling the EK solver with source term	84
5.1	Parameters used in simulations	93
5.2	Shell properties for 2D simulations	95
5.3	Shell properties for 1D simulations	103
5.4	Characteristic quantities of the simulations	110
5.5	Results of analytic model fit	128
A.1	Test of the fitting algorithm	143

List of Figures

1.1	M87 optical jet.	12
1.2	Cygnus A	13
1.3	Schematic picture of a radio source	14
1.4	Montage of different images of the radio galaxy M87.	16
1.5	2cm image of 3C345	19
1.6	Four simultaneous spectra of BL Lac	20
1.7	Averaged spectral energy distributions (SEDs) of the 126 blazars	21
1.8	X-ray light curves of Mrk 421	23
1.9	Structure function of Mrk 421	24
1.10	Apparent superluminal motion	25
1.11	AGN model in the unification scenario	27
1.12	The internal shock scenario	28
1.13	Interaction of two shells	28
1.14	Generic flare shape of Kobayashi et al. (1997)	29
1.15	Moderski et al. (2003) integration procedure	30
1.16	Radiative efficiency (Spada et al. 2001)	32
1.17	Structure function (Tanihata et al. 2003)	33
2.1	Particle trajectory in magnetic field	37
2.2	Plot of the function $F(x)$	41
2.3	Emissivity for the inverse-Compton scattering	49
2.4	Logarithm of the emissivity for the inverse-Compton scattering	50
2.5	Emissivity for a power law electron distribution	52
2.6	Comparison of the anisotropic and isotropic scattering emissivities	55
2.7	Dependence of the emissivity on electron power law index	55
3.1	A parallel shock in its rest frame	58
3.2	A relativistic shock with the loss cone	61
3.3	Temporal evolution of the initial power law distribution	64
3.4	Temporal evolution of injected electron distribution	65
4.1	Energy distribution for the model of type-E	76
4.2	Energy distribution for the model of type-N	77
4.3	Synchrotron emissivity for the model of type-E	78
4.4	Synchrotron emissivity for the model of type-N	79
4.5	Light curve computation scheme	80

4.6	Validation of the KE solver without source term	83
4.7	Errors of KE solver for small time steps	85
4.8	Validation of the KE solver with source term	86
4.9	Zoom in around the break in the solution	87
4.10	Synchrotron emissivity for the test with no source term . . .	88
4.11	Synchrotron emissivity for the test with the source term . .	89
5.1	A model of the blazar jet	92
5.2	Re-mapping procedure	94
5.3	Four stages of the hydrodynamic evolution	96
5.4	Four stages of the hydrodynamic evolution in 1D	97
5.5	Shocks and rarefactions near shell edges	98
5.6	S0 light curve	99
5.7	S0, D1 and D2 light curve	100
5.8	S0, D1 and D2 light curves in logarithmic scale	101
5.9	S0, P1 and P2 light curves	102
5.10	Relation between laboratory and observer-xy frames	105
5.11	Light curves of G0, G1 and G2	106
5.12	Light curves of G3, G6 and G8	107
5.13	Light curves of G4, G5 and G7	108
5.14	Light curves of G1, G7 and G8	109
5.15	G0 observer-xy emissivity plot	112
5.16	G1 observer-xy emissivity plot	113
5.17	G2 observer-xy emissivity plot	114
5.18	Spectral evolution of the light curves of G0, G1 and G2 . . .	115
5.19	Spectral evolution of the light curves of G3, G4 and G5 . . .	116
5.20	Spectral evolution of the light curves of G6, G7 and G8 . . .	117
5.21	A model of the expanding region	119
5.22	A typical light curve obtained with the analytic model . . .	121
5.23	A model of the three-phase expanding region	121
5.24	An example for the three-phase expanding region	126
5.25	Fit to the light curve of model G0E	127
5.26	Fit to the light curve of model G1E	129
5.27	Fit to the light curve of model G2E	129
5.28	Temporal evolution of the average emissivity	130
5.29	Observation of Mrk 421 during XMM orbit 084	131
5.30	Observation of Mrk 421 during XMM orbit 171 – 1	131
5.31	A model of an inhomogeneous onedimensional jet	132
5.32	GA1 soft light curve	133
5.33	GA2 soft light curve	134
5.34	GA3 soft light curve	134
5.35	T1 soft light curve	136
5.36	T2 soft light curve	136
A.1	A synthetic light curve used to test the fitting algorithm . .	143

Bibliography

- Achterberg, A., Gallant, Y. A., Kirk, J. G., and Guthmann, A. W., "Particle acceleration by ultrarelativistic shocks: theory and simulations". (2001), *Monthly Notices of the Royal Astronomical Society*, **328**, 393
- Aloy, M. A., Ibáñez, J. M., Martí, J. M., and Mueller, E., "GENESIS: A High-Resolution Code for Three-dimensional Relativistic Hydrodynamics". (1999), *Astrophysical Journal, Supplement*, **122**, 151
- Baade, W., "Polarization in the Jet of Messier 87". (1956), *Astrophysical Journal*, **123**, 550
- Bednarz, J. and Ostrowski, M., "The acceleration time-scale for first-order Fermi acceleration in relativistic shock waves". (1996), *Monthly Notices of the Royal Astronomical Society*, **283**, 447
- Bednarz, J. and Ostrowski, M., "Energy Spectra of Cosmic Rays Accelerated at Ultrarelativistic Shock Waves". (1998), *Physical Review Letters*, **80**, 3911
- Begelman, M. and Rees, M., "Gravity's fatal attraction. Black holes in the universe". (1996), Scientific American Library, New York: W.H. Freeman, —c1996
- Begelman, M. C., Blandford, R. D., and Rees, M. J., "Theory of extragalactic radio sources". (1984), *Reviews of Modern Physics*, **56**, 256
- Bell, A. R., "The acceleration of cosmic rays in shock fronts. I". (1978), *Monthly Notices of the Royal Astronomical Society*, **182**, 147
- Berezinskii, V. S., Bulanov, S. V., Dogiel, V. A., Ginzburg, V. L., and Putskin, V. S., "Astrophysics Of Cosmic Rays". (1990), North-Holland
- Bicknell, G. V. and Wagner, S. J., "The Evolution of Shocks in Blazar Jets". (2002), Publications of the Astronomical Society of Australia, **19**, 129
- Biraud, F. and Veron, P., "VRO 42 22 01 - A Variable Source with Circular Polarization". (1968), *Nature*, **219**, 254
- Blandford, R. D. and McKee, C. F., "Fluid dynamics of relativistic blast

- waves". (1976), *Physics of Fluids*, **19**, 1130
- Blandford, R. D. and Ressler, M. J., "A 'twin-exhaust' model for double radio sources". (1974), *Monthly Notices of the Royal Astronomical Society*, **169**, 395
- Bridle, A. H., "Sidedness, field configuration, and collimation of extragalactic radio jets". (1984), *Astronomical Journal*, **89**, 979
- Bridle, A. H., Henriksen, R. N., Chan, K. L., Fomalont, E. B., Willis, A. G., and Perley, R. A., Collimation of the radio jets in 3C 31. (1980), *Astrophysical Journal, Letters*, **241**, L145
- Bridle, A. H., Hough, D. H., Lonsdale, C. J., Burns, J. O., and Laing, R. A., "Deep VLA imaging of twelve extended 3CR quasars". (1994), *Astronomical Journal*, **108**, 766
- Bridle, A. H. and Perley, R. A., "Extragalactic Radio Jets". (1984), *Annual Review of Astronomy and Astrophysics*, **22**, 319
- Brinkmann, W., Papadakis, I. E., den Herder, J. W. A., and Haberl, F., "Temporal variability of Mrk 421 from XMM-Newton observations". (2003), *Astronomy and Astrophysics*, **402**, 929
- Brinkmann, W., Sembay, S., Griffiths, R. G., Branduardi-Raymont, G., Gliozzi, M., Boller, T., Tiengo, A., Molendi, S., and Zane, S., "XMM-Newton observations of Markarian 421". (2001), *Astronomy and Astrophysics*, **365**, L162
- Bykov, A. M. and Meszaros, P., "Electron Acceleration and Efficiency in Nonthermal Gamma-Ray Sources". (1996), *Astrophysical Journal, Letters*, **461**, L37+
- Cawthorne, T. V.. (1991), "*Interpretation of parsec scale jets*", pp 187–+, Beams and Jets in Astrophysics
- Celotti, A., "Composition and energetics of relativistic jets". (2003), *Astrophysics and Space Science*, **288**, 175
- Chang, J. S. and Cooper, G., "A practical difference scheme for Fokker-Planck equations". (1970), *Journal of Computational Physics*, **6**, 1
- Chiaberge, M. and Ghisellini, G., "Rapid variability in the synchrotron self-Compton model for blazars". (1999), *Monthly Notices of the Royal Astronomical Society*, **306**, 551
- Colella, P. and Woodward, P. R., "The Piecewise Parabolic Method (PPM) for Gas-Dynamical Simulations". (1984), *Journal of Computational Physics*, **54**, 174

- Curtis, H. D.. (1918), Publications of Lick Observatory, **13**, 9
- Daigne, F. and Mochkovitch, R., "Gamma-ray bursts from internal shocks in a relativistic wind: temporal and spectral properties". (1998), *Monthly Notices of the Royal Astronomical Society*, **296**, 275
- Davis, R. J., Muxlow, T. W. B., and Unwin, S. C., "Large-scale superluminal motion in the quasar 3C273". (1991), *Nature*, **354**, 374
- Donat, R., Font, J. A., Ibanez, J. M., and Marquina, A., "A Flux-Split Algorithm Applied to Relativistic Flows". (1998), *Journal of Computational Physics*, **146**, 58
- Edelson, R., Griffiths, G., Markowitz, A., Sembay, S., Turner, M. J. L., and Warwick, R., "High Temporal Resolution XMM-Newton Monitoring of PKS 2155-304". (2001), *Astrophysical Journal*, **554**, 274
- Fabian, A. C., "Theories of the nuclei of active galaxies". (1979), Royal Society of London Proceedings Series A, **366**, 449
- Fanaroff, B. L. and Riley, J. M., "The morphology of extragalactic radio sources of high and low luminosity". (1974), *Monthly Notices of the Royal Astronomical Society*, **167**, 31P
- Feigelson, E. D., Bradt, H., McClintock, J., Remillard, R., Urry, C. M., Tapia, S., Geldzahler, B., Johnston, K., Romanishin, W., Wehinger, P. A., Wyckoff, S., Madejski, G., Schwartz, D. A., Thorstensen, J., and Schaefer, B. E., "H 0323 + 022 - A new BL Lacertae object with extremely rapid variability". (1986), *Astrophysical Journal*, **302**, 337
- Fermi, E., "On the Origin of the Cosmic Radiation". (1949), *Physical Review*, **75**, 1169
- Fossati, G., Maraschi, L., Celotti, A., Comastri, A., and Ghisellini, G., "A unifying view of the spectral energy distributions of blazars". (1998), *Monthly Notices of the Royal Astronomical Society*, **299**, 433
- Gallant, Y. A. and Achterberg, A., "Ultra-high-energy cosmic ray acceleration by relativistic blast waves". (1999), *Monthly Notices of the Royal Astronomical Society*, **305**, L6
- Gratton, L., "Source Models with Electron Diffusion". (1972), *Astrophysics and Space Science*, **16**, 81
- Hoffmeister, C., "354 neue Veränderliche". (1929), *Astronomische Nachrichten*, **236**, 233
- Holt, S. S., Neff, S. G., and Urry, C. M. (eds.). (1992), "Testing the AGN paradigm; Proceedings of the 2nd Annual Topical Astrophysics Confer-

ence, Univ. of Maryland, College Park, Oct. 14-16, 1991”

- Hoyle, F., Burbidge, G. R., and Sargent, W. L. W., "On Nature of Quasistellar Sources". (1966), *Nature*, **209**, 751
- Hummel, C. A., Muxlow, T. W. B., Krichbaum, T. P., Quirrenbach, A., Schalinski, C. J., Witzel, A., and Johnston, K. J., "MERLIN and VLBI observations of the quasar 0836 + 710 - Morphology of a parsec-kiloparsec scale jet". (1992), *Astronomy and Astrophysics*, **266**, 93
- Jackson, W. D., "Classical Electrodynamics". (1962), John Wiley & Sons, Inc., New York-London
- Jennison, R. C. and Das Gupta, M. K.. (1953), *Nature*, **172**, 996
- Jones, T. W., Ryu, D., and Engel, A., "Simulating Electron Transport and Synchrotron Emission in Radio Galaxies: Shock Acceleration and Synchrotron Aging in Axisymmetric Flows". (1999), *Astrophysical Journal*, **512**, 105
- Kardashev, N. S., "Nonstationarity of Spectra of Young Sources of Nonthermal Radio Emission". (1962), *Soviet Astronomy*, **6**, 317
- Kirk, J. G., Guthmann, A. W., Gallant, Y. A., and Achterberg, A., "Particle Acceleration at Ultrarelativistic Shocks: An Eigenfunction Method". (2000), *Astrophysical Journal*, **542**, 235
- Kobayashi, S., Piran, T., and Sari, R., "Can Internal Shocks Produce the Variability in Gamma-Ray Bursts?". (1997), *Astrophysical Journal*, **490**, 92
- Le Veque, R. J., "Numerical Methods for Conservation Laws". (1991), Birkhaeuser, Basel
- Leismann, T.. (2004), "*Relativistic Magnetohydrodynamic Simulations of Extragalactic Jets*", *Ph.D. thesis*, Technische Universitaet, Muenchen
- Linfield, R. and Perley, R., "3C 111 - A luminous radio galaxy with a highly collimated jet". (1984), *Astrophysical Journal*, **279**, 60
- Makino, F., Edelson, R., Fujimoto, R., Kii, T., Idesawa, E., Makishima, K., Takahashi, T., Sasaki, K., Kamae, T., Kubo, H., Mathis, D., Tashiro, M., Teräsranta, H., and Urry, C. M.. (1996), in *Roentgenstrahlung from the Universe*, pp 413–416
- Marquardt, D. W., "An Algorithm for Least-Squares Estimation of Nonlinear Parameters". (1963), *SIAM Journal on Applied Mathematics*, **11**, 431
- Marti, J. M. and Mueller, E., "Extension of the Piecewise Parabolic Method

- to One-Dimensional Relativistic Hydrodynamics". (1996), *Journal of Computational Physics*, **123**, 1
- Marti, J. M., Mueller, E., and Ibanez, J. M., "Hydrodynamical simulations of relativistic jets". (1994), *Astronomy and Astrophysics*, **281**, L9
- Mimica, P., Aloy, M. A., Müller, E., and Brinkmann, W., "Synthetic X-ray light curves of BL Lacs from relativistic hydrodynamic simulations". (2004), *Astronomy and Astrophysics*, **418**, 947
- Moderski, R., Sikora, M., and Błażejowski, M., "Numerical simulations of radiation from blazar jets". (2003), *Astronomy and Astrophysics*, **406**, 855
- Muxlow, T. W. B. and Garrington, S. T.. (1991), in *Beams and Jets in Astrophysics*, pp 52–+
- Padovani, P. and Giommi, P., "The connection between x-ray- and radio-selected BL Lacertae objects". (1995), *Astrophysical Journal*, **444**, 567
- Pearson, T. J.. (1996), in *ASP Conf. Ser. 100: Energy Transport in Radio Galaxies and Quasars*, pp 97–+
- Pearson, T. J. and Readhead, A. C. S., "The milliarcsecond structure of a complete sample of radio sources. II - First-epoch maps at 5 GHz". (1988), *Astrophysical Journal*, **328**, 114
- Pedlar, A., Unger, S. W., and Dyson, J. E., Radio Seyferts and the forbidden-line region. (1985), *Monthly Notices of the Royal Astronomical Society*, **214**, 463
- Pier, E. A. and Krolik, J. H., "Radiation-pressure-supported obscuring tori around active galactic nuclei". (1992), *Astrophysical Journal, Letters*, **399**, L23
- Ravasio, M., Tagliaferri, G., Ghisellini, G., Giommi, P., Nesci, R., Massaro, E., Chiappetti, L., Celotti, A., Costamante, L., Maraschi, L., Tavecchio, F., Tosti, G., Treves, A., Wolter, A., Balonek, T., Carini, M., Kato, T., Kurtanidze, O., Montagni, F., Nikolashvili, M., Noble, J., Nucciarelli, G., Raiteri, C. M., Sclavi, S., Uemura, M., and Villata, M., "BL Lacertae: Complex spectral variability and rapid synchrotron flare detected with BeppoSAX". (2002), *Astronomy and Astrophysics*, **383**, 763
- Rees, M. J. and Meszaros, P., "Unsteady outflow models for cosmological gamma-ray bursts". (1994), *Astrophysical Journal, Letters*, **430**, L93
- Rowan-Robinson, M., "On the unity of activity in galaxies". (1977), *Astrophysical Journal*, **213**, 635

- Rybicki, G. B. and Lightman, A. P., "Radiative Processes in Astrophysics". (1979), Wiley Interscience Publication
- Sambruna, R. M., Maraschi, L., Tavecchio, F., Urry, C. M., Cheung, C. C., Chartas, G., Scarpa, R., and Gambill, J. K., "A Survey of Extended Radio Jets in Active Galactic Nuclei with Chandra and the Hubble Space Telescope: First Results". (2002), *Astrophysical Journal*, **571**, 206
- Schmitt, J. L., "BL Lac Identified as a Radio Source". (1968), *Nature*, **218**, 663
- Shklovskii, I. S., "On the Nature of Radio Galaxies". (1963), *Soviet Astronomy*, **6**, 465
- Shu, C. W. and Osher, S. J., "Efficient Implementation of Essentially Non-oscillatory Shock-Capturing Schemes". (1988), *Journal of Computational Physics*, **77**, 439
- Simonetti, J. H., Cordes, J. M., and Heeschen, D. S., "Flicker of extragalactic radio sources at two frequencies". (1985), *Astrophysical Journal*, **296**, 46
- Spada, M., Ghisellini, G., Lazzati, D., and Celotti, A., "Internal shocks in the jets of radio-loud quasars". (2001), *Monthly Notices of the Royal Astronomical Society*, **325**, 1559
- Stein, W. A., Odell, S. L., and Strittmatter, P. A., "The BL Lacertae objects". (1976), *Annual Review of Astronomy and Astrophysics*, **14**, 173
- Strittmatter, P. A., Serkowski, K., Carswell, R., Stein, W. A., Merrill, K. M., and Burbidge, E. M., "Compact Extragalactic Nonthermal Sources". (1972), *Astrophysical Journal, Letters*, **175**, L7+
- Takahashi, T., Tashiro, M., Madejski, G., Kubo, H., Kamae, T., Kataoka, J., Kii, T., Makino, F., Makishima, K., and Yamasaki, N., "ASCA Observation of an X-Ray/TeV Flare from the BL Lacertae Object Markarian 421". (1996), *Astrophysical Journal, Letters*, **470**, L89+
- Tanihata, C., Takahashi, T., Kataoka, J., and Madejski, G. M., "Implications of Variability Patterns Observed in TeV Blazars on the Structure of the Inner Jet". (2003), *Astrophysical Journal*, **584**, 153
- Ulrich, M., Maraschi, L., and Urry, C. M., "Variability of Active Galactic Nuclei". (1997), *Annual Review of Astronomy and Astrophysics*, **35**, 445
- Urry, C. M. and Padovani, P., "Unified Schemes for Radio-Loud Active Galactic Nuclei". (1995), *Publications of the ASP*, **107**, 803

- Wagner, S. J. and Witzel, A., "Intraday Variability In Quasars and BL Lac Objects". (1995), *Annual Review of Astronomy and Astrophysics*, **33**, 163
- Wilson, A. S., "Kiloparsec scale radio structure in active galaxies". (1983), *Highlights in Astronomy*, **6**, 467
- Zensus, J. A., "Parsec-Scale Jets in Extragalactic Radio Sources". (1997), *Annual Review of Astronomy and Astrophysics*, **35**, 607
- Zensus, J. A., Cohen, M. H., and Unwin, S. C., "The Parsec-scale jet in quasar 3C 345". (1995), *Astrophysical Journal*, **443**, 35

Acknowledgements

It is with great pride and gratitude that I can say that I am not the first student whose burden of a PhD thesis was carried in large part by Miguel-Ángel Aloy. Without his code *GENESIS* this work would not be possible. His door was always open to me, his comments constructive and his humor encouraging (“If you do all I want you to do, you will never finish!”). And most of all, he did not let me waste PhD (and postdoc) time. Moltes gràcies!

Ich danke meinem Betreuer Ewald Müller für das kritische Durchsehen dieser Doktorarbeit. Sehr dankbar bin ich ihm auch dafür dass er mir das IMPRS-Stipendium zu bekommen geholfen hat, und für die motivierende Atmosphäre die in unserer Hydro Gruppe herrscht.

Tobias Leismann bin ich dankbar für die Idee, meine Methode auf seine Ergebnisse anzuwenden und wunderschöne Cyg-A-like Radiokarte zu produzieren.

I would like to thank José-María Martí and José-María Ibañez and the rest of the group in Valencia for their hospitality during my visit in April 2004.

I thank my thesis advisor at PMF-Zagreb Krešimir Pavlovski for suggesting that I apply for the IMPRS fellowship and for helping me with my thesis. Hvala, Krešo!

I acknowledge the support of the International Max-Planck Research School on Astrophysics whos fellow I was from September 2001 till September 2004.

Jens teilt seit März 2002 das Büro mit mir. Ich bin ihm dankbar dass er mir mit meinem Deutsch (manchmal auch zu eifrig ;)) geholfen hat.

I thank Serena for all the car trips, bike trips, ski trips, Sneak Previews, ... Thanx, Sere!

Ich danke Corina für die Einführung in die Welt der Fantasy-Literatur und dass sie mir ihren neuen Astra anvertraut hat!

I thank Patricia and Jorge for all the barbecues and dinners and Carcassonne evenings at their place!

I thank Don Carlos, Kaustuv, Señor Alberto and the rest of the “lunch-bunch” for eating too fast and too slow and for helping imagine that the IPP-Kantine food is edible.

Jessi bin ich für alle Rollerbladen/Radfahren Nachmittage die ich im Englischen Garten statt vor dem Computer verbrachte dankbar!

Bojan mi je bio cimer skoro tri godine. Zahvalan san mu za zajedničko kuhanje, za sve legalne i ilegalne fajlove, za duge znanstvene i političke diskusije i, najvažnije, za to šta mi je pokazao kako opuštenije pristupiti životu u Njemačkoj. Fala majstore!

Renati fala za “podršku iz daljine”, za sve telefonske razgovore i za “Ne daj se Floki, ostani psina!”.

Dijani fala za gostoprimstvo u Minhenu i kasnije u Potsdamu i za to šta dilimo isti entuzijazam za trance!

Roku san zahvalan na dugogodišnjem prijateljstvu i razumijevanju.

Ujki Jošku fala za to šta me 1989. uveo u svijet kompjutera.

Braći Rudi i Anti san zahvalan sta su mi uvijek bili prijatelji i podrška.

Mami Mileni i tati Špiru fala za to šta ni meni ni mojoj braći nisu nametali stavove niti određivali životni put.

Curriculum Vitae

- **Personal information**

- Born on March 22nd, 1978 in Split, Croatia
- Nationality: Croatian

- **Education and academical history**

- **September 2001 - September 2004.** Ph.D. student in astrophysics at the Max-Planck-Institut für Astrophysik in Garching (Germany) as a fellow of the International Max-Planck Research School (IMPRS) on Astrophysics. PhD thesis under the supervision of Dr. Miguel-Angel Aloy, Dr. Ewald Müller and Dr. Wolfgang Brinkmann.
- **September 1996 - January 2001.** Physics graduate at the University of Zagreb, Croatia. Diploma Thesis: “Accretion Disk Image Reconstruction using Genetic Algorithms” under the supervision of prof. Krešimir Pavlovski.
- **September 1992 - June 1996.** Graduate of the 3rd Mathematical Gymnasium in Split, Croatia
- **September 1984 - June 1992.** elementary school “Pjero Perak” in Omiš, Croatia

- **Research publications**

1. Mimica P., Aloy M-A., Müller E., Brinkmann W., *Synthetic X-ray light Curves of BL Lacs from Relativistic Hydrodynamic Simulations*, 2004, *Astronomy & Astrophysics*, 418, 947
2. Mimica P., Aloy M-A., Müller E., Brinkmann W., *Computation of X-ray Blazar Light Curves using RHD Simulations*. Proceedings of the conference “Virtual Jets”, Dogliani October 2-4, 2003, in press

- **Participation in conferences and workshops**

- **October 2-4, 2003:** conference “Virtual Jets” in Dogliani (Italy), given a talk “Computation of X-ray Blazar Light Curves using RHD Simulations”
- **September 16-19, 2003:** 23rd Young European Radio Astronomers Conference in Bonn (Germany), given a talk “Computing X-ray Blazar Light Curves”
- **June 24-28, 2003:** conference “Particle Acceleration in Astrophysical Objects” in Cracow (Poland), presented a poster “Using RHD Simulations to study Internal Shocks in Blazar Jets”
- **November 5-7, 2002:** “Introduction to Parallel Computing Workshop” in Heidelberg (Germany)
- **September 23-27, 2002:** conference “The Physics Of Relativistic Jets in the CHANDRA and XMM Era” in Bologna (Italy)